POLYTECHNIQUE MONTRÉAL

affiliée à l'Université de Montréal

Development of Prestressed Fibre-Reinforced Concrete Girders For Short-Span Bridges

LUIZ MARCHETTI

Département des génies civil, géologique et des mines

Mémoire présenté en vue de l'obtention du diplôme de *Maîtrise ès sciences appliquées*

Génie civil

Avril 2026

POLYTECHNIQUE MONTRÉAL

affiliée à l'Université de Montréal

Ce mémoire intitulé :

Development of Prestressed Fibre-Reinforced Concrete Girders For Short-Span Bridges

présenté par **Luiz MARCHETTI**

en vue de l'obtention du diplôme de *Maîtrise ès sciences appliquées*

a été dûment accepté par le jury d'examen constitué de :

Najib BOUAANANI, président

Jean-Philippe CHARRON, membre et directeur de recherche

Bruno MASSICOTTE, membre et codirecteur de recherche

Sébastien VERGER LEBOEUF, membre

ACKNOWLEDGEMENTS

I would like to express my deepest gratitude to my supervisor, **Jean-Philippe Charron**, for his unwavering support, insightful guidance. Your willingness to meet weekly and your readiness to answer questions at all times made a significant difference in the progress and quality of this work. I have learned a great deal from your remarkable organizational skills and the calm, thoughtful way in which you approach decisions—qualities that I deeply admire and aspire to carry forward.

I am also thankful to my co-supervisor, **Bruno Massicotte**, for the high-level discussions and valuable technical insights that greatly enriched this thesis. The depth of our conversations made every meeting intellectually stimulating and challenged me to continuously refine my work.

Special thanks are due to the laboratory staff, whose technical assistance made the experimental phase possible. In particular, I would like to thank **Abdelhak Draoui**, whose expertise, patience, and commitment were fundamental to the successful execution of the laboratory work. Your support went far beyond technical help—thank you.

I wish to thank **BPDL**, **Euclid** and the team involved in the fabrication of the specimens. Your hard work, precision, and the high quality of your contributions were essential to the successful completion of this research. My sincere thanks to **Stéphane Martel**, **Nicolas Dupuis**, **Sebastien Fontaine** from BPDL and **Eric Boisvert** and **Etienne Moris** from Euclid for your professionalism and dedication.

I would also like to thank the fellow students who supported me throughout this journey. Your collaboration, camaraderie, and shared struggles made this experience much more manageable and enjoyable. A special thank you to **Espoir Kahama**, for the constant discussions, shared ideas, and many political discussions that were always a delight. And to **Danilo Vaz**, thank you: for being there to listen— even without understanding a word of structural engineering—, for your support and for your patience. For sure the many laughs we shared helped lighten even the most intense days.

Finally, I extend my heartfelt appreciation to my family, who, despite being thousands of kilometres away, stood by me with unconditional love, emotional support, and encouragement. Your belief in me carried me through the most challenging moments of this journey. Thank you, **Pai, Mãe, Giugiu and Belinha**.

RÉSUMÉ

La détérioration des infrastructures de ponts en béton armé dans les régions froides est fortement accélérée par des conditions environnementales agressives et par des impacts mécaniques répétés, entraînant une réduction de la durée de vie en service et une augmentation des coûts d'entretien. En milieu urbain dense, la faible hauteur libre sous les ponts limite également les solutions de réhabilitation, ce qui motive le développement de systèmes de ponts plus minces, plus durables et rapides à construire. Cette thèse porte sur le développement et le comportement structural de poutres de ponts précontraintes en béton fibré à hautes performances (BFHP) avec dalle intégrée, connectées longitudinalement par des joints en béton fibré à ultra-hautes performances (BFUP).

L'objectif principal de cette recherche est de finaliser et de valider la conception de ces poutres tout en améliorant la compréhension des mécanismes de résistance au cisaillement dans les éléments en BFHP précontraints. L'étude combine une conception structurale conforme aux normes canadiennes en vigueur, un programme expérimental approfondi sur des poutres à l'échelle réelle et des analyses numériques avancées. Quatre poutres précontraintes en BFHP, présentant différentes géométries, portées de cisaillement et niveaux de précontrainte, ont été fabriquées en usine de préfabrication et soumises à des essais de flexion trois-points afin d'évaluer leur comportement en flexion et en cisaillement. La caractérisation des matériaux, la corrélation d'images numériques (DIC), l'analyse de l'orientation des fibres et la modélisation numérique non linéaire par éléments finis ont été utilisées pour quantifier la contribution des différents mécanismes de résistance au cisaillement, notamment la traction des fibres, l'engrènement des granulats, l'effet de goujon et l'action de la bielle comprimée.

Les résultats expérimentaux démontrent que les poutres en BFHP présentent une résistance au cisaillement accrue, un contrôle efficace de la fissuration et des modes de rupture ductiles, permettant une réduction significative, voire l'élimination, des armatures transversales conventionnelles. Les analyses montrent que la précontrainte et l'orientation des fibres influencent fortement la contribution relative des mécanismes de cisaillement, la traction des fibres et l'action de la bielle comprimée étant dominantes. La comparaison avec les prédictions des normes de conception actuelles met en évidence des estimations conservatrices de la résistance au cisaillement. Les résultats confirment la faisabilité de poutres précontraintes en BFHP optimisées

pour la construction accélérée de ponts et fournissent des pistes pour l’amélioration des méthodes de dimensionnement au cisaillement dans les normes futures.

ABSTRACT

The deterioration of reinforced concrete bridge infrastructure in cold regions is strongly accelerated by aggressive environmental exposure and repeated mechanical impacts, leading to reduced service life and increased maintenance costs. In dense urban environments, limited vertical clearance under bridges further constrains rehabilitation solutions, motivating the development of thinner, more durable, and rapidly constructible bridge systems. This thesis investigates the development and structural behaviour of prestressed bridge girders made of high-performance fibre-reinforced concrete (HPFRC) with an integrated deck slab, connected longitudinally using ultra-high-performance fibre-reinforced concrete (UHPFRC) joints.

The research aims to finalize and validate the design of such girders while improving the understanding of shear resistance mechanisms in prestressed HPFRC members. The study combines structural design according to current Canadian standards, an extensive experimental program on full-scale girders, and advanced analytical investigations. Four prestressed HPFRC girders with varying geometries, shear spans, and prestressing levels were fabricated in a precast plant and tested under three-point bending to assess flexural and shear behaviour. Material characterization, digital image correlation (DIC), fibre orientation analysis, and nonlinear finite element modelling were employed to quantify the contribution of individual shear-resisting mechanisms, including fibre tensile resistance, aggregate interlock, dowel action, and compression chord action.

Experimental results demonstrate that HPFRC girders exhibit enhanced shear resistance, controlled cracking, and ductile failure modes, allowing for a significant reduction or elimination of conventional shear reinforcement. The analysis reveals that prestressing and fibre orientation strongly influence the relative contribution of shear mechanisms, with fibre tensile resistance and compression chord action playing dominant roles. Comparisons with current design code predictions highlight conservative estimations of shear capacity. The findings support the feasibility of optimized prestressed HPFRC girders for accelerated bridge construction and provide insights for improving shear design approaches in future codes.

TABLE OF CONTENTS

LIST OF TABLES

LIST OF FIGURES

LIST OF SYMBOLS AND ABBREVIATIONS

A_g	Gross area of section
A_p	Area of prestressing tendons
A_s	Area of longitudinal reinforcement
A_{sw}	Reinforcement area
A_v	Shear reinforcement area
b_w	Beam web width
$C_{rd,c}$	Lower inbound parameter
D_b	Diameter of reinforcing bar
d_g	Average aggregate size (fib)
DIC	Digital Image Correlation System
d_v	Effective shear depth
e_p	Eccentricity of load or prestressing force parallel to axis measured from centroid of section
E_p	Modulus of elasticity of prestressing tendons
E_s	Modulus of elasticity of steel reinforcement
f_c	Compressive strength of concrete
f_c'	Nominal (or specified) compressive strength of concrete.
f_{ci}'	Short-term compressive strength of concrete.
f_{ck}	Compressive strength of concrete (fib)
f_{cri}'	Short-term tensile strength of concrete.
FLS	Fatigue Limit State
f_{po}	Stress in prestressing tendons
FRC	Fibre Reinforced Concrete
f_t'	Nominal tensile strength of concrete.
f_y	Reinforcement yield stress
f_{ywd}	Design yield strength of the shear reinforcement
HPC	High Performance Concrete
HPFRC	High Performance Fibre Reinforced Concrete
HS	High Strength
I	Moment of inertia about centroidal axis.

k	Size factor
k_{dg}	Aggregate size influence parameter
k_v	Shear resistance reduction factor
M_{ed}	Design value of applied bending moment
M_f	Factored bending moment
M_{sd}	Bending moment due to superimposed dead load
M_{sls}	Design bending moment at SLS-1
M_{sw}	Bending moment due to self weight
M_{uls}	Design bending moment at ULS-1
N_{ed}	Design value of applied axial force
N_f	Factored axial load normal to the cross-section
NLFE	Non Linear Finite Element model
NSC	Normal Strength Concrete
P_i	Prestressing force immediately after transfer
s	Reinforcement spacing
SLS	Service Limit State
S_z	Equivalent value of that accounts for the influence of aggregate size
s_{ze}	Crack spacing parameter
SFRC	Steel Fiber Reinforced Concrete
UHPFRC	Ultra-High Performance Fibre Reinforced Concrete
ULS	Ultimate Limit State
v_c	Contribution of the tensile for in the concrete contribution to the shear resistance
v_{ed}	Design value of applied shear force
V_{fib}	Contribution of the fibres to the shear resistance
V_f	Factored shear force
V_p	Contribution of prestressing force to the shear resistance
$v_{rd,c}$	Contribution of the tensile force in the concrete to the shear resistance (fib)
$v_{rd,s}$	Contribution of the stirrups to the shear resistance (fib)
v_s	Contribution of the stirrups to the shear resistance
w/c	Water to cement ratio
z	Internal lever arm

z_p	Distance between the centerline of the compressive chord and the tendon axis
z_s	Distance between the centerline of the compressive chord and the reinforcement axis
B	Damage factor for tensile stresses in the cracked concrete
γ_c	Material safety factor
ε_x	Longitudinal strain at mid-depth of the member due to factored loads
θ	Crack angle
$\lambda_{\gamma F}$	Fibre efficiency factor to account for low-density concrete
ρ_l	Longitudinal reinforcement ratio
ϕ_c	Resistance factor for concrete

LIST OF APPENDICES

CHAPTER 1 INTRODUCTION

1.1 Context

Cracking is the key initiating mechanism of concrete degradation. Cracks appear due to shrinkage, creep, service loads, and thermal or moisture variations. Among the consequences of cracking, reinforcement corrosion is the most prevalent form of deterioration, triggered by concrete carbonation or chloride penetration, and leading to steel cross-section loss, cracking, spalling, and delamination of the concrete cover (Bah et al., 2024). In Quebec, freeze–thaw cycles, particularly in the presence of de-icing salts, cause internal cracking and surface scaling. In addition, chemical mechanisms such as alkali–aggregate reaction and sulfate attack generate expansive reaction products within the cement matrix, resulting in progressive cracking and a significant reduction in the structural durability of reinforced concrete elements (Charron & Desmettre, 2013a). According to the Quebec Ministry of Transport and Sustainable Mobility, 28% of the 9,913 bridges and engineering structures managed by the Ministry require major maintenance work within the next five years (Ministère des transports et de la mobilité durable, 2024).

Besides environmental conditions, truck impacts are increasingly becoming a problem. The vertical clearance under bridges in urban areas is sometimes too limited for truck traffic, which frequently leads to damage to the bottom web of the girders. Le Journal de Montréal (Journal Montreal, 2021) reported, for example, that three trucks struck the pont des Carrières located on Papineau Avenue between 2017 and 2021.

Figure 1.1 – Truck trapped under Viaduc des Carrières in 2021

Raising the bridge to avoid damaging the beams would require very complex work in an urban environment to adjust the new profile of the roadway. It is also not economically feasible to lower the level of the roadway under the bridge, as public utilities (sewers, electrical network, etc.) are located underground. The foundations in some cases would also have to be lowered, which would further increase the cost of the structure. In Montreal, several of these roadway bridges have twin railway bridges which also limit practical options. The most efficient remaining solution is to reduce the thickness of the bridge deck to increase the vertical clearance under the viaduct without changing the profile of the roadway above and below the bridge.

Hence, one of the goals of this project is to propose a replacement solution for existing underpass bridge superstructures in the City of Montreal. The idea is to provide a construction system that fall into the philosophy of accelerated bridge construction (ABC). This methodology uses prefabrication with the objective of having a more compact geometry to increase the clearance under the bridges using new designs and enhanced durability with utilization of fibre reinforced concretes. The proposed solution is composed of prestressed bridge girders made of high-performance fibre-reinforced concrete (HPFRC) with an integrated deck slab connected by a longitudinal joint made of ultra-high-performance fibre-reinforced concrete (UHPC).

According to Massicotte et al. (2012), the use of HPFRC in prestressed girders would allow for the following improvements:

• simplify the reinforcing steel in the deck by using only a single layer in the transverse direction;

• reduce the number of stirrups in the beam;

• achieve low cracking during service.

It is known that the addition of steel fibres increases the shear resistance which can lead to using less stirrups whereas fibre ability of control cracking facilitates adopting straight tendon layout which also contributes to reducing fabrication costs. The other objective of the present study will be to further understand the contribution of fibres to the shear resistance of the girders.

1.2 Objectives

The general objective of this study is to finalize design of prestressed bridge girders made of high-performance fibre-reinforced concrete (HPFRC) with an integrated deck slab as well as evaluate the shear resistance mechanisms involved in the behaviour of HPFRC girders.

The specific objectives are as follows:

- optimize and validate the design of HPFRC prestressed bridge girders;
- evaluate in laboratory how prestressing, shear span and girder's shape influences the shear resistance of HPFRC girders;
- understand how different shear resisting mechanisms act in HPFRC girders;
- provide recommendations to improve shear strength evaluation of design codes for HPFRC girders.

1.3 Methodology

This study combines the design of prestressed HPFRC bridge girders with integrated deck slabs, the experimental validation and numerical investigations. The following steps were carried out in this study:

- identification of beam design requirements;
- selection of HPFRC properties and longitudinal reinforcement for prestress and passive reinforcement for the HPFRC girder;

- design of prototype girders according to the research needs using conventional design tools;
- production of HPFRC girders in a precast plant;
- laboratory testing of material characterization specimens, and of bridge girder specimens;
- coring of girders to determine experimental fibre orientation factor;
- development of a MATLAB code to interpret the digital image correlations (DIC) data;
- development of a nonlinear finite element (NLFE) numerical model validated with the experimental results and its application for determining the compression chord contribution;
- conclusions and recommendations.

1.4 Thesis structure

This thesis contains six chapters. In addition to the Chapter 1 which is an introduction, the literature review in Chapter 2 presents the past projects that were used as an inspiration for the current thesis, as well as a state-of-the-art review on the topics necessary to conduct the research on the shear behaviour of HPFRC girders. In Chapter 3, the design of the specimens is presented with all the steps involved in dimensioning the girders. Chapter 4 details the experimental campaign conducted to validate the design and provides an analysis of the results obtained. Chapter 5 presents an in-depth analysis of the shear mechanisms using the DIC data as input and a MATLAB algorithm to treat those data, as well of NLFE numerical models. Finally, the conclusions and recommendations for the project are presented in Chapter 6. The main documents generated as well as the main design information are provided in the appendix.

CHAPTER 2 LITERATURE REVIEW

2.1 Past development on HPFRC bridge girders

The current research project is a continuation of numerous research projects on the development of HPFRC bridge girders that took place in the past. All of them improved the bridge standard that would in sum, accelerate construction works on site, lower the costs of fabrication and maintenance of urban bridges while increasing its lifespan for the city of Montreal. Figure 2.1a illustrates the different research projects conducted over the years to optimize the bridge deck.

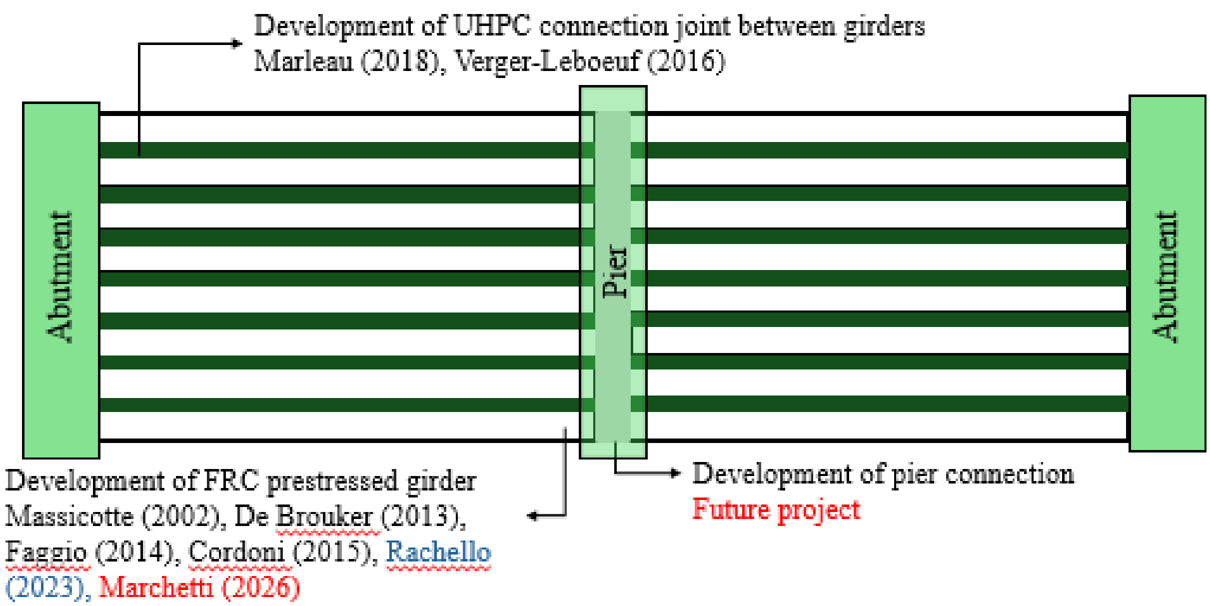

Figure 2.1 – Simplified plan view of a bridge superstructure

FRC deck slab design with reduced conventional reinforcement has been developed at Polytechnique Montréal from 1996 to 2002 (see Massicotte et al. 2016). De Brouker (2013) was the first to test FRC prestressed girders in bending and shear, while Faggio (2014) optimized the shape of the deck between adjacent girders and proposed a parabolic soffit that enabled using only one reinforcement layer that would be sufficient to resist bending moments in positive and negative regions in the same spirit of the worked carried out in the 1996-2002 project. She was the first to test the flexural behaviour of cast-in-place UHPC joints. Building on these past studies, Cordoni

(2015) completed the design prestressed HPFRC T-girders with an integrated slab based on the two previous studies, as illustrated in Figure 2.2.

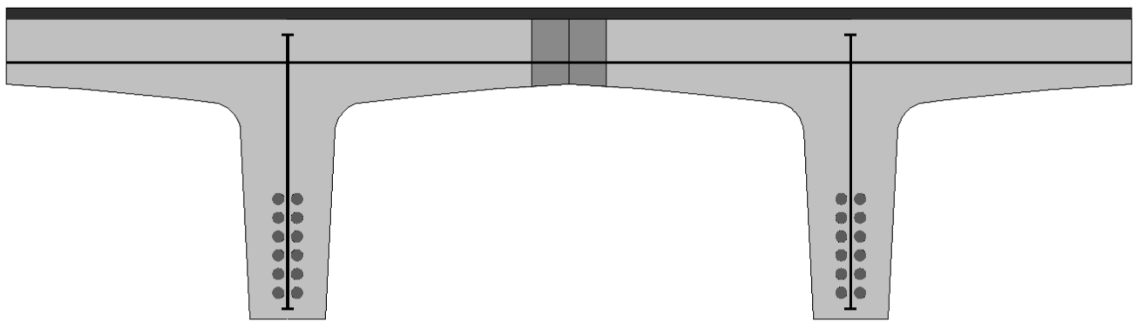

Figure 2.2 – Original precast prestressed HPFRC girders cross section with UHPC longitudinal field connection (Cordoni, 2015)

Rachello (2023) refined the design prestressed HPFRC T-girders for applications where limiting the girder depth was a constraint as for the City of Montreal applications. The final cross-section of the bridge girder with an integrated deck recommended by Rachello is presented in Figure 2.3.

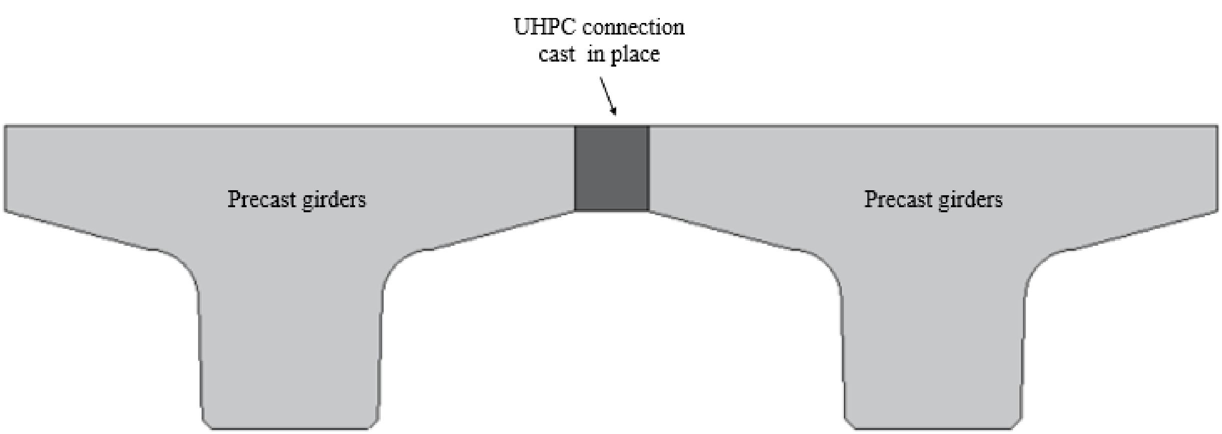

Figure 2.3 – Compact precast prestressed HPFRC girders cross section with UHPC longitudinal field connection (adapted from Rachello, 2023)

As suggested in previous studies, UHPC connections will be used between adjacent precast girders. Verger-Leboeuf (2016) and Marleau (2018) carried out extensive studies on UHPC connections to transversely connect precast bridge deck elements. Details on these developments are provided in the next sections.

2.1.1 UHPC connection joints, Verger-Leboeuf (2016)

Sébastien Verger-Leboeuf's (2016) research project (Verger Leboeuf, 2016) focused on the development and evaluation of UHPC connection joints for precast bridge deck slabs. The study aimed to design innovative transverse and longitudinal connection joints that ensure the mechanical continuity, durability, and serviceability of precast slabs assembled on-site. Using a combination of numerical modelling, laboratory experimentation, and parametric analysis, Verger-Leboeuf optimized joint geometry, reinforcement overlap length, bar spacing, and interface conditions between the joint and slabs. The experimental program included full-scale slab specimens made of high-performance concrete (HPC), high-performance fibre-reinforced concrete (HPFRC), and hybrid HPFRC–UHPC configurations, tested under static and cyclic loading to simulate one million truck axle passes. The results demonstrated that UHPC joints as narrow as 150 to 200 mm can effectively transfer loads and control cracking without post-tensioning, achieving mechanical performance equal to monolithic cast-in-place slabs.

Figure 2.4 presents the moment–deflection and moment–crack opening responses for all slab configurations, revealing that UHPC joints combined with FRC slabs significantly increased stiffness and limited crack openings compared to conventional HPC systems. Complementary finite element modelling confirmed the experimental findings and showed that using precast slabs with UHPC joints does not compromise overall bridge behaviour, validating this technology as a reliable and efficient solution for accelerated construction and durable bridge decks.

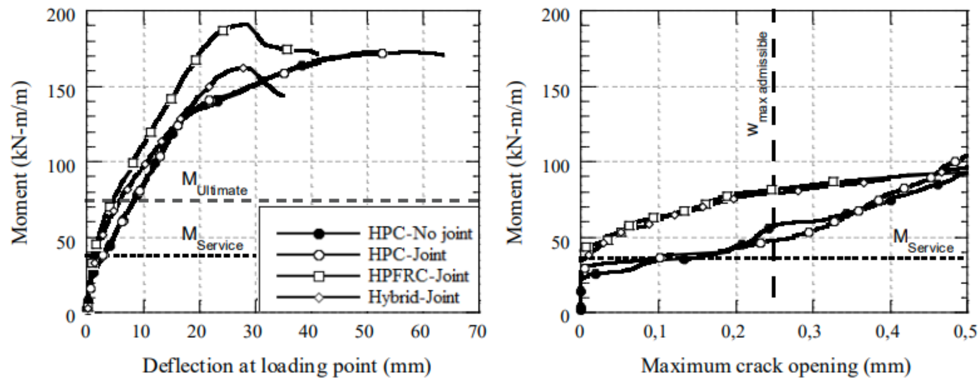

a) Moment – deflection response b) Moment – maximum crack opening response

Figure 2.4 - Specimen behaviour under quasi-static loading (Verger Leboeuf, 2016)

2.1.2 UHPC connection joints fatigue resistance, Marleau (2018)

Benoît Marleau's (2018) research project focussed on the experimental study of the fatigue behaviour of UHPC joints used between precast bridge deck slabs. The study aimed to further investigate the fatigue performance of UHPC joints for Quebec bridge infrastructure. The project included an extensive experimental program with 20 full-scale slab specimens, 17 using UHPC joints and 3 made of conventional reinforced concrete joint (RC), tested under cyclic and monotonic loading to simulate real bridge conditions. Various parameters were investigated, including UHPC fibre dosage, bar overlap configuration in joint, joint orientation (longitudinal and transverse), curing methods, and concrete types in joints. By analyzing the structural performance, fatigue endurance, and failure mechanisms of these joints, the research sought to define design guidelines and performance criteria ensuring the reliability, durability, and efficiency of UHPC connections in bridge construction and rehabilitation.

The main results of Marleau's research demonstrated that UHPC joints provide superior fatigue performance and structural durability compared to conventional concrete joints used in precast bridge slabs. Figure 2.5 presents the fatigue behaviour of all tested slabs, clearly showing that UHPC joints maintain structural stiffness and limit deflection over millions of load cycles, unlike conventional concrete joints (yellow curves) that exhibited early stiffness loss. Collectively, these findings validate the UHPC joint design for both longitudinal and transverse configurations, providing a robust framework for implementing this technology in bridge construction and rehabilitation.

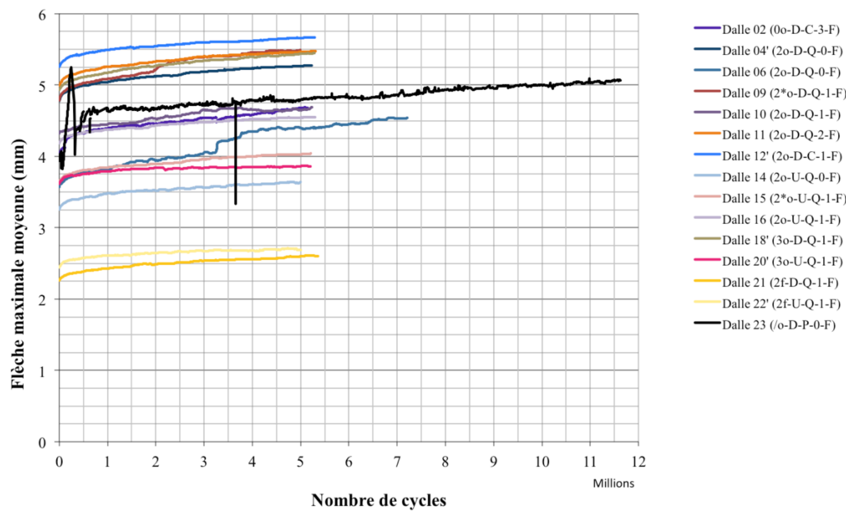

Figure 2.5 - Global fatigue performance of all specimens(Marleau, 2017)

2.1.3 Bridge slab configuration, Faggio (2014)

Léa Faggio’s (2014) research project (Massicotte et al., 2014) focused on the design, modelling, and validation of steel fibre–reinforced concrete (SFRC) bridge decks, building upon prior Canadian and international experience with fibre-reinforced materials in structural applications. The study aimed to develop a simplified and reliable design method for SFRC bridge decks that could replace traditional reinforced concrete (RC) systems while maintaining equivalent safety, serviceability, and durability. Through a combination of analytical modelling, laboratory experiments, and finite element simulations, Faggio evaluated the mechanical behaviour of SFRC slabs under static and cyclic loads, comparing them to conventionally reinforced decks.

Figure 2.6 illustrates the comparative flexural behaviour of SFRC and conventional reinforced concrete slabs under both static and cyclic loads, revealing that SFRC members exhibit superior ductility, reduced stiffness loss, and enhanced post-cracking strength retention. The project ultimately proposed a simplified plastic design approach that integrates direct tensile test results, fracture mechanics, and serviceability criteria, enabling engineers to design SFRC decks with reduced reinforcement while ensuring long-term durability and load-bearing capacity. This research provided the theoretical and practical foundation for using high-performance SFRC materials in accelerated bridge construction and deck rehabilitation.

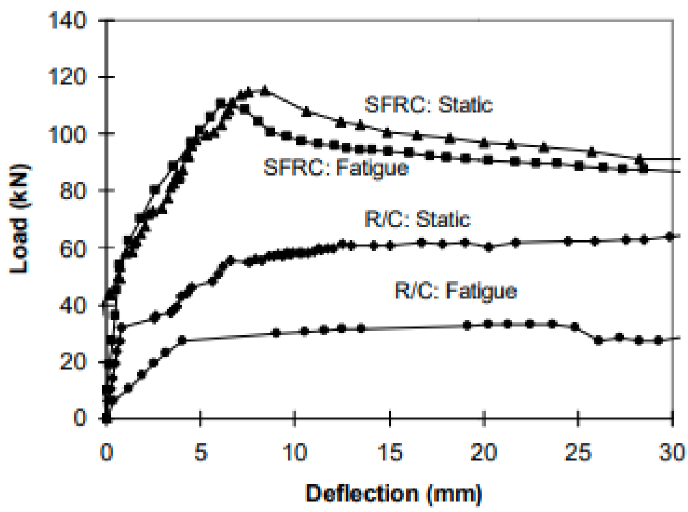

Figure 2.6 – Behaviour of SFRC member under bending in static and cyclical conditions (Massicotte et al., 2014)

2.1.4 Bridge girder configuration, Cordoni (2015)

Nicola Cordoni's (2015) master research project focussed on the numerical design and validation of a new generation of fully precast bridge girders made of SFRC and connected with UHPC joints. The project aimed to improve bridge durability and constructability under Quebec severe climate. Cordoni's work addressed the lack of design standards for SFRC by integrating experimental results from previous large-scale beam tests with advanced finite element simulations (EPM3D model in ABAQUS/Explicit) to predict the flexural and shear response of prestressed SFRC T-girders. The main results of Cordoni demonstrated that SFRC can effectively replace traditional RC and post-tensioned connections in precast, prestressed T-girders without compromising strength, ductility, or serviceability.

Using the validated EPM3D nonlinear finite element model, Cordoni showed that fibre reinforcement significantly enhanced both flexural and shear behaviours, reducing maximum crack widths by up to 50% and increasing post-cracking stiffness and energy absorption (Figure 2.7).

The numerical simulations closely matched previous experimental beam tests from the same research program, confirming the model predictive accuracy.

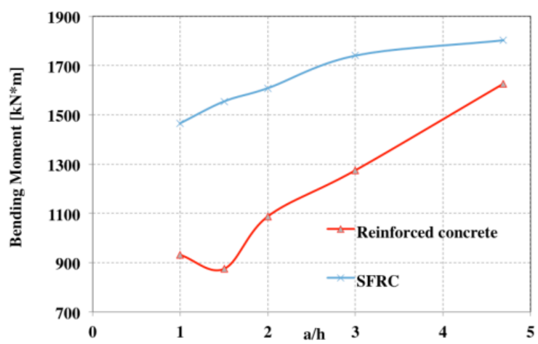

a) Bending-slenderness graphic with and without steel fibres

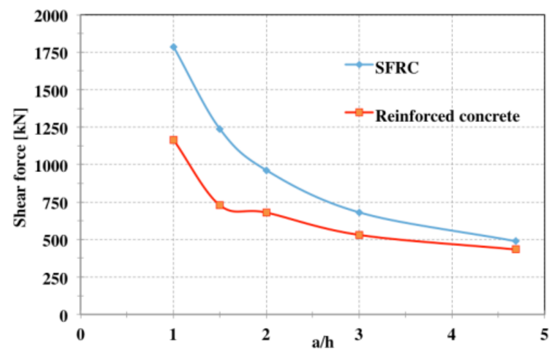

b) Shear- slenderness graphic with and without steel fibres

Figure 2.7 – Variance of forces according to the shear span to depth ratio a/h in the concrete mix (Cordoni, 2015)

Overall, results demonstrated that the addition of steel fibres significantly reduced crack width, improved ductility and shear strength, and enabled the use of a single reinforcement layer in the slab, simplifying fabrication and reducing costs. Ultimately, Cordoni's research established the numerical and conceptual basis for implementing prefabricated SFRC bridge systems, combining durability, efficiency, and accelerated construction methods.

2.1.5 Bridge girder configuration with integrated slabs, Rachello (2023)

Adrien Rachello's (2023) master research project focussed on the development, experimental testing, and optimization of a new prestressed bridge girder made of HPFRC with an integrated deck slab. The project aimed to design and validate a prototype beam system integrating prestressing and fibre reinforcement to reduce conventional reinforcement, simplify construction, and enhance long-term durability in harsh northern climates. Using a combination of experimental large-scale beam tests and analytical evaluations, Rachello investigated key parameters such as fibre dosage, prestressing force, shear performance, and bond behaviour between the girder and the integrated slab.

The main results of Rachello's thesis demonstrated that prestressed fibre-reinforced concrete (FRC) girders with integrated deck slabs can achieve superior cracking control, flexural strength, and durability compared to traditional reinforced or prestressed concrete bridge systems. The experimental program, which included full-scale bridge girders tested under service and ultimate loads, confirmed that incorporating 60 to 80 kg/m³ of hooked-end steel fibres allows for a significant reduction in conventional reinforcement while maintaining ductility and safety under loading. Unfortunately, due to fabrication problems (lack of UHPC flowability near the tendons) it was not possible to fully validate the girders since they had an early shear failure in laboratory as shown in Figure 2.8. The study also pointed out the large difference between the theoretical shear resistance calculated with CSA-S6 (Rachello Adrien, 2023) and the experimental one of girders tested in the laboratory. Nevertheless, Rachello's numerical models confirmed that, without the fabrication problem, the girders would have shown adequate shear resistance.

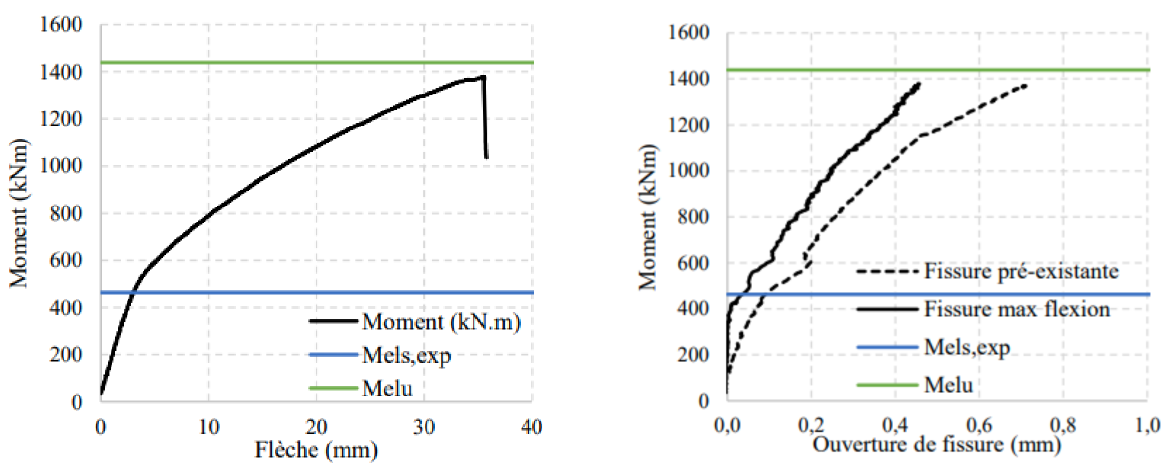

a) Moment-deflection curve

b) Moment-maximum bending crack opening curve

Figure 2.8 - Bending behaviour of experimental Beam 2 (Rachello Adrien, 2023)

Rachello's findings confirmed that precast, prestressed FRC girders with integrated slabs represent a viable and efficient solution for accelerated bridge construction, offering reduced material use and enhanced long-term durability under Quebec demanding climate conditions.

The present research project aims to finalize the design of the HPFRC prestressed girder with integrated slab developed by Rachello, by proposing an alternative configuration to improve the shear resistance. Also, the shear behaviour of HPFRC girders will be investigated to better understand shear resistance mechanisms and suggest code modifications for their evaluation.

2.2 Fibre Reinforced Concrete

Concrete has become the most extensively utilized construction material. It has, however, some defects such as low cracking resistance, limited toughness and moderate durability (Zhang et al., 2018). The addition of various types of fibres can enhance the mechanical and durability properties of concrete and thus fix some of its defects. Even though fibre reinforced concretes exist for more than 100 years, only in the last decades that it’s has been extensively studied (Naaman, 2018). Yet there is still a lot to be studied so that this material can be wildly used just like conventional concrete.

2.2.1 Composition

Table 2.1 summarizes the composition of Normal Strength Concrete (NSC), High Performance Concrete (HPC) and High-performance fibre reinforced concrete (HPFRC). To move from NSC to HPC with higher strength, several modifications were made to the mixes. Unlike NSC, HPC has a lower water/binder ration and uses superplasticizers to maintain a good workability (Walraven, 2009). The mixture can further be improved with mineral additives, which makes the paste more compact and thus increase the resistance. In general terms, a HPC consists of a cementitious matrix with higher compressive strength (50-90 MPa) compared to a NSC (20-40MPa).

A HPFRC is obtain with introducing a small percentage of long fibres (>30mm), typically 0.5% to 1.5%, in replacement of the same volume of aggregate (Afroughsabet et al., 2016). The fibre addition generally not modified the compressive and tensile strengths, but it modifies significantly the tensile fracture energy with the fibre bridging effect.

Table 2.1 – Summary of different concrete compositions (Charron & Desmettre, 2013b)

Properties	NSC	HPC	HPFRC
Water cement ratio	>=0.4	0.30–0.40	0.3 - 0.4
Cement	300–400 kg/m³	350–450 kg/m³	350–550 kg/m³
Mineral admixtures	Maybe	Yes	Yes
Sand	Yes	Yes	Yes
Gravel	Yes	Yes	Yes
Fibres	No	No	40 - 120 kg/m3 (0.5 - 1.5%-vol.)
Compression	20 - 40 Mpa	50 - 90 MPa	50 - 90 MPa
Traction	1.5 - 2.5 MPa	3.0 - 4.5 MPa	3.0 - 4.5 MPa
Module of Elasticity	20 - 25 GPa	25 - 35 GPa	25–35 GPa

2.2.2 Characteristics of fibres

Several compositions (natural, synthetic or steel) and shapes (straight, hooked ends, twisted or crimped) of fibres can be added in concrete to improve its mechanical performance (Naaman, 2018). For this review of the literature, only steel fibres will be considered, as they are the only ones used in this project.

Some important aspects regarding the fibre characteristics can be listed that greatly affect the mechanical properties of the FRC:

- Fibre length (l_f) significantly affects the mechanical performance of FRC. Steel fibres with lengths of 30–60 mm are commonly used for structural applications, while shorter fibres (6–20 mm) are suitable for crack control and enhancing ductility depending of the mechanical properties of the matrix (Paul et al., 2020).
- Deformed fibre shapes, e.g., hooked end, crimped, or twisted, improve mechanical bond and pullout resistance by up to 50 % compared to straight fibres (Hassan & Saeed, 2024; Pham, 2025).
- High modulus fibres, such as steel (200 GPa) are better suited to bridge cracks and transfer stress when compared to low modulus fibres, like polypropylene (3–5 GPa) and polyethylene (80–120 GPa) fibres (Hassan & Saeed, 2024; Pham, 2025).
- Fibre aspect ratio (l_f/d_f). Higher aspect ratios improve crack bridging and tensile strength while lower ratios enhance workability and dispersion. The optimal range varies with application but ideally it should be higher than 50 (Yazici et al., 2007).

2.2.3 Mechanical properties

2.2.3.1 Compression

The increase in paste density mentioned in the previous paragraph for HPC increases compressive strength. There is a drawback to the increase of compressive strength. The more resistant the concrete, the more brittle it becomes. The addition of fibres, if the FRC is well designed, can improve ductility in the compression failure by limiting crack propagation as it can be seen in Figure 2.9a. However, fibres can sometimes cause imperfections in the matrix that initiate crack initiation and slightly reduce compressive strength as it can be seen on data series NF2 and NF3 of Figure 2.9b. In other words, even though the fibers can be beneficial to the compressive strength of the concrete (Figure 2.9a), it increases the variation of results (Figure 2.9b).

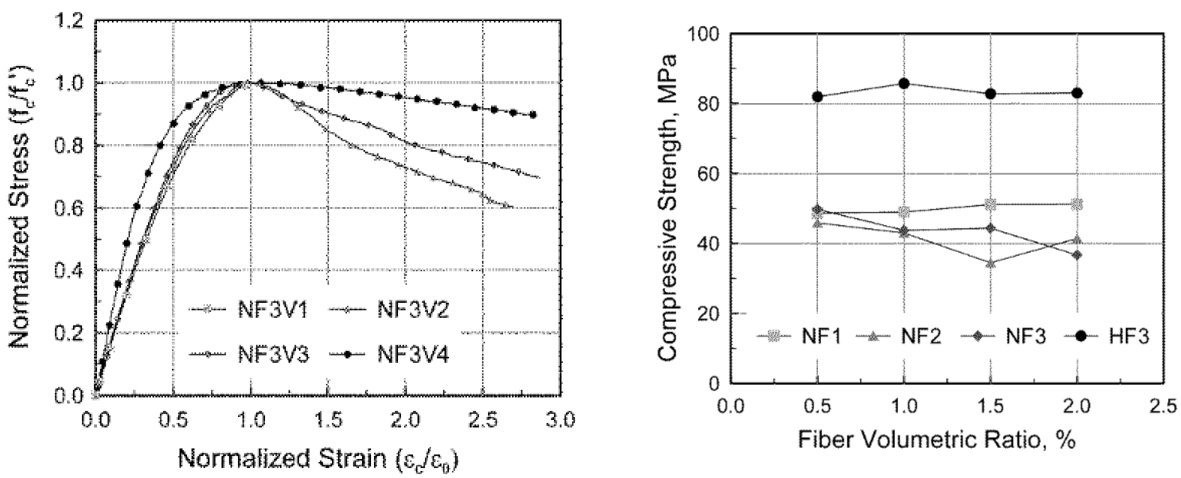

a) Effect of fibre volumetric ratio on the stress-strain response under compression

b) Measured compressive strength

Figure 2.9 – Effect of fibres on compressive behaviour of concrete (Lee et al., 2015)

2.2.3.2 Traction

Compared to plain concrete, HPFRC is much more ductile due to the crack bridging phase that will be described in the next paragraphs. In general, the FRC tensile behaviour can be divided into 3 different phases. Figure 2.10 shows the different phases divided by a straight line. The first one is the linear phase; the second one is considered the zone of micro cracking that can be controlled by microfibres (rarely use in HPFRC), and the third and final one is the zone of localization of a macrocrack controlled more efficiently by macrofibres (normally use in HPFRC) (Afroughsabet et al., 2016).

- Phase 1: Up until point A of Figure 2.10, HPFRC behaves like non-fibre-reinforced concrete. This is because the fibres do not change the propagation of microcracks. This section can be called of linear phase (Löfgren, 2005).
- Phase 2: From point A to B, microcracks will start to grow initially at the interface between the cement paste and the aggregates and eventually the microcracks propagate into the mortar. Once the peak is reached, crack localization occurs (Löfgren, 2005).
- Phase 3: From point B to C, some microcracks form a continuous pattern and lead to the localization of a macrocrack visible to the naked eye. Only when this macro crack opens do the microcracks stop developing. For FRC and HPFRC, a decrease in the resistance is noted (Löfgren, 2005).

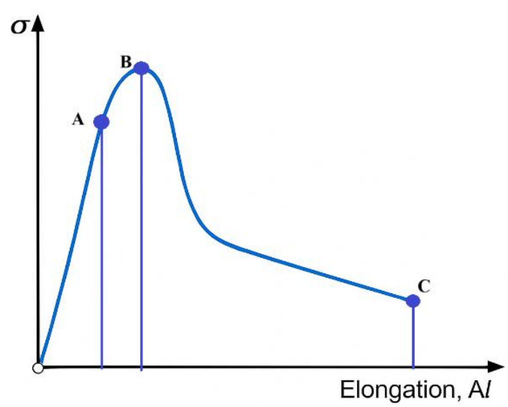

Figure 2.10 - Schematic description of the stress-crack opening relationships for FRC (Löfgren, 2005)

The tensile behaviour of concrete varies significantly depending on the presence and dosage of fibres, as well as the type of fibres. The Phase 1 of NSC (BO) and HPC (BHP), as well as HPFRC (BFHP) containing 1% vol. of steel macro-fibres, are illustrated in Figure 2.11a. while the post-peak or phase 3 is illustrated in Figure 2.11b.

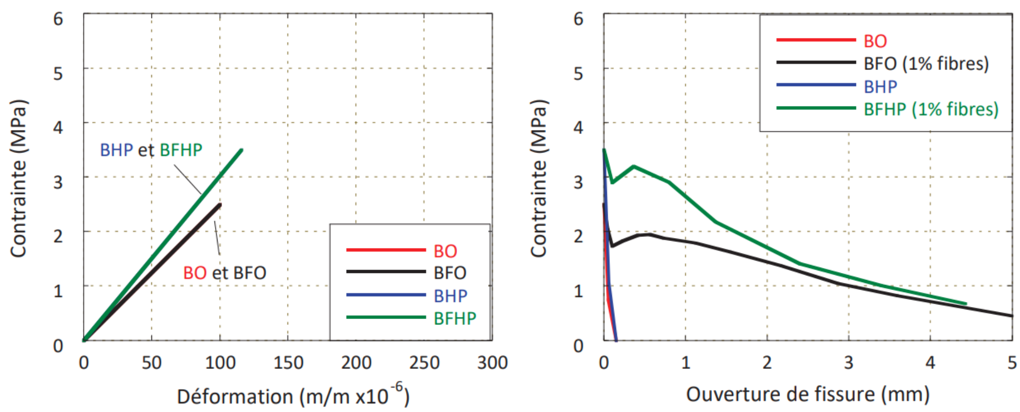

a) Pre-Peak behaviour b) Post-peak behaviour

Figure 2.11 – Uniaxial tensile behaviour of Ordinary and fibre reinforced concretes (Charron et al., 2016)

The pre-peak behaviour of NSC, HPC, and HPFRC is usually measured in microns and has a length of just a few hundred microns per meter (Figure 2.11a). For HPFRC, once the cracking strength is reached (end of phase 2), a macrocrack is created in the concrete, and the post-peak behaviour takes place (Figure 2.11b). The post-peak behaviour will differ depending on whether fibres are present or not. NSC and HPC exhibit very brittle behaviour (sudden drop in strength after the peak strength). This explains why the tensile strength contribution is neglected in reinforced concrete calculations. The concretes that are reinforced with fibres, on the other hand, have a considerably higher ductility in tension, which can be considered in design, particularly in service condition (Charron et al., 2016).

2.2.3.3 Impact of fibre orientation

The presence of fibres has a significant impact on tensile behaviour of FRC. The maximum performance of fibres is obtained when they are oriented perpendicular to the crack (Aidarov et al., 2024; Hassan & Saeed, 2024; Plagué et al., 2017) and is null when they are parallel to the crack. Variations in fibre orientation across the failure plan of FRC specimens lead to scatter in mechanical properties (Pham, 2025). Doyon-Barbant and Charron (2018) have quantified the impact of fibre orientation on the tensile behaviour of FRC. They used HPFRC with a strength f'c

= 106 MPa and a fibre content of 1%. To produce the specimen with varying fibre orientation, they manufactured a very large 150 mm thick slab first and then cylinders were core-drilled from the slab at different angles to obtain different fibre orientations. To obtain the tensile resistance, the cylinders were tested in direct tension. After the tensile tests, the fibre orientation was measured by cutting slices of the cylinder and analyzing the elliptical shape of the cross-section of the steel fibres. The idea used to determine the average fibre orientation of the concrete slice was that the more elliptical the cross-section of a fibre, the more it corresponds to an inclined fibre and the cross section closer to a circle, the closer the orientation will be perpendicular to the cut. The fibre orientation α, corresponding to the cosine of the inclination angle of each fibre, was used. $\alpha = 1$ corresponds to fibres perpendicular to the fracture plane, while $\alpha = 0$ identifies fibres parallel to the plane. The average fibre orientation is calculated for all fibres crossing the surface analysed.

In Figure 2.12 the tensile behaviour in the cylinders with different fibre orientation are plotted as a function of crack opening. It is clear shown that the fibre orientation influences the post-peak behaviour. Two things can be concluded from the study. The first one is that when dealing with fibres, a great variability of strength can be expected according to fibre orientation. For example, the post-peak tensile strength is approximately half as much for $\alpha = 0.68$ compared to $\alpha = 0.83$. The second one is that the best performance comes when the fibres are crossing more perpendicularly to the crack. Fibre orientation is therefore a key issue, which can have a significant impact on the post-peak strength of the FRC. Reduction factors are usually used in the design process of FRC structural components to account for this factor, as it will be seen on Section 2.3.3.1.

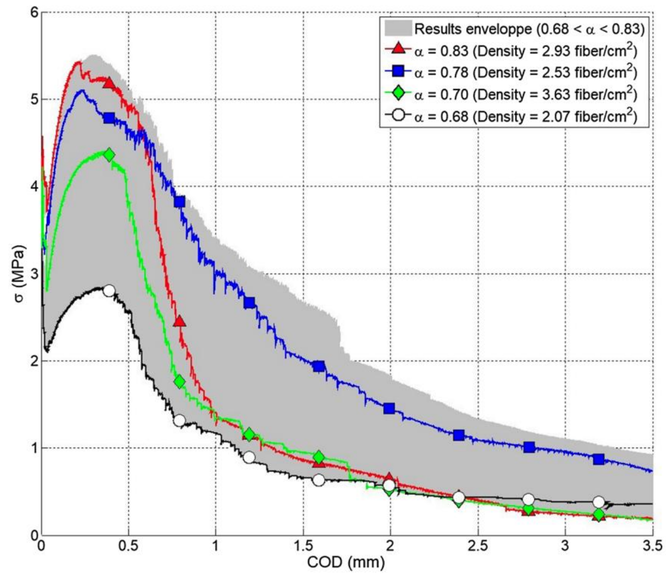

Figure 2.12 - Uniaxial tensile tests (Doyon-Barbant & Charron, 2018)

2.2.3.4 Bending resistance

The addition of steel fibres into reinforced and plain concrete has proven to be an innovation for enhancing some mechanical properties of ordinary concrete like ductility, energy absorption capacity and its flexural resistance . NSC presents a brittle behaviour under tension and therefore under bending. The addition of fibres is beneficial since it partially mitigates this brittleness by redistributing stresses across the matrix with fibres crossing the cracks (Sakthivel & Vijay Aravind, 2020; Soutsos et al., 2012).

Yoo et al. (Yoo et al., 2015) have shown that increasing the steel fibre content in concrete from 0.5% to 2.0% by volume caused a change in the bending capacity, from enhancing ductility to improving ultimate load (Figure 2.13). At lower fibre contents (around 0.5%), the primary effect was an increase in post-cracking deformation capacity, as the fibres bridged microcracks and delayed sudden failure without notably affecting the peak load. With dosages of 1% or more, the load–deflection curves began to exhibit a hardening behaviour, characterized by both higher peak loads and sustained load-carrying capacity after cracking.

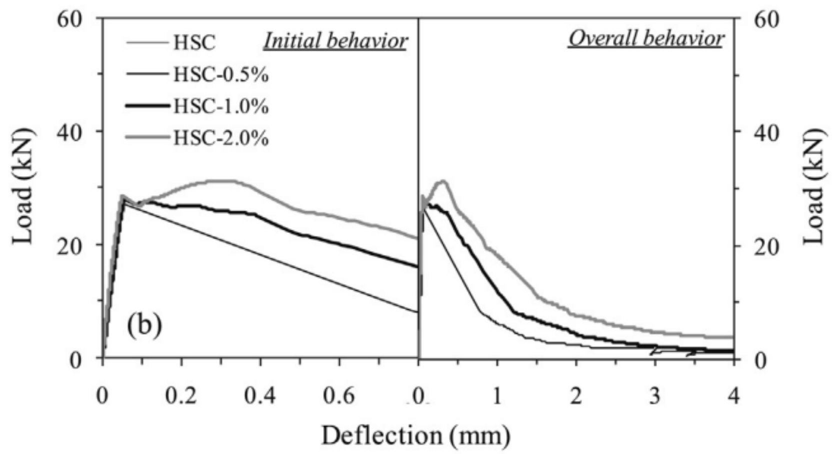

Figure 2.13 - Typical flexural response of HPFRC beams under quasi-static load. (Yoo et al., 2015)

Yoo et al. work indicates that beyond a critical fibre dosage, steel fibres contribute not only to controlling crack propagation but also to bearing additional tensile stress, effectively increasing both the bending strength and toughness of the material. Consequently, at higher fibre volumes, SFRC are stronger, slightly stiffer, and more ductile materials, capable of resisting larger loads while maintaining controlled failure mechanisms.

Fibres also positively affects reinforced concrete. Mertol et al. (Mertol et al., 2015) studied the effect of fibres on different reinforcement ratios and concluded that a steel fibre reinforced concrete (SFRC) beam has significantly improved toughness and post-peak ductility compared to conventional RC. Figure 2.14 proves this statement. For lightly reinforced specimens, the addition of fibres slightly decreases deflection, while for heavily reinforced beams, it leads to a significant extension of the post-peak region, reflecting the fibres' ability to control crack widening and delay failure. The fibres on reinforced concrete increased deflection and thus the beam ductility.

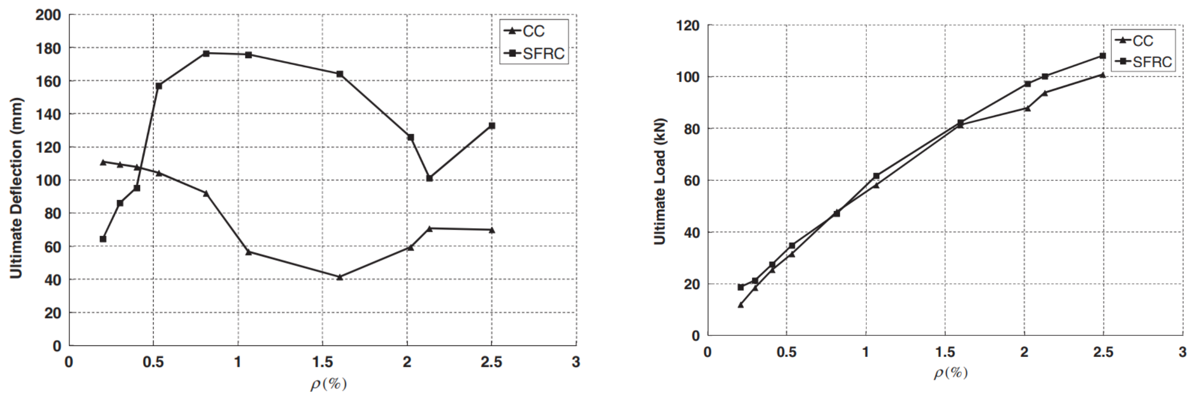

a) Ultimate deflection b) Ultimate load

Figure 2.14 – Effect of reinforcement ratio on ordinary concrete and SFRC (Mertol et al., 2015)

2.2.3.5 Shear force

The use of steel fibres to improve the shear resistance of concrete has been validated through both experimental and analytical studies throughout the years. Many authors demonstrate that steel fibres act as an effective shear reinforcement mechanism, improving crack control and ultimate load in beams with or without stirrups. Torres and Lantsoght (Torres & Lantsoght, 2019), for instance, established that increasing the steel fibre volume (from 0.3% to 1.2%) significantly improves shear resistance so that a transition on the failure mode occurs from brittle shear to ductile flexural failure. This effectively shows the potential for a partial or full replacement of traditional stirrups. Similarly, Merdas and Shallal (Merdas & Shallal, 2024) showed that adding 1% steel fibres increased the maximum shear strength of beams without stirrups by 30 to 50%, confirming that the tensile resistance of fibres and possibly the crack interlock enhance the overall shear response, particularly in beams with low shear span-to depth ratios.

In Dancygier and Savir (Dancygier & Savir, 2011), the inclusion of 0.75% hooked-end fibres notably increased the shear capacity of high-strength concrete beams, especially when no shear reinforcement was present, and enhanced ductility when combined with stirrups. Collectively, these studies confirm that steel fibres enhance shear resistance not only by increasing the concrete tensile strength and crack-bridging capacity, but also by improving the failure mode from brittle shear to a more ductile response, making SFRC an effective alternative to conventional shear reinforcement in modern structural applications.

2.2.4 Durability

Durability can be defined as the ability of concrete to withstand the environmental conditions to which it is subjected during service. In non-cracked concrete, water and aggressive agents penetrate through diffusion and absorption, while the appearance of cracks greatly accelerates the penetration of water and aggressive agents through permeability.

2.2.4.1 Permeability

Permeability is defined as the ability of a material to allow a liquid or other substance to pass through it under the effect of a pressure gradient. Permeability is measured in units of permeability (P), which is defined as the rate of flow of a substance through a unit length of a material per unit of pressure gradient (Xue et al., 2020).

This phenomenon therefore affects structures such as hydraulic dams where water pressure on the concrete is high. On a smaller scale, this phenomenon is also significant in cracks of concrete that are in contact with water. Water can then penetrate the cracks very quickly compared to the speed of penetration through the natural porosity of concrete. Permeability is therefore one of the main mechanisms for the transport of water and aggressive agents in concrete in service (cracked), and durability can thus be indirectly predicted by permeability tests. Conventional permeability tests on cracked concrete are carried out in two stages: cracking by mechanical loading of the specimen, followed by analysis of permeability. However, a structure in service, such as a bridge, is simultaneously subjected to mechanical loads and the penetration of water and aggressive agents.

To study how permeability is affected by these variables, (Desmettre. clelia, 2011) developed a new water permeability test to evaluate the permeability of a reinforced concrete tie specimen under cyclic loading. According to the results presented in Figure 2.15, for HPFRC with fibre content of 0.75%, 1.5%, and 2%, a reduction in water permeability of 31%, 92%, and 99% is observed, respectively, for the same loading level compared to HPC. The high rates of permeability reduction in HPFRC are a direct effect of improved crack control through the addition of fibres. Indeed, for an increase in fibre content from 0% to 0.75%, and then from 0% to 2%, a reduction in crack opening of 2% and 29% is observed, respectively.

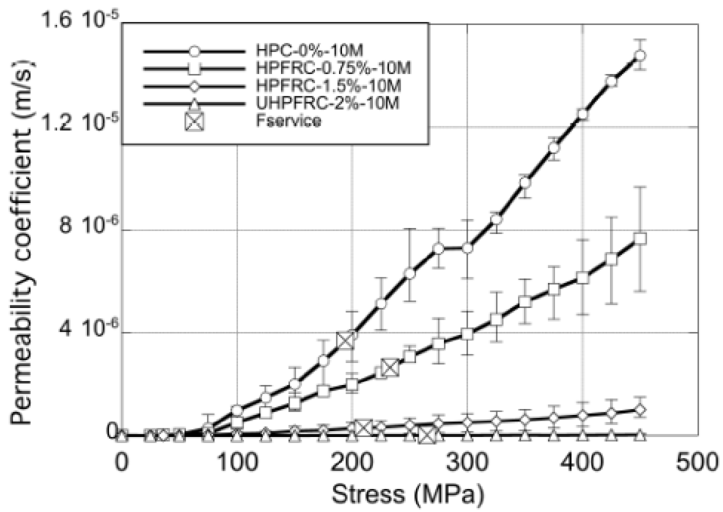

Figure 2.15 - Permeability as a function of fibre content (Desmettre. clelia, 2011)

2.3 Shear resistance of RC beams

2.3.1 Shear resisting mechanisms

2.3.1.1 Aggregate Interlock

Aggregate interlock is the name given to the shear transfer mechanism in cracked concrete, where coarse aggregate particles across a shear crack resist relative sliding due to normal and tangential contact forces (Figure 2.16).

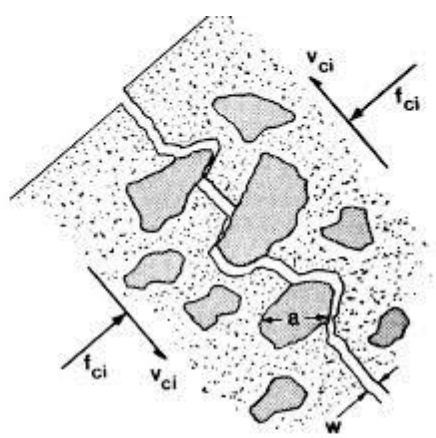

Figure 2.16 – Sketch of the aggregate interlock variables (Frank J. Vecchio & Michael P. Collins, 1986)

Fenwick and Paulay were the first to attempt to quantify the contribution of the aggregate interlock to the shear strength by comparing the shear capacity of specimens with smoothened cracks and naturally developed cracks (Montoya-Coronado et al., 2023). They concluded that the aggregate interlock and dowel force (contribution of the longitudinal rebar) contributed approximately 60% and 20%, respectively, to the shear resistance of a beam (Fenwick & Paulay, 1968). Then, Gambarova (Gambarova, 1981) proposed a more refined model assuming that aggregate interlock is only activated when two rough surfaces slip. The author realized that four variables were interconnected: shear stress, normal stress, tangential displacement and normal displacement. The highest shear stresses were produced with small crack openings and high normal stresses and a reduction in shear stresses was noticed when the crack openings were large or when the normal force decreased.

Walraven (Walraven, 1981) used Gambarova work as a basis to create a physical model that could reasonably predict the response of different concrete formulations. With his findings he concluded that the concrete strength and the aggregate size had also an impact on the resisting mechanism of the aggregate interlock.

Afterwards, extensive research has been done to understand the effect of aggregate size on shear resistance. For instance, Surendra (Surendra P. et al., 1979) reported that beams without reinforcement made with high strength concrete (f_c>70MPa) had a more brittle failure than beams made with normal concrete. Smoother shear cracks were noted and the explanation found was that those cracks tend to propagate through the coarse aggregates rather than around the aggregates as in normal strength concrete. Taylor (Taylor H. P. J., 1970) in the other hand went a bit further and concluded that as the compressive strength increased, the shear cracks became smother and the aggregate interlock resistance decreased.

Later, Vecchio et al. (Frank J. Vecchio & Michael P. Collins, 1986) used Walraven's work to define equation (2.5 of the MCFT model. Nowadays, the Bridge Canadian code considers the effect of the aggregate size, crack width and the concrete strength to indirectly define the contribution of the aggregate interlock.

2.3.1.2 Dowel action of longitudinal reinforcement

Dowel action of the longitudinal reinforcement can be defined as the capacity of reinforcing bars to transfer forces perpendicular to their axis. A representation of the force can be visualized in Figure 2.17. This effect arises as the shear crack surfaces slip, and this slip is then counteracted by the rebars. There is a lot of debate on how longitudinal reinforcement affects the shear resistance of a RC beam. Some approaches consider the dowel action as the governing shear transfer mechanism. Chana et al. concluded that for slender reinforced concrete beams (with $a/d > 3$), the horizontal crack occurs just prior to the beam failure, meaning that the mechanism of shear failure is closely associated with the loss of the dowel force (Chana, 1987). More recently, however, with the help of Digital Image Correlation (DIC), several authors (Autrup et al., 2023; Huber et al., 2016; Košćak et al., 2022) agreed on a more physical model that can explain the dowel action mechanism.

The dowel action starts to act when the critical shear crack propagates through the concrete section and reaches the longitudinal reinforcement. Two crack openings can occur, an opening normal to the crack face (w illustrated in Figure 2.17) or an opening vertical to the longitudinal reinforcement (s illustrated in Figure 2.17).

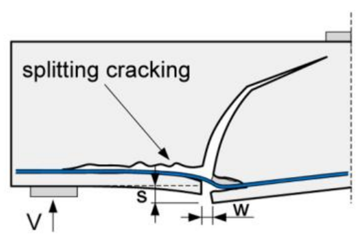

Figure 2.17 – Sketch of the crack openings related to the dowel action phenomenon (Autrup et al., 2023)

Because of these two different displacements, two mechanisms of dowel action can be identified: (a) shear transfer due to rebar slippage (V_{da_I}) and (b) shear transfer due to the tensile resistance of the concrete cover (V_{da_II}) (Figure 2.18).

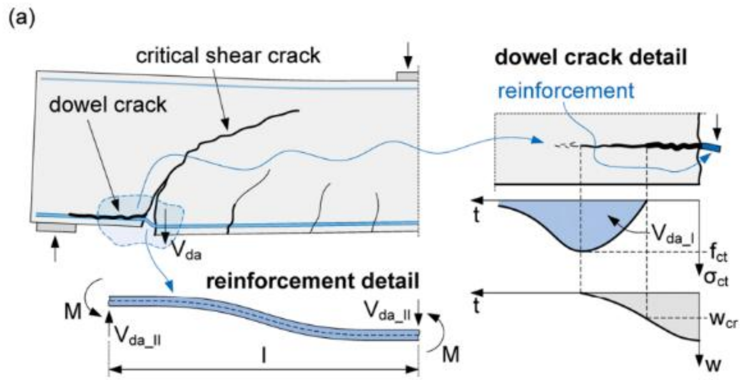

Figure 2.18 – Sketch of the dowel action mechanism named V_{da_I} and V_{da_II} (Autrup et al., 2023)

It should be noted that the capacity of the dowel mechanism is not the sum of V_{da_I} and V_{da_II}. Generally, only one shear transfer mechanism is dominant. Vintzēleou et al. proved that if enough concrete cover is provided, the failure is determined by the yielding of the reinforcement (Vintzēleou & Tassios, 1986). In this scenario, the shear force is mainly carried by the deformation of the longitudinal reinforcement (V_{da_II}). On the contrary, for smaller concrete cover, the failure is governed by the concrete tensile strength, and a splitting crack develops along the reinforcement (V_{da_I}). Lantsoght also confirmed this effect when analyzing the mechanism of dowel action on SFRC (Lantsoght, 2019c). Since the tensile strength and cracking control offered by SFRC, the bond properties (especially the resistance against splitting bond failure) are improved as compared to RC, therefore the dowel action resistance of SFRC is improved.

2.3.1.3 Compression chord

Since the first models created to predict the shear behaviour of reinforced concrete, the compression chord was already considered as part of the resisting mechanism . The first models used truss analogies where struts were represented by the concrete under compression and the ties were represented by the steel reinforcement under tension (Kani, 1964).

Kani carried out extensive experimental investigations and developed the basis for a rational theory of shear resistance in reinforced concrete (Kani, 1964). According to his theory, the resistance of beams without transverse reinforcement relies on two internal resisting mechanisms and their interaction, namely beam action and arch action (compression chord) as it can be seen in Figure 2.19.

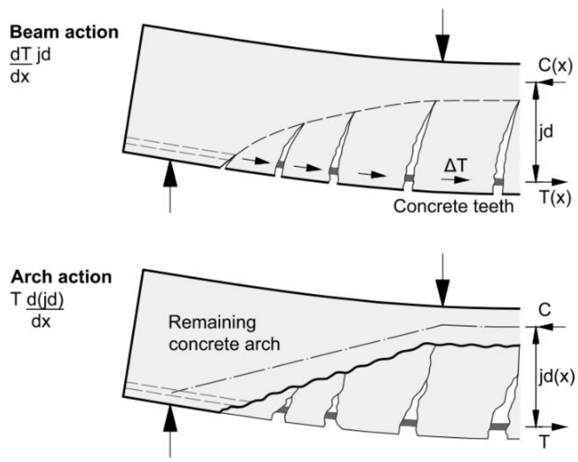

Figure 2.19 – Sketch of the compression chord effect (Mak & Lees, 2023)

It was found that the shear span to depth ratio *a/d* had an impact on how much of these resisting mechanisms affected the shear resistance. For slender beams with high values of *a/d,* the beam action was the main resisting mechanism, whereas for low values, the arch action or compression chord not only governs the shear strength but is responsible for an increased resistance. It should be noted that the boundary between cases governed by either arch or beam behaviour corresponds to values of *a/d* of approximately 2.5 (Kani, 1964)(Kotsovos, 1983). With T-beams however, the crack geometry allows the compression chord to be a representative shear resisting mechanism for more slender beams. This implies that the boundary between Kani's resisting modes is shifted with respect to beams with a rectangular section, from *a/d* = 2.5 to *a/d* = 4 (Ribas González & Fernández Ruiz, 2017).

Besides, increasing the effect of the compression chord on slender beams, the flanges also increase the shear resistance of T-shaped beams. There are two main reasons that explain this phenomenon. Firstly, the neutral axis depth of a T-shaped section is closer to the top compressed fibre. So, for the same reinforcement area and effective depth, the crack opening is higher in a T-shaped section beam than in a rectangular beam of the same web width, so the aggregate interlock is lower (Cladera et al., 2015). Secondly, when the beam is close to the Ultimate Limit State (ULS), there is a shear stress concentration on the flanges (Figure 2.20), which means that the contribution to the shear strength of the concrete chord is higher than in a rectangular section of same width, resulting in higher total shear strength (Ayensa et al., 2019).

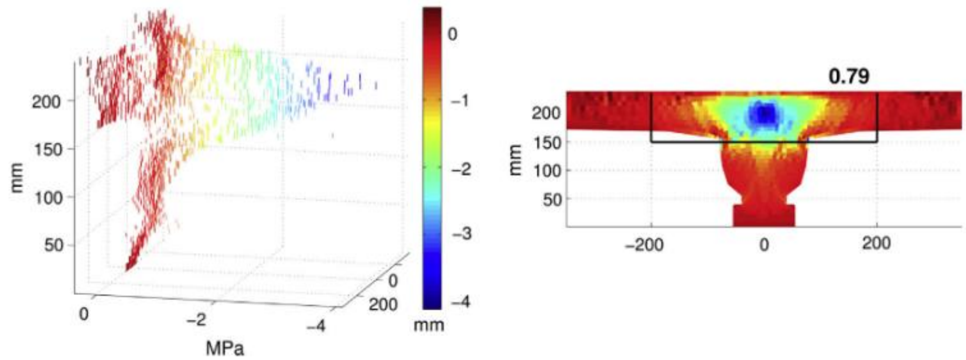

Figure 2.20 – Example of the shear stress distribution on a T-shaped beam (Cladera et al., 2015)

2.3.2 Variance on shear resisting mechanism

As it was discussed in the previous chapters, there are several shear resisting mechanisms contributing to the shear resistance of a reinforced concrete beam. Moreover, the amount of shear transferred by each of the mechanisms varies greatly for members, particularly with low transverse reinforcement (Campana et al., 2013a).

Several studies have been conducted using DIC to study the kinematics of the cracks and thus present the findings regarding each of the shear resisting mechanisms. All of them used theoretical models to define the contribution in kN of each shear mechanism (Campana et al., 2013a; Cavagnis et al., 2018; Fernández Ruiz et al., 2015; Ruiz et al., 2024).

Campana et al. (Campana et al., 2013a) for instance analyzed 8 RC beams with and without stirrups to study the shear resistance mechanism. They considered 5 resisting mechanisms: aggregate interlock, transversal reinforcement contribution, concrete residual tensile strength contribution, dowel action of flexural reinforcement and inclined compression chord. Each beam had a quite different shear resistance mechanisms contributions due to the different crack shapes and measured kinematics. The beams could be divided in 2 groups: beams with and without stirrups. The group without stirrups usually showed steep shear cracks and consequently the aggregate interlock was the dominant shear resisting. For beams with stirrups, the dowel action and stirrups were the main contributors for the shear resistance. The tensile resistance of the concrete and the inclined compression chord had a negligible contribution in both groups. The authors recognized, however, that the inclined compression chord could have higher contributions for a different beam setup (changes in beam geometry or shear span).

Cavagnis et al. (Cavagnis et al., 2018) continued Campana's study and analyzed 20 beams without shear reinforcement with different shear spans for simply supported and cantilever beams. The findings confirmed Campana's conclusions and deepen the understanding of the shear resistance mechanisms. Cavagnis et al. (Cavagnis et al., 2018) realized that the shear resistance is very dependant of the position in which the crack appears. For the aggregate interlock mechanism, for instance, stresses are mobilized when both opening and sliding develop and are activated in the steeper and upper parts of the crack. For cracks developing above or in the vicinity of the support (usually when beam has a small shear span), hardly any aggregate interlock develops, since almost no crack sliding occurs. The dowel action of the longitudinal reinforcement depends mainly on the location of the critical crack and is very limited when the crack develops far from the end support, whereas it is more notable if the critical crack is located close to it. When cracks appeared far from the support (usually when beam has a larger shear span), the contribution of the inclined compression chord at maximum load is rather limited (less than 30%), and, in some cases, almost negligible. The inclined compression chord becomes the governing shear transfer action only when the critical shear crack develops above the support.

More recently, Ruiz et al. used a similar methodology to study the effect of prestress on the shear resistance of FRC (Ruiz et al., 2024). Unlike the findings from past authors, the contribution of the compression chord is governing for prestressed members, followed by the contribution of fibres, while aggregate interlock and dowel action could be neglected. When the crack openings were small (around 2-4 mm) the tensile resistance provided by the fibres represented the governing shear resisting mechanism. For beams without prestressing (with crack opening of approximately 2 mm at failure), the response was comparable to that of prestressed beams with low crack openings. However, the aggregate interlock played a more significant role, which is due to the shape of the cracks (steeper close to the tension chord and flatter close to the compression chord).

2.3.3 Model overview for shear resistance

2.3.3.1 Modified Compression Field Theory (MCFT)

Before the Modified Compression Field Theory was created, purely empirical equations were used to predict shear resistance of RC structures. The MCFT is a successful attempt to use a more rational mechanically based theory to define which parameters affect the shear resistance and how they correlate with each other.

The model uses assumptions that simplifies the shear mechanism of reinforced concrete to ease the physical correlation between parameters. Cracked reinforced concrete transmits load in a relatively complex manner involving opening or closing of pre-existing cracks, formation of new cracks, interface shear transfer at rough crack surfaces, and significant variation of the stresses in reinforcing bars due to bond, with the highest steel stresses occurring at crack locations. The modified compression field model attempts to capture the essential features of this behaviour without considering all the details. The crack pattern is idealized as a series of parallel cracks all occurring at angle θ to the longitudinal direction as in Figure 2.21. Also, instead of considering the complex stress variation in the cracked concrete, only average stresses are used.

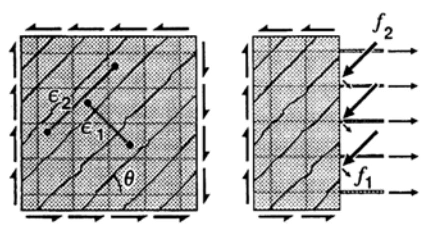

Figure 2.21 – Simplified model of cracked reinforced concrete under shear

With these assumptions made, it is easier to divide the analyzed area into 2 stress states: cracked and uncracked (Figure 2.22).

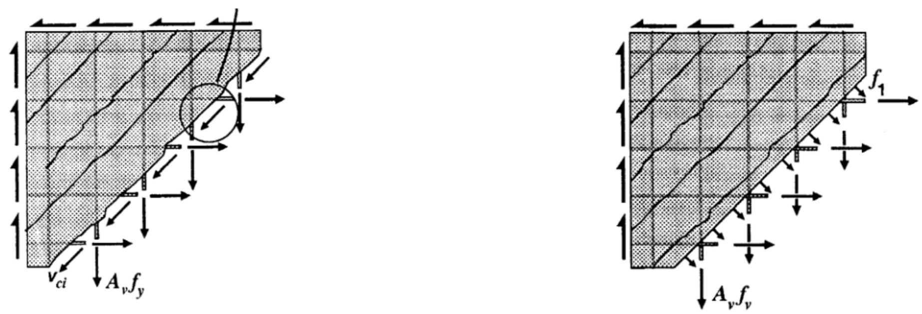

a) Cracked state b) Uncracked state

Figure 2.22 – Sketches of stress distribution on reinforced concrete

For the uncracked state, 4 variables are analyzed: f_1, ε_1, f_2 and ε_2 and have a physical relationship. The average principal tensile strain ε_1 in the uncracked concrete is used as a "damage indicator" that controls the average tensile stress f_1 in the cracked concrete and the ability of the diagonally cracked concrete to carry compressive stresses f_2. The principal compressive stress in the concrete f_2 is related to both the principal compressive strain ε_2 and the principal tensile strain ε_1 in the following manner (2.1).

$$f_2 = f_{2_{\max}}\left[\frac{2\varepsilon_2}{\varepsilon_c'} - \left(\frac{\varepsilon_2}{\varepsilon_c'}\right)^2\right] \tag{2.1}$$

Where:

$$f_{2_{\max}} = \frac{f_c'}{0.8 + 170\,\varepsilon_1} \leq f_c' \tag{2.2}$$

The authors of the model could also conclude that after cracking, the principal tensile stress in the concrete f_1 is related to the principal tensile strain ε_1 as follows. (2.3)

$$f_1 = \frac{f_{cr}}{1 + \sqrt{500\,\varepsilon_1}} \tag{2.3}$$

For large values of ε_2, however, Equation (2.3 has a limitation. When cracks become wide the magnitude of f_1 will be controlled by the yielding of the reinforcement at the crack and by the ability to transmit shear stresses v_{ci} across the cracked interface. Since the uncracked state stress is in equilibrium with the cracked state stress, it is possible to affirm that when the stirrups yield and the crack slip, the average tensile stress in the concrete f_1 is limited to:

$$f_l = v_{ci}\, tan\, \theta \tag{2.4}$$

Thanks to the simplifying assumptions and the equilibrium equations, authors (Frank J. Vecchio & Michael P. Collins, 1986) could use existing works to explain the change in behaviour when reinforcement yields. For instance, Walraven work was the basis for the formula implemented at the MCFT that correlates the shear stress that can be transmitted across the crack to the crack width w and the aggregate size a. Such formulation is presented in Equation (2.5.

$$v_{ci} = \frac{2.16\sqrt{f_c^{'}}}{0.3 + \frac{24w}{a + 0.63}} \tag{2.5}$$

In Figure 2.23, it is possible to see the results of the experimental work that culminated on a more mechanically based model to describe the shear resistance of reinforced concrete. Before the yielding of the vertical reinforcement, (2.3) is valid, after this point (2.5) becomes more representative of the behaviour.

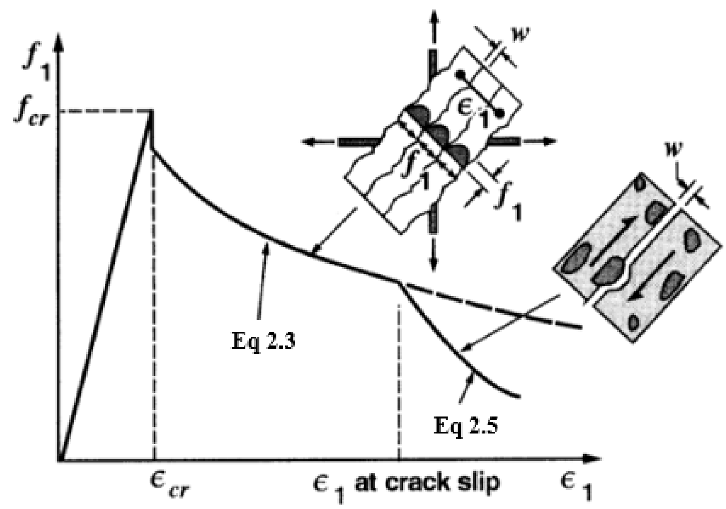

Figure 2.23 – Tensile law of the uncracked concrete adapted from (Michael P. Collins et al., 1996)

Finally, with f_l it is possible to calculate the shear resisting portion of the concrete. Multiplying the area of the shear crack with f_1 equals V_c Equation (2.6).

$$V_n = V_c + V_s + V_p = f_l\, b_v\, d_v \cot\theta + \frac{A_v f_y}{s}\, d_v \cot\theta + V_p \tag{2.6}$$

2.3.3.2 CSA S6:19: Canadian Highway Bridge Design Code

The calculation of shear resistance by the Canadian code (S6:19) is somewhat different from the shear resistance calculation process provided by the MCFT when it was published in 1986. According to (Evan C. Bentz et al., 2006), "*Shear design procedures should be simple to understand and to use not only for ease of calculation but, more critically, for ease of comprehension.*" Before the implementation of the Simplified Modified Compression Field Theory (SMCFT), a table was required to design shear with the MCFT, thus it was harder for the engineer to give physical significance to the parameters calculated and to understand why they are important. So, the SMCFT used the basis of the MCFT to create formulas that could be used to determine the parameters β and θ for the design in shear.

The S6.19 establishes 4 different shear resisting mechanisms that in sum represent the shear resistance of a FRC slender beam ((2.7).

$$V_r = V_c + V_s + V_p \tag{2.7}$$

V_s, as can be seen in (2.8), depends purely on geometrical constraints (d_v, s and A_v), material properties (f_y) and the shear crack angle (θ).

$$V_s = \frac{A_v f_y d_v}{s tan\theta} \tag{2.8}$$

V_c, on the other hand, depends on geometrical constraints (d_v and b_w), material properties (f_c) and β.

$$V_c = 2.5\beta\phi_c f_{cr} b_v d_v \tag{2.9}$$

β and θ can be determined using 2 methods. The simplified and the general methods. The simplified method can be used if the longitudinal reinforcement does not surpass 400 MPa and concrete compressive strength does not surpass 60 MPa. On both cases, the term f_{cr} according to the code, must not be greater than 3.2 MPa.

The simplified method fixes θ = 35 and if the section contains at least the minimum transverse reinforcement, β = 0.18 can be considered; if not, β will depend on s_{ze} as can be seen o.

$$\beta = \frac{230}{1000 + S_{ze}} \tag{2.10}$$

S_{ze} is the equivalent value of s_z that allows for the influence of aggregate size. s_{ze} cannot be taken less than 0.85s_z (2.11).

$$s_{ze} = \frac{35 s_z}{15 + a_g} \geq 0.85 s_z \tag{2.11}$$

s_z, for instance, is a crack spacing parameter depending on the crack control characteristics provided by the longitudinal reinforcement. Therefore, if a beam does not have intermediate reinforcement, s_z can be taken as d_v, if the beam has intermediate reinforcement, s_z must be taken as the spacing between the intermediate layers (Figure 2.24).

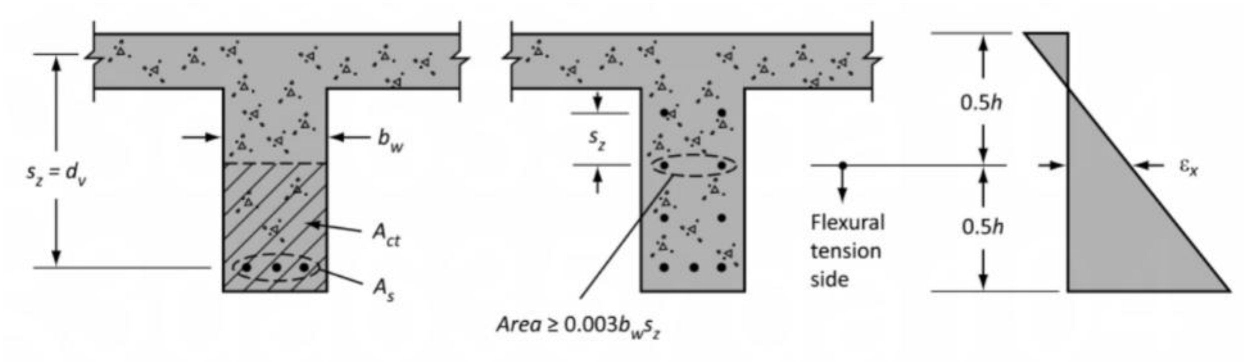

Figure 2.24 – Definition of the term s_z S6:19 (CSA, 2019)

The other method is called the general method, which can be used for concrete with more than 60 MPa compressive strength and with reinforcement that has more than 400 MPa. The biggest disadvantage of using this model is that it takes considerably more time to calculate since multiple iterations of calculations are necessary for determining the ultimate shear resistance. Besides, β and θ varies according to ε_x, not being anymore a fixed value.

For the general method, the value of β shall be determined according to (2.11):

$$\beta = \frac{0.4}{(1 + 1500\varepsilon_x)} \frac{1300}{(1000 + s_{ze})} \tag{2.11}$$

For sections containing at least the minimum transverse reinforcement, the equivalent crack spacing parameter, S_{ze}, shall be taken as equal to 300 mm. In other words, the second term of Equation (2.11) will be equal to 1. The reduction of β using $\frac{1300}{(1000+Sze)}$ with s_{ze} larger than 300 mm is to take into consideration the size effect on sections that don't have minimum transverse reinforcement.

The angle of inclination θ of the diagonal compressive stresses varies according to the longitudinal strain, ε_x, at mid-depth of the cross-section, and it shall be calculated according to (2.12).

$$\theta = 29 + 7000\varepsilon_x \tag{2.12}$$

In lieu of more accurate calculations, the longitudinal strain, ε_x, at mid-depth of the cross-section shall be computed from (2.13):

$$\varepsilon_x = \frac{\frac{M_f}{d_v} + V_f - V_p + 0.5N_f - A_p f_{po}}{2(E_s A_s + E_p A_p)} \tag{2.13}$$

2.3.3.3 MC2010

The fib Model Code 2010 (2010) represents a shift in concrete shear design by replacing traditional empirical formulations with physically based mechanical models grounded in meso-scale behaviour observations. For members with and without shear reinforcement, the fib Model Code 2010 uses the theory of the simplified compression field theory (CSA S6:19), however unlike the Canadian Bridge standard, the fib model code has 3 calculations methods while the CSA has 2 (simplified and general method) (Sigrist et al., 2013).

The fib model code provides 3 different levels of accuracy for calculating the shear resistance of vertically reinforced structures and 2 levels for non vertically reinforced structures. The fib model code has differences to the CSA standard, however, as it will be explained, the second level of approximation of the fib uses the same methodology as the one used in the general method from the Canadian standard. It is important to compare the second level of approximation to the general method of the Canadian standard since most of the studies that assess the accuracy of standards tests the fib Model Code and not the CSA. By proving that the fib Model Code is equivalent to the Canadian standard, it will be possible to use the studies made with fib Model Code to evaluate indirectly how the Canadian standard predicts shear resistance of beams.

Only the second level of approximation equations will be discussed in this section. The set of equations for a non vertically reinforced beam is presented below on Equations (2.14) to (2.17).

$$V_{Rd,s} = 0\ kN \tag{2.14}$$

$$V_{Rd,c} = k_v \cdot \frac{\sqrt{f_{ck}}}{\gamma_c} \cdot b_w z \tag{2.15}$$

$$\varepsilon_x = \frac{\left(\frac{M_{Ed}}{z} + V_{Ed} + N_{Ed}\left(\frac{(z_p - e_p)}{z}\right)\right)}{2 * \left(\left(\frac{z_s}{z}\right) E_s A_s + \left(\frac{z_p}{z}\right) E_p A_p\right)} \tag{2.16}$$

$$k_v = \frac{0.4}{1 + 1500\varepsilon_x} \cdot \frac{1300}{1000 + k_{dg} z}$$

$$k_{dg} = \frac{32}{16 + d_g} \geq 0.75 \tag{2.17}$$

Most of the differences between the fib Model Code and the Canadian Standard come from using different variables. For instance, regarding the shear resistance prediction of vertically unreinforced structures, Equation (2.15) is the same as equation (2.9). Instead of β, the fib uses k_v and instead of d_v, the fib uses *z*.

Parameter *z* is not the effective depth of the beam, but the internal lever arm (Figure 2.25). The only difference is that instead of d_v being considered always as 0.9 of *d, z* is calculated according to the geometry of the beam. The difference between *z* and d_v is small and won't affect the prediction of shear resistance.

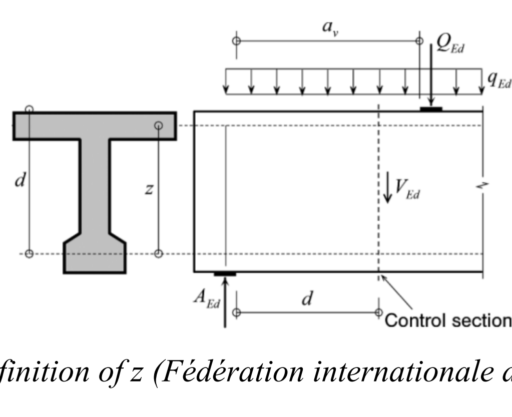

Figure 2.25 – Definition of z (Fédération internationale du béton, 2013)

Because fib model uses z and not d_v, it is not necessary to explicitly considerer the effect of prestress on Equation (2.13. As it is possible to note on Equation (2.16, V_p, A_p and f_{po} are not present, only the normal force is considered (N_{ed}). z_p and e_p are used so that the strain profile can be calculated at each position of the beam as show in Figure 2.26.

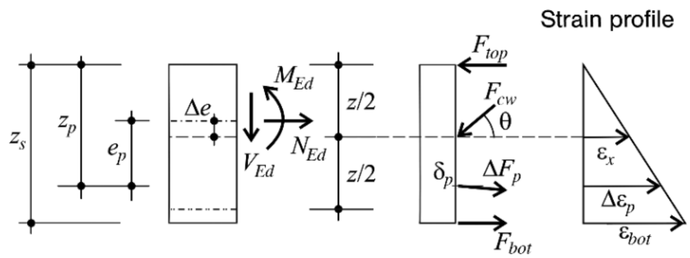

Figure 2.26 – Definitions of variables fib (fédération internationale du béton, 2013)

Equation (2.11) and Equation (2.17) are very similar with the only difference being that the Canadian standard uses s_{ze} to account for the aggregate size influence and the fib uses k_{dg} and z to define the influence of the aggregate influence. As stated by Sigrist et al. the fib model code and the Canadian standard approaches have a common background (SMCFT), which is why they yield similar results even if the calculation procedures differ from each other in several aspects.

The same process of changing the name of the variables happens for the set of formulas of vertically reinforced structures presented in equations (2.18) to (2.21).

$$V_{Rd,s} = \frac{A_{sw}}{s_w} \cdot z f_{ywd} \cot\theta \tag{2.18}$$

$$V_{Rd,c} = k_v \cdot \frac{\sqrt{f_{ck}}}{\gamma_c} \cdot b_w z \tag{2.19}$$

$$\theta_{min} = 20° + 10000\varepsilon_x \tag{2.20}$$

$$k_v = \frac{0.4}{1 + 1500\varepsilon_x} \cdot \frac{1300}{1000 + k_{dg} z}$$
$$k_{dg} = \frac{32}{16 + d_g} \geq 0.75 \tag{2.21}$$

Equation (2.18) is used to define the stirrup contribution to the shear resistance as it is the same as Equation (2.8) present in the CSA standard but with different variable names. The same can be said about Equation (2.12) and (2.20).

2.3.3.4 Eurocode 2 (2004)

In the current version of Eurocode 2 (CEN, 2010), the shear resistance verification of members without shear reinforcement is based on an empirical formulation proposed in 1968 from tests on non-axially loaded reinforced concrete beams. The formulation includes a k coefficient to account for the size effect, a ρ_l coefficient to account for the longitudinal reinforcement ratio and a $C_{Rd,c}$ coefficient to ensure safe design. (Equation (2.22) For members with shear reinforcement, only the contribution of stirrups is considered (Equation (2.23). This simplification ensures safety but often underestimating capacity of the structures (Miguel et al., 2023).

$$V_{Rd,c} = C_{Rd,c} k \left(100\, \rho_l f_{ck}\right)^{\left\{\frac{1}{3}\right\}} b_w d \tag{2.22}$$

$$V_{Rd,s} = \frac{A_{sw}}{s}\, z\, f_{ywd} \cot\theta \tag{2.23}$$

The Eurocode formulation is very simple and straightforward for design. It is important to note that a new version of the Eurocode is about to be released and will use a more mechanically based formulation and thus a more complex design process. The new version of the Eurocode was not found online, but a few papers discuss the capability of the new code to predict the shear resistance of structures with conventional reinforcement and with fibre reinforced concrete. The capability of the new Eurocode for estimating shear capacity of FRC structural components will be discussed in Section 2.3.3.5.

2.3.3.5 Model accuracy

The analytical models for shear in the most updated design standards vary from empirical or semi-empirical approaches (Eurocode) to more complex rational models based on Modified Compression Field Theory (S6.19, fib model code). As mentioned previously, the fib model code has 3 level of approximation for vertically reinforced structures and 2 levels of approximation for non-reinforced structures. In Figure 2.27a, the ratios of observed to predicted shear strength for 839 beams without stirrups are plotted for Level II as well as the 567 beams that meet the requirements of a Level I analysis. As can be seen, both methods provide conservative predictions of shear strength, with the Level II method providing significantly more accurate predictions. The average predicted ratios of shear strength ($V_{exp}/\ V_{pre}$) is 1.98 for Level I, and 1.15 for Level II. The coefficient of variation is 18.1 % for Level I and 10.6 % for Level II.

The same analysis has been done for beams vertically reinforced. A total of 243 experimental points of beams with stirrups is plotted in Figure 2.27b. Here, the average of predicted ratios ($V_{exp}/\ V_{pre}$) are 1.49, 1.35 and 1.20, and the coefficients of variation are 21, 17 and 13 % for LoAs I, II and III respectively. The authors decided to omit the LoA II points for clarity, because the difference between LoA II (same as CSA) and LoA III is not relevant.

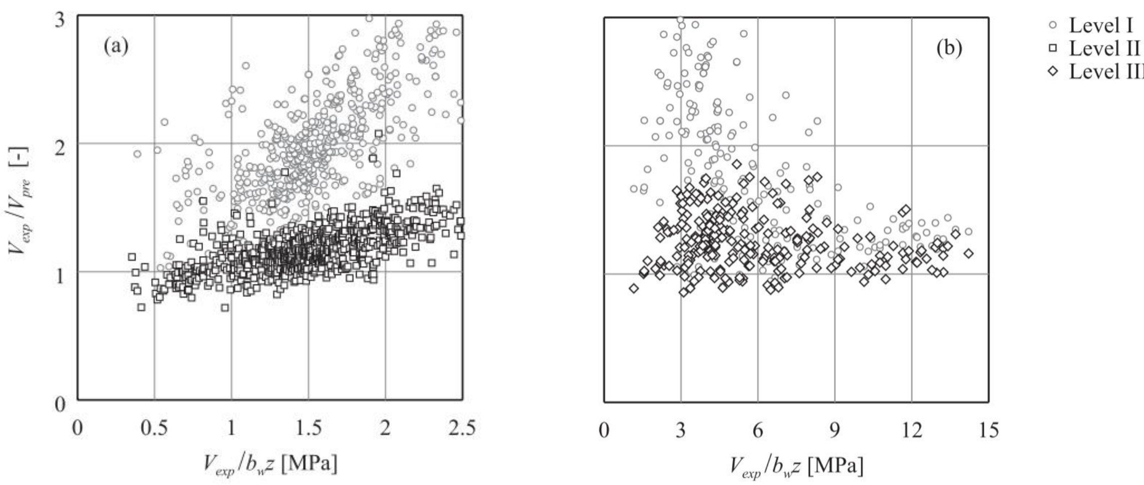

(a) without shear reinforcement

(b) with shear reinforcement

Figure 2.27 – Predictions by different Levels of Approximation for members (Olalusi & Viljoen, 2019)

Another interesting study was made comparing the Eurocode, the fib Model Code 2010 and, what can be classified as LoA IV estimates of shear resistance according to the Fib MC 2010 classification system, R2K. (Olalusi & Viljoen, 2019) assessed the prediction capability of these 4 shear resistance models for beams with stirrups. Over 160 tests on slender rectangular and flanged beams with stirrups subjected to point loads were used to verify the code predictions. The mean and design value predictions from the codes were compared to one another and to the experimental database, over the parametric range of shear reinforcement, concrete strength and beam depth. The results are presented in Figure 2.28.

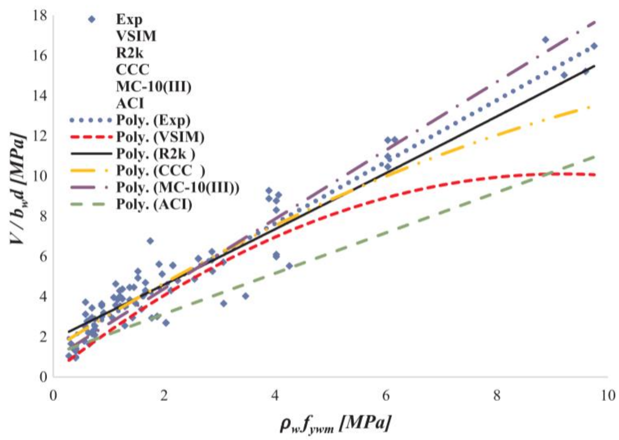

Figure 2.28 - Comparison of normalised mean shear capacity to experimental observations. (Olalusi & Viljoen, 2019)

The predictions of MCFT based models (R2k and MC-10 III) bear the closest comparison to that of the experimental observations for the range of shear reinforcement analyzed. The results of EC2 revealed that the mean value predictions differ considerably from the experimental results, even more when the shear reinforcement starts to increase. This reflects the difficulty of accurately predict shear resistance in structural design without using the calculation philosophy of MCFT.

2.4 Shear resistance of FRC beams

2.4.1 Shear resisting mechanisms

For many decades, the influence of steel fibres has been studied on shear resistance of beams and many authors concluded that a moderate amount of fibres (between 0.5% to 1%) can considerably increase the shear resistance and the ductility of beams without vertical reinforcement (Araújo et al., 2014; R. Narayam Swamy, 1993; Sharma, 1986). The shear resisting mechanisms present in FRC are like the mechanisms present in plain concrete, but with the addition of one different mechanism: the tensile resistance of fibres (Singh Negi & Jain, 2022; Slater et al., 2012; Sturm et al., 2021).

The tensile resistance of fibres in FRC is provided by the fibres bridging the crack. Usually, small to moderate amounts of fibres (0.25% to 1%) can transform shear brittle failure into ductile failure of the longitudinal reinforcement (Gehri et al., 2025). Many parameters affect this resisting mechanism, including bond between fibres and concrete, the type of fibres (geometry and material properties), the maximum aggregate size, the fibre content and the fibre orientation (Sahoo & Sharma, 2014).

It is important to point out, however, that the increase of shear resistance is not only caused by the increase in the tensile resistance. In statically indeterminate structures, hardening shear resistance can be guaranteed despite the tensile softening behaviour of the FRC, even without additional bar reinforcement. Thus, some researchers affirm that fibres positively affect the resisting mechanisms already present on plain concrete (Kaufmann et al., 2019a).

For instance, even though fibres don't affect the compression strength of concrete as discussed previously, they do increase the contribution of the compression chord. The influence of the fibres on the capacity in the compression zone is related to the height of the compression zone (Marì Bernat et al., 2020). Adding steel fibres changes the force horizontal distribution, thus increasing the height of the compression zone. As such, the capacity in the compression zone will be larger in FRC than in plain RC (Lantsoght, 2019d).

Since the material properties of FRC are improved as compared to RC, the dowel action also is affected by the fibres (R. Narayanan & I. Y. S. Darwish, 1987). The bond properties (effective mainly against the Vda I failure mode described in Chapter 2.3.1.2 are improved as compared to RC (Dinh et al., 2011), resulting in a stronger dowel action in SFRC.

Finally, the aggregate interlock is also positively affected by the addition of fibres (Marar et al., 2017). However, unlike the previous mechanisms, there is not yet a general agreement on how the fibres enhance the aggregate interlock resistance since experiments with direct and detailed measurements of the kinematics and stresses at the cracks are scarce in FRC (Kaufmann et al., 2019a). Because of that, it is thought that the consideration of aggregate interlock stresses established for RC is not entirely suitable for FRC.

2.4.2 Model for shear of FRC beams

2.4.2.1 CSA S6:19

The SMCFT can predict very well the shear resistance of RC beams with various characteristics (geometry, amount of reinforcement, compressive strength, etc.). However, it is very important to point out that the SMCFT is nevertheless an empirical model that is based on a few hypotheses. When adding the effect of steel fibres to this physical problem, do the same hypotheses still stand? As seen on section 2.4.1, the addition of fibres has a positive effect on all shear resisting mechanisms. With different resisting mechanisms that the fibres have, it is possible that the equilibrium equations will change and thus f_1 as it is described in Figure 2.23 may have a different behaviour (Section 2.4). It is important to point this out since the most updated standards (CSA and MC2010) don't consider the effect that fibres have on the different resisting mechanisms (compression chord, dowel action and aggregate interlock). To consider the contribution of fibres (V_{fib}), the S6.19 uses the work from Foster as basis (Foster et al., 2018). Foster adds the contribution of fibres to Equation (2.7) of the code creating a new formulation for the total resisting shear force presented in Equation (2.24).

$$V_r = V_c + V_s + V_p + V_{fib} \tag{2.24}$$

According to Foster's model, V_{fib} depends on geometrical constraints, material properties, crack opening and θ. (Equation (2.25)

$$V_{fib} = k_s f_w b_v d_v cot\theta \tag{2.25}$$

where k_s is a fibre orientation and dispersion variability factor at the structural, or member level, f_w is the post-cracking residual tensile strength corresponding to a crack width w_v, and b_v is the width of the beam web. It is interesting to note that when transposing Equation (2.25) into S6.19, some changes were made (CSA, 2019).

$$V_{fib} = 0.8\,\gamma_F\,\phi_F\,f_{fw}\,b_w\,d_v\,\cot\theta \tag{2.26}$$

The main difference is that besides the two safety factors, $\emptyset_f$ (material performance factor) and γ_f (fibre orientation factor), (2.26 has a reduction of 20% on the overall resistance of the fibre contribution, which may be due to the difficulty of predicting the structural behaviour of FRC. Besides, in the code they explicitly say that V_c cannot be smaller than V_{fib} , which also contributes to the conservativeness of the design method when designing for shear with fibres.

Foster (Foster et al., 2018) also proposed a formula to calculate crack opening w_v of Tensile Softening Fibre Reinforced Concrete (TSFRC), which is presented in (2.27:

$$w_v = (0.2 + 1000\,\varepsilon_x)\left(\frac{1000 + s_{ze}}{1300}\right)\frac{1}{\cos\theta} \geq 0.125\ \text{mm} \tag{2.27}$$

As shown in Equation (2.27), w_v is increased by the inversed term $\left(\frac{1300}{(1000+Sze)}\right)$ described previously which is known to be used to take into consideration the size effect on beams. w_v is increased by a size effect term on (2.27) - even though it is known that fibres decrease crack opening - because Foster (Foster et al., 2018) analyzed the work from Cuenca et al. (Cuenca, 2015) which studied fibre reinforced 1500 mm deep beams. In these beams, the horizontal spacing between mid-height cracks in the critical region for shear is about 0.5 - 0.7 times the beam depth and thus are considerably larger than the fibre length. The fibres have an effect mostly on service life and cannot reverse the size effect on those beams. Thus, the size effect term is maintained to ensure safe designs using fibres.

To ensure that his hypotheses were reasonable, (Foster et al., 2018) assessed his model with 72 FRC beam tests collected from the literature. Only beams with a shear span-to-depth ratio a/ d ≥ 2.5 and with a fibre content of 0.25 or 0.5% were considered in defining the database. Figure 2.29 show the accuracy of his model for estimating the shear contribution of FRC beams.

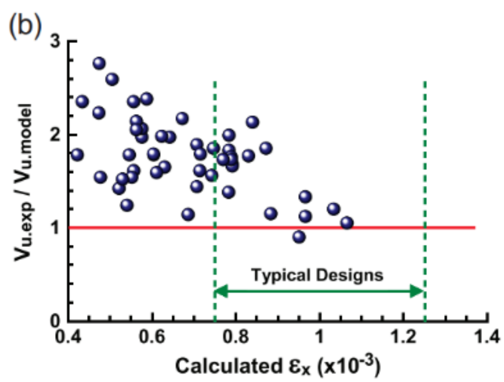

Figure 2.29 – Quality of level fib level II approximation model reinforced with steel fibres (Foster et al., 2018)

The analysis is made based on fib second level of approximation model which yields similar results as the general method of the S6.19 code since they are based on the same theoretical background.

For small strains, the model can be considered overly conservative. In average the ratio of the experimental shear resistance and the expected shear resistance is around 2. However, for beams that have a strain at mid height larger than 0.75×10^{-3}, the ratio $V_{experiment}/V_{model}$ is equal to 1.73 with a Coefficient of Variation of 0.19. A smaller value that can still be considered quite conservative.

2.4.2.2 Model accuracy

The Fib Model code, the Australian Code and the Canadian code, all based in the MCFT, consider that all the contribution of the fibres to the shear resistance of beams comes from the uniaxial tensile stresses of the fibres crossing the crack. Some studies stated that while being relatively simple to implement in practice, such approach fails to capture the physical-mechanical behaviour of the transfer of shear stresses across cracks (Kaufmann et al., 2019b). This is due to the fact that the aggregate interlock and the crack kinematics may be affected by the presence of fibres.

There is a lot of divergence between researchers on how fibres affect shear resistance of FRC beams. Ruiz et al. (Ruiz et al., 2023) compared experimental beam shear test values to various code predictions to understand how accuracy behaves for different experimental conditions. They used a database composed of 80 prestressed FRC beams without stirrups and a database of over 488 non-prestressed FRC beams. The models analyzed were the last draft of EN 1992-1-1:2022 (EC2-2020), the Model Code 2010 (MC-2010), last draft of Model Code 2020 (MC-2020) and the Spanish National Code (SNC).

For the non-prestressed FRC beam analysis, a distribution analysis of the FRC compressive strength and fibre volume as well as beams effective depth was made (Figure 2.30) (Lantsoght, 2019a). The average compression strength is around 55 MPa, mean fibre content 1% and the average effective depth around 350 mm.

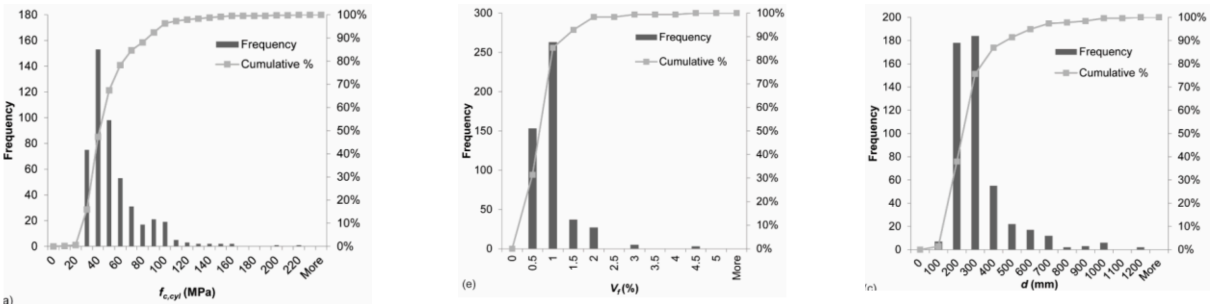

a) Compressive strength b) Volume of fibres c) Effective depth

Figure 2.30 - Distribution of parameters in database (Lantsoght, 2019b)

To analyse the effectiveness of the standards, Ruiz et al. (Ruiz et al., 2023) used a variable called γ_{mod}, which is the ratio between the experimental shear force at failure and the expected shear strength of each code. The analysis has been carried out with all the material safety factors equal to 1. A value of $\gamma_{mod} > 1$ means that the standard is conservative and a value of $\gamma_{mod} < 1$ means the standard overestimates the strength. Table 2.2 summarized the results for the non-prestressed beams (m value). Overall, all standards had a γ_{mod} average close but higher than 1, meaning they are generally conservative. The MC10 model based on SMCFT had the average closest to 1 and the smallest variance of the codes analyzed. Meanwhile, EC2 had the highest average and the highest variance of all the codes analyzed.

Table 2.2 Comparison of statistical values for γ_{mod} of Langtsoght database (Lantsoght, 2019a)

Statistical values for γ_{mod}	EC2	SNC	MC10	MC10 SMCFT	MC20 SMCFT
n	255	239	261	261	261
m	1.30	1.15	1.26	1.02	1.05
s	0.58	0.44	0.50	0.39	0.41
$v = s/m$	0.45	0.38	0.40	0.38	0.39
$\gamma_{\mathrm{mod}} < 1$ (%)	32	44	33	59	56

For the non-prestressed FRC beam analysis, different beams geometries were considered (Figure 2.31). Over 90% of the girder studies had an I-shaped geometry with a web thickness of 50 mm up to 148 mm and a height of 270 mm up to 1092 mm.

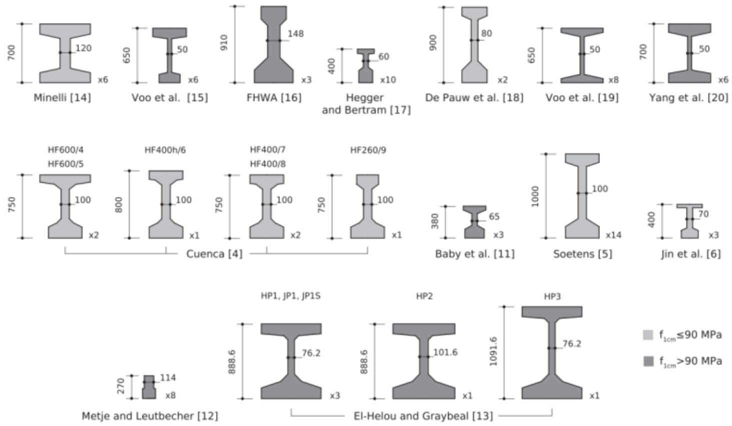

Figure 2.31 – Cross-sections of the beams present in Ruiz et al. database (Ruiz et al., 2023)

The mechanical properties of the concrete used in the prestress analysis can be seen in Figure 2.32 which show the distribution of the concrete strength as well as the fibre reinforcement volume. Most of the beams analysed have a FRC with ultra-high compressive strength and about 1% of fibre dosage.

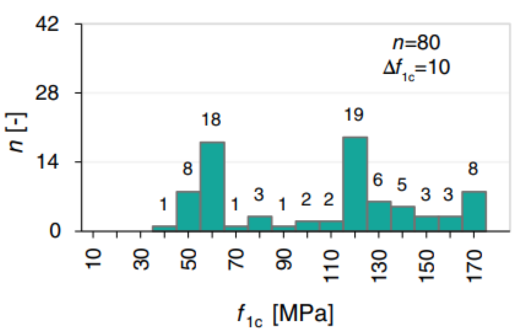

a) Compression strength

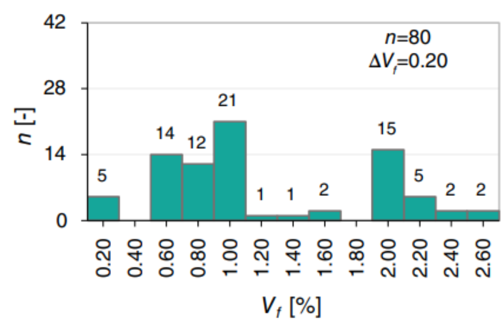

b) Volume percentage

Figure 2.32 – Concrete property distribution of the database (Ruiz et al., 2024)

The shear prediction accuracy of models for the prestressed beams is presented in Figure 2.33. The results show that the models are very conservative, much more than what was shown for the non-prestressed beams analysis. The main formulation of the MC-2020 presents a very high average value m = 3.39. Scatter is also high with a coefficient of variation v = 0.35. The SMCFT-based approach of MC-2010, which is the same model used by the Canadian Standard, shows a better accuracy of the model with a value of 1.78, as well as a lower scatter of 0.35. However, the best statistical indicators are obtained for the EC2-2020 formulation with m = 1.54 and v = 0.23.

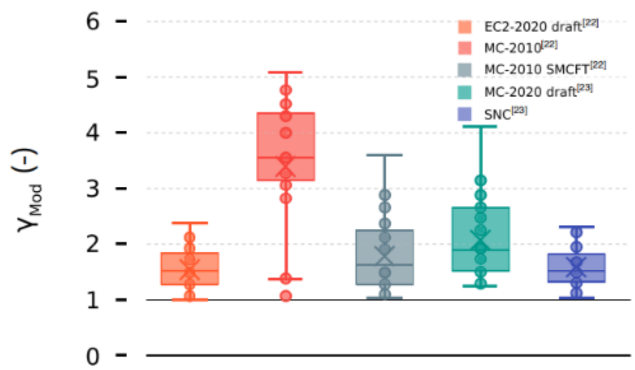

Figure 2.33 – Model accuracy factors (γ_{mod}) values of Ruiz database (Ruiz et al., 2023)

Ruiz et al. concluded that, because the codes could better predict the shear resistance of FRC beams without prestress and were conservative on the shear resistance of prestressed FRC beams, the prestress was the cause of over conservatism of the standards. His conclusion would be 100% true if both databases had similar concrete grades and similar beams dimensions. The non-prestressed database had mostly 55 MPa compressive strength concrete and 350 mm height rectangular beams. The prestressed database had mostly I-girders made with higher strength concrete and beams over 600 mm of height.

The mechanical properties of the concrete matrix as well as the geometry have a strong impact on the shear resistance. It is probable that, if the non-prestressed database had beams with high strength concrete and I-shaped geometry, the codes would also be more conservative.

Moreover, the significant overestimation of the prestressed FRC shear capacity may indicate that the shear mechanisms resistances are not well considered in the models. This aspect will be further studied in this research project.

2.5 Summary

The development of more durable structures is welcome, because of the high costs associated with rehabilitating a bridge and the high quantities of salt used in Quebec due to harsh environment. The introduction of High-Performance Fibre-Reinforced Concrete (HPFRC) has the potential to solve this problem, allowing enhanced mechanical performance, reduced reinforcement, and improved long-term serviceability to Quebec road infrastructure.

The early development of HPFRC bridge components at Polytechnique Montréal progressively evolved from studies on prestressed FRC girders (Cordoni, 2015), to fibre-reinforced slabs (Faggio, 2014) and then to UHPC connections (Verger-Leboeuf, 2016; Marleau, 2018). The most recent development by Rachello (2022) combined these technologies into a fully prestressed HPFRC girder with an integrated deck slab, offering a robust and efficient system for accelerated bridge construction. However, due to premature shear failures observed during testing, it became clear that the shear behaviour of FRC girders is not yet fully understood, and further research is required to ensure accurate and safe design.

The shear resistance of reinforced and prestressed concrete members results from the combination of several mechanisms: namely aggregate interlock, dowel action of the longitudinal reinforcement, compression chord contribution, and the tensile resistance of the concrete or fibres. Semi-empirical models, such as the Modified Compression Field Theory (MCFT) have improved the understanding and prediction of shear resistance in reinforced concrete (RC). These models even though provide the most reliable estimates, they tend to be slightly conservative.

However, for Fibre Reinforced Concrete (FRC) members, these same models are found to be much more conservative. This conservatism is mainly attributed to the limited understanding of how fibres alter the contribution of each shear mechanism. Specifically, the interaction between fibre bridging, aggregate interlock, dowel action, and compression chord effects is still not well quantified, leading to significant uncertainty in shear capacity prediction. Consequently, available design models tend to underestimate the actual resistance of FRC beams, which limits the material efficient use in structural applications.

In conclusion, although HPFRC bridge girders represent a promising advancement for durable and sustainable bridge infrastructure, further development and verification are still required to design HPFRC structures in shear in a safe and economical way.

CHAPTER 3 BRIDGE ANALYSIS

As previously explained, the current project is a continuation of past research projects that took place throughout the years. More precisely, the current project will be the continuation of Rachello's project, in which a study case will be used as a reference to design prestressed HPFRC girders.

3.1 Study Case

A reference bridge was chosen to calculate the design loads to which the HPFRC girders will be subjected. The bridge characteristics reflect the constraints of a structure situated in an urban environment, where the vertical clearance under the bridge and the bridge span are limited by surrounding conditions (nearby buildings, roads, etc.). An underpass bridge geometry commonly found in Montreal is illustrated in Figure 3.1, and will be considered for reference.

Figure 3.1 - Example of an underpass bridge in Montreal

The existing bridge has two simply supported spans of 15 m, for a total length of approximately 30 m. Because the spans are independent, only one span will be considered in the rest of the design, which is conservative. Although the connection between the two spans has not been considered, a continuous structural system could be selected for the actual replacement without impairing the conclusions of this study. There are multiple ways of designing connections between the two spans. The usual practice is to make the two spans continuous for live loads. However, it is also possible to use a link slab that substitutes the expansion joint. This approach often used when existing girders are kept could also be adopted for new structures. This is, however, out of the scope of this thesis, but the design of a UHPC link slab may be considered in a future research project.

3.1.1 Bridge geometry

The HPFRC girders were designed for three different bridge widths, corresponding to typical bridges with two, three or four traffic lanes without sidewalks, which is more conservative. The width of the concrete barrier walls was set at 0.45 m, which is the usual value for curbs. Finally, the number of girders corresponding to each width was then determined as 6, 8 and 11 for 2, 3 and 4 lanes respectively, with the corresponding widths of 8.20, 10.95 and 15.0 m respectively. The dimensions of the 3 selected bridge widths are shown in Figure 3.2. A simply supported 15 m span was considered.

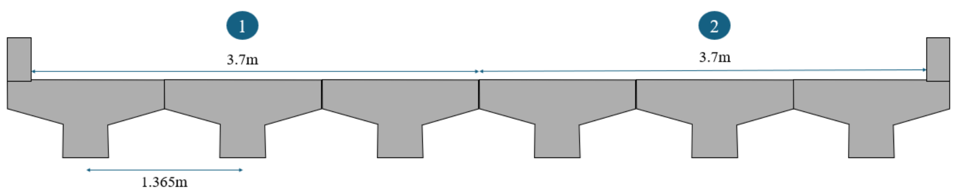

a) 2 lanes – 6 girders – Total width:8.20 m

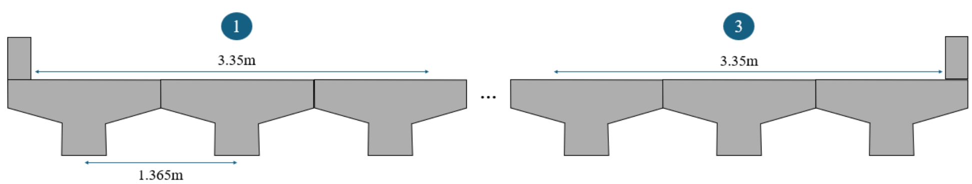

b) 3 lanes – 8 girders – Total width:10.95 m

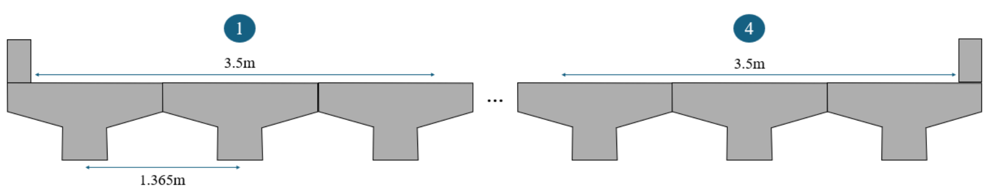

c) 4 lanes – 11 girders – Total width:15.0 m

Figure 3.2 - Three bridge widths considered for the design

3.1.2 Girder geometry

As explained previously, the geometry used in this project is based on the recommendations made by Rachello (2023) in his research project. The Rachello's original and modified girder cross-sections are shown in Figure 3.3.

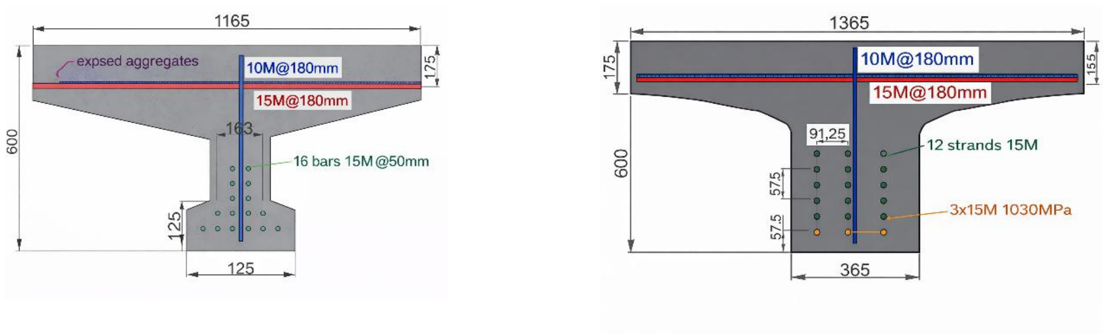

a) Original girder geometry　　　　b) Modified girder geometry

Figure 3.3 – HPFRC girder designed by Rachello

The main design improvements suggested by Rachello were the simplification of the girder cross-section geometry (T-shape instead of the I-shape) and the increase of the thickness of the web. This was proposed to facilitate the HPFRC flow in the web. Indeed, Rachello indicated that the horizontal spacing of 67 mm between tendons in the original geometry caused a HPFRC flow problem, which ended up in a bad fibre alignment in the web. However, the horizontal spacing of 91mm between tendons proposed by Rachello in the modified geometry was not feasible due to the geometrical constrains on the prestress bench of BPDL, the precast producer partner of the project (Figure 3.4).

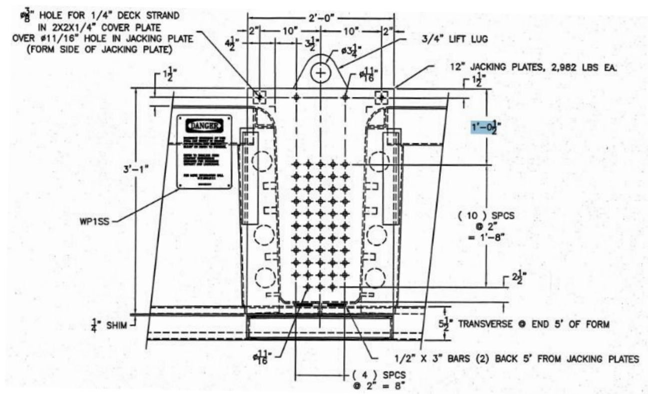

Figure 3.4 - Cross-section of the prestress bench used at BPDL

The possible tendons' spacing were either 2 or 4 inches (50.8 mm or 101.6 mm), so the horizontal spacing of 4 inches was chosen. The spacing between the tendons and the formwork were determined to follow the recommendations of CSA-S6 (Canadian Standards Association, 2019), which requires a spacing of at least 1.5 the length of the fibre (s_{min} =1.5 x 35 mm = 52.5 mm). A spacing of 60 mm between the tendons and the formwork was then chosen.

For longitudinal flexural reinforcement, a combination of prestressing tendons and high-strength steel (HSS) reinforcing bars was used for partial prestressing. While Rachello used 15 mm diameter HSS rebars, 22 mm diameter HSS rebars were used in this research project to account for the heavier CL750 truck used in this thesis. For the shear reinforcement, 400W 15M single branch stirrups placed in the centre of the web were used following Rachello's suggestion.

Only the number of tendons and stirrups was needed to finalize the design of the 15 m girder with the CL750 truck. Figure 3.5 shows the geometry used for the design.

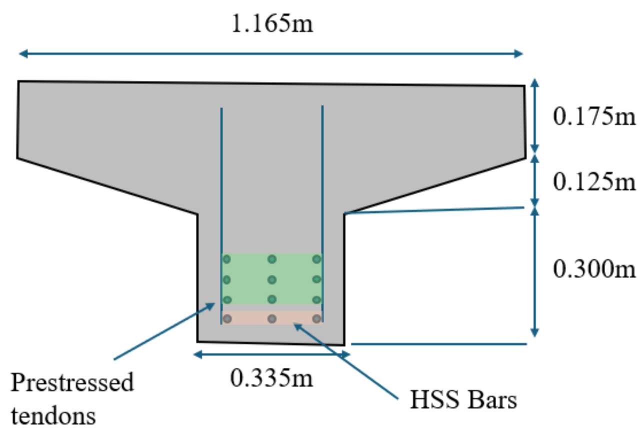

Figure 3.5 – Final formwork geometry

3.1.3 Material properties

The HPFRC considered in this study is based on the formulation of previous projects (De Broucker, 2013; Faggio, 2014; Rachello 2023). The concrete used for the beam is an HPFRC with a nominal compressive strength of 100 MPa reinforced with 35 mm long hooked-end steel fibres. The tensile strength of the concrete was determined from past direct traction test of dog-bone specimens. Figure 3.6 shows the HPFRC tensile properties used by Rachello (2023) and adopted in this study for the girder design.

According to CSA-S6 (Canadian Standards Association, 2019), the design tensile strength is equal to 4.0 MPa. However, a value of 4.4 MPa was considered. Because of the fabrication process of dog-bone specimens cast from one end, fibres are favourably oriented along the 50×100 mm cross-section. This leads to an overestimation of the post-cracking strength compared to an actual condition such as beams where the fibres are generally oriented less favourably. A fibre efficiency factor γ_f must therefore be considered. The CSA-S6 (Canadian Standards Association, 2019) code suggests different fibre orientation factors that vary according to the fabrication method. According to the standard, a factor of 0.4 should be used for elements with three-dimensional fibre distribution and a factor of 0.8 should be used for elements with two-dimensional fibre distribution. The web of the girder corresponds to a section with three-dimensional fibre distribution, while the slab corresponds to a region of two-dimensional fibre distribution. To be conservative and to simplify the design, a fibre efficiency factor of 0.4 was chosen for the whole girder.

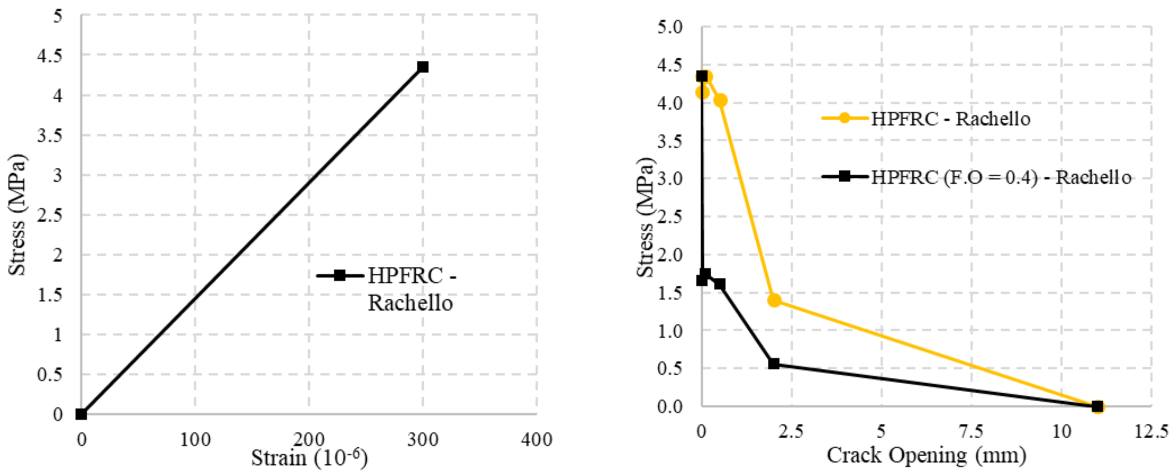

a) Pre-cracking b) Post-cracking

Figure 3.6 - Tensile strength adopted for the girder design

Different steels were used for the beam reinforcement. The prestress design used tendons with a modulus of elasticity of 190 GPa, a yield stress of 1630 MPa, and a maximum strength of 1860 MPa for a corresponding maximum strain of 6%. Non-prestressed reinforcement was also used for the longitudinal reinforcement of the beams. High-strength steel (HSS) reinforcement was chosen to maintain high mechanical performance and minimize the height of the beam. The ChromX A1035 CL bars have a nominal yield strength and maximum tensile strength of 830 MPa and 1035 MPa respectively. The nominal value of 830 MPa was adopted in the calculations as usually required in design codes, with a modulus of elasticity of 200 GPa.

Finally, the standard 400W grade reinforcement was used for the stirrups. This reinforcement has a modulus of elasticity of 200 GPa, a nominal yield strength of 400 MPa, and an ultimate strength around 600 MPa. The nominal yield strength of 400 MPa was retained as required by design codes. The tensile properties of the different types of reinforcing steel are shown in Figure 3.7.

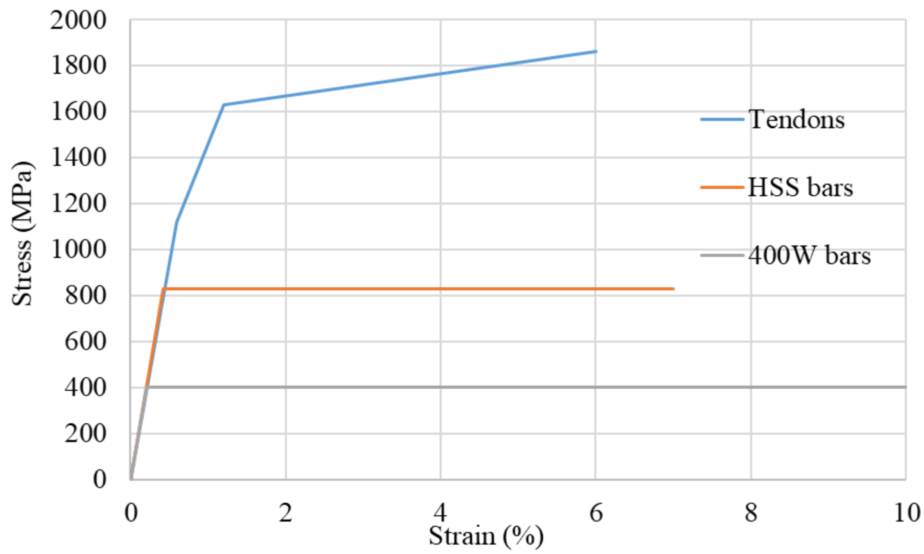

Figure 3.7 - Tensile properties used for the characterization of the reinforcement

3.2 Design methodology

The information used in this section was taken from the Polytechnique course material "*CIV8520 – Conception des ponts"* (Massicotte, 2023), and the Canadian Highway Bridge Design Code (CSA-S6:) (Canadian Standards Association, 2019).

3.2.1 Load combinations and material performance factors

The CSA-S6:19 (Canadian Standards Association, 2019) code design method considers several factored load combinations with each load multiplied by load coefficients. The different factored loads correspond to different conditions of use of the structure. For each condition of use, a load effect is calculated and then used to design the structure. The load combinations suggested by CSA-S6:19 (Canadian Standards Association, 2019) for prestressed girders are presented below.

- Serviceability Limit State 1 (SLS-1), corresponding to the load to which the beam will be subjected during service. Normally, concrete cracking is not allowed for prestressed girders. However, with FRC, limited cracking may be allowed. SLS-1 is used in this study to assess the maximum crack width in service.

- Serviceability Limit State 2 (SLS-2) is used to verify if the girder deflection caused by the traffic load respect the allowed values.
- Fatigue Limit State (FLS) is used to verify the fatigue resistance of rebars and tendons. This only occurs when concrete cracks under service load and is usually not verified for prestressed concrete member design. Because cracking is allowed with FRC, this condition must be checked. The stress variation must be measured between the application of dead loads and the live load at the FLS considering cracked cross section.
- Ultimate Limit State 1 (ULS-1) corresponds to the most critical load that the beam must be able to resist.

To calculate the factored load effects, the various loads applied to the girder must be multiplied by the load coefficients shown in Table 3.1.

Table 3.1 - Load coefficients for girder design CSA-S6:19 (Canadian Standards Association, 2019)

Load	SLS-1	SLS-2	FLS	ULS
Girders	1.0	0.0	1.0	1.1
Barrier walls	1.0	0.0	1.0	1.1
Asphalt	1.0	0.0	1.0	1.5
Cl-750	0.9	0.9	1.0	1.7

Besides that, the strength of materials is reduced by multiplying the specified values by material performance factors that are smaller than 1 for the design at ultimate limit state. The material performance factors are presented in Table 3.2.

Table 3.2 – Material performance factors used for design at ULS

Material	ϕ material
Prestressing tendons	0.95
Steel reinforcement	0.9
FRC in tension	0.75
Concrete in compression	0.75

3.2.2 Dead loads

The dead loads considered for the design of the girder are the self-weight of the girder, the self-weight of the barrier walls and the self-weight of the asphalt pavement. Conservative values were selected at this preliminary stage. The dead weight was calculated by multiplying the girder cross-section (0.398 m²) by the density of 24.5 kN/m³ for prestressed concrete. Figure 3.8 shows the cross sections for the girder and the barrier wall considered.

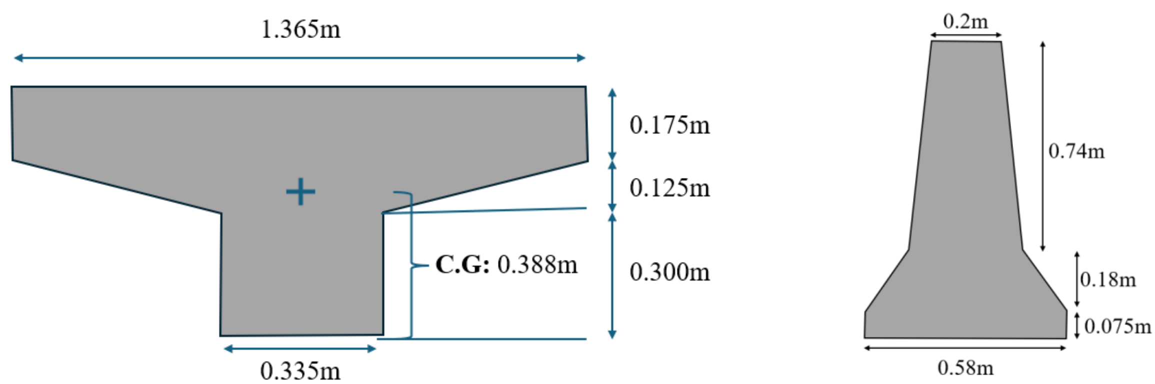

a) Girder self weight b) Barrier wall self weight

Figure 3.8 – Dimensions used to calculate self weight

The load associated with the asphalt was calculated by considering a thickness of 80 mm and a density of 23.5 kN/m³. The load of the barrier walls was calculated by multiplying the barrier cross-section (0.32 m²) by the density of 23.5 kN/m³. The weight of the barrier walls, for simplification purposes, were equally divided among the girders. Conservatively, the number of girders chosen to define the average load of the barrier walls was 6. The maximum moment and maximum shear force created by the various permanent loads were determined for a 15 m long and 1.365 m wide girder and are presented in Table 3.3.

Table 3.3 – Unfactored load effects due to self-weight

Efforts	Girder	Asphalt	Barrier wall	Total
Uniform load (kN/m)	9.6	2.6	2.5	14.7
Bending moment (kNm)	269	72	70	411
Shear force (kN)	72	20	19	110

3.2.3 Live loads

3.2.3.1 Truck and lane loads

For this research project the CL-750-QC truck used in Quebec (Ministère des Transports et de la Mobilité durable., 2024)was chosen. The axle loads of this design truck differ from those of the CL-W loading, as shown in Figure 3.9. This truck has 5 axles and a total load of 750 kN. The dynamic amplification factors specified in the CSA-S6:19 (Canadian Standards Association, 2019) code for CL-W loading are applied.

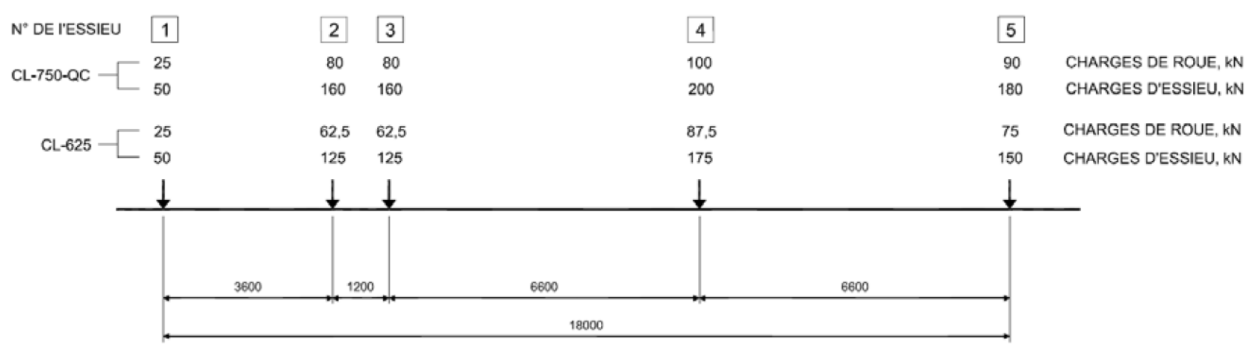

Figure 3.9 - Dimensions and weight distribution of the CL-750-QC truck road overload

In addition to the truck load, a lane load must be considered. In this configuration, the load on each axle of the CL-750-QC truck is reduced to 63% for simply supported span, as indicated in MTMD design manual (Ministère des Transports et de la Mobilité durable., 2024), but a uniformly distributed load of 12.6 kN/m is added for each lane (see Figure 3.10 for the CL-W loading). No dynamic amplification factor applies to the lane load. The governing live load considered is, of course, the one that yields the highest load effects. For a 15 m girder, the lane load gives values lower than the truck load.

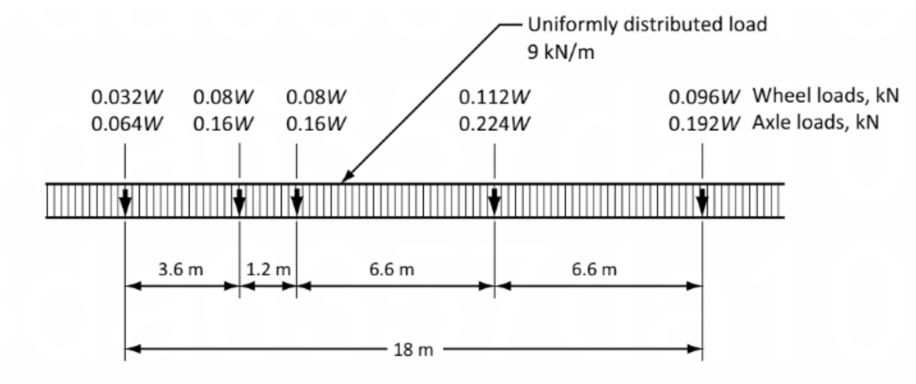

Figure 3.10 - CL-W lane load

Several load cases must be considered for the CL-750-QC truck to find the most critical configuration. These cases correspond to the load effects created by a certain number of truck axles and are presented in Table 3.4. In addition, the load effects obtained with the truck must be multiplied by a dynamic load factor specific to each case. As specified in the Canadian Bridge Code, the dynamic load factor should not be applied to the lane load.

Table 3.4 - Dynamic load factor for the truck load specified CSA-S6:19 (Canadian Standards Association, 2019)

Axle grouping	dynamic load factor
1,2,3,4,5	1.25
1,2,3	1.30
2,4	1.30
2,5	1.30
4,5	1.30
4	1.40

3.2.3.2 Number of lanes

The number of lanes on a bridge must be determined based on the width of its deck, according to the information provided in Table 3.5, where W_c refers to the width of the deck which is the total width of the bridge minus 0.9 m corresponding to the two barrier walls. The width of the lane is then simply obtained by dividing W_c by the number of design lanes. The simultaneous loading of several lanes must also be considered. In this case, a reduction factor must be applied to the loads obtained according to the number of loaded lanes (Table 3.6).

Table 3.5 - Number of design lanes

Deck width Wc (m)	Number of lanes
3.0<Wc≤6.0	1
6.0<Wc≤10.0	2
10.0<Wc≤13.5	3
13.5<Wc≤17.0	4

Table 3.6 - Modification factor of different numbers of loaded lanes

Number of design lanes	Modification factor
1	1.0
2	0.9
3	0.8
4	0.7

According to the Canadian bridge code, two different lane configurations must be considered when applying the truck load. The first one, the lanes are considered of equal width, and one or more lanes are simultaneously loaded. In this situation, the truck must be transversely positioned within each of the loaded lanes to create the maximum load effects in any of the girder. The total load effect in each girder is multiplied by the modification factor according to the number of loaded lanes. The second lane configuration considers only 2 adjacent lanes of 3.7 m positioned transversely to generate the maximum load in any girder. In this 2-loaded traffic lane condition, a modification factor of 0.9 is applied. For ELU-1 and ELS-1 load combinations, all possibilities of truck positions must be analyzed to determine the most critical. For ELF and ELS-2 combinations, however, only a single truck in the centre of a single lane of traffic, without verifying the lane load, must be considered.

3.3 Bending design

3.3.1 Longitudinal reinforcement

Taking into consideration the suggestions proposed by Rachello (Rachello Adrien, 2023), the only variable left was to determine the number of tendons so that the girder would meet CSA-S6 requirements for SLS-1 and ULS. It was ultimately decided to use 9 tendons spaced 100 mm apart (due to fabrication constraints) distributed over 3 layers, as well as a layer of 3 high strength steel (HSS) bars in the lowest position (Figure 3.11a). Unlike Rachello's solution that used non-adherent tendons to account for the high tensile stresses generated by the prestress at the extremities, the solution chosen for this problem in the current design was to add two prestress tendons on the upper portion of the girder cross-section (Figure 3.11b). The reason for choosing this solution was justified by the fact that during transportation, one of Rachello's girder cracked close to the support, probably because of low amount of prestress at the section.

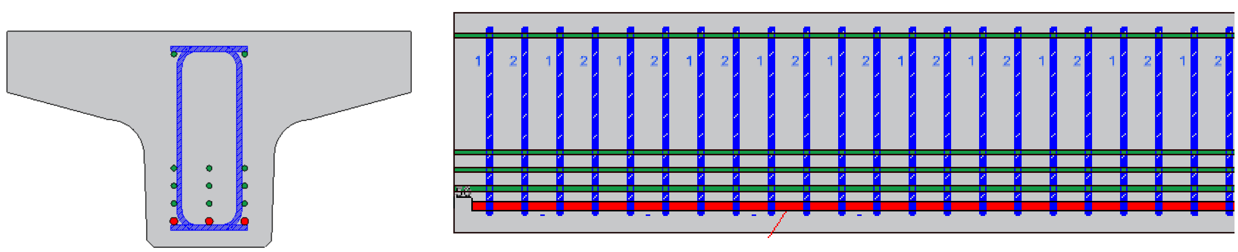

a) Cross-section

b) Longitudinal view of one end

Figure 3.11 – Bending and shear reinforcement.

3.3.2 Load effects

The longitudinal bending moments and shear forces were calculated using a grillage model with software SAP 2000 (CSI, 2023). Three bridge widths were modelled and are described in Appendix A.1. The principle of an influence line for each girder was used. For each bridge configuration, the truck load and the lane load were applied along lines transversely spaced at every 0.6825 m (half-flange length). Every axle combination with its corresponding dynamic load factor was tested and the longitudinal moment created at each point of the beam was recorded. Based on these results, an influence line was drawn for each girder. The influence lines of the different girders for the three bridge widths studied are shown in Figure 3.12. The line of influence shows the effect of a truck load on each lane. For symmetry, half of the girders are shown, with girder 1 located at the far left of the deck.

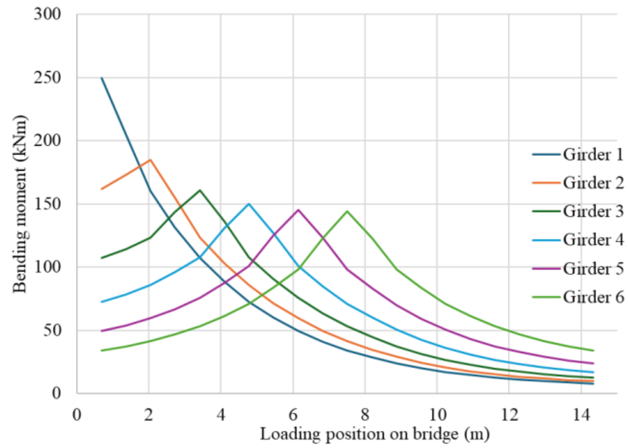

a) 15 m deck (11 girders)

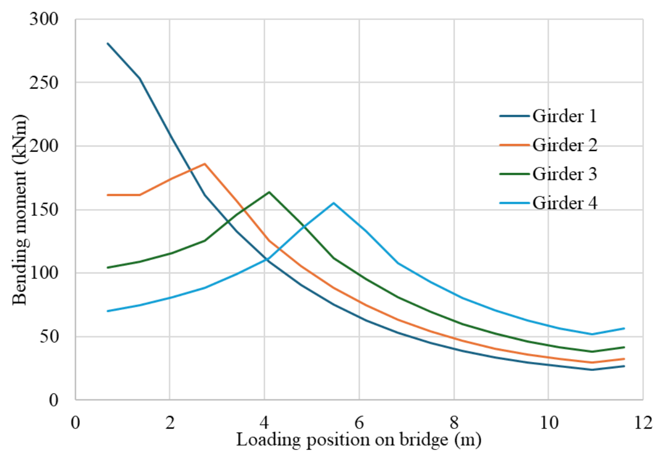

b) 11 m deck (8 girders)

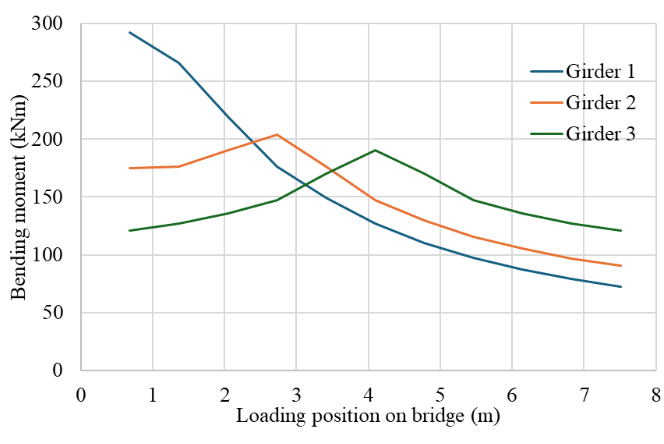

c) 8 m deck (6 girders)

Figure 3.12 - Lines of influence for the CL-750 QC loading

For each girder of the three bridge widths, the different load configurations described in Figure 3.2 are considered with the appropriate reduction factors. For each lane configuration, the axles of the CL-750-QC truck are positioned so that the maximum moment is generated at the girders. The worst-case scenario is shown in Figure 3.13. It happens when 2 trucks with the variable lane-width scenario are loaded on the smallest bridge (6 girders) at same time. The maximum moment is: $0.9 \times (180 + 130 + 175 + 130) = 550$ kNm.

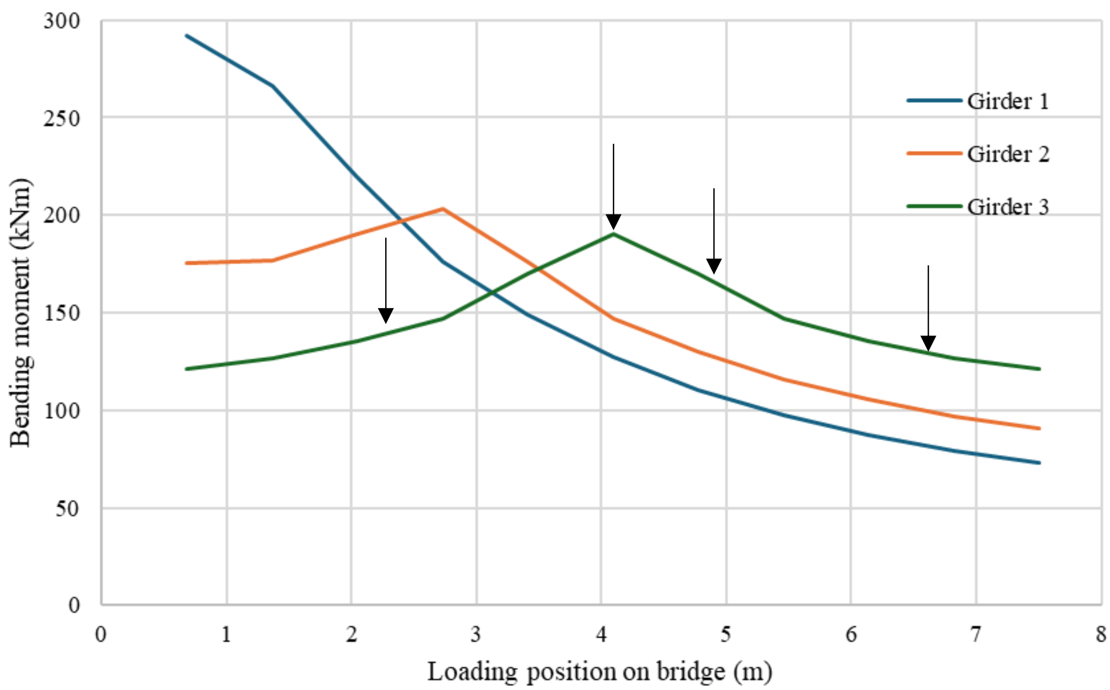

Figure 3.13 - Maximum live load moment calculated with truck load

The same analysis has been done considering a single truck load in the center of one lane to calculate the maximum moment for the FLS. For each bridge width studied, the maximum moment obtained across all beams was then selected and is presented in Table 3.7. Values obtained with the simplified method of CSA-S6 are shown for validation purposes.

Table 3.7 - Maximum moments according to different width configurations

Bridge width (m)	Bending moment (kNm)		Shear (kN)
	ULS and SLS-1	SLS-2 and FLS	ULS
8	550	455	185
11	530	410	172
15	475	370	166

The factored design moments were calculated using equation 3.1, applying the load coefficients in Table 3.1 and the permanent loads in Table 3.3.

$$M_{SLS-1} = M_D + 0.9M_L = 430 + 0.9 \times 550 = 925k\ Nm$$

$$M_{FLS} = M_D + M_L = 430 + 455 = 885\ kNm$$

$$M_{ULS} = 1.1 \times \left(M_{girder} + M_{barrier\ walls}\right) + 1.5 \times M_{asphalt} + 1.7 \times M_{Live}$$

$$M_{ULS} = 1.1 \times (269 + 72) + 1.5 \times 72 + 1.7 \times 550 = 1440\ kNm \tag{3.1}$$

3.3.3 Bending resistance

The bending resistance was calculated based on the provisions of the CSA-S6:19 code. Since a softening behaviour HPFRC was considered for the design, the contribution of fibres was disregarded at the ULS design of the girder. The material factors present in Table 3.2 were applied to the material resistances shown in Table 3.8.

Table 3.8 - Material resistance considered in the design of ULS

Concrete	
f'_c	100 MPa
Steel	
f_{py} (tendons)	1680 MPa
f_y (rebars)	830 MPa

The position of the rebars and the sum of the area at each layer of the girder, is presented in Table 3.9.

Table 3.9 – Flexural reinforcement distribution

y	Number of bars	Number of tendons	Area (mm²)	Total area (mm²)
57.5	3	0	390	1170
107.5	0	3	140	420
157.5	0	3	140	420
207.5	0	3	140	420

Table 3.10 presents the area, the moment of inertia and the Center of gravity of the girder.

Table 3.10 – Geometric information of girder analysed

Geometric Information		
A	0.40	m²
I_x	0.0103	m^4
C.G	0.388	m

The Equation (3.2) from the CSA-S6 code was used to calculate the effective height of the area of concrete under compression.

$$\alpha_1 = 0.85 - 0.0015f_c' \geq 0.67 \tag{3.2}$$

With α_1 and the sum of the factored forces of the reinforcement (T_s), it was possible to calculate the height of the concrete compression stress bloc (a) and finally calculate the resisting bending moment (M_r). All the values mentioned previously are presented in Table 3.11. As it is possible to see, the resisting bending moment is higher than the factored bending load at ULS (M_f = 1440 kNm).

Table 3.11 - Summary of values to define the resisting bending moment

Variables	Value	Notation
T_s	3124	kN
a_1	0.71	-
a	51.03	mm
M_r	1452	kNm

3.3.4 Crack opening

The cracked behaviour of the HPFRC girder throughout SLS and ULS conditions was calculated using AIS (Analyse Inélastique des Sections) software developed at Polytechnique Montréal (Massicotte et al., 2011). It calculates the bending behaviour of a girder cross-section taking into consideration the contribution of fibres to the overall resistance and crack opening.

The parameters considered for the design were introduced into the software, as detailed in Appendix A.2. The characteristic length for the bending crack spacing was taken as L_f = 80 mm, based on experimental data from De Broucker (2013) and Rachello (2023). This corresponds to the average spacing of bending cracks in the beam and is necessary to determine the crack opening using the AIS software. The moment-crack opening curve for the HPFRC girder is shown in Figure 3.14.

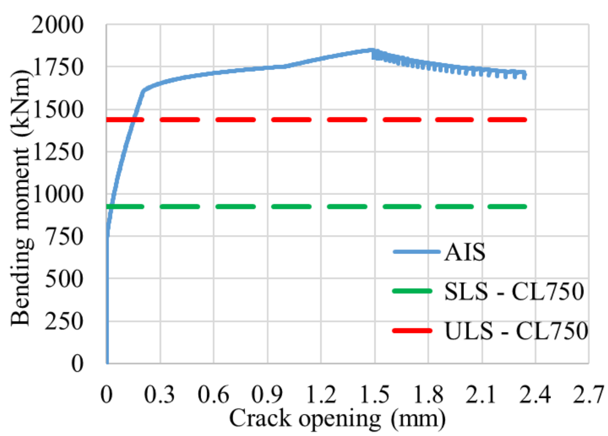

Figure 3.14 - Crack opening vs bending moment, AIS modelling

As it is possible to see, the crack opening at the service moment M_{SLS-1} = 925 kNm is 0.035 mm, which fulfills the limit of 0.15 mm allowed by the code.

3.3.5 Fatigue

The fatigue resistance of the high strength rebars has been also verified with the software AIS (Analyse Inélastique des Sections) developed at Polytechnique Montréal (Massicotte et al., 2011). The only rebars analyzed were the high strength rebars since they are the closest to the bottom of the girder, meaning they have the highest variation of stresses under loads. The stress variation is calculated between the stress state of the bridge loaded with permanent loads and the stress state of the bridge loaded with live loads. The maximum stress variation in the high-strength reinforcement bars is specified by Equation (3.3) of the CSA-S6:19 (Canadian Standards Association, 2019):

$$\Delta\sigma_{fls} = 165 - 138 \cdot \frac{f_{sf}}{f_y} \tag{3.3}$$

where f_{sf} is the stress in the bar under the "permanent loads only" loading condition and f_y is the yield stress of the bar.

Using the yielding stress of 1630 MPa for the high strength rebars presented in Section 3.1.3, and the AIS stress value for permanent load of -5.3 MPa, Equation (3.3) yields a permissible stress variation of 165.4 MPa.

The "permanent loads only" loading case corresponds to a moment of 430 kNm, and the FLS load combination to a moment of 885 kNm. For those bending moments, the stresses yielded by AIS are -5.3 MPa and 131.2 MPa respectively. The stress variation obtained is equal to 136.5 MPa which is less than the limit 165.4 MPa. This validates the fatigue strength of the longitudinal flexural reinforcement.

3.3.6 Deflection

Three verifications were made for the verification of the girder' deflection. The first one is based on the *Manuel de conception des structures* (Ministère des Transports et de la Mobilité durable., 2024) of the MTMD. The type of bridge considered was the bridge without sidewalk to demonstrate the benefits of the technology developed since a smaller girder height was possible. A maximum deflection of $L/800 = 15000/800 = 18.8\, mm$ was obtain for the girder design. The second verification was done based on the recommendations of the CSA-S6:19 code. The deflection was calculated with the SAP software in the same way as the moment, using the influence line method. At each calculation step, the moment was replaced by the deflection. Assuming that the behaviour of the structure is linear, it is possible to add the deflections in the same way as the moments. The influence lines of the deflections are shown in Figure 3.15.

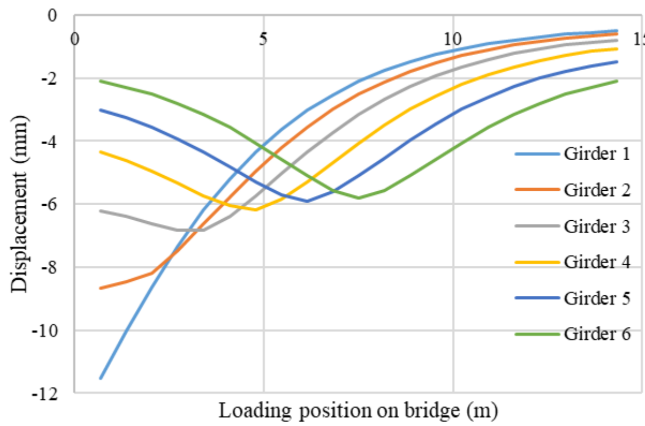

a) 15 m deck (11 girders)

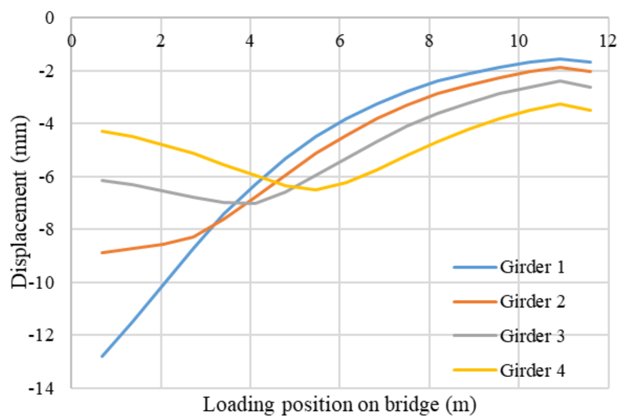

b) 11 m deck (8 girders)

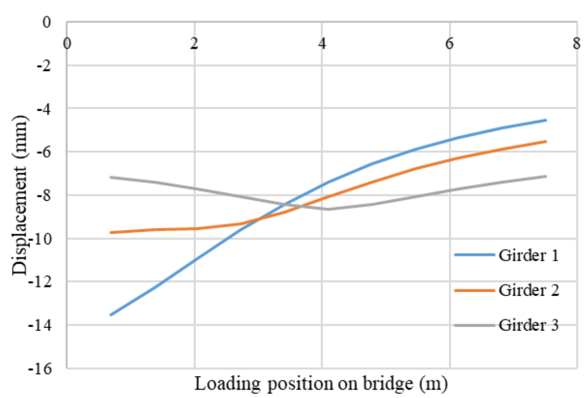

c) 8 m deck (6 girders)

Figure 3.15 - Influence lines of the displacement for the loading of the CL750-QC

As explained in Section 3.3.5, only a single truck loaded in the center of a single lane was used to calculate the maximum deflection (at 2.30 m from the extremity of the bridge), whose value is

17.2 mm from the 8 m wide deck (6 girders) bridge. Finally, according to Figure 3.16 MTMD, a reduction factor of 0.9 must be applied to the deflection. Because the calculation of the deflection is proportional to the load, it is equivalent to apply the reduction factor to the load or to the deflection. Thus, the maximum deflection obtained is equal to 17.2 × 0.9 = 15.5 mm and meets the criterion of 18.8 mm of the MTMD(Ministère des Transports et de la Mobilité durable., 2024).

Besides, a third verification was made according to the CSA-S6:19 code. The first frequency of the smallest bridge analysed was found to be 4.19 Hz. For a bridge without sidewalks with this natural frequency, the code stablishes a limit of around 18 mm (Figure 3.16). So, the bridge also meets the deflection criteria of CSA-S6:19 code.

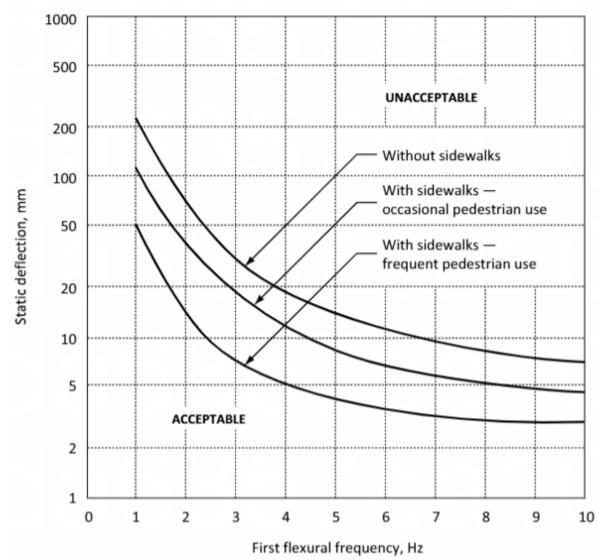

Figure 3.16 - Deflection limits for highway bridge superstructure vibration extracted from CSA S6 (2019)

3.4 Prestress Design

3.4.1 Design Criterias

For a simply supported non-prestressed beam, stresses produced by the self-weight and all additional loads during its service life, are usually only compressive stresses in the upper fibre and tensile stresses in the lower fibre of the beam.

The use of prestressing is made to counteract these stresses creating compressive stresses in the bottom fibre and tensile stress in the top fibre. Prestressing design aims to ensure that the compressive and tensile stresses in the beam remain within the limits defined by the code at all stages of the girder fabrication phase and bridge service life. The code criteria for forces in the beam are based on the compressive and tensile strengths of the concrete at two period in the life cycle: at the transfer of the prestressing forces and in the long term. The design criteria set by the CSA-S6 code are presented in Table 3.12.

Table 3.12 – Design criteria for prestressed girders, according to CSA-S6-19

Permissible concrete stresses	At release (transfer) of prestress	In services conditions
Compression	$0.6f_{ci}'$	$0.6f_c'$
Tension	$0.5\lambda\sqrt{f_{ci}'}$	$0.5\lambda\sqrt{f_c'}$

3.4.2 Permissible stresses at different design phases

The strength values selected for the project are presented in Table 3.13 and are related to the choice of HPFRC, described in Section 3.1.3. The stress f_{ci} was set at 50 MPa because it was reported by Rachello that the mixture would achieve this strength after one day. Prestressing at one day was chosen so that the production of all girders could be produced within a week. f'_{cri} on the other hand, comes from a formula extracted from the code: $f'_{cri} = 0.4 * \sqrt{f'_{ci}}$.

Table 3.13 – Prestress design stresses

Variable	f'_c	f'_{ci}	f'_t	f'_{cri}
Stress (MPa)	100	50	4	2.8

Then, the maximum allowable tensile and compressive stresses were determined according to the CSA-S6 code and are presented in Table 3.14.

Table 3.14 - Allowable stresses for prestressing (CSA-S6-19)

Permissible concrete stresses	**At release (transfer) of prestress**	**In services conditions**
Compression	30 MPa	60 MPa
Tension	1.41 MPa	4 MPa

3.4.3 Prestress loss

The method used to calculate the prestressing losses was the simplified method described in CPCI (2017). The stress loss is determined by computing the value of f_{co} (concrete compressive stress at centroid of tendon at critical section immediately after transfer) and f_{c1} (concrete stress at centroid of tendon at the critical section caused by sustained loads) and substituting them in the appropriate empirical equations.

The equations for f_{co} and f_{c1} are presented below:

$$f_{co} = \frac{P_i}{A_g} + \frac{P_i e^2}{I} - \frac{M_{sw} e}{I} \tag{3.4}$$

$$f_{c1} = \frac{M_{sd} e}{I} \tag{3.5}$$

The empirical equation to define the prestress loss provided by CSA-S6:19 is :

$$\Delta_{fp} = 137\ MPa + 16.3\, f_{co} + 5.4\, f_{c1} \tag{3.6}$$

When substituting the corresponding variable in the formula above, the prestress loss of 325 MPa is obtained for the 15 m girder. All calculations are detailed on Appendix A.1.

3.4.4 Concrete stresses at different design phases

Three different design phases were considered at this point. The first one was the stress state in the girder just after the tendons release, with short term prestress loss, loaded only with the girder self-weight. The second stress state was after long term prestress loss with the permanent load applied to the girder. And the third stress state was after long term prestress loss at SLS-1. Figure 3.17 shows the stress distribution of the girder under different fabrication phases as well as the stress limits imposed by the Canadian bridge code.

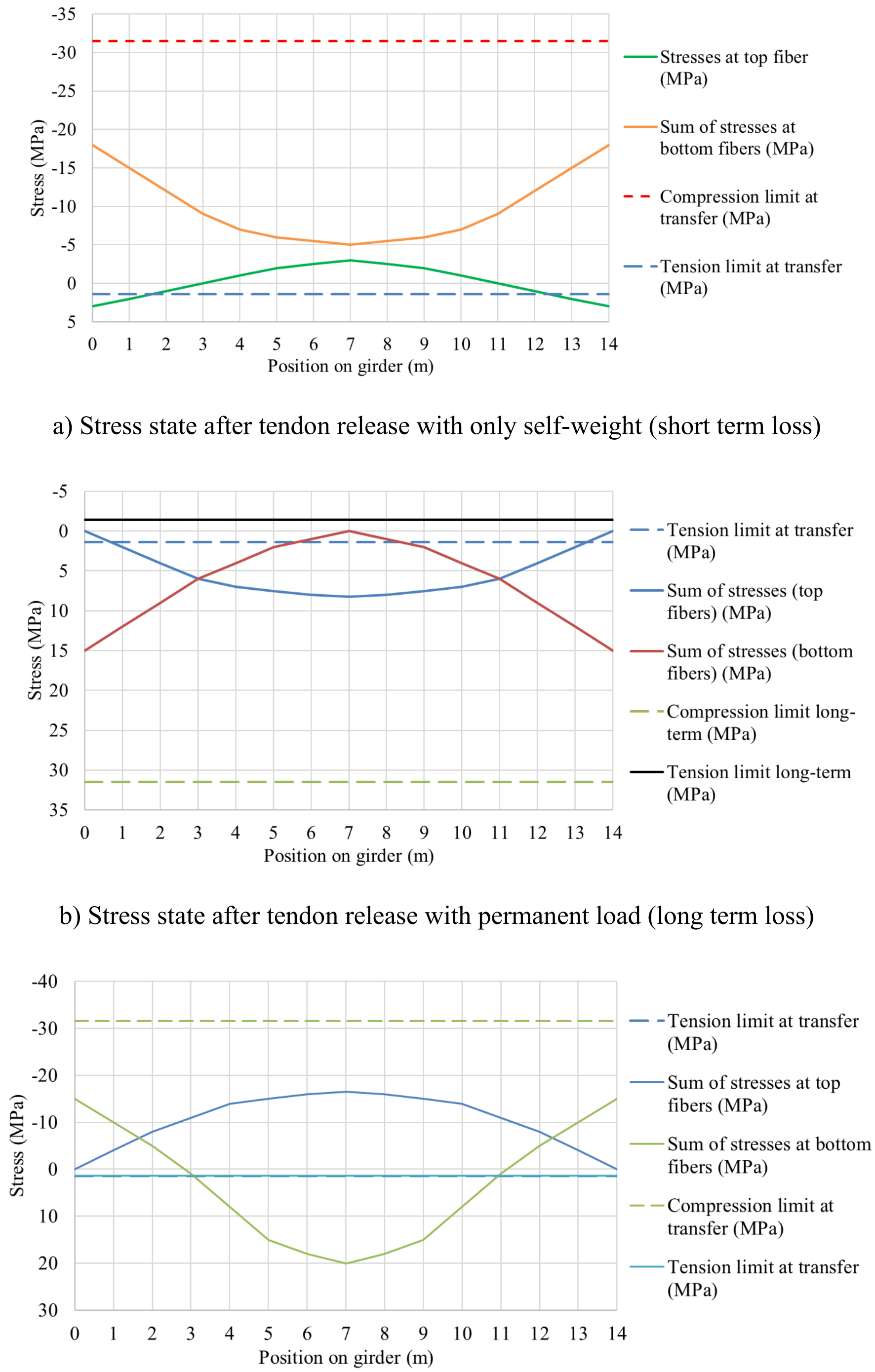

a) Stress state after tendon release with only self-weight (short term loss)

b) Stress state after tendon release with permanent load (long term loss)

c) Stress state at SLS-1

Figure 3.17 – Stress states on different loading positions

For the loading stages during transfer and permanent loads alone, the stresses in the top and bottom fibres comply with the permitted values. At SLS-1, the tension in the concrete is too high along the bottom fibre. This means that cracking will be present in the service state, and therefore that the girder is partially prestressed.

In this case, the crack opening must be less than 0.15 mm, according to the CSA-S6:19 code. It was seen previously that the crack opening at SLS-1 is 0.035mm < 0.15 mm. This criterion is therefore also met and validates the prestressing design.

3.5 Shear Design

3.5.1 Bearing load

The girder verification concerning shear resistance was performed at ULS condition. The shear force generated by permanent loads are shown in Table 3.7. The shear forces applied on the structure by live loads were extracted from the FE software SAP2000. The highest live loads shear force was obtained on the 2-lane bridge for the girder 1 located at the extremity of the bridge (Figure 3.12). The shear load distribution of girder 1 is shown in Figure 3.18.

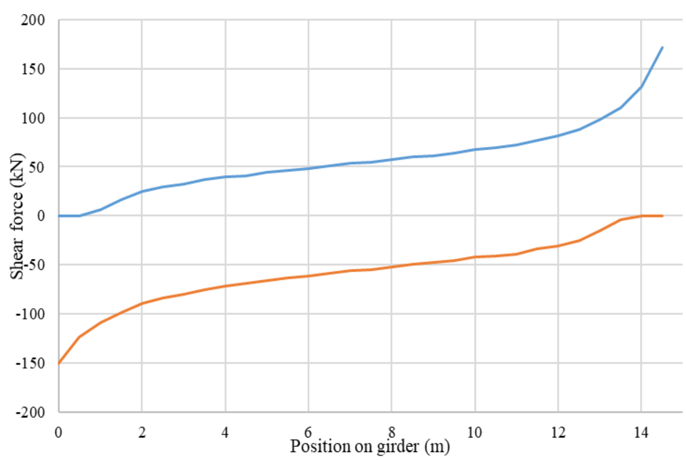

Figure 3.18 – Maximum and minimum shear forces distribution of girder 1 of 2 lane bridge

The truck load shear force was extracted at a distance d_v from the support, as indicated in the CSA-S6:19 code, the maximal value is 135 kN. Substituting the corresponding values to equation (3.7), the factored design shear load V_{ULS} is 410 kN.

$$V_{ULS} = 1.1 * (M_{concrete} + M_{wall}) + 1.5 * M_{asphalt} + 1.7 * M_{truck} \tag{3.7}$$
$$= 410kN$$

$$V_{ULS} = 1.1 * (114.5 + 23.6) + 1.5 * 19.2 + 1.7 * 135 = 410 \; kN$$

3.5.2 Design

To design the HPFRC girder for shear, every section of the girder must be analysed because each structure has a different critical design section. The shear resistance according to the general method of CSA-S6:19 varies with ε_x (longitudinal mid-depth strain in the girder). Thus, the critical design location of the girder may occur along the girder, not necessarily close to the support where the shear force is larger, but closer to mid-span of the girder where the concrete component of the shear resistance (V_c) is the lowest. The factored shear force distribution is shown in Figure 3.19 to find the critical sections.

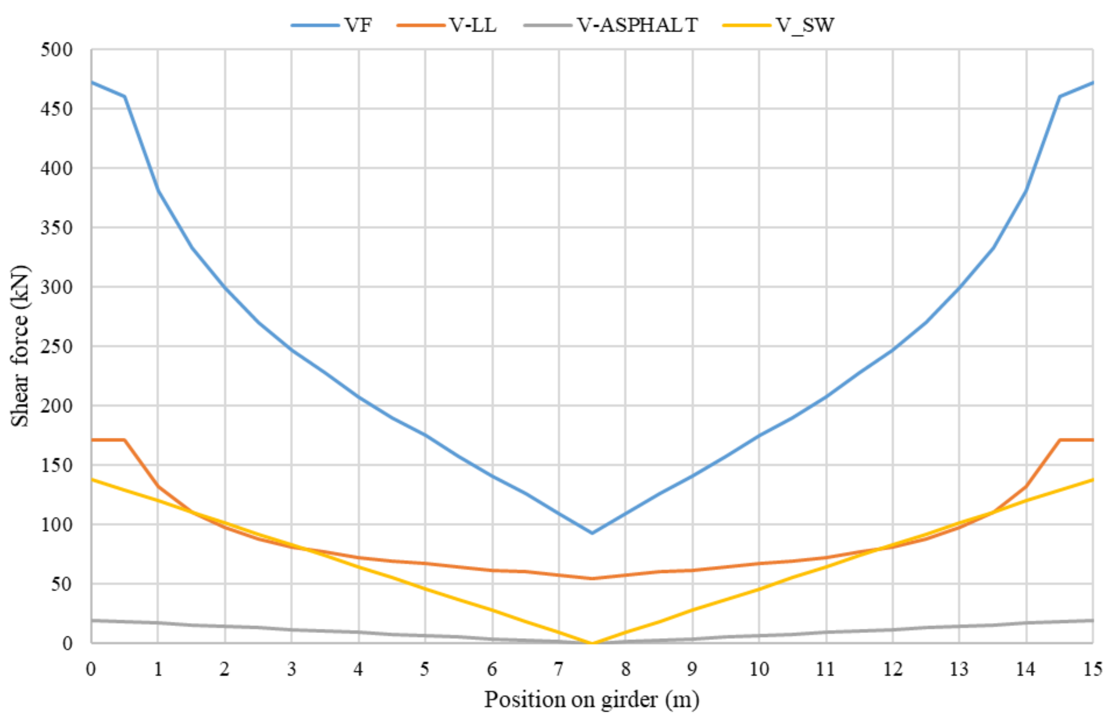

Figure 3.19 - Factored shear force distribution

The shear resistance was calculated with the general method of the CSA-S6:19 code. The general method was already explained in Section 2.3.3.2 and the same guidelines will be used here. Two design possibilities will be described. The first one is a design considering the minimal vertical reinforcement according to the standard, while the second is a design without stirrups. For the shear design, the material performance factors shown in Table 3.2 were used. A material performance factor for the fibres of 0.75 and a fibre orientation factor of 0.5 were also considered. The design variables used for the shear design of the 15 m girder with minimum reinforcement are presented in Table 3.15.

Table 3.15 - Shear design variables with minimum reinforcement

Variable	Value	Units
d_v	441	mm
E_s	200000	MPa
A_p	1260	mm^2
A_s	1170	mm^2
f_{po}	1000	MPa
s_{ze}	300	mm
f_c	100	MPa
b_w	335	mm

Stirrups with only one branch were selected for the design of the HPFRC girder. For a single branch of a 10M rebar, the minimum spacing calculated was around 180 mm. Figure 3.20 presents a comparison between the shear resistance for the 15 m girder and the factored shear load with this stirrups spacing. The shear contribution of V_c and V_{fib} when considering the design parameters of a minimally reinforced structure (s_{ze} = 300 mm) is already higher than V_f. The contribution of stirrups further increases the capacity and the V_r resistance is obtained

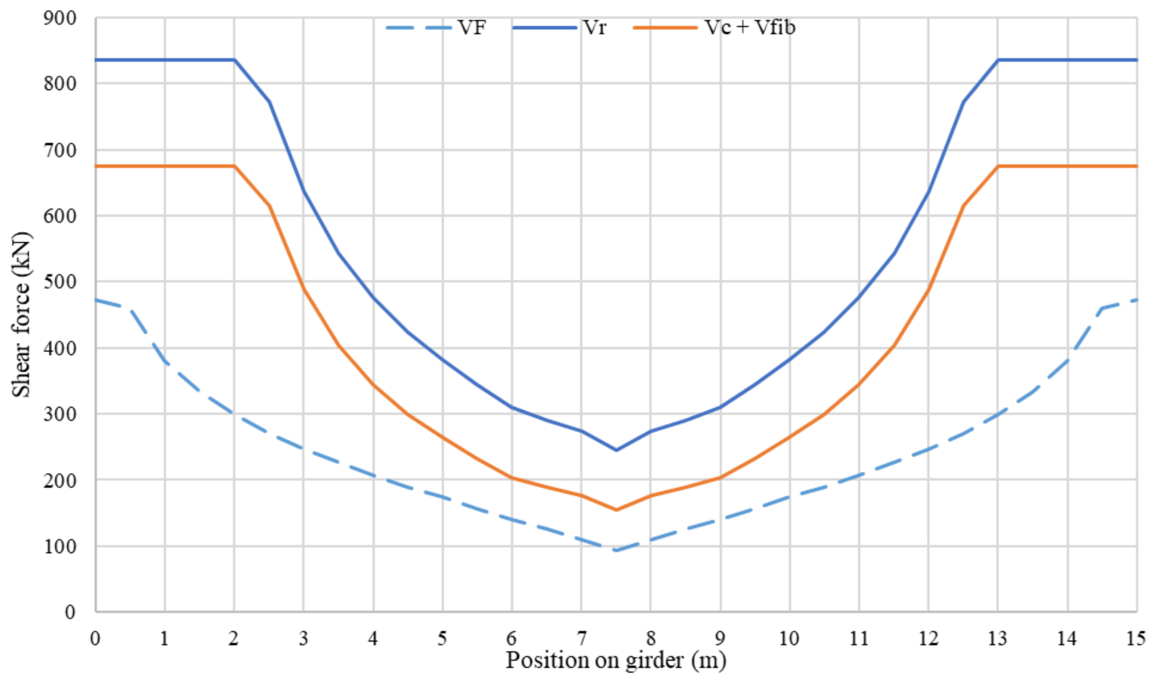

Figure 3.20 – Shear resistances with stirrups and factored shear loads

For a girder without stirrup, the variables for the design are presented in Table 3.16. One can observe difference in the shear variable for vertically reinforced and unreinforced girders. The general method considers that a girder, even though reinforced with 1% volume of steel fibres, has the same strength reduction due to size effect as a vertically unreinforced beam.

Table 3.16 - Shear design variables without reinforcement

Variable	Value	Units
d_v	441	mm
E_s	200000	MPa
A_p	1260	mm^2
A_s	1170	mm^2
f_{po}	1000	MPa
s_z	441	mm
s_{ze}	1029	mm
f_c	100	MPa
b_w	335	mm

The distribution of the factored shear load for the vertically unreinforced girder is shown in Figure 3.21. The factored load is very slightly superior to the HPFRC shear resistance close to the mid-span. In that context, this second design should be put aside. However, it is known that the FRC contribution to the shear resistance of girder is largely underestimate.

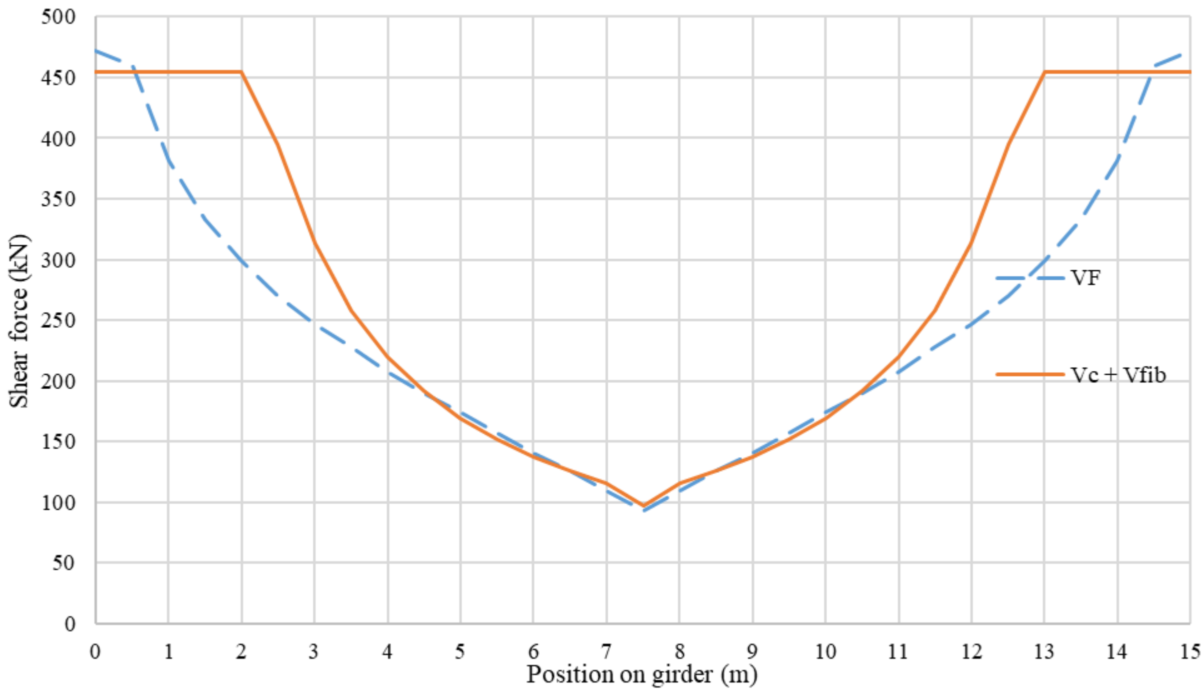

Figure 3.21 – Shear resistances without stirrups vs factored shear loads

Therefore, before taking decision for the final shear design of the 15 m prestressed HPFRC girder, an experimental campaign will be conducted. This campaign will allow verification of the accuracy of the bending and shear provisions of the CSA-S6:19 code for the design of HPFRC girders, but also focus on the contribution of the different mechanisms in the shear resistance.

CHAPTER 4 EXPERIMENTAL RESEARCH

An experimental study was conducted to verify the design of precast HPFRC prestressed bridge girders for the City of Montreal and to study the effect of different variables on the shear resistance of the HPFRC girders. First, the experimental program is presented with the details of the four-specimen design and their specificities. The specimen fabrication process is detailed, followed by the description of the experimental setups. Finally, the results of the experimental of the specimens are analyzed.

4.1 Experimental program

The experimental program was planed such that the design in bending of the prestressed HPFRC T-shaped girders and the effect of various variables on shear resistance could be verified. The design for bending according to the City of Montréal needs, the ultimate flexural strength, the crack opening at SLS-1 and ULS and the performance at FLS were considered. For the shear study, the effects of girder geometry, prestressing and shear span were considered to study the shear failure mechanisms and the associated shear resistance. It was decided to limit the length of the specimens between 3 to 6 m, allowing the desired information mentioned to be obtained while minimizing the size of the specimens. The details of the four girders of the experimental program are shown in Figure 4.1 whereas Table 4.1 presents a comparison between the specimens. Their description and justification are provided in the next section.

Table 4.1 - Experimental program

<table>
<tr><th colspan="2">Variables</th><th>G1</th><th>G2</th><th>G3</th><th>G4</th></tr>
<tr><td colspan="2">Length</td><td>6.0m</td><td>6.0m</td><td>3.0m</td><td>3.0m</td></tr>
<tr><td colspan="2">Span</td><td>5.7m</td><td>5.7m</td><td>2.7m</td><td>2.7m</td></tr>
<tr><td rowspan="2">Initial prestress values</td><td>Top tendons</td><td>825 MPa</td><td>450 MPa</td><td rowspan="2">-</td><td rowspan="2">-</td></tr>
<tr><td>Bottom tendons</td><td>1395 MPa</td><td>1010 MPa</td></tr>
<tr><td rowspan="2">Prestress values after losses</td><td>Top tendons</td><td>800 MPa</td><td>430 MPa</td><td rowspan="2">-</td><td rowspan="2">-</td></tr>
<tr><td>Bottom tendons</td><td>1250 MPa</td><td>910 MPa</td></tr>
<tr><td colspan="2">Stirrups</td><td>Yes</td><td>No</td><td>No</td><td>No</td></tr>
<tr><td colspan="2">Failure mechanism</td><td>Bending</td><td>Shear</td><td>Shear</td><td>Shear</td></tr>
<tr><td colspan="2">Geometry</td><td>T-shape</td><td>T-shape</td><td>T-shape</td><td>Rectangular</td></tr>
</table>

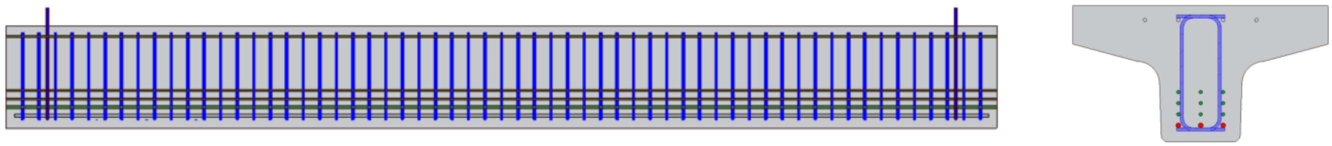

a) Girder 1 (G1) – Bending behaviour of a prestressed T-girder

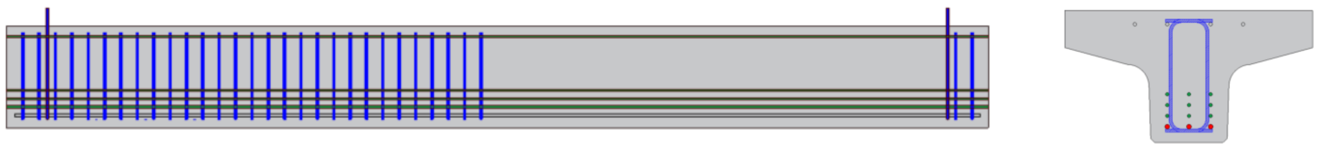

b) Girder 2 (G2) – Shear behaviour of a prestressed T-girder

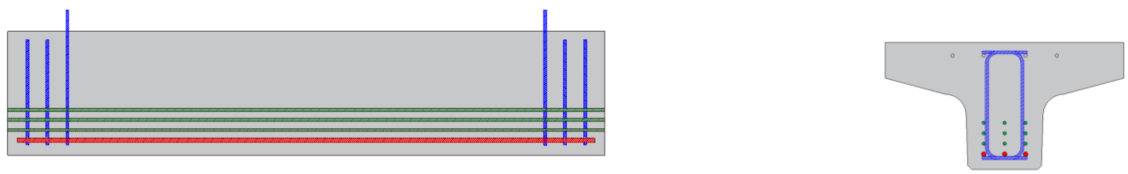

c) Girder 3 (G3) – Shear behaviour of a T-girder

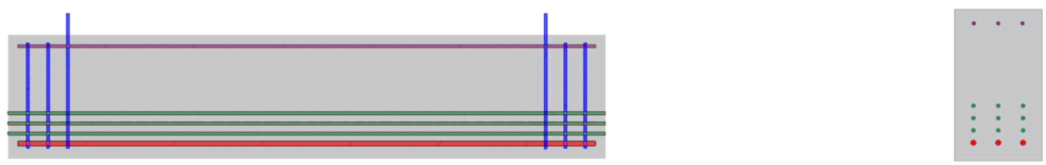

d) Girder 4 (G4) – Shear behaviour of a rectangular girder

Figure 4.1 – Bridge girders of the experimental program

4.1.1 Girder 1

Girder 1 (Figure 4.1a) is a fully prestressed girder with the same reinforcement layout and prestressing level as the prototype 15 m girder optimized for a typical bridge of the City of Montreal. Girder 1 was designed to evaluate the bending strength of the beam, including the necessary verifications at the service limit state and at the ultimate limit state, and compare the results with sectional analysis (AIS).

The differences of this specimen with the prototype 15 m girder are the stirrup layout, the number of tendons on the upper side and its length of 6 m, giving a 5.7 m span. A single branch of 15M rebar spaced every 100 mm was selected for the stirrup layout. As it will be explained later, due to the smaller length of the specimen in comparison to the actual 15 m girder, the specimen must resist a larger shear force to obtain a bending failure. Regarding the tendons disposition, because the bending moment due to self weight of a 6 m girder is less than for the 15 m one, top prestressing is needed to avoid cracking at top surface with the initial prestressing. The drawings with all details are presented in Annex A.3.

4.1.2 Girder 2

Girder 2 (Figure 4.1b) was designed to assess the shear resistance of the prestressed T-shaped girder. This girder has the same horizontal reinforcement layout as the 15 m girder design. However, the prestressing force was lowered in comparison to G1 to generate a shear failure. Only one side of the girder was reinforced with stirrups to ensure a shear failure on the unreinforced side and facilitate DIC instrumentation. The complete drawings are available in Annex A.3.

4.1.3 Girder 3

Girder 3 (Figure 4.1c) aims to study the effect of prestressing and shear span ratio when compared to G2. To make this comparison possible, the prestress was removed from Girder 3, while keeping the same longitudinal reinforcement as the previous girders. To study the effect of the shear span ratio, its length was also reduced to 3 m, with a 2.7 m span. The complete drawings are provided in Annex A.3.

4.1.4 Girder 4

Girder 4 (Figure 4.1d) was designed to evaluate the effect of the girder shape on the shear resistance. The T-shaped geometry of G1 to G3 was replaced by a rectangular shape for G4. Girder 4 is also fundamental for the shear study because it serves as a reference to evaluate the shear mechanisms in a conventional fibre reinforced beam. The drawings with all details are available in Annex A.3.

4.2 Specimen design and fabrication process

The beams were manufactured at *Béton Préfabriqué du Lac* (BPDL) plant in Saint-Eugène-de-Grantham. The production required a great deal of preparation prior to casting. The specimen geometry, tendons position and stirrup layout were slightly modified from the initial design to fit in the NEXT beam formwork available at BPDL manufacture plant. The HPFRC mix was also adjusted according to the mixer and components available at the plant. Finally, several logistical issues concerning the production of HPFRC, its handling to the formwork, and the casting method were studied.

4.2.1 Design modifications for the formwork

Small modifications to the specimen design were required to build the specimens at the precast plant. The main modifications were made on the girder geometry to reduce their cost of production for using the available formwork. The overlapping images of the initial design of the specimens (in red) and the prestressing steel bench configuration of BPDL (in black and blue) are shown in Figure 4.2a. An intermediate solution was found. The web of the girder was thickened following the contour of the NEXT beam formwork, and the flanges were obtained with the introduction of a wood formwork in the steel one (dashed area, Figure 4.2b). The drawings of all specimens as built are present on Appendix C of this thesis.

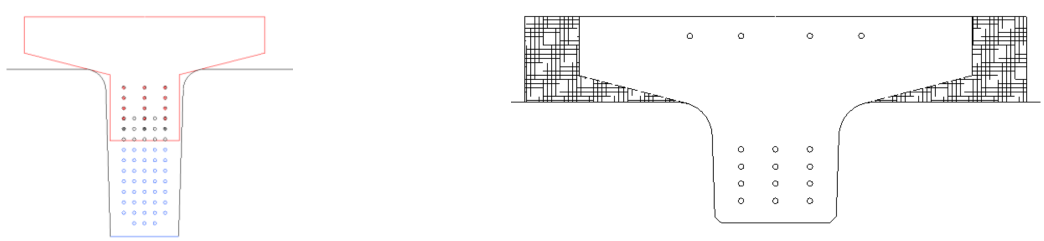

a) Initial girder design in the prestress bench b) Final girder cross-section

Figure 4.2 – Sketch of the cross section of the formwork used at BPDL

4.2.2 Shear and prestress design

As briefly explained in Section 4.1.1, the number of stirrups of girder specimens was adjusted to obtain a bending failure for G1 and a shear failure for G2 to G4. The shear design process was the same used for the 15 m girder (Chapter 3), but the stirrup layout and diameter were modified. Instead of 10M U-shaped stirrups spaced at 180 mm, single-leg 15M stirrups spaced at 100 mm were used. A value for s_{ze} of 300 mm was adopted because the selected stirrup configuration was larger than the minimum reinforcement. For sake of simplification, the same spacing was considered for the whole specimen. Figure 4.3 shows each shear resistance contributions (V_c, V_s, V_{fib}) and the total resistance (V_r) obtained according to the Canadian Bridge Code (CSA-S6, 2019), as well as the factored shear load (V_f) that the specimen must resist. Further calculation details can be found in Appendix A.2.

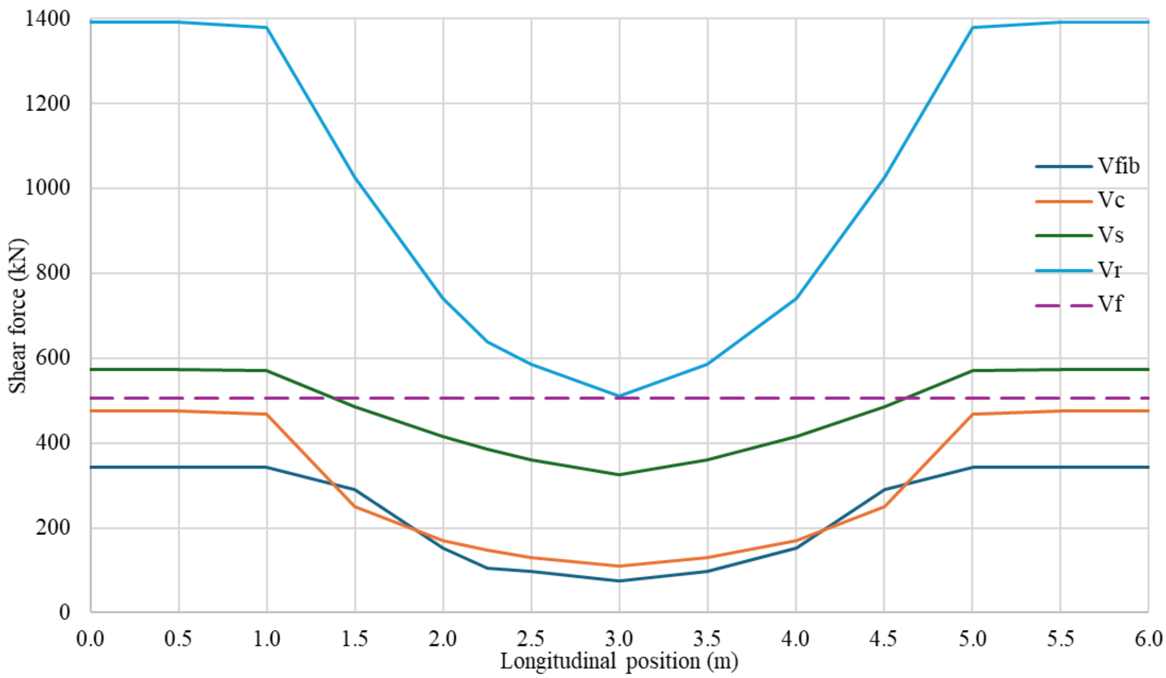

Figure 4.3 – Shear resistance contribution of each resisting mechanism and factored shear load.

The critical shear sections considered were located at d_v (with d_v = 440 mm) from the middle of the beam, so all the design was made considering x = 2.5 m and x = 3.5 m as the most critical sections. The shear resistance is very high in girder support zones because the same reinforcement spacing was considered throughout the specimen. Another important modification made to the detailing of the stirrups was that instead of considering vertical rebars, C-shape bars were used (Figure 4.4). This was done to match S6.19 guidelines requiring that every stirrup must have at least a 90 degrees angle at its extremity to ensure a good anchorage between concrete and steel.

The C-shape stirrups also helped to support the non prestressed high strength rebars at the first layer. Besides, to avoid placing all the vertical branches of stirrups on the same side and maybe compromise concrete flowability, the vertical branch was alternatively installed on the left and right sides.

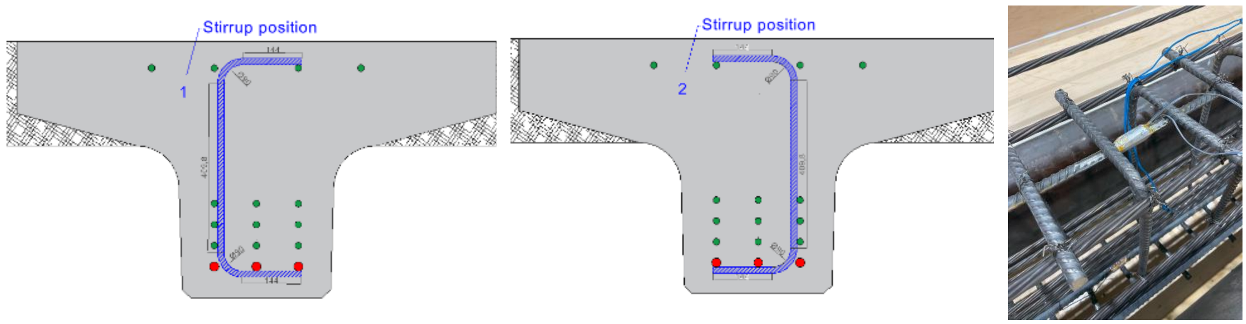

a) Left position

b) Right position

c) Picture of actual stirrup setup

Figure 4.4 – Stirrup positions on specimens

Because the self-weight of a 6-m girder is smaller than the one of a 15-m girder, the top prestress also needed to be modified. Instead of 2 tendons, 4 tendons were used at the top face (Figure 4.4). The prestressing calculations are presented in Appendix B with the new prestress loss.

4.2.3 HPFRC mixture design

The aim of the development was to obtain a self-compacting HPFRC with a compressive strength f'_c around 100 MPa, with good homogeneity and fibre distribution. The existing HPFRC mixture formulation of Rachello (Rachello Adrien, 2023), used for the previous girder development, was taken as the starting point. A w/c ratio of 0.28 was adopted to obtain the necessary compressive strength. A dosage of 1% by volume of Dramix 4D 65-35 fibres (78 kg/m^3) was introduced in the mixture. The fibres were 35 mm long and had a length/diameter ratio of 65. Unlike for Rachello's mixture, a more powerful superplasticizer was used for this research project using Lafarge cement. Plastol 6400 superplasticizer was chosen because a considerable smaller quantity was required to obtain the desired flowability of the mixture. Several HPFRC batches were produced in the laboratory to adjust the amount of superplasticizer and achieve the minimum spread criterion of

600 mm using the Abrams' cone. Two verification mixes were also made at BPDL plant before the specimens were manufactured. The HPFRC final composition used to manufacture the specimens is given in Table 4.2.

Table 4.2 - Final composition of the HPFRC mixture

Component	Component name	Mass (kg)	Volume (L)
Ciment	HSF (Lafarge)	674.6	214.2
Water	-	198.3	198.3
Superplasticizer	Plastol 6400	6.7	6.1
Sand	80mm - 5 mm Lafarge	826.9	30.6
Gravel	5-10 mm Choquette	651.6	240.6
Fibers	Dramix 4D 65-35	78.0	10.0

4.2.4 Specimen casting

4.2.4.1 Pouring and fibre orientation

The precast plant in Saint-Eugene is equipped with an automated loading system that feeds a mixer truck. Only the fibres and the superplasticizer were loaded manually in the truck (Figure 4.5). The truck capacity was 3 m^3, but the precast plant technicians recommended not to exceed 2.75 m^3 of concrete to guarantee the mixture uniformity.

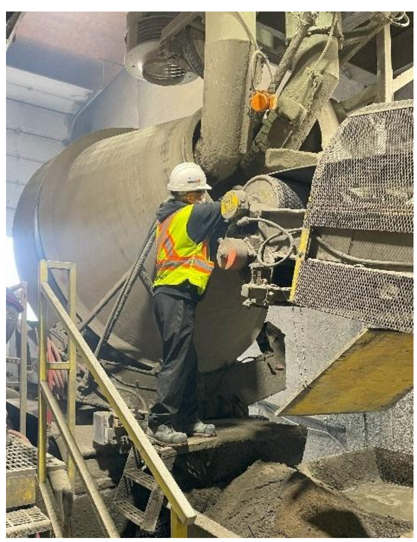

Figure 4.5 – Concrete mixing infrastructure at BPDL Saint-Eugène

The amount of concrete needed to manufacture the specimens was 2.75 m^3 for G1 and G2, 1.5 m^3 for G3 and 1.0 m^3 for G4. It was decided to produce three batches, one for G1, one for G2 and one for G3 and G4 to optimize the productions. To obtain a favorable fibre orientation in girders, a pouring technique was applied with the help of BPDL staff. The technique consisted of pouring the concrete at one end of the girder and letting it flows to the other end of the formwork by itself. The vibrator was used just to ensure a good flowability of the HPFRC around the tendons (Figure 4.6). Whenever the HPFRC reached the top of formwork, the pouring bucket was advancing to fill the next section of the formwork.

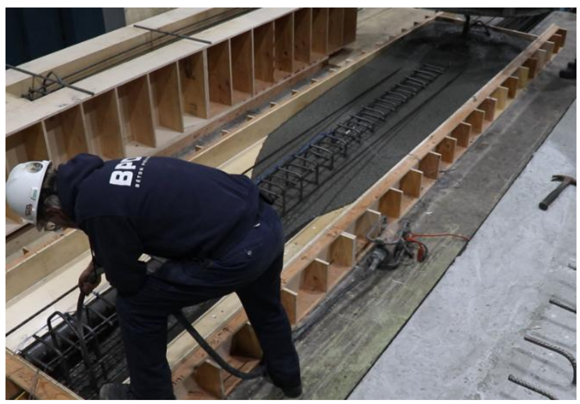

Figure 4.6 – Pouring technique used for all girders at BPDL

4.2.4.2 Manufacturing process

The logistics of manufacturing the specimens is detailed in this section. At the mixing station, all the concrete necessary was made with one single batch. Firstly, a plain concrete mixture was prepared. The mix viscosity was adjusted at the end of mixing, and the fibres were added just when the flow cone test of the plain concrete mixture was around 700 mm. Fibre addition usually reduces the flowability of the concrete, sometimes small superplasticizer correction was necessary to ensure that the HPFRC spread reached 550 to 600 mm. Since the girder formworks were elevated, it was necessary to handle the HPFRC from the mixer to the formwork using a large bucket attached to a crane. Photos of the handling procedure of the HPFRC are shown in Figure 4.7.

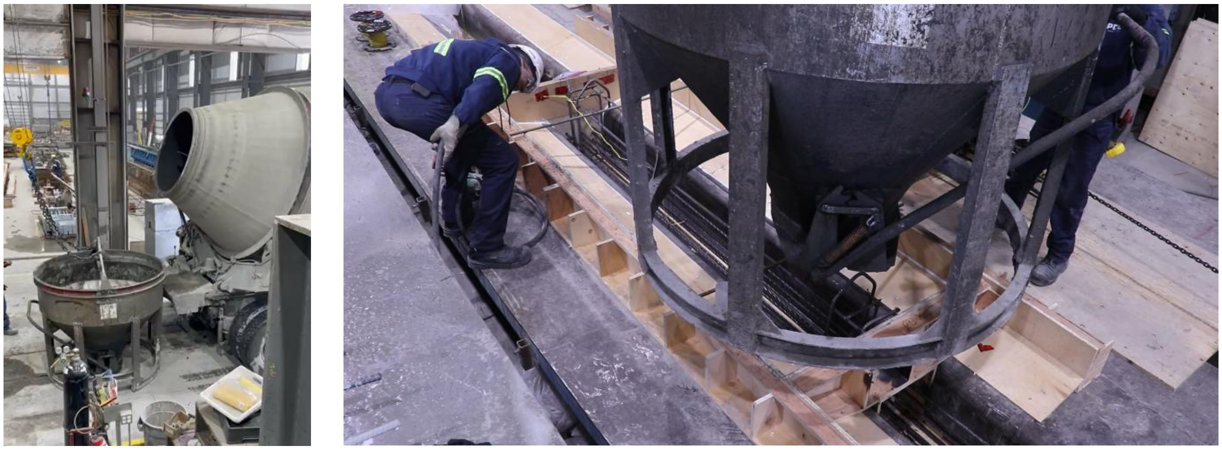

Figure 4.7 – HPFRC transfer from the truck to the bucket and from the bucket to the formwork

Two technicians were responsible for the casting of the girders. One technician controlled the bucket, while the other used the vibrator in the vicinity of tendons to ensure a good flowability of the HPFRC in this area. Later, finishing was done to the girder surface, and a protective plastic cover was added to avoid early water evaporation.

4.2.4.3 Sensors in girders

At least two strain gauges were used for all girders, as it will be discussed in more details in Section 4.3, and two temperature sensors were used to track the evolution of temperature over time. One of the temperature sensors was positioned at the surface and the other was positioned in the web core. The cables layouts are shown in Figure 4.8. The gray cables were used for the strain gauges glued to the reinforcement and the yellow cables were used for the temperature sensors.

Figure 4.8 – Sensor cable layout

4.2.4.4 Temperature evolution

The evolution the HPFRC temperature is presented in Figure 4.9 for each girder until their demolding. Three curves are shown: core temperature, surface temperature and room temperature. Only room and core temperatures are presented for G4 because a problem on the acquisition device occurred.

Each curve type has its own evolution, but it is similar for the 4 girders. Room temperature in the precast plan was stable at around 20 °C. The HPFRC peak temperature varied between 55 to 75°C and was reached after one day for all girders. According to standard A23.1, maximum temperatures during curing shall not be greater than 70°C to prevent delayed ettringite formation. This aspect should be considered in an industrial process to reduce ideally the HPFRC heat of hydration, for example by reducing the cement content in the mixture or by replacing water by ice in the production.

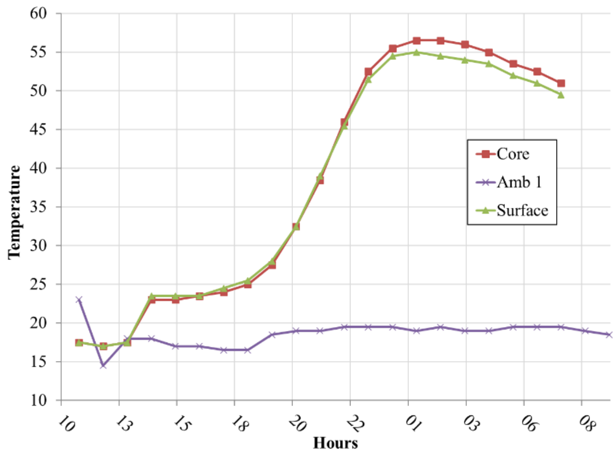

a) G1

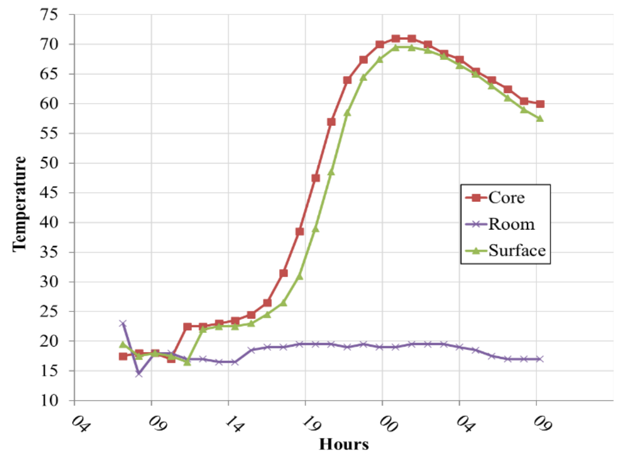

b) G2

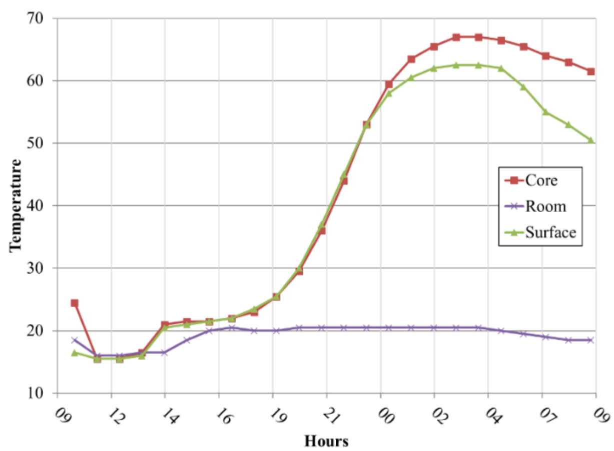

c) G3

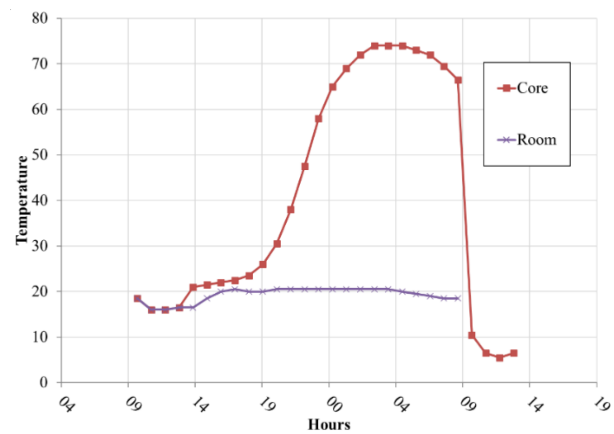

d) G4

Figure 4.9 – Temperature of specimens from casting up until unmolding

4.2.4.5 Tendons cut and unmolding

It was necessary to wait until the HPFRC had a compressive strength of 50 MPa before cutting the tendons to avoid cracking at top surface of the girders during the transfer of prestressing. To verify the compressive strength of the concrete at 3 different moments, 6 concrete cylinders (2 cylinders per test) with a diameter of 4 inches were manufactured at the same time as the specimens and then placed right next to the girders to benefit from the same curing conditions. When compressive tests showed that the tendons could be cut, a planned sequence of cut was followed to ensure that tensile stresses at girder surface would not exceed the limit of 1.4 MPa imposed by the code. Figure 4.10

presents the order of cut or each tendon. For all beams, the cut of tendons started around 24 hours after pouring and the formwork was removed right after the cutting of the tendons.

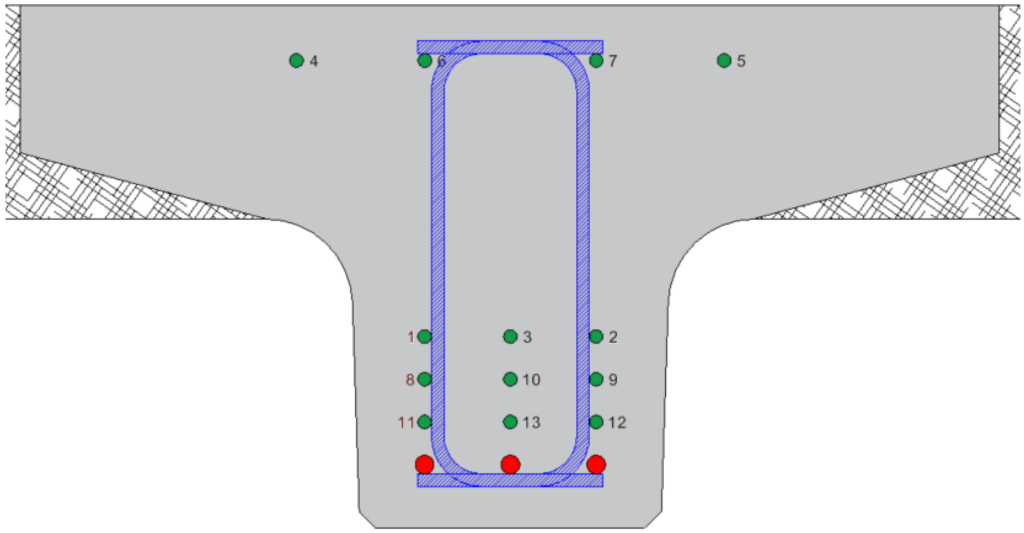

Figure 4.10 – Tendons cutting procedure

4.3 Experimental setups

The experimental setups used to evaluate the strength of Girders 1 to 4 will be detailed in this section.

4.3.1 Three-point bending setup of 6 m girders

A centered three-point bending setup was used to evaluate the bending strength of G1 and the shear strength of G2. A shear span ratio a/d = 2850/441 = 6.45 was chosen. A diagram and photo of the assembly are shown in Figure 4.11.

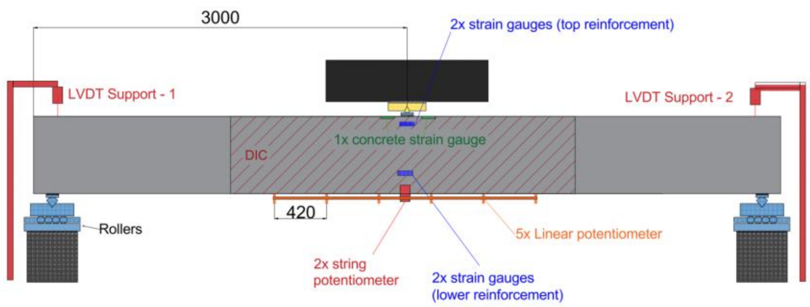

a) Elevation view

b) Photo

Figure 4.11 - Setup for evaluating the flexural and shear strength of 6 m prestressed beams

The beam was supported at each end by a simple support, allowing longitudinal movement via rollers and rotation via a pivot. The load was applied using a 12 MN load frame on a steel plate 100-mm wide and 1-m long. A pivot was installed on the loading plate to allow rotation. The support-to-support distance was 5.70 m.

Vertical displacement was measured above each support using linear voltage displacement transducer (LVDT) sensors. The deflection was measured at mid-span of the beam, under the web on each side of the beam. The average deflection of the beam was obtained by removing the average displacement measured at the supports to the mid-span deflection.

The girder's strains were measured using a digital image correlation (DIC) system in the zone identify at Figure 4.11a. Two pairs of cameras were used. The entire length of the girder could not be covered by the DIC system because the columns of the 12 MN press blocked the cameras viewing planes. Details of the DIC system setup is given in Section 4.3.3. The tensile strains were also measured under the girder (as a safety measure in case the DIC did not work) using LVDT sensors with a measurement range of 420 mm.

The strains of the concrete on the specimen top fibre were measured using one strain gauge bonded to the concrete just at the edge of the loading plate. Two strain gauges were also installed in the center of one high-strength bar before casting.

A preload of 10 kN was first applied to ensure uniform contact at the loading plate before releasing the roller displacement at girder supports. The load frame actuator was displacement-controlled at a rate of 2 mm/min during the loading and at a rate of 10 mm/min while unloading beyond the maximum load o have a 60-minute duration time approximately. Data acquisition during the tests were made on the load frame force, LVDT displacements and gauge strains at a rate of 1 Hz.

4.3.2 Three-point bending setup of 3-m girders

A centered three-point bending test was used to evaluate the shear strength of G3 and G4. A shear span ratio a/d = 1350/441 = 3.1 was chosen. A diagram and photo of the assembly are shown in Figure 4.12.

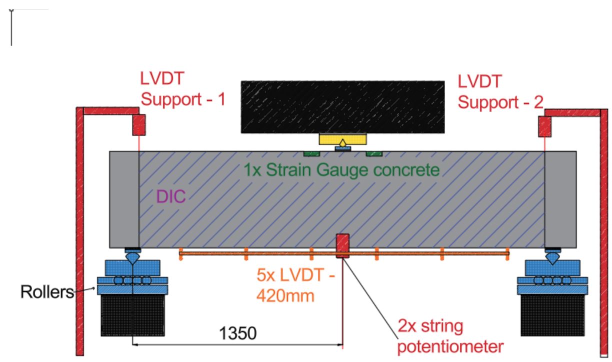

a) Elevation view

b) Photo

Figure 4.12 - Setup for evaluating the shear strength of 3-m prestressed beams

The setup for the 3 m girders used the same number and type of sensors and measured the same type of data detailed for 6 m girders. Even though the area of interest was different from the 6 m to the 3 m, two pairs of cameras were needed since the press columns did not allow for a full view of the girder with just one pair. More details on the DIC setup are given in Section 4.3.3. The support-to-support distance was 2.7 m.

4.3.3 DIC system setup

A digital image correlation (DIC) system was used to measure accurately girder deformations and crack openings. The DIC technique captures images with high resolution cameras at regular intervals on a surface during the test. The surfaces analyzed are the lateral face of the web and flange of the girder (Figure 4.13).

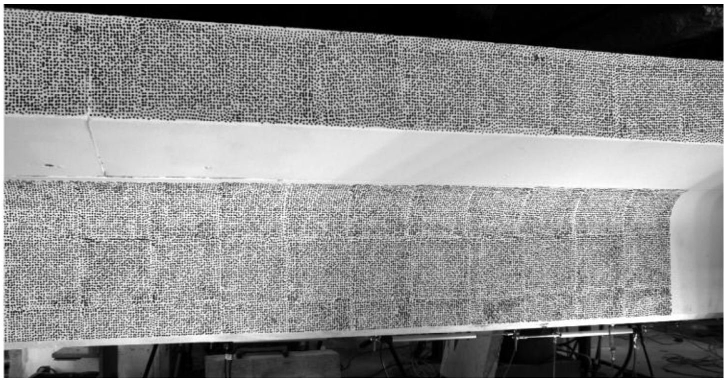

Figure 4.13 – Side of G2 with speckles applied to the flange and the web

The DIC system evaluates, from the relative displacement of specific points, the strain fields and the crack openings on analysed surface (Correlated Solutions, n.d.). To extract these values, the areas analyzed must be prepared. It is necessary to first apply several coats of white paint, and then apply a layer of black speckles, as shown in Figure 4.14. The quality of the speckles directly affects the quality of the data extracted. The darker the speckles used and the rounder the dots applied, the lesser will be the noise in the acquired data.

Figure 4.14 – Painting process of G1

Another important step of the process is to ensure a good lightning condition. According to Correlated Solutions (Correlated Solutions, n.d.), the best lighting setup is one which uses LED lamps in dark rooms. The LED lamps are optimal because they produced very limited heat that can increase the noise in the acquired data. The dark room is also important to avoid light intensity variations over time. A dark room was created around the cameras and the girder (Figure 4.15).

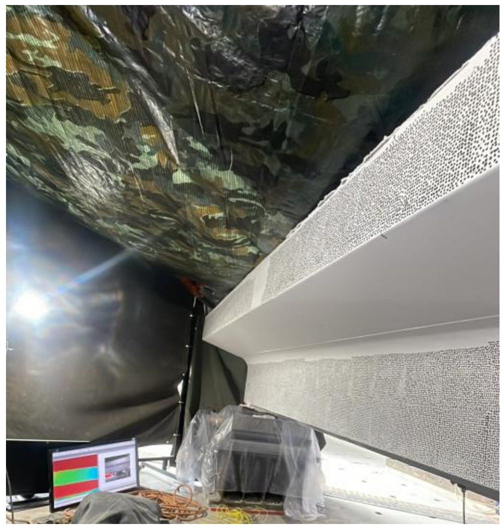

Figure 4.15 – Photo taken inside the dark room

The size and spacing of the speckles, as well as the focal length of the cameras and their position, were adjusted according to the dimensions of the area to be analyzed. Since the area of the surface analysed was too large for the space available between the columns of the press to install one set of cameras, 2 sets of cameras were required (Figure 4.16). Dividing the area in two made it possible to capture the central span and one extremity of the girder, while increasing the accuracy of the data since the cameras were positioned closer to the area of interest.

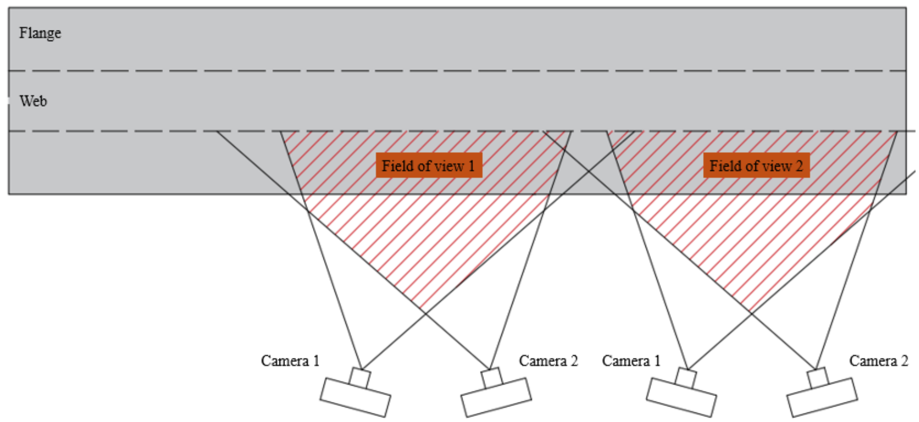

Figure 4.16 – Sketch of cameras field of view on a 6 m girder

The cameras were arranged to form fields of view with the shape of isocele triangles, with a 30° angle at the center of the girder. This position of the two sets of cameras has maximized the area to be analysed. Before starting the test, the DIC system was first calibrated using a calibration panel. Then, the focus, contrast, and brightness settings were adjusted to minimize uncertainty errors. The system was set to captures photos at intervals of half a second throughout the test. In total, around 6000 pictures were captured for each test. On the other side of the girder (opposite side of the DIC system), a thin layer of white paint, diluted with water, was applied to allow better observation of cracks during the test.

4.4 Material characterization results

4.4.1 Concrete

4.4.1.1 <u>Fresh concrete properties</u>

Fresh concrete properties were measured for each batch of each beam. Slump was measured using a flow cone in accordance with ASTM C143 and ASTM C1611. The density of the concrete was measured using a 7-litre container in accordance with ASTM C29. The air content was measured using a concrete air meter in accordance with ASTM C231. The average results for each beam are presented in Table 4.3 below.

Table 4.3 – Fresh concrete properties

Properties	Standard	Girder 1	Girder 2	Girder 3	Girder 4
Slump (mm)	ASTM C143 ASTM C1611	617 – 634	616 – 638	712 – 732	712 – 732
Volumetric mass (kg/m^3)	ASTM C29	2322	2475	2303	2303
Air percentage (%)	ASTM C231	2.1	2.2	2.0	2.0

4.4.1.2 Compressive strength

For each HPFRC batch, eleven cylinders were manufactured. The cylinders were removed from the formwork after 24 hours and then placed in a humid chamber until the day of the testing. Cylinders of 4 inches in diameter and 8 inches in length were used to measure the compressive strength of the HPFRC in accordance with ASTM C39. For each test date, three cylinders were used, and the average was considered. The compressive strength was measured at one day, to ensure that the required strength reached 50 MPa to cut tendons, at 28 days, and at the day of structural tests on girders (between 60 to 71 days). Two cylinders were used to measure the elastic modulus and Poisson ratio of the concrete at 28 days and at day of the structural tests, according to ASTM C469. The average results are showed in Table 4.4 for each girder. The compression strength significantly increased in the first 28 days and then stabilised. The average compressive strength at 28 days and at girder tests were 103 MPa and 106 MPa.

Table 4.4 – Compressive strength of HPFRC

Date	Data	Standard	Girder 1	Girder 2	Girders 3 and 4
28 days	f'_c (MPa)	ASTM C39	96.6	102.6	109.8
Girder test	f'_c (MPa)	ASTM C39	102.7	107.1	111.1
	E_c (GPa)	ASTM C469	43.2	40.2	41.8
	n		0.24	0.23	0.21

4.4.1.3 Tensile strength

Dog-bones shaped specimens (Figure 4.17) were used to characterize the tensile strength of the HPFRC. Three specimens were produced for each batch. They were cast horizontally from one extremity to another with the intent of obtaining a favorable fibre orientation and maximized pre- and post-peak tensile properties. The specimens were removed from the molds after 24 hours, then placed in a humid chamber until testing. The tensile tests were performed in the same week as the structural test on girders.

The dog-bones were tested under direct tension, according to the procedure developed by (Beaurivage, 2009). Four displacement sensors were positioned on each side of the dog-bones. The specimen wide ends were clamped in the 2500 kN hydraulic press jaws and then the specimen was submitted to the tensile load. The tensile setup is shown in Figure 4.17.

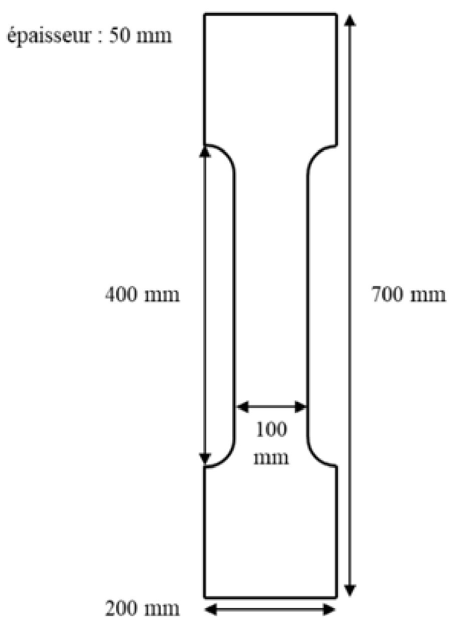

a) Dog-bone specimen

b) Test setup

Figure 4.17 – Tensile test

The average results obtained for dog-bones specimens produced for each beam are shown in

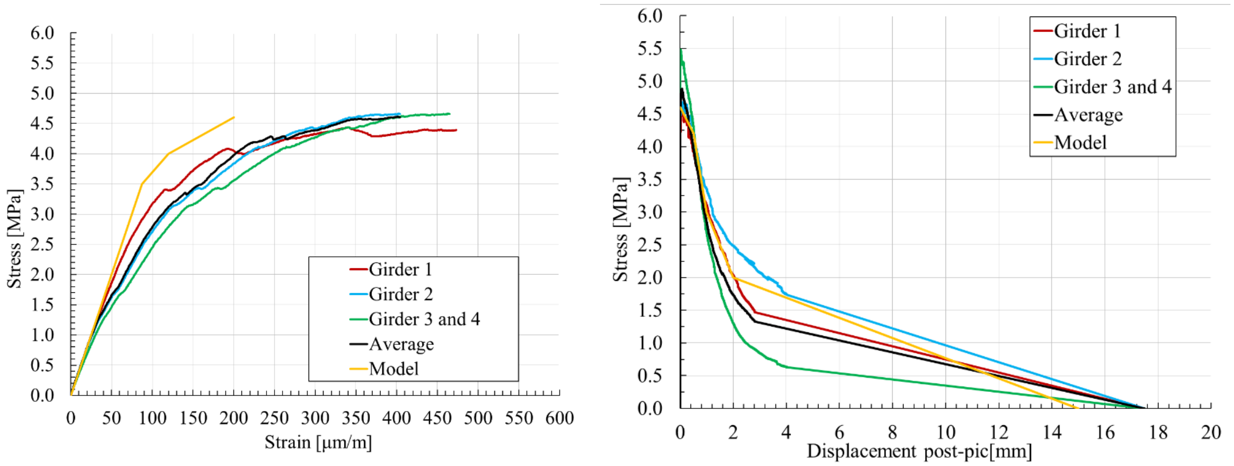

a) Pre-peak *b) Post-peak*

Figure 4.18. The curves show the tensile stress as a function of deformation before the opening of a macrocrack, then tensile stress as a function of the macrocrack opening. The tensile strength of the HPFRC varied from 4MPa to 5MPa and the post-peak behaviour was similar until a crack opening of 1.5 mm was measured. The retained values for analysis are given in Table 4.5.

Table 4.5 – Tensile strength of HPFRC

Stress (Mpa)	**Crack opening (mm)**
4.6	0.0
3.9	0.5
3.0	1.0
2.0	2.0
0.0	15.0

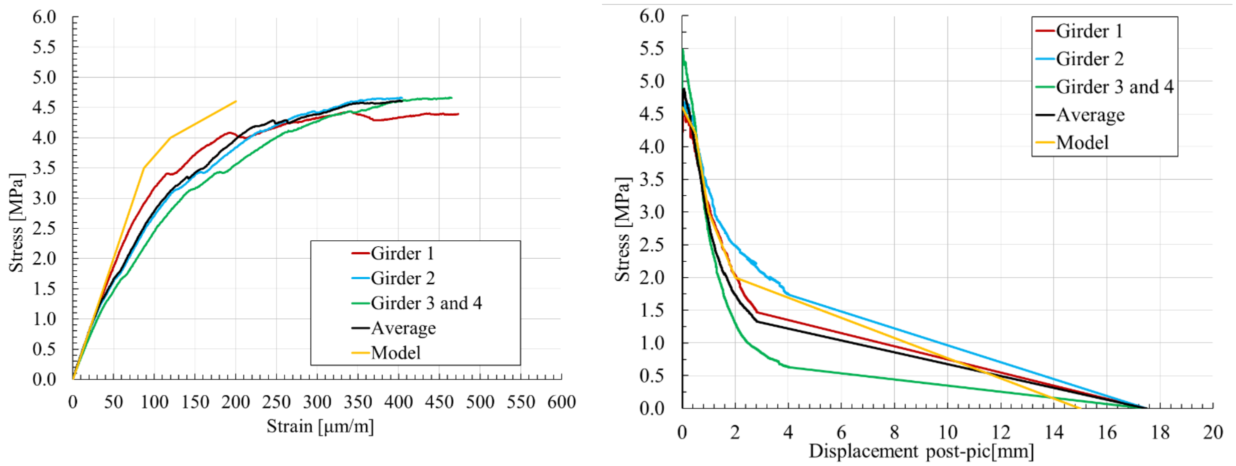

a) Pre-peak *b) Post-peak*

Figure 4.18 – Tensile behaviour of HPFRC

4.4.2 Reinforcement

Rachello (2023) conducted tensile tests on the 400W and A1035 rebars. Because A1035 bars used in this project come for the same batch as those of Rachello, no tests were carried out. The properties of the 15M 400W bars used for stirrups were not tested and the properties were assumed as those of Rachello although they do not come for the same batch. The average results for each type of bar are shown in Figure 4.19. The tensile behaviour of the prestressing strands was determined from the technical data provided by the manufacturer. The simplified properties assumed for the three types of reinforcement are shown in Figure 4.19.

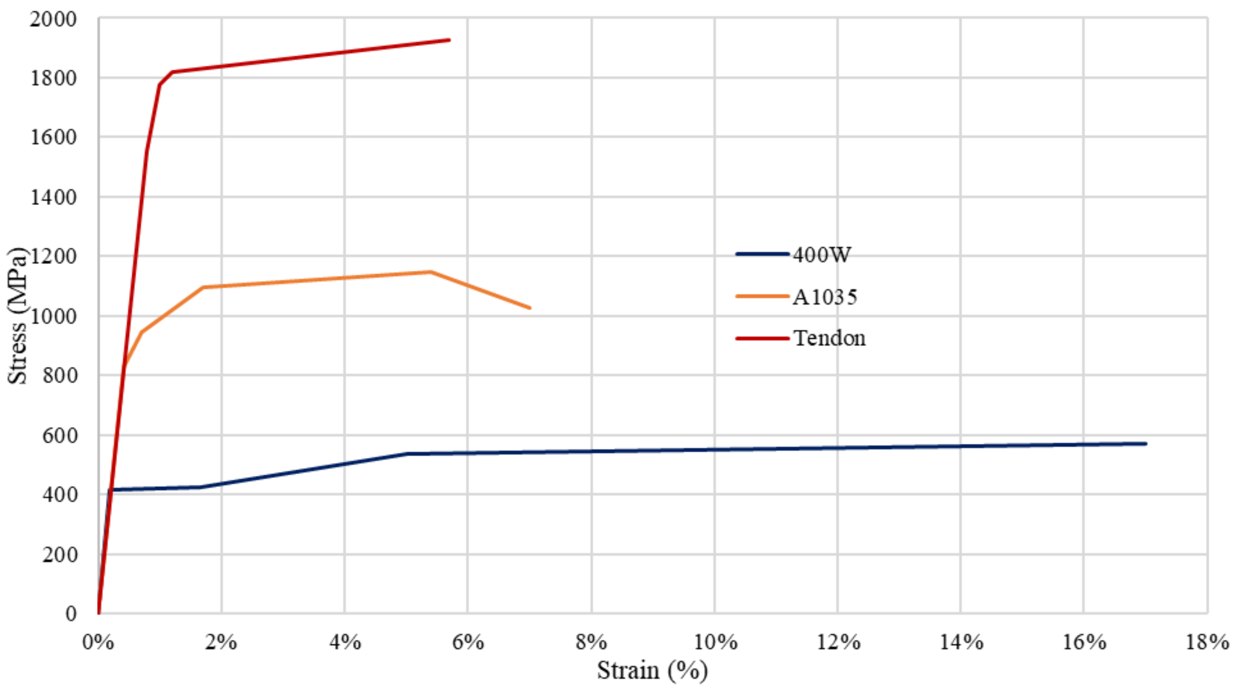

Figure 4.19 - Stress/strain laws for different types of reinforcement in tension

The following properties are adopted for the numerical analysis. According to Rachello's tests, the 400W bars have a yield strength $f_y = 418$ MPa and an ultimate strength $f_u = 573$ MPa for a deformation of 17%, with the end of the yield plateau at a strain of 170 000 µm/m. The A1035 bars tested by Rachello behaved linearly up to yielding followed by a gradual nonlinear hardening behaviour up to an ultimate strength of 1148 MPa whereas failure occurred at a stress of 1027 MPa and at a strain of 7%. He did not measure the elastic modulus. According to Renaud-Laprise (2022) who tested bars from the same supplier (different batch and diameter), the elastic modulus is equal to 212 700 MPa, with a nonlinear second order hardening behaviour beginning at a stress of 550 MPa. For the analysis carried out with AIS, the linear and nonlinear properties of Renaud-Laprise are retained whereas Rachello's ultimate values are adopted. The maximum strength of 1150 MPa is retained with a corresponding strain of 50 000 µm/m. The strands behaved linearly up to a yielding stress of 1776 MPa. They had an ultimate stress of 1924 MPa for a deformation of 5.7%. The elastic modulus considered for 400W and prestressing strands is $E_s = 200\,000$ MPa as recommended by CSA-S6 as minimum conservative value.

4.5 Girder test results

Experimental results presented include the effects of self weight which was added to the measured data. The values are 41 kN-m and 29 kN for the bending moment and shear force respectively. The instrumentation used to measure the initial strains and their variation with time due to prestressing, shrinkage, creep and relaxation did not function properly. Those values will be estimated according to available models.

4.5.1 Girder 1

Girder 1 (G1) has the equivalent bending reinforcement and prestressing level considered for the prototype 15 m bridge girders. Thus, the test should confirm the flexural behaviour and bending capacity of the girder for the application.

4.5.1.1 Flexural resistance

The bending moment – displacement response of Girder 1, including girder self-weigh, is shown in Figure 4.20a. The girder exhibited a linear elastic behaviour up to 691 kNm. Subsequently, a nonlinear behaviour was observed with the appearance of flexural cracks. Shear cracks appeared on both sides of the girder around 1241 kNm but did not grow whereas failure occurred in bending with one governing flexural crack at mid-span. The ultimate bending moment was obtained at 1940 kNm, after the yielding of the flexural rebars (400W and A1035) and tendons which corresponds to a shear force of 724 kN. The girder was unloaded after reaching a deflection of 86 mm. Cracks developed in the vicinity of the loading point following a fan pattern. The critical bending crack developed close to the middle of the girder with an angle of around 80° with respect to horizontal (Figure 4.20a). The bending capacity of the girder G1 met the prediction assumed in design. In Figure 4.20b, the ULS for the CL750 truck was divided by 0.85 to account for the presence of safety factors.

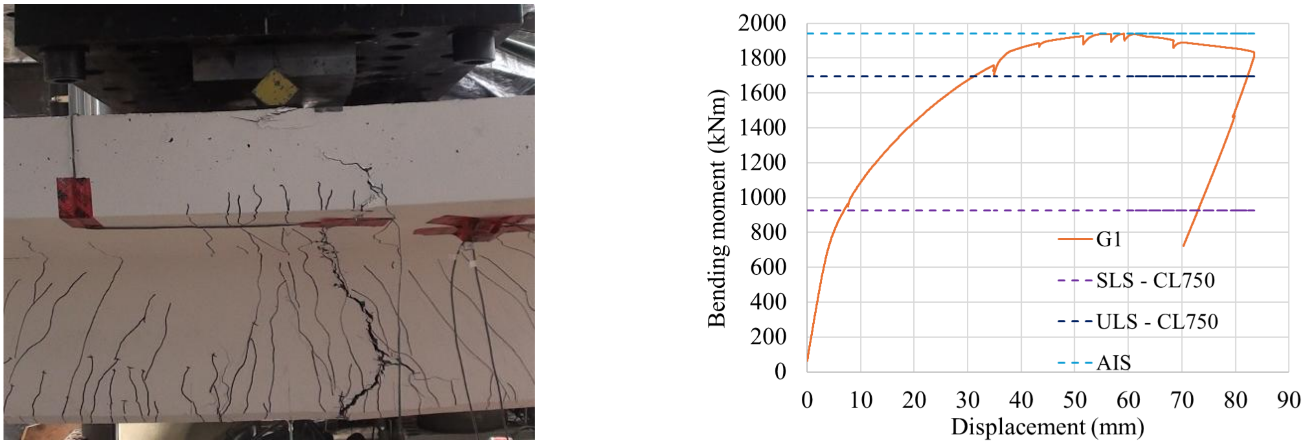

a) Cracking pattern

b) Bending moment-displacement behaviour

Figure 4.20 - Bending behaviour of girder G1

4.5.1.2 Strain gauge data

The strain gauge data measured at the top surface of the girder and on the A1035 rebars are shown in Figure 4.19. The maximum compressive strain (Figure 4.21a) on the top fibre of the girder was around -2500 µm/m. This value must be added to the computed initial strain due to self weight and prestressing which is not available. However, the computed value with software AIS presented later indicate a stress nearly equal to zero. This measured value is less but close to the usual strain at peal stress. The maximum tensile strain registered in A1035 bars was of 14 000 µm/m at 1940 kNm. According to Figure 4.19, that strain level in the hardening domain of the A1035 rebars. These observations confirm girder G1 had a bending failure.

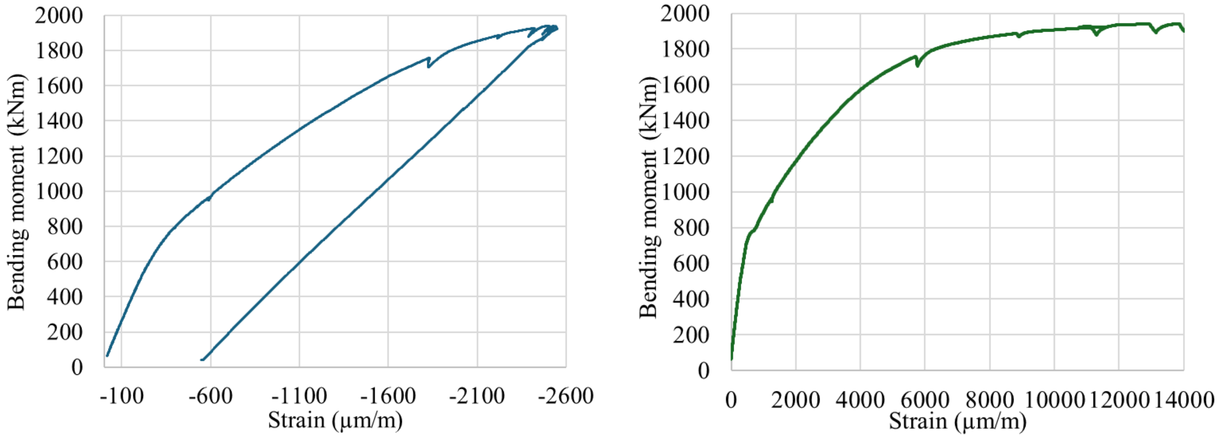

a) Compression strain on girder top surface

b) Tensile strain on A1035rebars

Figure 4.21 – Strain gauges data of girder G1

4.5.1.3 DIC data

Deformations within the girder were calculated for the analysed area. The deformations in the longitudinal direction ε_1 are shown in Figure 4.22 at intermediate and maximal bending moments, the two set of camera measurement areas have been merged into a single image. This first analysis of the DIC results shows several bending cracks in the central span and a few shear cracks towards the supports. A detailed analysis of DIC results will be made in Chapter 5. In this section, only the crack spacing and crack opening are evaluated.

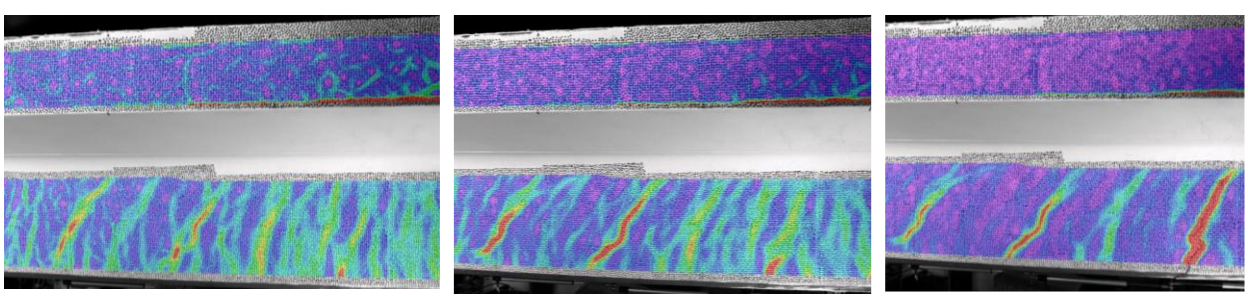

a) At 52% of peak bending moment

b) At 67% of peak bending moment

c) At 95% of peak bending moment

Figure 4.22 – Strain distribution extracted from the DIC for girder G1

The average crack spacing of girder G1 at 52% of the maximal bending moment was around 47 mm (Figure 4.22a). Latter, when the specimen reached 67% of the maximal bending moment, bigger cracks appeared at larger spacing (Figure 4.22b). The critical bending crack appeared suddenly between 67% and 95% of the peak bending force (Figure 4.22c). The crack spacing in the vicinity of the critical point was about 47 mm. The shear crack at this point stopped growing.

Figure 4.23 presents the critical crack opening measured during the bending test. The crack opening values provided by the DIC are lower than those obtained by the LVDTs. This may be explained by the fact that some bending cracks could have been missed in the visual inspection, thus the LVDT displacement were not divided by the actual number of cracks and opening values are larger.

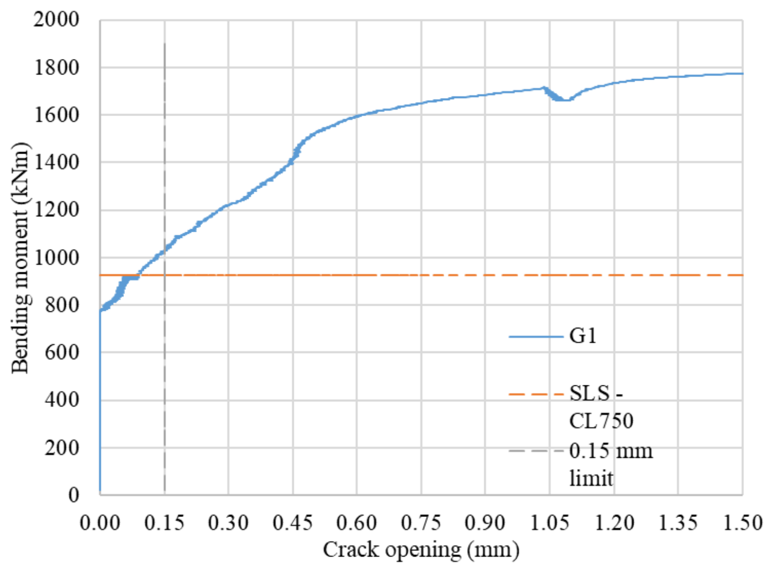

Figure 4.23 – Critical crack opening extracted from the DIC for specimen G1

4.5.2 Girder 2

Girder 2 (G2) has the equivalent bending reinforcement and prestressing level considered for the prototype 15-m bridge girder. The shear reinforcement is however different with the objective of obtaining a shear failure. For that purpose, one half girder has enough stirrups to ensure that no shear failure occur whereas the other half has no stirrup to provide a shear failure. Thus, the test has served to estimate the shear capacity provided by the HPFRC and the prestressing force.

4.5.2.1 Shear resistance

The shear force – displacement behaviour of girder G2, including girder self-weight, is shown in Figure 4.24. The girder exhibited a linear elastic behaviour up to 244 kN, then several bending and shear cracks developed. The critical shear crack appeared on the girder side without stirrup as foreseen. The maximum shear force reached by the girder was 593 kN, which corresponds to a bending moment of 1601 kNm, at 34 mm of deflection. Thus, the girder without stirrup nearly achieved the maximal bending capacity obtain with girder G1 of 1940 kNm. The maximal shear force was maintained up to 52 mm. The test was then stopped to avoid a sudden failure and to be able to safely remove the specimen from underneath the press.

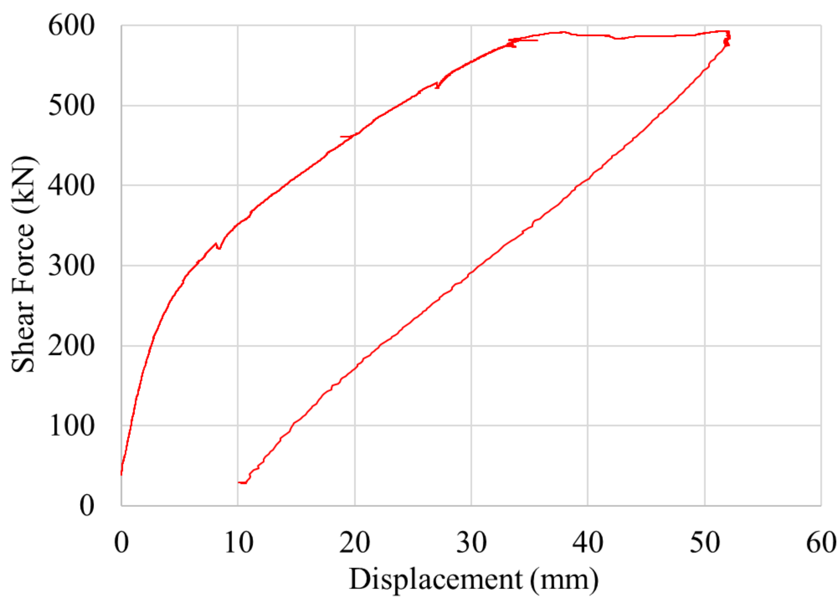

Figure 4.24 – Force vs displacement of Girder 2

Beyond the linear phase, several thin flexural cracks first appeared, followed by several large shear cracks that were observed during the rest of the experiment. The specimen behaviour was characterised by a governing shear crack which began from the top of the web near the flange at a distance of 490 mm from the middle of the girder and extended to the bottom of the girder at 1650 mm of the middle of the girder (Figure 4.25).

Figure 4.25 – Cracking pattern of girder G2

4.5.2.2 <u>Strain gauge data</u>

The strain gauge data measured at the top surface of the girder and in the A1035 rebars are shown in Figure 4.26. The maximum strain reached by A1035 rebars was almost 5 000 µm/m or 0.5%. According to Figure 4.19, that is equal to a stress state of approximately 984 MPa, which is less than the yielding strength of the rebar. The maximum compression strain registered was about -1700 µm/m, which is considerably lower than the compression strain necessary for concrete crushing. Therefore, the strain gauge data confirmed that a shear failure occurred in girder G2.

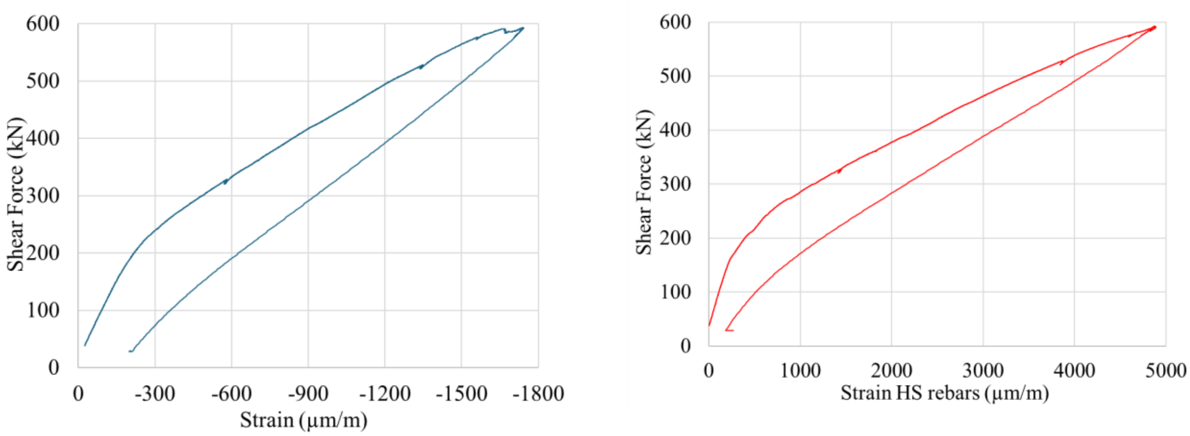

a) Compression strain on girder top surface

b) Tensile strain on A1035rebars

Figure 4.26 - Strain gauges data from G2

4.5.2.3 DIC data

Deformations within the girder were calculated by the DIC system for the analysed area. The strains ε_1 in the principal direction are shown in Figure 4.27 at 90% of the peak force. Thin bending cracks and large shear cracks are visible. Close to the middle of the girder the spacing of the cracks is smaller and increasing toward the support. The average crack spacing in girder G2 was 52 mm. This value is slightly larger that one of girder G1 and is due to the lower prestress force in girder G2. Most of the cracks are inclined with crack openings evenly distributed throughout the test (Figure 4.27).

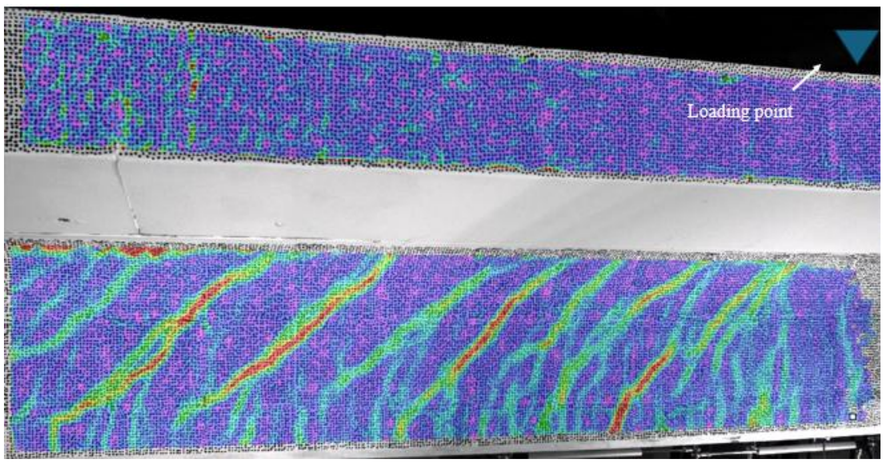

Figure 4.27 – DIC strain distribution for girder G2 at 90% of peak force

The shear behaviour of the girder is highly influenced by the shear crack angle. Before reaching a shear force of 541 kN, the two main shear cracks had an angle of around 33.7° from the horizontal plan (shear crack 1 and 2, Figure 4.28a). The theoretical crack angle predicted by the general method of CSA-S6 for the section located at d_v from the mid-span is 35.2°. The experimental results match the theorical crack angle until this loading level. Beyond a shear force of 541 kN (or 90% of the peak force), a third shear crack appeared (shear crack 3, Figure 4.28b) and connected to the two existing cracks, creating a new crack at inclined at 17.0°.

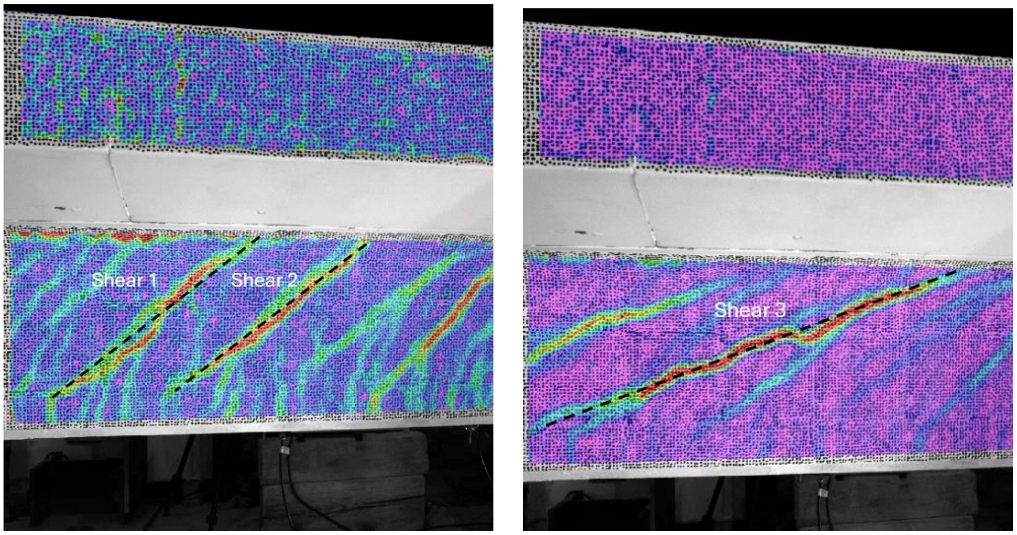

a) Governing cracks up to 500 kN b) Crack 3 after merging of cracks 1 and 2

Figure 4.28 – Critical shear crack angle for girder G2

4.5.3 Girder 3

Girder 3 (G3) has the equivalent bending reinforcement considered for the prototype 15-m bridge girder, however without the presence of prestressing. No stirrups were added for the entire specimen length because enough DIC cameras were available to capture cracks at both sides of the girders. The test has served to verify the effect of the shear span and the geometry on the shear capacity of the girder.

4.5.3.1 Shear resistance

The shear force - displacement behaviour of girder G3 is shown in Figure 4.29. The girder exhibited a linear elastic behaviour up to 230 kN and then a non-linear phase took place. The difference between the linear phase and the nonlinear phase is more gradual than the previous girder. The maximum force was reached at 822 kN, which corresponds to a bending moment of 1110 kNm, for a deflection of 18.5 mm. Afterwards, the resistance dropped. The shear strength of specimen G3 in comparison to specimen G2 is explained by two main factors, both affecting the governing mid-depth axial strain (ε_x) of the general method. which favored arching effect. While specimen G2 had a shear span a/d_{max} equal to 5.1 (2.85/0.56), this value is equal to 2.4 (1.35/0.56) for specimen G3 which is known to lead to a different resisting mechanism and a higher shear strength. Conversely, the absence of a prestressing force also affects the resisting mechanism, leading to a reduced value.

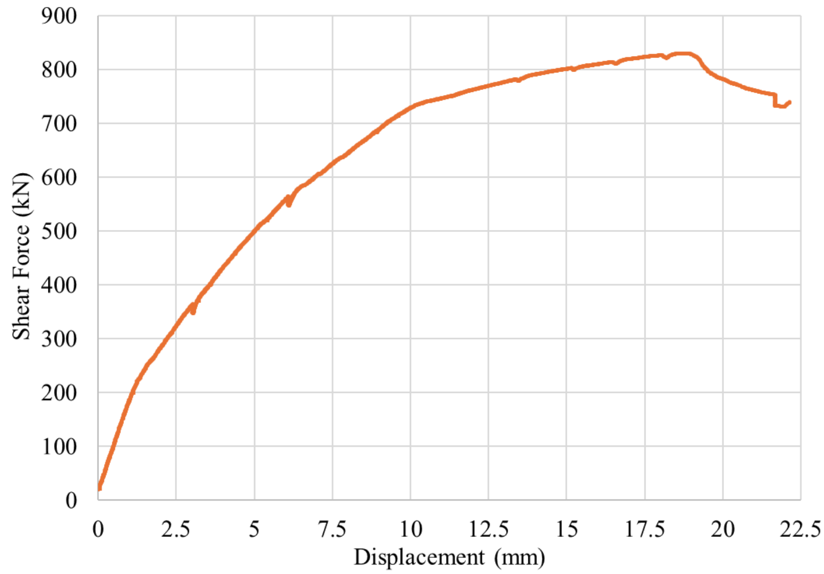

Figure 4.29 - Force vs displacement of Girder 3

The cracking process of the girder G3 was similar to the one of girder G2 (Figure 4.30). Thin flexural cracks appeared at the beginning while several large shear cracks formed and governed the behavior during the rest of the experiment. The critical shear crack almost crossed the whole girder for the loading point to the support. An important difference between girders G2 and G3 was that the shear crack of girder G3 did not stop at the connection between the web and the flanges but extended into the flange. Significant shear crack openings were observed in the flanges at mid-span of the girder. The critical shear crack ended at the bottom of the web at 300 mm from the support.

a) After bending test

b) crack pattern extrated from the DIC

Figure 4.30 - Cracking pattern of girder 3

4.5.3.2 <u>Strain gauge data</u>

The strain gauge data measured at the top surface of the girder and in the A1035 rebars are shown in Figure 4.31. The A1035 rebars reached a maximum strain of 4200 µm/m or 0.4%. According to Figure 4.19, that is a stress state around 800 MPa, which is significantly less than the yielding strength of the rebar. The minimum compression strain measured was about -1400 µm/m, which is considerably less than the compression strain necessary for concrete crushing. Thus, the strain gauge data confirmed that a shear failure occurred in girder G3.

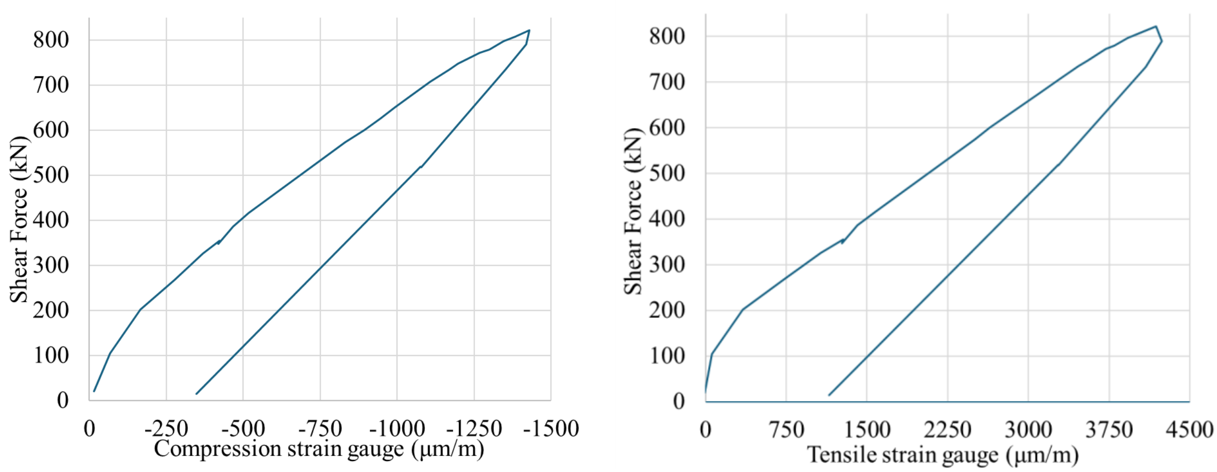

a) Compression strain on girder top surface

b) Tensile strain on A1035rebars

Figure 4.31 - Strain gauges data from G3

4.5.3.3 DIC data

Strains within the girder were calculated by the DIC system for the analysed area. The principal strain in the longitudinal direction ε_1 are shown in Figure 4.32 at 67% of the peak force. Unlike girders G1 and G2 where multiple bending and shear cracks were seen, girder G3 presented fewer cracks with larger spacing. The average crack spacing was 75 mm. The larger crack spacings were expected since girder G3 did not have prestressing.

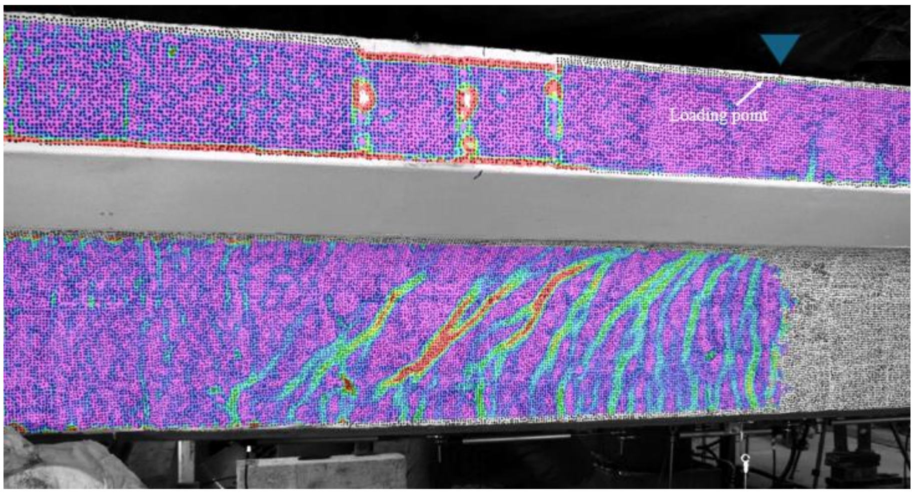

Figure 4.32 – DIC strain distribution for girder G3 at 67% of peak force

Girder G3 presented also a merge of shear crack during the experiment. The merge of cracks appeared sooner than G2. Before 605 kN of shear force, the shear cracks grew linearly according to the crack pattern presented in Figure 4.33a. The average angle of the 3 major shear cracks was 32° (Figure 4.33a). The theoretical crack angle of the section obtained with the general method of CSA-S6 at d_v from the mid-span is 36°. Again, the crack angle estimation is accurate before shear cracks merges.

Beyond a shear force of 605 kN (or 72% of the peak force), the three main shear cracks connected and formed the critical shear crack (Figure 4.33b). The final critical crack has an inclination of approximately 22°.

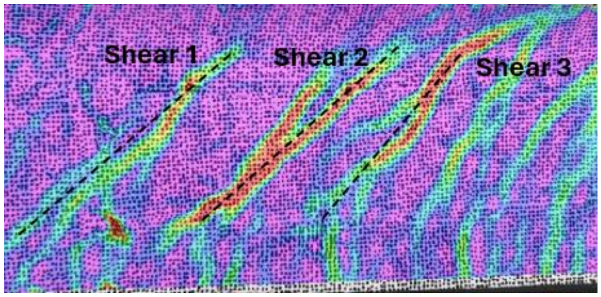

a) Before merge of shear cracks

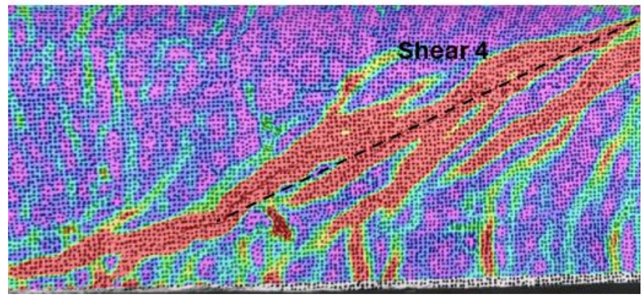

b) After merge of shear cracks

Figure 4.33 - Critical shear crack angle from girder G2

4.5.4 Girder 4

Girder 4 (G4) has the equivalent bending reinforcement considered for the 15-m prototype bridge girder; however, it does not have the presence of prestress just like G3. Specimen G4 had a rectangular shape. No stirrups were added since G4 was 2.7 m long. The test has served to verify the effect of the shear span and the geometry on the shear capacity of the girder.

4.5.4.1 Shear resistance

The shear force – displacement response of girder G4 is shown in Figure 4.34. The girder exhibited a linear elastic behaviour up to 195 kN with a gradual transition to the non-linear phase, then a strength plateau was observed. The maximum shear force was 772 kN, which is equal to a bending moment of 1041 kNm, at a displacement of 18 mm. After the maximum load, the force started to decrease slightly and then dropped suddenly to 260 kN. The reduction in shear capacity from girders G3 to G4 is due to the beam shape, the rectangular cross-section provided a lower shear strength in comparison to the T-shape cross-section.

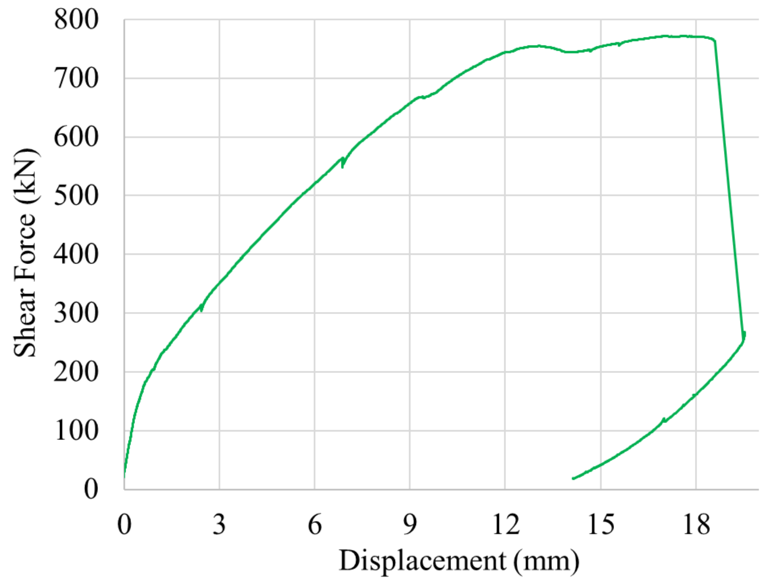

Figure 4.34 - Force vs displacement of Girder 4

4.5.4.2 Strain gage data

The strain gauge data measured at the top surface of the girder and in the A1035 rebars are shown in Figure 4.35. The A1035 rebars have reached a maximum strain of 5000 μm/m or 0.5%. According to Figure 4.19, this strain represents a stress state of around 984 MPa, which is inferior to the yielding strength of the rebar. The minimum compression strain registered was more than -2200 μm/m, which is lower than the compression strain necessary for concrete crushing. Consequently, the strain gauge data confirmed that a shear failure occurred.

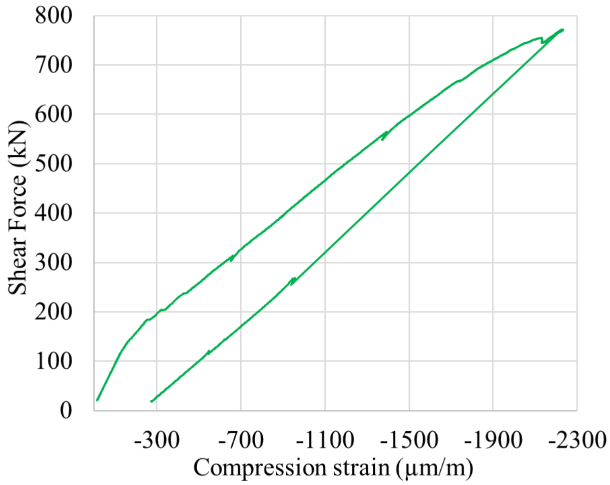

a) Compression strain on girder top surface

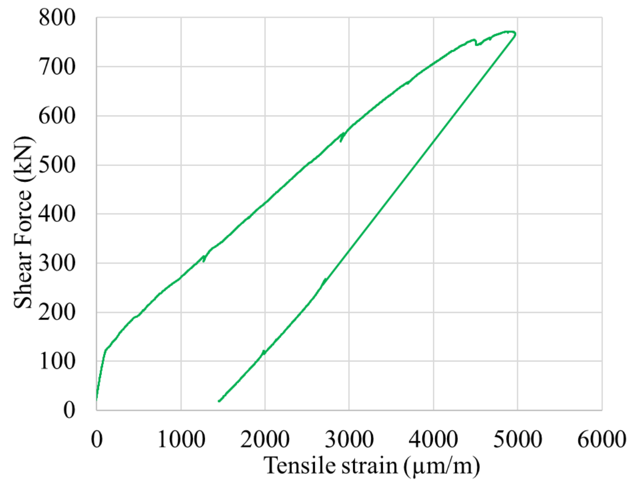

b) Tensile strain on A1035rebars

Figure 4.35 - Strain gauges data from G4

4.5.4.3 DIC data

Deformations within the girder were calculated by the DIC system for the analysed area. The deformations in the longitudinal direction ε_1 are shown in Figure 4.36 at 88% of the peak force. Girder G4 presented fewer bending and shear cracks with larger spacing between the cracks, like girder G3. This observation may be due to the absence of prestress for these girders. The average spacing of the bending cracks was 44 mm.

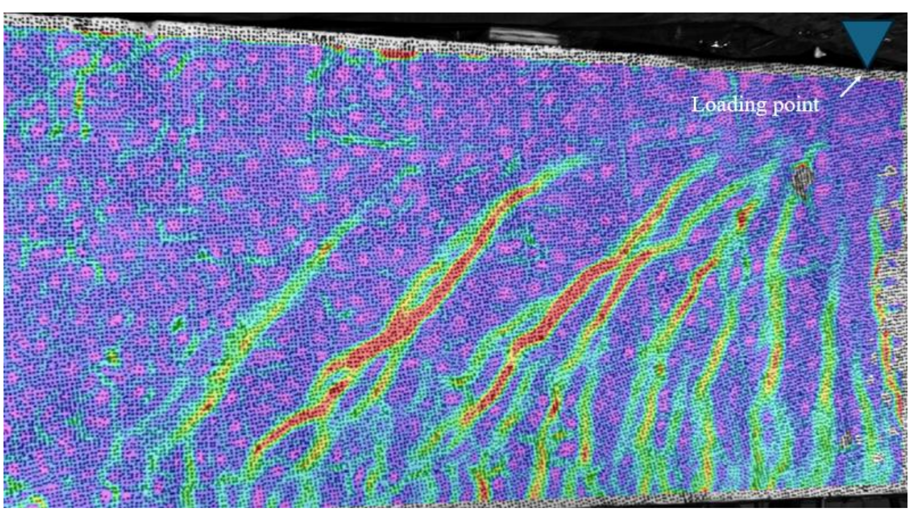

Figure 4.36 – DIC strain distribution for girder G4 at 88% of peak force

As for girders G2 and G3, girder G4 presented a change on the shear crack angle during the experiment. Before a shear force of 665 kN, the cracks grew linearly according to the crack pattern presented in Figure 4.37a. The average angle of the 3 main cracks was 47°. The theoretical crack angle of the section according to the general method at 0.75 m from the mid-span is 36°. For the rectangular girder, the crack angle estimated by CSA-S6 standard is not accurate.

Beyond a shear force of 665 kN (or 88% of the peak shear force), the three main shear cracks connected and formed the critical shear crack shown in Figure 4.37b. The critical shear crack has an inclination approximately equal to 20°.

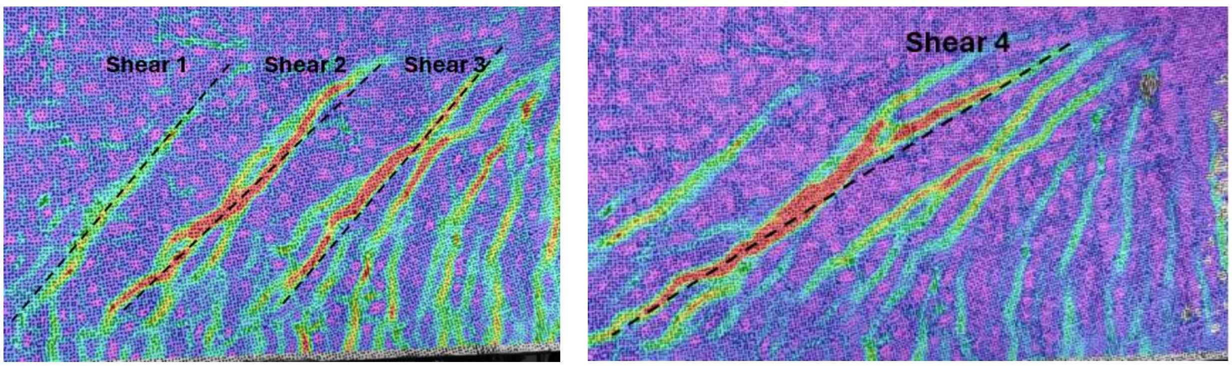

a) Before merge of shear cracks b) After merge of shear cracks

Figure 4.37 - Critical shear crack angle from girder G4

4.5.5 Comparison between shear resistance of specimens

In Figure 4.38, the mechanical behaviour of all specimens is displayed to provide a direct comparison. Two different groups of curves can be seen. The differences between these two groups are very noticeable. The difference in behaviour between the 2 groups can be explained by the prestress and the shear span. The 5.7 m long girders G1 and G2 were prestressed, they are characterized by high displacement (over 40 mm). Girders G3 and G4 with a span of 2.7 m had no prestress and were characterized by low displacement (less than 20 mm). Another difference between the two groups is the maximum capacity. The group characterized by low displacement (less than 20 mm) has around 150 kN more shear resistance than the group characterized by large displacement (over 40 mm). The difference between the curves inside each group however is smaller. Girders G3 and G1 had the highest shear resistance in each group. Girder G3 higher shear resistance compared to G4 can be explained by the influence of the T-shaped geometry, while girder G1 higher shear resistance compared to G2 can be explained by the presence of stirrups.

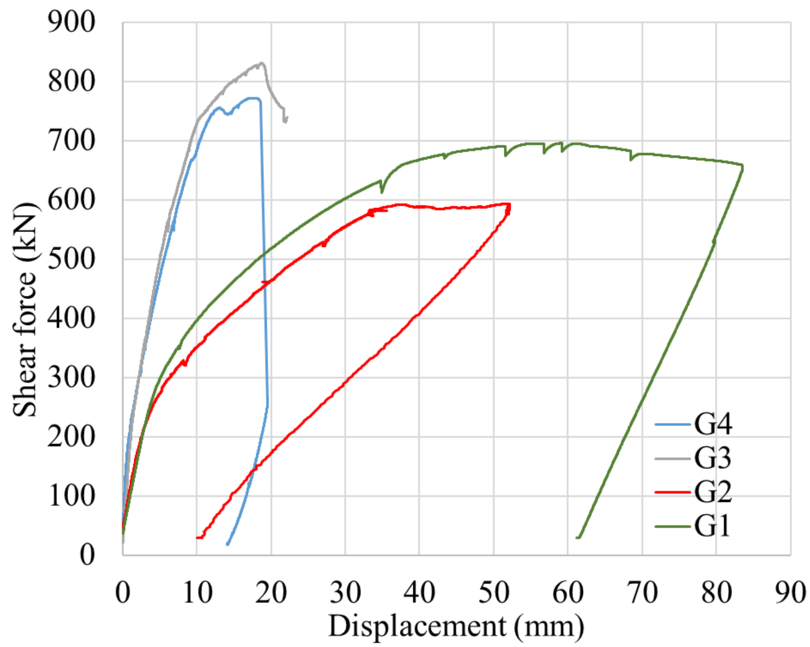

Figure 4.38 - Force vs displacement comparison

4.6 Fibre orientation and density results

According to the CSA-S6 standard, the bending and shear capacities of FRC components depend on the fibre efficiency factor (g_f). This factor takes account for the less optimal fibre orientation a_f and fibre density d_f in structural components compared to the ideal values in the dog-bone characterization specimens, due to material heterogeneity and casting process. This section presents the experimental procedure used to measure a_f and d_f and combine them to estimate g_f.

4.6.1 Experimental procedure

The fibre orientation and density of cores extracted from characterization specimens and girders were measured with an image processing method developed at Polytechnique Montréal by Delsol (2013). This method was carried out in four key steps. First, the plates or cylindrical core samples were cut according to the desired analysis planes (Figure 4.39).

a) Example of cut dog bone b) Example of core sample extracted

Figure 4.39 – Fibre orientation samples analysed

Figure 4.40 illustrates the positions where core samples were extracted from dog-bone specimens and girders, close to the critical cracks that lead to the failure. In this study, one analysis plane was studied in dog-bone specimens, perpendicular to the tensile stress and longitudinal axis (Figure 4.39a, Figure 4.40a), whereas two analysis plans (vertical and inclined) were considered in girders.

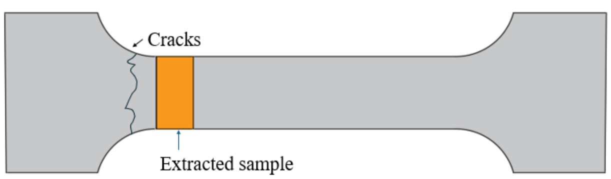

a) Dog-bone

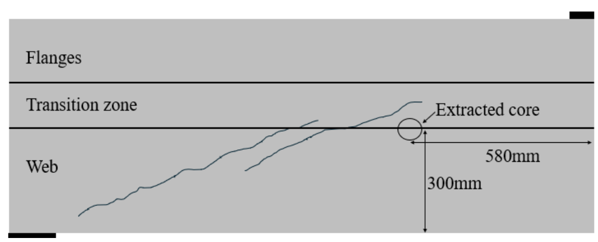

b) G2

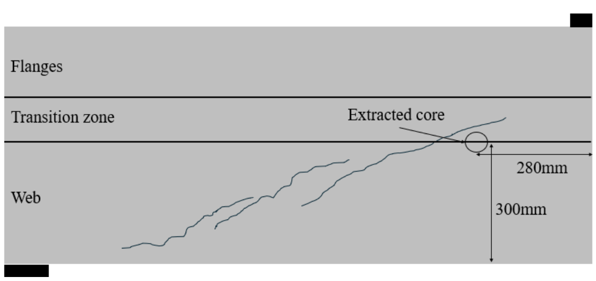

c) G3

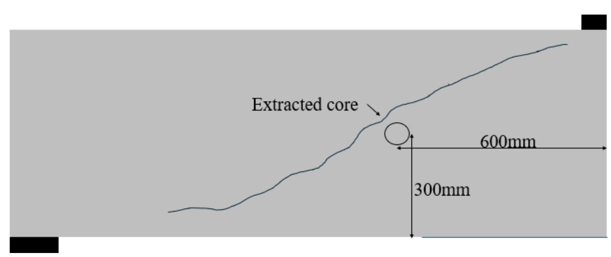

d)G4

Figure 4.40 – Extracted samples positions

The vertical plane was perpendicular to the longitudinal axis of girders; this analysis should provide information on fibre efficiency for the bending behaviour of girders as bending cracks are parallel to this plan and fibres bridge the cracks (Figure 4.41b). The inclined plane was parallel to the critical shear crack (Figure 4.41a) to provide information on fibre efficiency for the shear behaviour of girders. Vertical and inclined plans were obtained by saw cuts in the cylindrical cores.

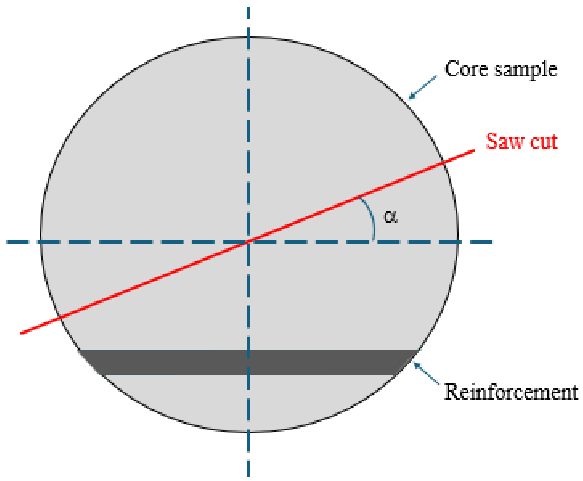

a) Inclined plane

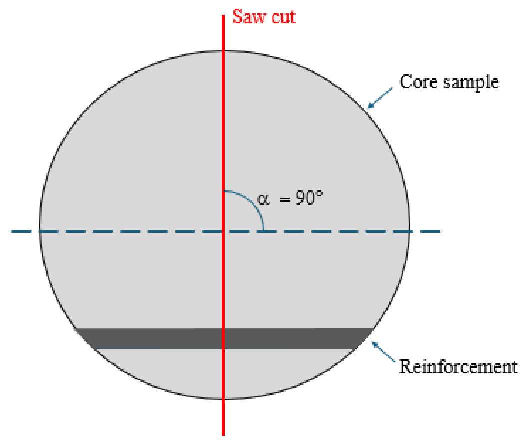

b) Vertical plane

Figure 4.41 – Angle of inclined planes

The next step was to polish the samples to obtain smooth and straight analyzing surfaces. This surface was then painted to highlight the steel fibres in the HPFRC. Third, the analysis plans of samples were digitalized with a 2400 dpi resolution scanner. Forth, the image processed by the program developed by (Delsol & Charron, 2013). The program detects the contours of the fibres, identifies them, measures them, and calculates their orientation relative to a line that is perpendicular to the surface being studied (Figure 4.42).

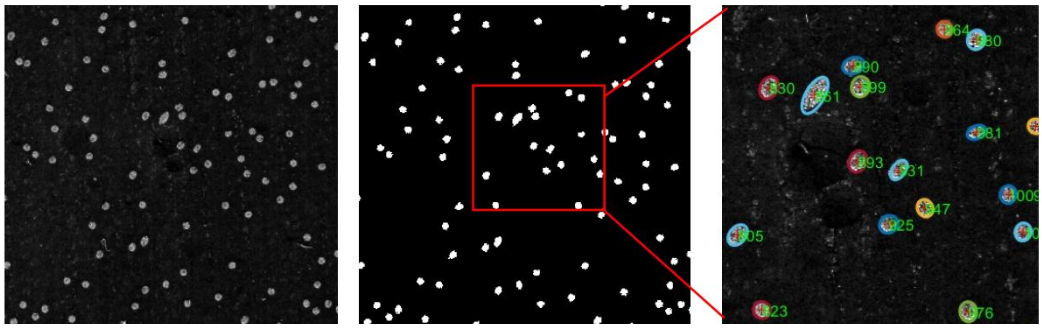

a) Digitalization b) Binary transformation c) Fibre orientation values

Figure 4.42 – Step of analysis of the Delsol's program (Delsol & Charron, 2013)

The program allows for the identification of each fibre and global fibre density (d_f), the individual and average fibre angle (θ_f) or orientation factor (a_f) with respect to the normal axis of the surface analyzed. The two last parameters are illustrated in Figure 4.43.

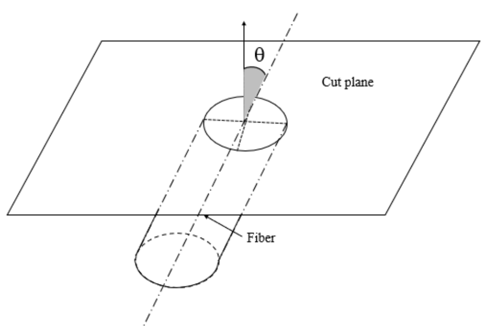

Figure 4.43 – Sketch of fibre orientation in respect to cut plane

In this project, the fibre efficiency in girders was calculated with Equation (4.1), where the term $\mathrm{a}_f \times d_f$ corresponds to the fibre characteristics in the analysis plans of girders divided by the same term measured in dog-bone specimens. This assumption means that fibre efficiency varies linearly as a function of the fibre density and the fibre orientation factors. The fibre orientation and density of the dog-bones were considered as $\gamma_f = 1$. If the fibre characteristics measured in core samples of girders presented a lower number of fibres per area d_f and or a lower fibre orientation a_f than the ones measured in dog-bone specimens, the fibre efficiency γ_f in girders would be lower than 1.

$$\gamma_f = \alpha_f d_f \quad (4.1)$$

Where:

$$\alpha_f = \cos\theta \quad (4.2)$$

4.6.2 Fibre efficiency results

The results of fibre density, fibre orientation and fibre efficiency are summarized in Table 4.6 and Table 4.7 for the analysis made when the vertical and inclined analysis plans, respectively, were considered in core samples extracted from girders.

In the vertical plane of girders (Figure 4.41b), the density of fibres in the extracted core is smaller than the density of fibres from the dog-bone. Besides the fibre orientation of the cores is also smaller (lees oriented) than the dog-bone. Consequently, γ_f values calculated with (4.1) are close to 0.6 for girders G1, G3 and G4 and 0.72 for G2. Fibre efficiency in the vertical plane was analysed mainly for the bending behaviour of girder G1, which has failed in bending. The experimental fibre efficiency of 0.6 in the vertical plane for bending is higher than what is recommended in the CSA-S6 standard ($\gamma_f = 0.4$) for design in bending of beams. The specification for fibre efficiency is thus conservative for bending.

Table 4.6 - Fibre characteristics in vertical planes analysed in girders

Vertical plane	Dobbone	G1	G2	G3	G4
Fiber density (number/area)	0.029	0.020	0.024	0.021	0.020
Fiber orientation (-)	0.97	0.85	0.84	0.84	0.86
Density x F.O.	0.028	0.017	0.020	0.017	0.017
γ_f	1.00	0.60	0.72	0.61	0.60

In the inclined plane of girders (Figure 4.41a), the density of fibres in the extracted core is smaller than the density of fibres from the dog-bone. Besides the fibre orientation of the cores is also smaller (lees oriented) than the dog-bone. Consequently, all γ_f values estimated in girders are close to 0.35. It can be concluded that the fibre orientation factor is anisotropic with a better orientation on the vertical plane than in the inclined plane. This is due to the heterogeneity of HPFRC and to the casting process, which favored a unidirectional flow of the HPFRC along the girder longitudinal axis and a fibre orientation mainly parallel to that axis. The experimental fibre efficiency for shear is much smaller than what is recommended by CSA-S6 standard ($\gamma_f = 0.8$).

However, one must note that the assumed tensile properties in CSA-S6 for tension softening FRC are determined from an inverse analysis from bending test results. Therefore, the comparison carried out in this section with the Canadian Bridge Code (CSA-S6, 2019) is for discussion purposes only.

Table 4.7 - Fibre characteristics in inclined planes analysed in girders

Inclined plane	**Dobbone**	**G2**	**G3**	**G4**
Fiber density (number/area)	0.029	0.017	0.021	0.019
Fiber orientation (-)	0.97	0.52	0.46	0.5671
Density x F.O.	0.028	0.009	0.010	0.011
γ_f	1.00	0.32	0.35	0.37

4.7 Comparison of experimental observations and theoretical predictions

This section presents a comparison between the experimental bending and shear behaviour observed on girders with the theoretical ones obtained with AIS software for bending and equations of the CSA-S6 standard for bending and shear. The theoretical evaluation could be refined with information retrieved by DIC measurements (shear crack angle and crack opening) and fibre orientation and density measurements (fibre efficiency factor).

The bending behaviour of girder G1 will be compared directly to the theoretical value. For the shear behaviour of girders G2 to G4, two sets of experimental data will be displayed. The first one is the set of variables related to the intermediate shear capacity reached before the shear cracks merged. This moment will be referred to as *"load at crack merging"*. The second set of variables refer to the ultimate shear capacity, which will be referred to as *"ultimate load"*. Variables required for the shear evaluation were extracted at the mid-depth of the cross section for a direct comparison to the standard.

4.7.1 Bending behaviour of girder G1

To analyse the bending behaviour of girder 1, the software AIS was used. Figure 4.44 presents the predicted behavior considering no prestressing losses and 100% FRC efficiency. The maximum flexural strength reached 1980 kNm. The results overestimate the flexural capacity by only 2%. This is expected since the ultimate strength is governed by the flexural reinforcement behaviour. However, cracking occurred at a moment of 750 kNm, larger than the observed values while the predicted crack growth is too small. It is worth noting that the peak strength is associated with a crack width of less than 2 mm.

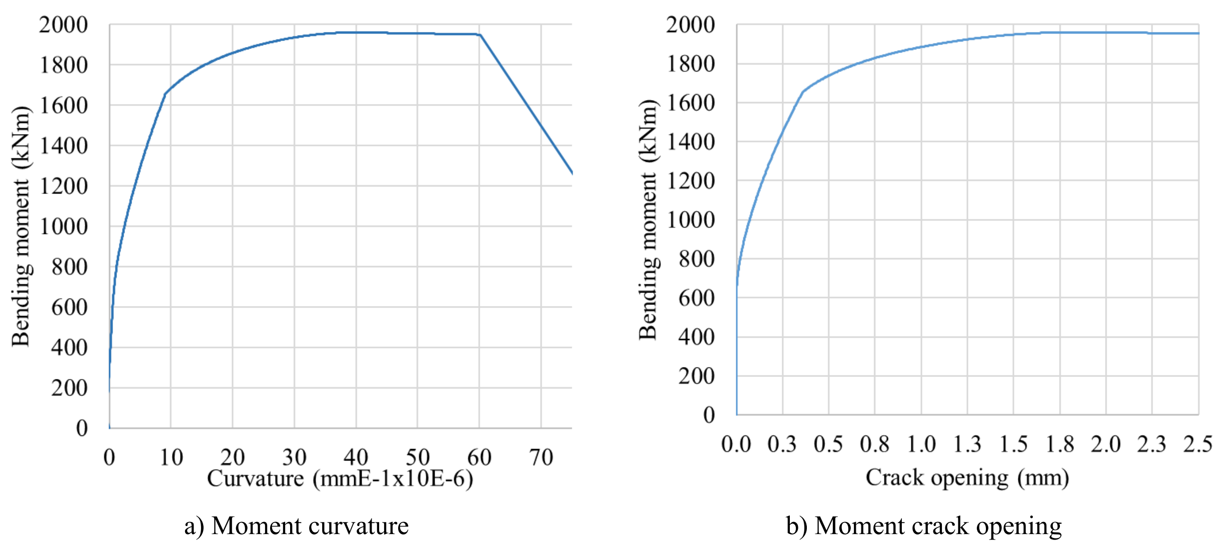

Figure 4.44 – Predicted flexural behaviour with original material property

The contribution of fibres is considered using an efficiency factor of 0.6 applied to the post-cracking behaviour of FRC. The ultimate flexural strength considerably reduced to 1890 kNm. A cracking bending moment of 750 kNm is still obtained.

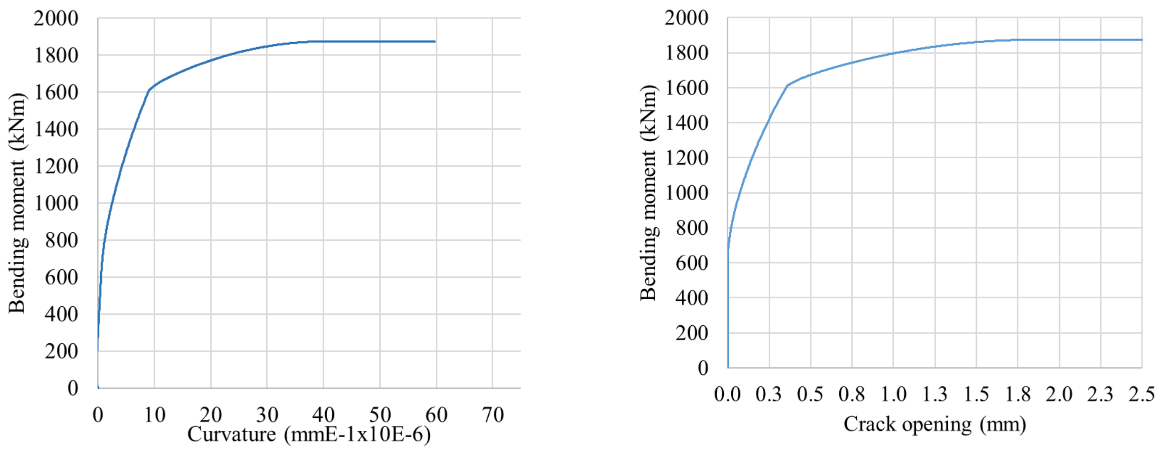

a) Moment curvature b) Moment crack opening

Figure 4.45 – Predicted flexural behaviour with original material property and FRC efficiency

Prestressing losses were estimated from calculation from time dependant analysis carried out using ACI-209 Committee (2007) recommendation. The parameters shown in Table 4.8 were used. The time analysis allows determining the effective stresses in the A1035 which was further reduced by 115 MPa due to the girder shortening. Because stress variation in reinforcing bar cannot be handled by AIS, the tensile properties were increased by that amount to account for the initial shift related to the volumetric change of concrete.

Table 4.8 - Fibre characteristics in vertical planes analysed in girders

Parameter	**Value**
Relaxation for G1 bottom tendons	-25 MPa
Relaxation for G1 top tendons	0 MPa
Maximum shrinkage ($t = \infty$)	-650 µm/m
Maximum creep factor ($t = \infty$)	1.38
Time of testing	Between 60 and 70 days
Creep and shrinkage losses G1 bottom tendons	-75 MPa
Creep and shrinkage losses G1 top tendons	-25 MPa
Effective stress G1 bottom tendons	1250 MPa
Effective stress G1 top tendons	800 MPa
Additional yield strength of A1015 bars	+115 MPa
A1035 shifted yield stress	665 MPa
A1035 shifted ultimate strength	1265 MPa

AIS results indicate a cracking bending moment of 633 kNm, a yielding of the A1035 bars at 1490 kNm with a corresponding crack opening of 0.3 mm. While the first two values agree with the experimental measurements, the measured corresponding crack width is in the order of 0.5 mm. At that stage, crack spacing tends to increase, partly because adjacent cracks are closing. Increasing the crack spacing to 125 mm, lead to A1035 yielding at 1468 kNm with a corresponding crack width of 0.43 mm, closer to the DIC observations. Figure 4.46 present the results of the analysis compared with the experimental results. The AIS model considers the fibre orientation factor for bending (g_f = 0.6) extracted from section 4.6.2. The crack analysed in the DIC is the biggest bending crack available, in other words, the critical crack. AIS prediction replicates accurately the moment-crack opening behavior of the girder G1.

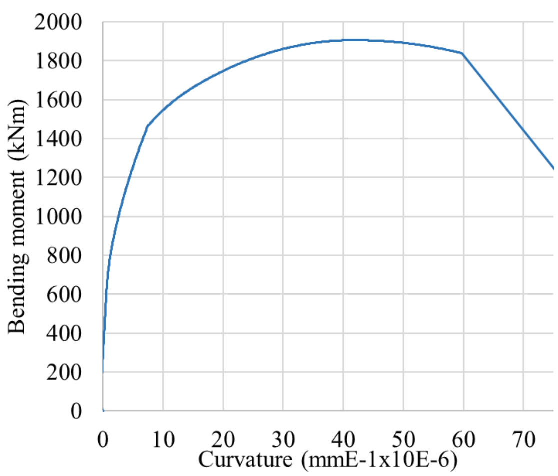

a) Moment curvature

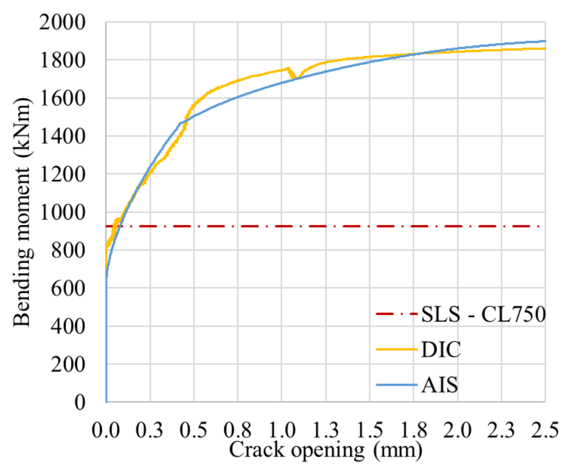

b) Moment crack opening

Figure 4.46 – Predicted bending behaviour with time dependent losses and FRC efficiency

4.7.2 Shear behaviour of girder G2

The main data required to evaluate the shear capacity of girder G2 are presented in Table 4.9. The experimental shear crack angle and the crack opening were measured at mid-depth of the cross section for a direct comparison with the values provided by the standard. The tensile strength related to the crack opening was obtained from the tensile behaviour of the HPFRC shown previously in Figure 4.18. These values, as well as the experimental shear load and bending moment at are provided at two loading levels, before the merge of shear cracks (around 88 to 90% of the ultimate load, as shown in Section 4.5) and at ultimate load.

The standard equations could not well predict all the parameters related to the ultimate shear resistance of the girder (after cracks merge). The shear crack angle is greater, the crack opening in the HPFRC is underestimated and thus the tensile contribution of the HPFRC is overestimated (Table 4.7). Therefore, the theoretical ultimate shear load represents about half of the experimental value. It is interesting to observe that at an intermediate load level before the shear cracks merged into one (90% of ultimate load), the shear crack angle is well predicted. However, the associated theoretical shear resistance predicted still underestimates significantly the experimental strength of the girder. This comparison demonstrates that the equations integrated in the S6.19 strongly underestimate the HPFRC shear contribution in the girder G2. First, the rectangular cross-section considered by equations neglect a large part of the shallow T-shape cross-section in girder G2. Second, the tensile resistance of the fibres and the aggregate interlock acting in the girder may be underestimated, and/or other resisting mechanisms could be neglected.

Girder G2 had the same configuration of girder G1 (prestressed T-shaped girder of 6 m) without stirrups. The ultimate shear capacity of girder G2 was 593 kN. Although the shear conditions differ between a 6 m girder of the experimental campaign and those expected for the 15 m bridge girder (a/d ratio, shear crack angle, etc.), the ultimate shear capacity of girder G2 is superior to the factored design shear load of the 15 m girder. Therefore, even without stirrup, the prestressed T-shaped HPFRC girder fulfilled requirement in shear.

Table 4.9 – Comparison of shear resistance for girder G2

Variables	Experimental		CSA S6.19
	Load at crack merging	Ultimate load	
Crack angle (degree)	34	17	34
W_v (mm)	0.6	10.6	1.8
M_f (kNm)	1449	1601	1048
V_f (kN)	537	593	388

4.7.3 Shear behaviour of girder G3

The influence of the prestress on the accuracy of the theoretical shear strength was verified with girder G3 without prestress. The main data required to evaluate the shear capacity of girder G3 are presented in Table 4.10.

Again, the standard equations could not well predict all the parameters related to the ultimate shear resistance of the girder (after cracks merge), discrepancies are even larger with experimental results. The theoretical shear crack angle is greater, the crack opening in the HPFRC is underestimated and thus the tensile contribution of the HPFRC is overestimated. Consequently, the theoretical ultimate shear load represents about one third of the experimental value. It is again interesting to note that at an intermediate load level (72% of ultimate load) before the shear cracks merged into one, the shear crack angle is well predicted. However, the associated theoretical shear resistance still underestimates significantly the experimental strength of the girder. One important difference between girders G3 and G2 is that the shear crack merging happened considerably later at 88% of the force peak, instead of 72% for girder G3. Maybe this situation amplified the discrepancies between the theoretical and experimental ultimate shear resistance. Therefore, the S6.19 standard design equations do not predict properly the shear resistance of a HPFRC T-shaped girder, with even less accuracy than for the prestress girder. Again, the consideration of the rectangular cross-section of the girder for the shear resistance may explained this observation, as well as the underestimation of shear resisting mechanisms (tensile resistance of the fibres, aggregate interlock, or other one).

Table 4.10 – Comparison of shear resistance for girder G3

Variables	Experimental		CSA S6.19
	Load at crack merging	Ultimate load	
Crack angle (degree)	32	22	36
W_v (mm)	0.8	10.2	2.2
M_f (kNm)	817	1120	404
V_f (kN)	605	830	299

4.7.4 Shear behaviour of girder G4

The influence of the girder cross-section on the accuracy of the theoretical shear strength was verified with the rectangular cross-section of girder G4. The main data required to evaluate the shear capacity of girder G4 are presented in Table 4.11.

Again, the standard equations could not well predict all the parameters related to the ultimate shear resistance of the girder (after cracks merge), discrepancies with experimental results are still important, but slightly less than those observed for girder G3. The theoretical shear crack angle is greater, but this time the crack opening in the HPFRC is similar to the experimental one and the tensile contribution of the HPFRC should be well approximated. However, the theoretical ultimate shear load represents about one third of the experimental value. It is interesting to note that at an intermediate load level (88% of ultimate load) before the shear cracks merged into one, the shear crack angle is this time underestimated. The theoretical shear crack angle is equivalent to the ones of girders G1 and G3 as the same calculation assumptions are used with the rectangular cross-section. However, a better prediction of the shear crack angle was expected for girder G4 because of its rectangular cross-section. Consequently, the associated theoretical shear resistance still underestimates significantly the experimental strength of the girder. Therefore, the S6.19 standard design equations do not predict properly the shear resistance of a HPFRC rectangular girder. For the girder G4, the conclusion is most probably related to underestimation of shear resisting mechanisms such as the tensile resistance of the fibres, the aggregate interlock acting in the girder, and/or other resisting mechanisms.

Table 4.11 – Comparison of shear resistance for girder G4

Variables	**Experimental**		**CSA S6.19**
	Load at crack merging	**Ultimate load**	
Crack angle (degree)	47	21	36
W_v (mm)	0.85	2.7	2.2
M_f (kNm)	898	1042	404
V_f (kN)	665	772	299

4.8 Conclusions

An experimental investigation of four HPFRC girders (G1 to G4) with different configurations, prestressing levels, and cross-sectional geometries was presented in this chapter.

Girder G1, a 6 m prestressed T-shaped beam with stirrups, failed in bending after reaching a peak bending moment of approximately 1940 kNm, confirming that the bending capacity exceeded the factored bending moment requirement. The crack opening was 0.07 mm in service conditions, fulfilling also the standard requirement of maximum 0.15 mm.

Girder G2, the 6 m prestressed T-shaped girder without stirrup, exhibited a shear failure. The ultimate shear capacity obtained was 593 kN, which is superior to the factored design shear load for the 15 m girder.

Girder G3, a 3 m non-prestressed girder with the same T-shaped as girders G1 and G2, but without prestressing and lower shear span during the shear test, presented an earlier shear failure with wider crack spacing. Girder G4, a 3 m non-prestressed girder with a rectangular cross-section, also failed in shear and reached the lowest shear resistance among all specimens.

The comparative behaviour of girders G3 and G4 clearly highlighted the significant effect of the web geometry, as the rectangular section exhibited a lower shear resistance compared to the T-shaped configuration. The presence of prestress in girders G1 and G2 delayed bending and shear cracking, reduced deflections, and enhanced stiffness, confirming its positive effect on both flexural and shear performances.

The evaluation of the fibre contribution in the mechanical behaviour of girders was carried out by determining the fibre content and fibre orientation in vertical and inclined planes. These values allowed calculation of efficiency factors considered in the theoretical estimation of the fibre contribution of the HPFRC supporting bending and shear loads. From the fibre content and fibre orientation results, average fibre efficiency factors of γ_f = 0.6 for bending (vertical plane) and γ_f = 0.35 for shear (inclined plane) were obtained. The difference between the fibre orientation in vertical and inclined planes can be explained by the anisotropic mechanical properties of HPFRC. The casting procedure used to fill the girder has favored a unidirectional and horizontal flow of the HPFRC along the longitudinal axis of girder, which resulted in fibres more favorably oriented horizontally. This fibre alignment is more favorable to bridge vertical bending cracks than inclined shear cracks.

When comparing experimental results to theoretical predictions, it was found that the analytical software AIS replicates accurately the bending capacity and the crack opening behavior of the HPFRC girder G1. Besides, the current design equations from the CSA S6.19 standard underestimate significantly the shear capacity of HPFRC girders. For shear, the design equations proved to be overly conservative, primarily due to the use of a simplified rectangular section in the analytical model and the omission of compression chord contributions. As a result, the shear capacity predictions were on average two to three times lower than those observed experimentally.

CHAPTER 5 IN DEPTH ANALYSIS OF SHEAR MECHANISMS

5.1 Introduction

In Chapter 5, a detailed analysis of the shear tests on girders G2 to G4 is presented to evaluate different shear mechanisms participating to the resistance of HPFRC girders. The analysis is conducted with an in-depth interpretation of the DIC results and utilisation of finite element models.

The shear resistance is provided by 4 shear resisting mechanisms in a girder without stirrup (Figure 5.1):

- Tensile resistance of the fibres (V_{fib}, named V_{c_F} in Figure 5.1)
- Aggregate interlock (V_{agg})
- Compression chord (V_{cc})
- Dowel action of the rebars (V_{dow})

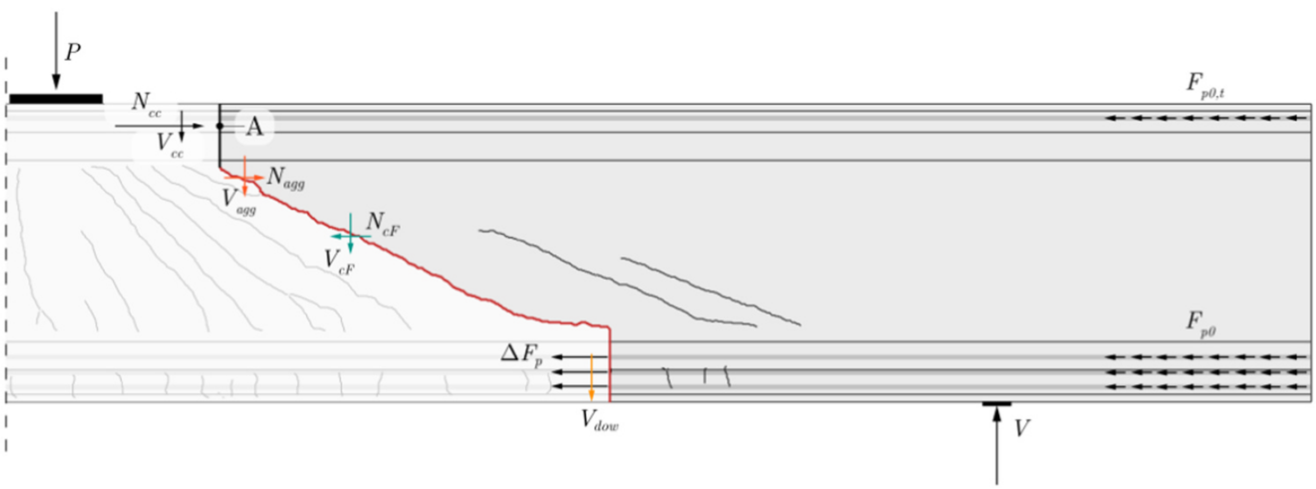

Figure 5.1 – Sketch of shear resisting mechanisms in a girder without stirrups (Ruiz et al., 2024)

In this project, 3 resisting mechanisms were experimentally evaluated: V_{fib}, V_{agg} and V_{cc}. V_{dow} was not considered since the literature review has demonstrated that this mechanism is usually negligible for prestressed FRC girders (Section 2.3.2).

The DIC system captured the relative displacement of the external vertical faces of girders during the tests, namely the faces of the flange and the web of the T-girders. The intersection between the flanges and the web (Figure 4.13) were not captured by the DIC since it was a curved section. Thus, the DIC results allowed a direct evaluation of the V_{fib} and V_{agg} mechanisms in the analysed zones using a in-house Matlab program developed in this project, and an approximation was made to evaluate these contributions in the curved section. Then, a Finite Element Model (FEM) was developed to evaluate the shear stress in the compression cord of the girder and then to estimate the V_{cc} contribution in the shear resistance.

The contributions of the three shear resistance mechanisms were sum up and compared to the experimental shear resistance shown in Chapter 4. The importance of each mechanism in the 3 girders studied allowed the evaluation of the effect of the prestress, the geometry and the shear span on the shear behaviour.

5.2 DIC analysis for V_{fib} and V_{agg} contributions

5.2.1 General procedure

The raw data extracted from the DIC was used as an input in a MATLAB program that was developed for the project. The general procedure of the program is illustrated in Figure 5.2 and the complete algorithm is provided in Appendix D.

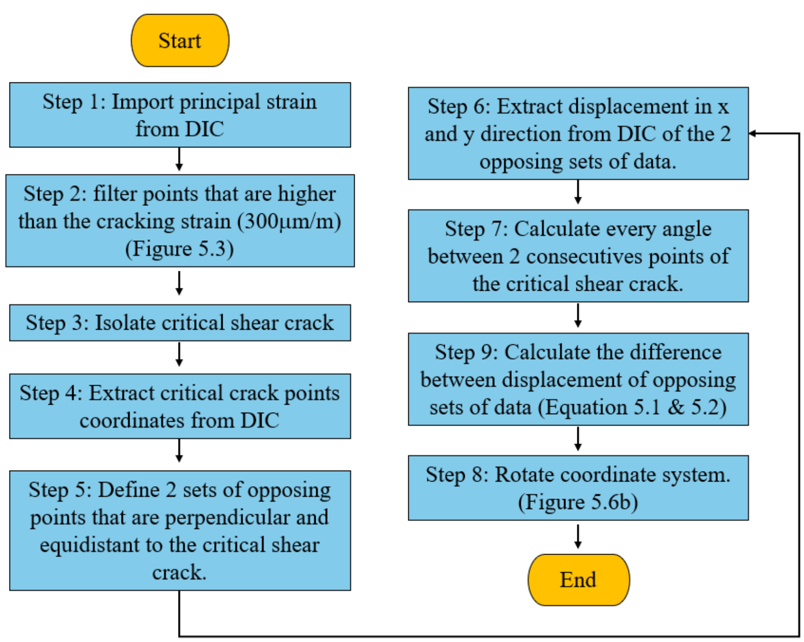

Figure 5.2 – Procedure of the Matlab program developed

The program analysing the DIC results was based on the work of Ruocci et al. (Ruocci et al., 2016) and Gehri et al. (Gehri et al., 2020). Points on bending and shear cracks are detected by analysing independently several horizontal measuring lines from the DIC. The crack points are detected at local maxima in the distribution of principal tensile strains. Later, only points that have a tensile strain bigger than the cracking strain are selected. This procedure is then repeated in all parallel measuring lines of the data set. By linking successive crack points, crack paths are traced. Figure 5.3 shows the crack paths plotted on the right-hand side of girder G4 at ultimate load.

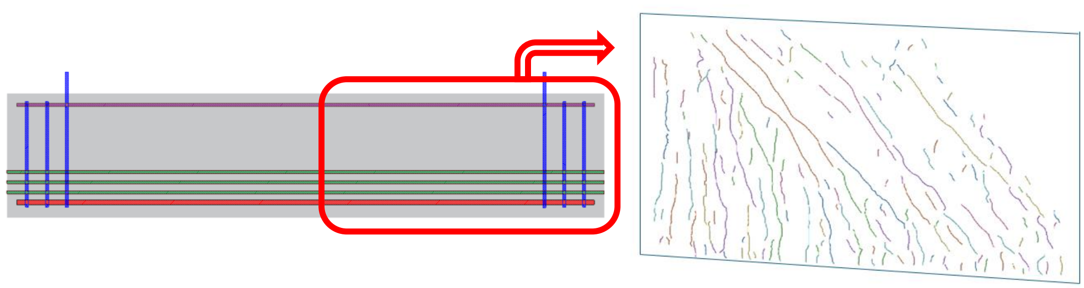

a) Area of Girder 4 analyzed b) Principal tensile strain extracted from DIC

Figure 5.3 – Local maxima extracted from principal strain grid in one side of the girder 4 at ultimate load

From this data it was possible to manually isolate the largest crack opening among all shear cracks and thus extract the necessary data from the points inside the critical shear crack (x and y coordinates of every point). Figure 5.4 presents the isolated critical crack for girder G4 with the principal tensile strain distribution over the crack length at ultimate load.

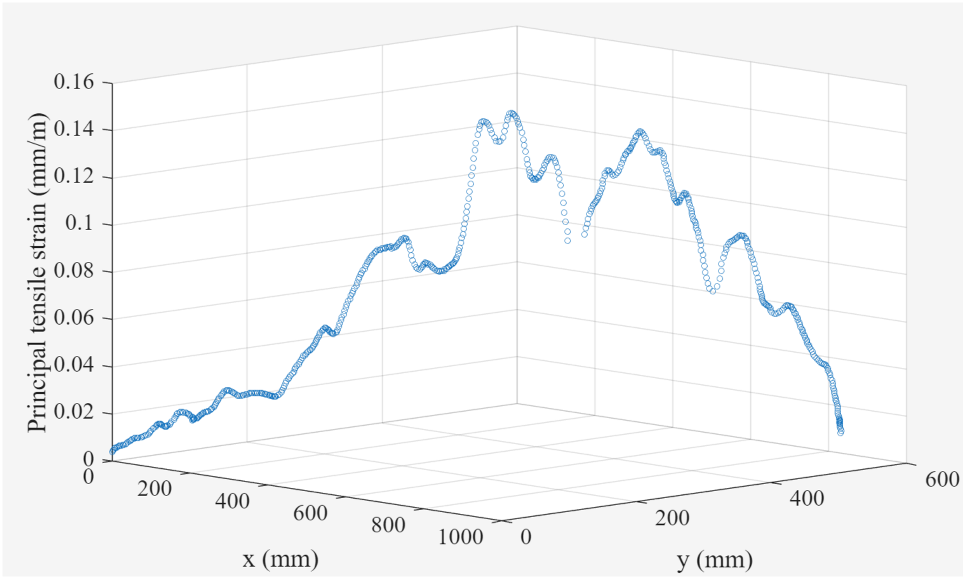

Figure 5.4 – Principal tensile strain of the critical crack extracted from girder G4 at ultimate load

The investigation of shear-transfer actions at failure is performed by considering each opposite side (light and dark grey zones) of the critical shear crack as a free body as shown in Figure 5.5. By using this hypothesis, it is possible to easily define the relative slip and crack opening at every location of the critical shear crack.

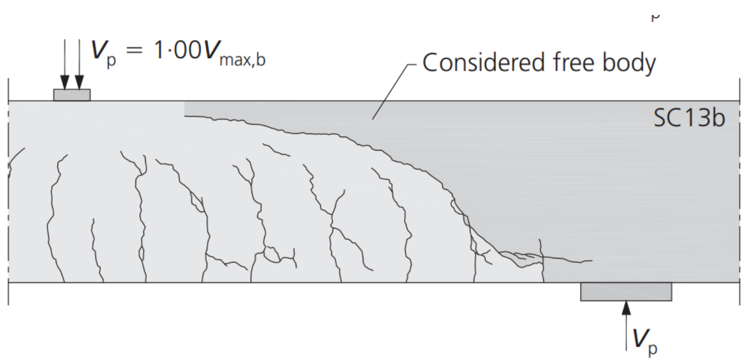

Figure 5.5 –Free body diagram of a half girder under shear (Campana et al., 2013b)

To do so, 2 sets of opposite points that are perpendicular and equidistant to the critical shear crack must be selected. Each set will represent one free body. The absolute displacement on x and y direction was extracted from every point of the two opposite data sets (Figure 5.6a).

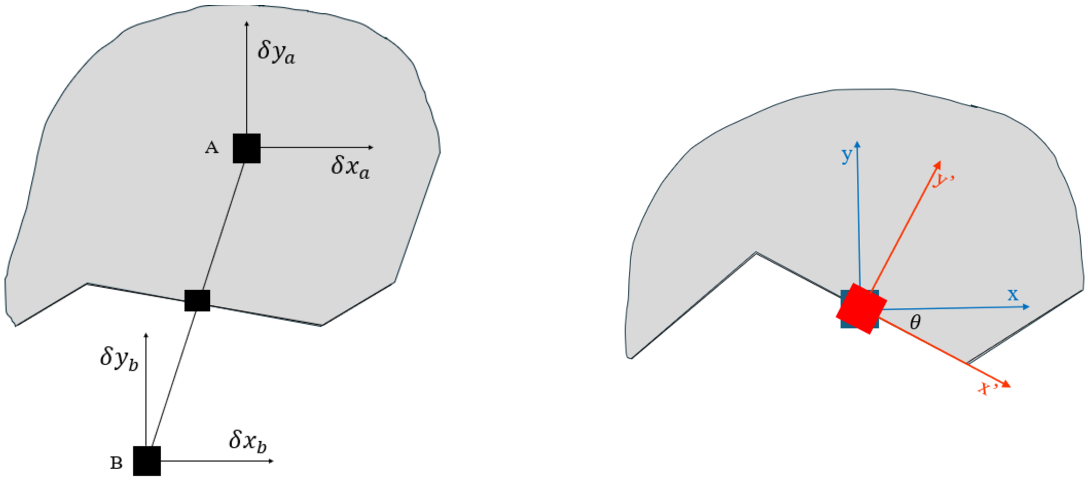

a) Relative displacement　　　　b) Angle conversion

Figure 5.6 – Sketch of algorithm logic for estimating crack opening and slip

To calculate the relative displacement between 2 opposite points, the difference between the absolute displacement was calculated. The equation for each relative displacement in coordinates (*x,y*) is presented in Equations (5.1) and (5.2):

$$\Delta y = \delta y_a - \delta y_b \tag{5.1}$$

$$\Delta x = \delta x_a - \delta x_b \tag{5.2}$$

Where: δ $= absolute\ displacement$

$\Delta = relative\ displacement$

To convert these relative displacements into physical forces, it is necessary to convert the DIC coordinate system (*x, y*) to a coordinate system in which the abscise is parallel to the crack (*x'*) and the ordinate is perpendicular to the crack (*y'*) (Figure 5.6b). The coordinate system conversion equations are presented in Equation (5.3 and (5.4).

$$s = \Delta x \cos\theta + \Delta y \sin\theta \tag{5.3}$$

$$w = -\Delta x \sin\theta + \Delta y \cos\theta \tag{5.4}$$

This step is necessary to convert the differential movement between each set of points at the shear crack in two components: the vertical crack opening (w) and the sliding of the crack (s). Finally, with physical models presented in the next sections, crack openings and sliding displacements at each set of points along the shear crack will be correlated to a tensile stress bridging the crack provided by the fibres and a shear stress provided by the aggregate interlock at crack surface, respectively. By multiplying these tensile and shear stresses by the correspondent area of each set of points, punctual tensile and shear forces are obtained. The total tensile and shear forces are obtained by the sum of all punctual forces over the crack length and represent the V_{fib} and V_{agg} contributions, respectively.

5.2.2 Procedure estimating the tensile contribution of the FRC in the crack region

Once the crack opening data perpendicular to the shear crack is known, the determination of the tensile stress at every point of the crack is possible. The experimental tensile curve of the HPFRC studied in the project was used to correlate the crack opening to the tensile resistance. The tensile curve of each HPFRC batch that served to produce the girders were presented in Section 4.4. By multiplying the tensile stresses by the correspondent area of each set of points, punctual tensile forces are obtained. The integration of the punctual tensile forces perpendicular to the shear crack and over its length is made directly. However, the estimation of the tensile contribution of the HPFRC along the crack is required in the same direction (vertical direction) as the applied shear force in the girder. Some considerations must be accounted for this conversion.

A sketch is presented in Figure 5.7 to illustrate the process of transforming a variable angle force into a single vertical force. Coordinate (x,y) and (x',y') described previously are identified, and θ is the shear crack angle between 2 consecutive points of the critical shear crack. The tensile stress (σ) is in the direction of the y' axis, while V_{fib} is in the direction of the y axis.

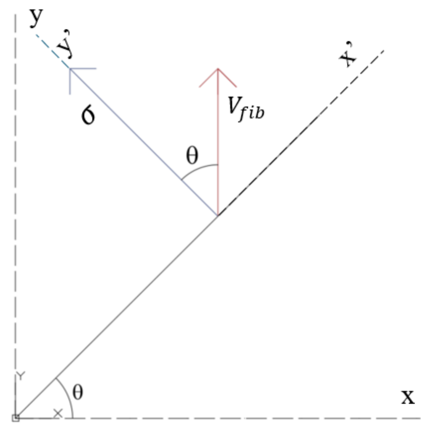

Figure 5.7 –Force diagram for tensile resistance present on the shear crack

To convert the tensile resistance (σ) perpendicular to the crack into V_{fib}, it is necessary to multiply the tensile resistance by cos(θ). Equation (5.5) allows transformation of the HPFRC tensile stress at each set of points into a punctual vertical force. The girder width varies along the shear crack, depending on where the set of points are localized in the constant web, the flange or in between. It is thus important to use the adequate width at each set of points.

$$V_{fib} = \sigma * b_t * \Delta_s * \cos\theta \qquad (5.5)$$

Where:

σ = *fiber tensile resistance*

b_t = *specimen width*

Δ_s = *distance between data points*

The results obtained for the HPFRC tensile stress along the shear crack and the total vertical tensile contribution V_{fib} are shown and analysed in Section 5.4.

5.2.3 Procedure estimating the aggregate interlock contribution with Walraven theory

As briefly explained in Section 2.3.1.1, Walraven (Walraven, 1981) has demonstrated that the aggregate interlock varies, among several parameters, with the crack width *w* and the crack slip *s*. His thesis results allowed to prepare several diagrams showing the aggregate interlock stress according to the *w* and *s*, following the maximum aggregate size and compressive strength of the concrete. Figure 5.8 is one example of these diagrams.

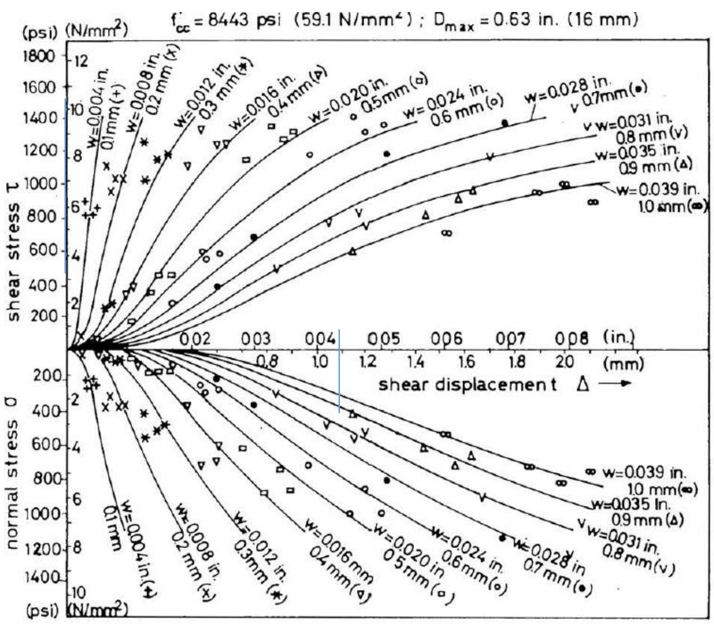

Figure 5.8 –Aggregate interlock stress vs crack opening and crack slip from Walraven theory, f'_c=59.1 MPa and D_{max}=16 mm (Walraven, 1981)

The most pertinent diagram was used for this project, the one with the highest concrete compressive strength (59 MPa) and the closest maximal aggregate size (16 mm) than the HPFRC studied (f_c=100 MPa and D_{max}=14 mm). Because of the discrepancies of concrete characteristics in Walraven study and this project, a certain uncertainty in results is expected. Moreover, Walraven study was conducted on concrete without fibre, it is possible that the aggregate interlock stress is different in HPFRC. This aspect is unknown presently. This project considers that if aggregate interlock is different in HPFRC, it would come mainly from the smaller crack opening provided by the fibres and thus increase the interlock stress as for normal concrete. This assumption would keep the diagram applicable.

If the sliding and crack opening at each set of point along the shear crack is known from the algorithm described in Section 5.2.1, determination of the aggregate interlock stress can be made.

Similar to the tensile stress analysis, the multiplication of the aggregate interlock stress (τ) by the correspondent area of each set of points provided the punctual shear forces. The integration of the punctual shear forces parallels to the shear crack and over its length is made directly. However, the estimation of the aggregate interlock (V_{agg}) of the HPFRC over the crack is required in the same direction (vertical direction) as the applied shear force in the girder. Some considerations are accounted for this conversion.

A sketch is presented in Figure 5.9 to illustrate the procedure for transforming a variable angle force into a single vertical force. Coordinate (*x, y*) and (*x', y'*) described previously are identified, and θ is the shear crack angle between 2 consecutive points of the critical shear crack.

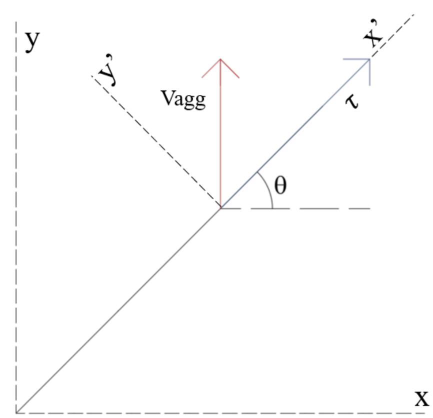

Figure 5.9 - Force diagram for the aggregate interlock present on the crack

Equation (5.6) allows transformation of the aggregate interlock stress τ at each set of points into a punctual vertical force V_{agg}. As for the tensile contribution of the HPFRC, the girder width varies along the shear crack, depending on where the set of points are localized in the constant web, the flange or in between. It is thus important to use the adequate width at each set of points.

$$V_{agg} = \tau * b_t * \Delta_s * \sin\theta \tag{5.6}$$

Where: $\tau = shear\ resistance\ of\ aggregate\ interlock$

$b_t = specimen\ width$

$\Delta_s = distance\ between\ data\ points$

The results obtained for the aggregate interlock along the shear crack and the associated vertical contribution V_{agg} are shown and analysed in Section 5.4.

5.2.4 Procedure of adjustment for non captured shear crack section

Some regions of the T-shape girder G2 and G3 could not be analysed by the DIC, as shown previously (Figure 4.13). Indeed, the speckles were only added on the girder faces perpendicular to the set of cameras, since only those surfaces could guarantee a high data accuracy according to the DIC system user manual (Correlated Solutions, 2021). To evaluate the aggregate interlock contribution and the tensile resistance of the FRC in the regions where DIC data was missing, some assumptions were made.

The first assumption was to consider that the shear crack has developed in the section in-between the web and the flange, as a straight line with the same angle measured in the web up to the crack tip measured in the flange (Figure 5.10a). Observation of the shear crack on the girder confirm this assumption is close to reality. The second assumption was that the crack opening measured at the top of the web section would vary linearly from the last value captured by the DIC to zero at the crack tip. The DIC results obtained on girder G4 where all the shear crack was captured has confirmed this second assumption is also acceptable. The third assumption was that the average crack slip measured on the whole beam was considered in the crack part non captured by the DIC (between the web and flange section). DIC results showed that the overall slip varies around an average value all along the girder, as it will be demonstrated in the next section.

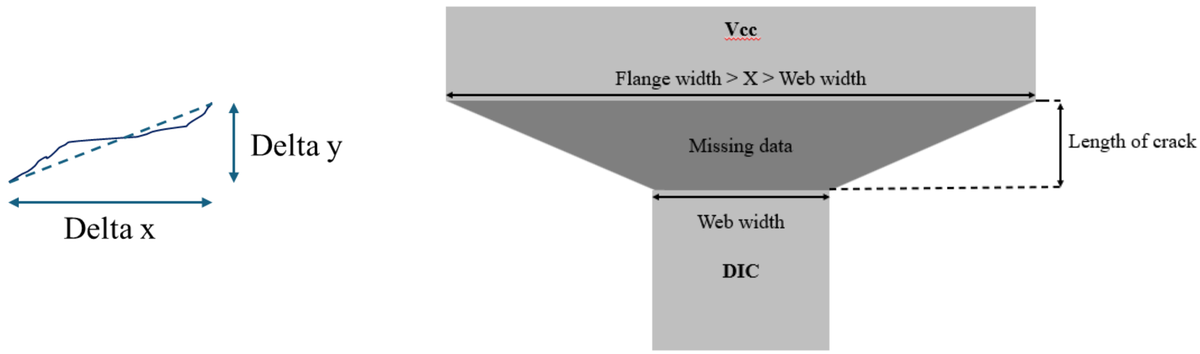

a) Straight line propagation of the shear crack between the web and the flange

b) Variation of the girder width from the web section to the flange section

Figure 5.10 – Illustration of assumption taken to evaluate contributions of the shear crack not captured in girders G2 and G3

To define the shear forces that take place at the missing section of the shear crack (between the web and the flange section), an integration of the stresses was made over the non captured cracked area. At that location, the girder section is not uniform (Figure 5.10b), so a varying width was considered. The length of the crack was considered to be height of the trapezoid section; the lower base was the same width as the web of the girder and the upper base is larger than the web but smaller than the flange. A total force perpendicular or parallel to the shear crack was found and later converted to the vertical axis with equations (5.5) and (5.6), respectively.

5.2.5 FRC tensile contribution (V_{fib}) and aggregate interlock (V_{agg}) results

The results of the in-depth DIC analysis described in Sections 5.2.1 to 5.2.4 will be shown. First, the moment in which the shear crack is analysed during the experiment will be presented for each girder. Second, the crack pattern captured with the DIC and the missing part will be described. Third, the stress distribution over the length of the crack will be shown for the tensile contribution of the fibres and the aggregate interlock. At the end of this section, a table will provide the main parameters of the shear crack analyses for each girder and the force contributions.

5.2.5.1 <u>Girder G2</u>

The load point selected for the analysis of girder G2 is shown by a cursor in Figure 5.11. The shear load at the point is 580 kN, which is slightly smaller than the maximum shear resistance measured during the test (593 kN). The reason for not choosing the maximum shear force was because the maximum shear force happened at the end of the force plateau , where the critical shear crack was large and had a much more complex pattern than at the beginning of the plateau.

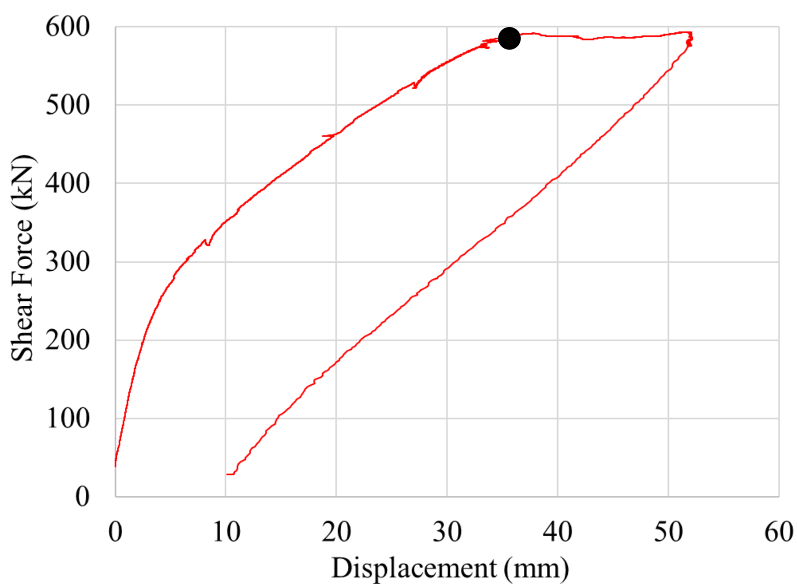

Figure 5.11 – DIC analysis on girder G2

Figure 5.12 shows the critical shear crack analysed at the ultimate point load. This shear crack was obtained with the analysis procedure detailed in Section 5.2.1. The red line is the shear crack captured by the DIC for which the analysis procedure detailed in Section 5.2.2 and 5.2.3 were applied, while the blue line is the missing part of the crack not captured by the DIC where assumptions were made to evaluate force contributions (Section 5.2.4).

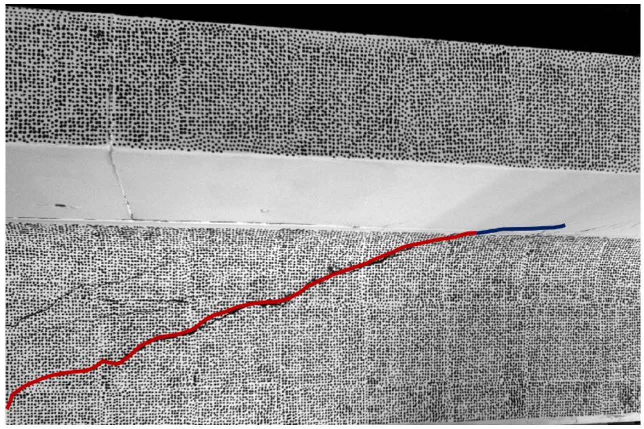

Figure 5.12 – Critical shear crack pattern obtained with the DIC on girder G2

Figure 5.13 shows the results of the analysis on the shear crack of girder G2 to obtain the tensile contribution provided by the HPFRC over the length of the crack. The blue curve is the crack opening (w) computed over the length of the shear crack and the orange one is the respective tensile stress (σ) from the post-peak behaviour shown in Figure 4.18. The zero in the x-axis is set at the beginning of the crack in the bottom of the girder. The continuous curves represent the results obtained with procedure detailed in Section 5.2.1, while the dotted lines show results obtained with procedure detailed in Section 5.2.4. When x is zero, the crack opening is close to zero and increase along the crack up to the middle length of the crack, then it starts to decrease. At the end of the shear crack detected by the DIC (interface of the constant and variable widths of the beam), the crack opening is still large (4 mm). The adjustment procedure allowed to complete the crack opening curve up to its extremity with 0 mm opening. The tensile stresses provided by the HPFRC along the shear crack show high values close to crack tips where crack opening is small, and lower value where crack opening is large. The tensile stress distributions at both crack tips are similar, this confirms the applicability of assumptions made in Section 5.2.4.

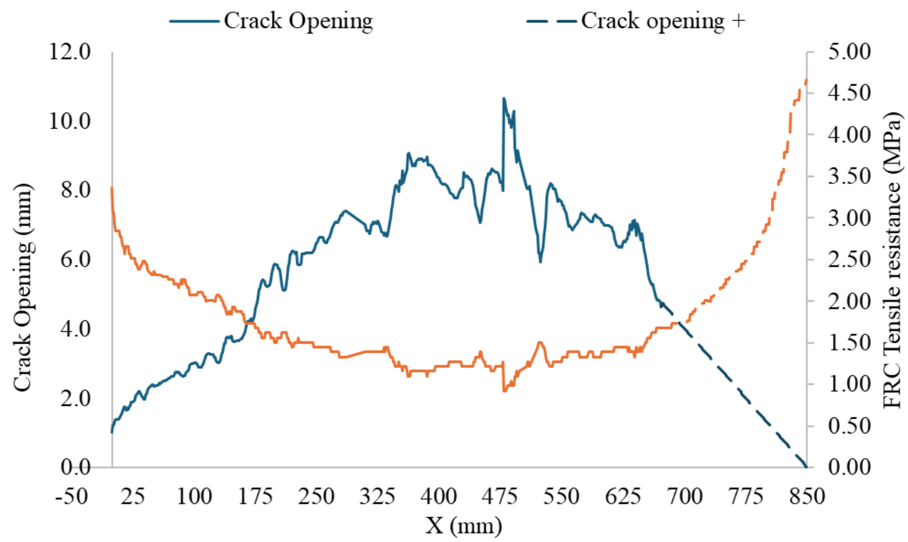

Figure 5.13 – Crack opening and tensile stress of FRC over the shear crack of girder G2

Figure 5.14 shows of the analysis of the shear crack of girder G2 to obtain the shear contribution provided by the aggregate interlock over the length of the crack. The blue curve is the crack opening (*w*) computed and described previously, the green curve is the crack slip (*s)* computed, and the orange one is the aggregate interlock stress distribution (τ). The crack opening and the crack slip are presented because the combination of these two values yields to a corresponding shear stress (Section 5.2.4). The continuous curves represent the results obtained with the procedure detailed in Section 5.2.1, while the dotted lines show results obtained with procedure detailed in Section 5.2.4. When *x* is zero, the crack opening is close to zero and it increases along the crack up to the middle length of the crack, then it starts to decrease. The crack slip is usually small (around 0.5 mm), except for some regions where the slip is large (around 2 mm). The shear stresses along the shear crack are zero through out most of the crack length. Between x = 800 mm and 850 mm in the crack position, however, high shear stresses can be noted. This is expected since the combination of low crack opening (<1 mm) and shear slip are required to yield shear stresses according to Walraven theory (Walraven, 1981).

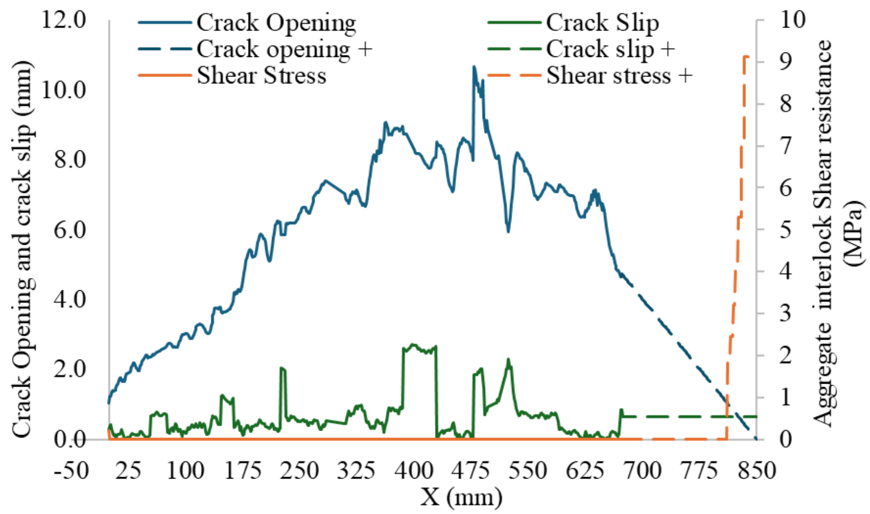

Figure 5.14 – Crack opening, crack slip and aggregate interlock stress over the shear crack of girder G2

The sum of forces obtained in the current analysis, including the section captured by the DIC and the missing section, is summarized in Section 5.2.5.4.

5.2.5.2 Girder G3

The ultimate load point selected for the analysis of girder G3 is the black cursor shown in the Figure 5.15. The maximum load was of 822 kN with a maximum vertical displacement of 18.5 mm.

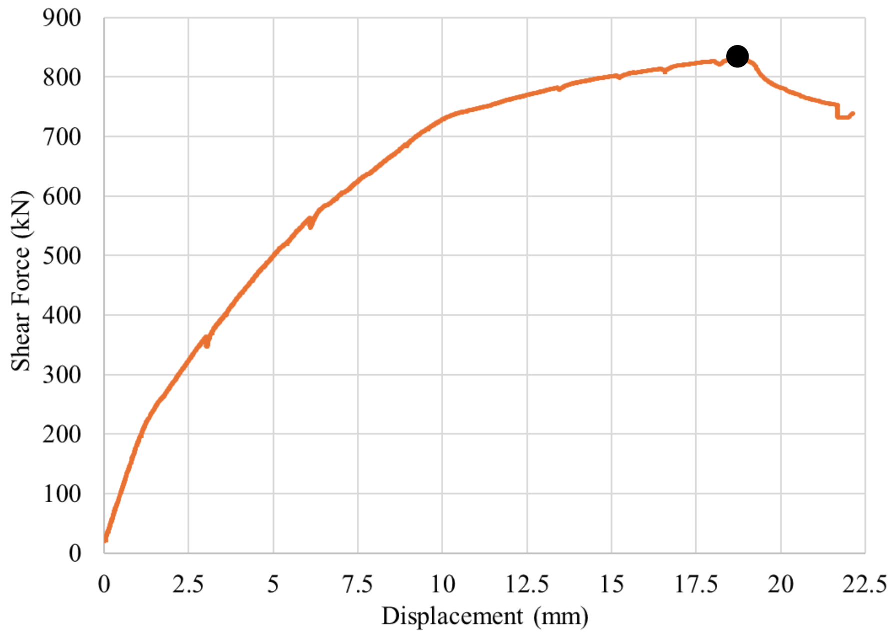

Figure 5.15 - Force by displacement curve of girder G3

Figure 5.16 shows the shear crack analysed at the ultimate point load. This shear crack was obtained with the analysis procedure detailed in Section 5.2.1. The red line is the shear crack captured by the DIC for which the analysis procedure detailed in Section 5.2.2 and 5.2.3 were applied, while the blue line is the missing part of the crack not captured by the DIC where assumptions were made to evaluate force contributions (Section 5.2.4). The crack pattern of girder G3 is more complex than the one presented forgirder G2, as it is composed of 3 distinct shear crack.

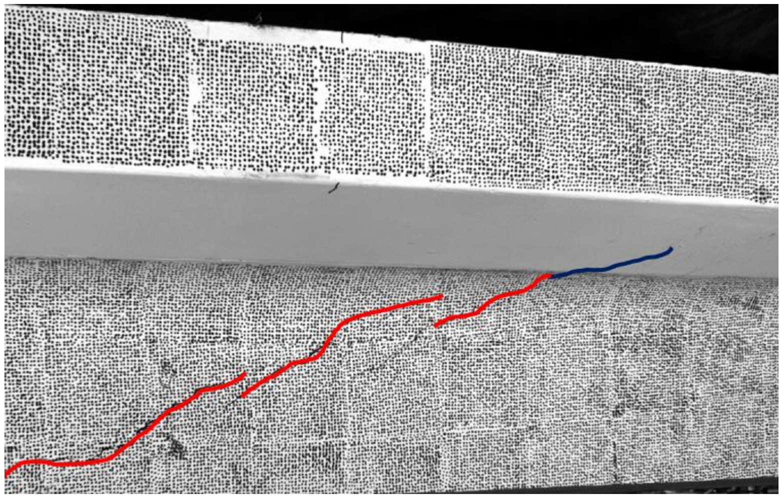

Figure 5.16 – Crack pattern analysed by the DIC on girder G3

520 shows the crack pattern detected by the algorithm. As it is possible to see at around 430 mm and 650 mm, there is a sudden change in the orientation of the crack. The regions from 0 mm to 430 mm, 430 mm to 650 mm, and 650 mm to 900 mm are the 3 distinct shear cracks (Figure 5.16). The sudden change happens due to the way the algorithm was developed. The shear and tensile peaks at those regions are not realistic and not considered during the data analysis.

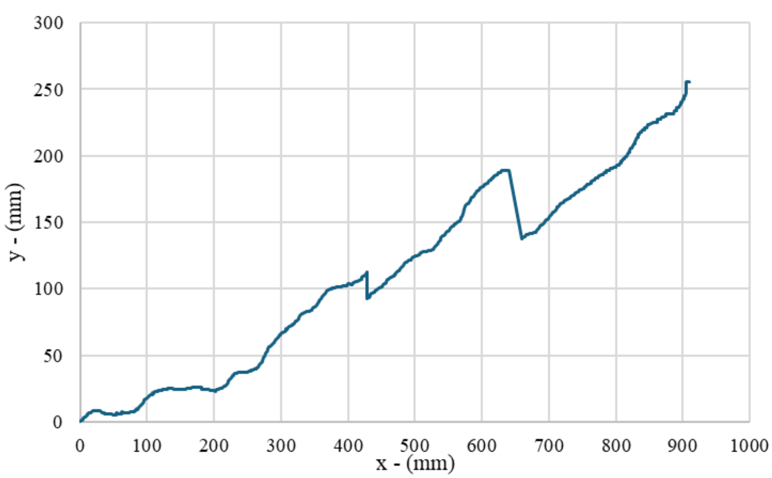

Figure 5.17 – Crack pattern of girder G3 used in the MATLAB algorithm

Figure 5.18 shows the results of the analysis of the critical shear crack of girder G3 to obtain the tensile contribution provided by the HPFRC over the length of the crack. The blue curve is the crack opening computed over the length of the shear crack and the orange one is the corresponding tensile stress obtained from the post-peak behaviour shown in Figure 4.18. The zero in the *x*-axis is set at the beginning of the crack at the bottom of the girder. The continuous curves represent the results obtained with the procedure detailed in Section 5.2.1, while the dotted lines show results obtained with the procedure detailed in Section 5.2.4. When *x* is zero, the crack opening is close to zero and increases up to the middle length of the crack, then it starts to decrease. At the end of DIC detection, the crack opening is still large (5 mm). The adjustment procedure allowed to complete the crack opening curve to zero at the crack extremity. The tensile stresses provided by the HPFRC along the shear crack show high values close to crack tips where the crack opening is small, and lower value where the crack opening is large. There is, however, a local variation around 650 mm that is related to the merging of the two sections of the critical shear crack. A sudden drop in the crack opening happens and, therefore, the corresponding tensile resistance is high. The tensile stress distributions at both crack tips are similar, this confirms the applicability of assumptions made in Section 5.2.4.

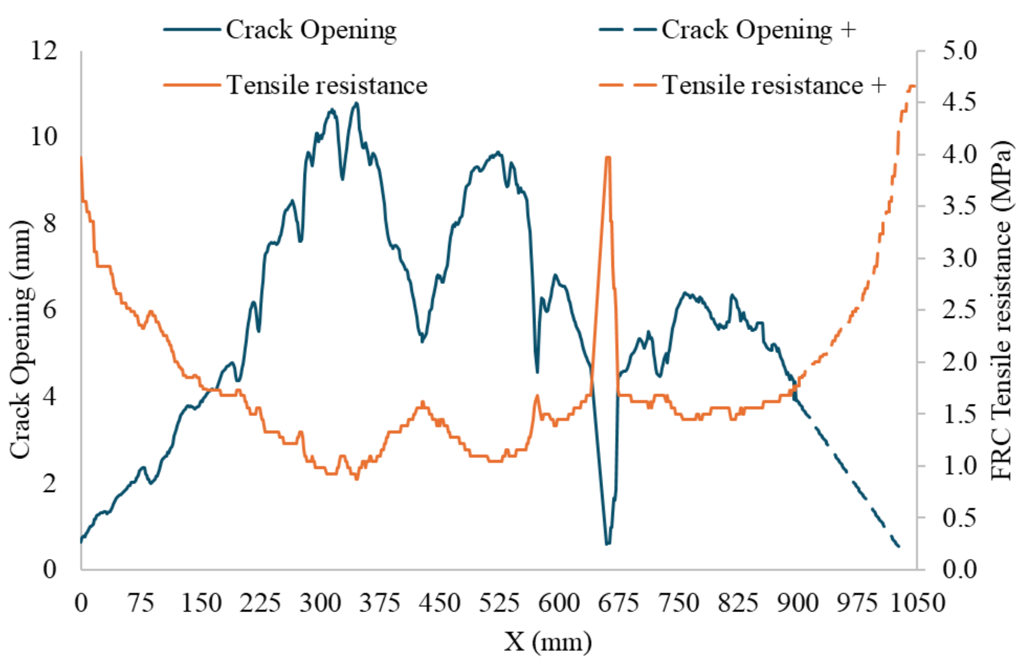

Figure 5.18 – Evolution of tensile resistance over the length of the shear crack of girder G3

Figure 5.19 shows of results of the analysis of the shear crack of girder G3 to obtain the shear contribution provided by the aggregate interlock over the length of the crack. The blue curve is the crack opening computed and described previously, the green curve is the crack slip computed, and the orange one is the aggregate interlock stress distribution. The crack opening and the crack slip are presented because the combination of these two values yields to a corresponding shear stress (Section 5.2.4). The continuous curves represent the results obtained with procedure detailed in Section 5.2.1, while the dotted lines show results obtained with procedure detailed in Section 5.2.4. When *x* is zero, the crack opening is close to zero and it increases up to the middle length of the crack, then it starts to decrease. The crack slip is usually small (around 0.75 mm), except for some regions where the slip is large (around 2 mm). The shear stresses along the shear crack are low for most of the crack length. However, between 0 mm and 50 mm, at 650 mm and between 800 mm and 850 mm, shear stresses are higher. This is expected since the combination of low crack opening (<1 mm) and shear slip are required to yield significant ￼￼.

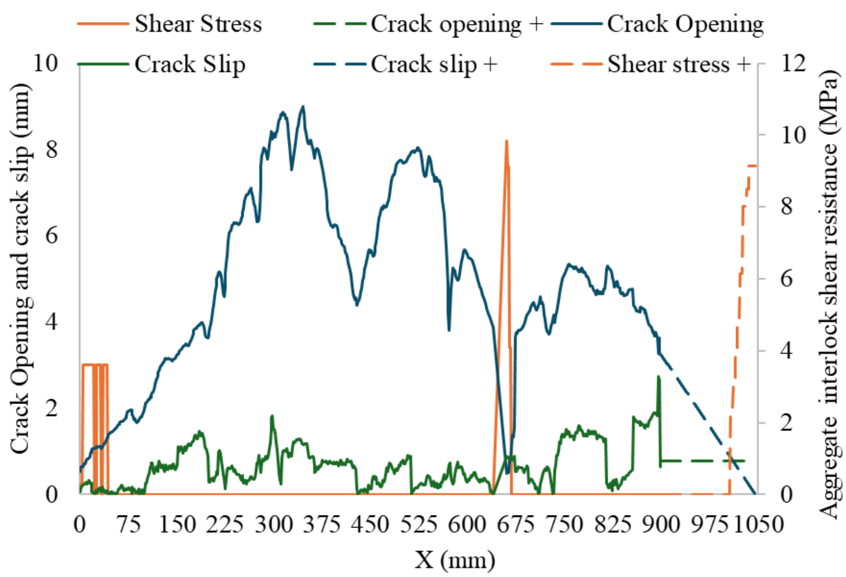

Figure 5.19 – Evolution of shear resistance over the length of the shear crack of girder G3

520Figure 5.16520

5.2.5.3 <u>Girder G4</u>

The ultimate load point selected for the analysis of girder 4 is the point shown by the black cursor shown in Figure 5.21. This point was chosen at the beginning of the load stabilization. After this point, the shear crack became much larger with a much more complex crack pattern. The shear force at the point selected was 741 kN with a corresponding vertical displacement of 12.0 mm.

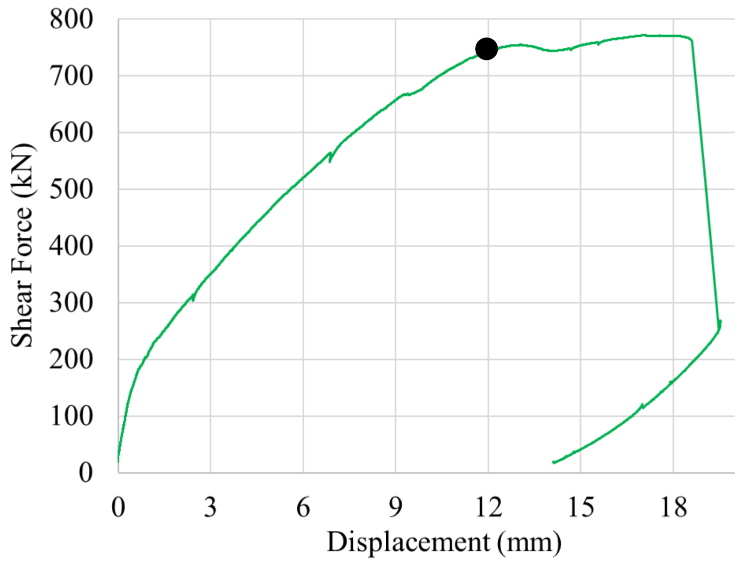

Figure 5.21 – Force by displacement curve of girder G4

The critical shear crack detected by the algorithm is shown in Figure 5.22. Girder G4 was the only specimen that the DIC could analyse the whole crack. No assumption was required to complete the crack width at the top of the girder, neither for calculation of the fiber tensile contribution and aggregate interlock contribution. Therefore, the girder G4 will be used as a reference for the analysis of the results in the following sections.

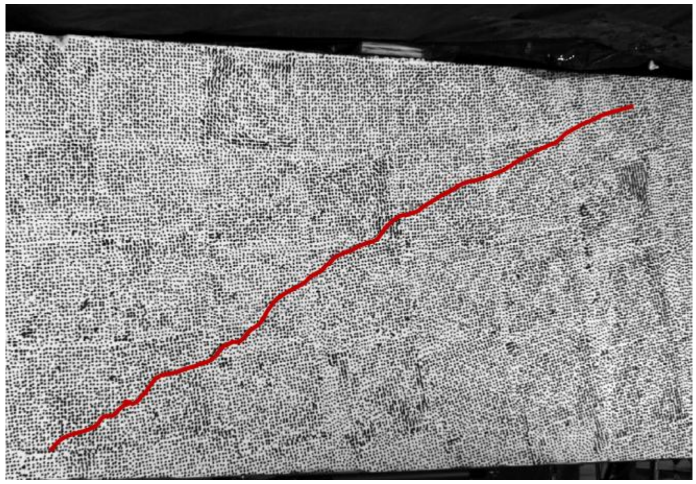

Figure 5.22 - Crack pattern analysed by the DIC on girder G4

Figure 5.23 shows two curves. The orange one is the tensile resistance, and the blue one is the crack opening over the length of the crack. The zero in the x-axis is set at the beginning of the crack in the bottom of the girder. The crack opening at the top of the girder tends to zero because it was captured completly by the DIC, unlike the results shown previously for girders G2 and G3. The FRC tensile contribution was maximal where the shear crack opening was small, at the two extremities of the crack.

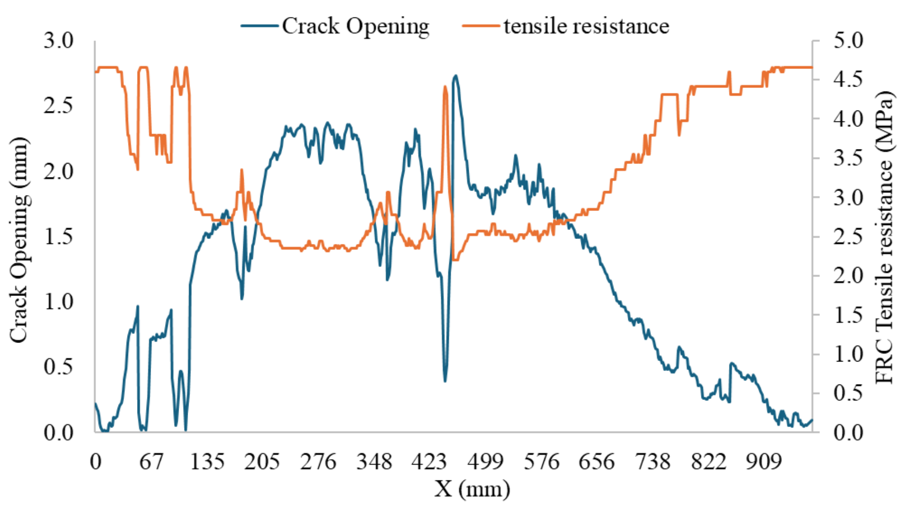

Figure 5.23 – Evolution of the tensile resistance over the length of the shear crack of girder G4

Figure 5.24 shows the evolution of the aggregate interlock stresses over the length of the crack. The blue line is the crack opening, the gray line is the crack slip, and the orange one is the shear resistance provided by the aggregate interlock. The crack opening and the crack slippage are presented because the combination of these two values yields the corresponding aggregate interlock stress.

Unlike girders G2 and G3, the importance of the aggregate interlock is more significant at the top extremity of the crack. A small crack opening (0.5 mm) with crack slippage (0.5 mm) between 820 mm and 1000 mm yield an average shear stress of around 4 MPa. The aggregate interlock at the tip of the crack is expected according to the literature (Chapter 2.3.2). A stress peak can be observed in the middle of the crack (around 450 mm), it is related to the analysis of the DIC algorithm at vicinity of crack merging as explained in Section 5.2.5.2. Between 0 mm and 100 mm, some shear peaks and a constant shear stress region are observed. The aggregate interlock at this region was not documented by Campana et al. (Campana et al., 2013b) in their study, thus it was unexpected to observe this contribution at the bottom of girder G4. Because the average shear stress is small at this region (around 1 MPa) and the shear stress appear in the first 100 mm of length, the aggregate interlock might just be noticeable at this section due to a non-linearity on the cracking pattern of the specimen. More observations would be needed to conclude that aggregate interlock at the base of the girder is characteristic in HPFRC beams. This contribution of the aggregate interlock at the base of the specimen was considered in the analysis.

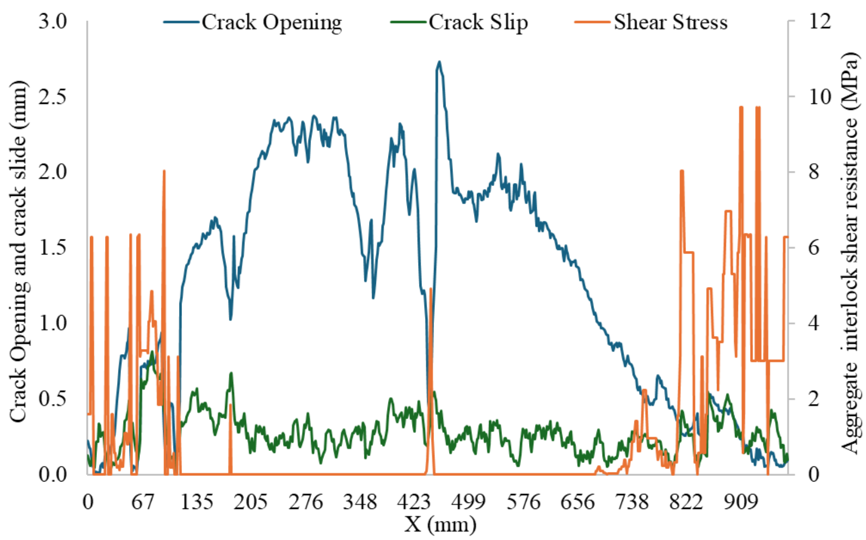

Figure 5.24 - Evolution of the shear resistance over the length of the shear crack of girder G4

5.2.5.4 Summary of contributions

Table 5.1 presents the main characteristics of the shear cracks developed in the girders. Crack length and height increase progressively from girders G2 to G4, with removal of prestress and using a rectangular beam. However, the average crack opening decreases significantly, from 6.0 mm in girders G2 and G3 to only 1.2 mm in girder G4, indicating an improved crack control at ultimate load for a rectangular beam.

Table 5.1 – Summary of shear crack characteristics at ultimate load of girders

Variable name	G2	G3	G4
Crack length	673	899	986
Crack height	214	243	511
Average crack angle	24	19	23
Average crack opening	6	5.9	1.2

The resisting forces identified for the fiber tensile contribution and the aggregate interlock contribution are shown in Table 5.2. They were obtained by integration of stress distribution evaluated with the DIC analysis (Section 5.2.1) and the zone captured manually (Section 5.2.4), and by consideration of the variable width of girders. The total forces are very different from one girder to the other. The tensile contribution of V_{fib} evaluated on girders G2 and G3 are present on Table 5.2. One can observe that the contributions at the top crack tips not captured by the DIC is significant and not considering them would have penalized significantly the results.

Table 5.2 - V_{fib} and V_{agg} resisting forces

Variable name		G2	G3	G4
Vfib (kN)	DIC	354	475	1098
	Not captured by DIC	297	225	-
	Total	651	700	1098
Vagg (kN)	DIC	0	15	116
	Not captured by DIC	87	156	-
	Total	87	171	116

The aggregate interlock contribution V_{agg} captured by the DIC on the web of girders G2 and G3 is negligible (Table 5.2). This can be explained by the large openings of the shear crack that provide very low shear stresses according to Walraven diagram (Figure 5.8) and thus a very limited force is obtained. The contribution comes only from the crack tips in between the web and the flange evaluated manually. The aggregate interlock contribution evaluated for girder G4 comes again mainly from the crack tips and was fully captured by the DIC as the web was of constant width. The total force contribution is in-between the ones of girders G2 and G3, which may confirm the manual adjustments made in zone non captured by the DIC on these girders yield realistic results.

Further analysis on the importance of V_{fib} and V_{agg} according to the girders' configuration will be done in a further section, as a remaining mechanism (V_{cc}) must be evaluated before to obtain a complete view of the shear resistance.

5.3 FEM analysis for V_{cc} contribution

The compression chord contribution to the shear resistance of girders is analysed in this section. According to the literature review (Section 2.3.2), researchers calculate the contribution of the uncracked region of the girder by simplified analysis based on assumptions difficult to validate, thus the results obtained are questionable. In this research project, the analysis of the compression chord contribution was performed using nonlinear finite element models (FEM). The pure shear stress distribution was extracted of the uncracked region of the girders on top of the critical shear crack, then an integration of those stresses was performed considering the variable width of the girder to obtain the force contribution.

The numerical models were developed using version 6.14 of the Abaqus software (Dassault Systems, 2014) and the concrete material law EPM3D (Massicotte & Ben Ftima, 2017).

5.3.1 FEM model

5.3.1.1 Model and mesh size

All girder models were created with the loading and support conditions described in the experimental program (Section 4.3). Figure 5.25 show the cross-sections and the mesh of each model used. The 3-point bending setup was replicate in models of 3-m girders G3 and G4. To reduce the computation time, a vertical symmetry plan was considered at mid-span of the 6-m girder G2.

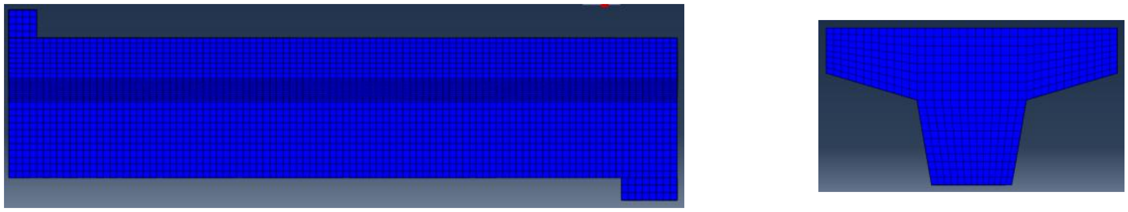

a) Girder G2, half specimen modeled

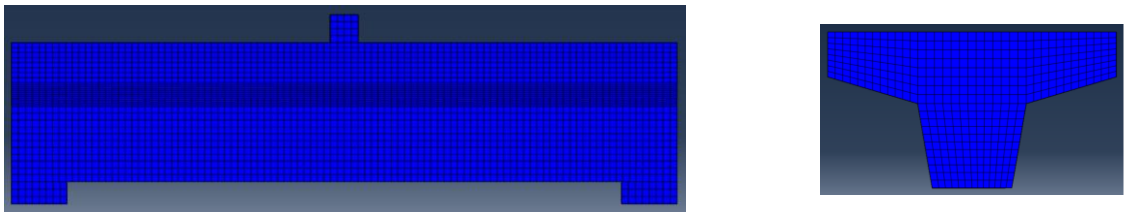

b) Girder G3, full specimen modeled

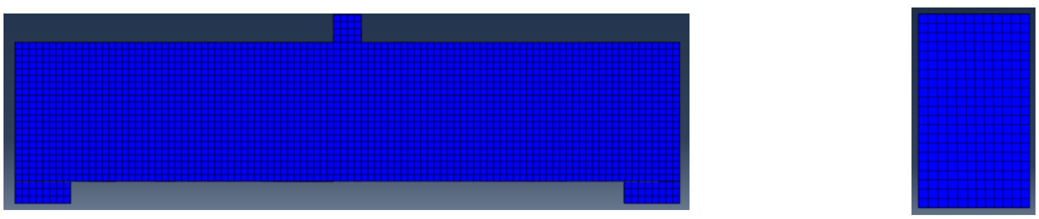

c) Girder G4, half specimen modeled

Figure 5.25 – Models and mesh

Linear cubic elements with 8 nodes, reduced integration, and hourglass control (C3D8R) were used to model the beams as well as the support and loading plates. The element size was chosen to achieve sufficient accuracy while maintaining a reasonable calculation time. The concrete elements had 30 mm size on all sides for Girders 2, 3 and 4. The support and loading plates were also modeled with elements of 30 mm. Two-node linear truss elements (T3D2) were used to model the reinforcing bars and tendons. A perfect contact was imposed between the reinforcement and the concrete of the beam.

5.3.1.2 Material laws

The concrete material law EPM3D developed by Massicotte and Ben Ftima (Massicotte & Ben Ftima, 2017) was used in the models. The compressive behaviour of the HPFRC was defined based on the compressive strength f'_c, modulus of elasticity E_c, Poisson ratio ν, and peak concrete strain ε_c measured experimentally in the project (Section 4.4.1). For tension, a smeared crack approach was chosen. The smeared crack approach adopts the concept of energy equivalence to reproduce the post-peak tensile failure. Multiple models were created with the girder G4 geometry and the model that could match the ultimate load found experimentally was chosen. Afterwards, the material property of this model was applied to different geometries, and the results are presented in Section 5.3.2.

The behaviour laws of reinforcing steels shown in Figure 4.19 were modeled using an elastoplastic behaviour law with the hardening phase after yielding.

5.3.1.3 Support and loading conditions

For the longitudinal bending tests, the load was applied using a steel plate of 1 m long, 120 mm wide, and 120 mm thick, located at the center of the beam. A vertical displacement was then imposed at the top surface of the plate during the loading stage.

The supports were modeled using plates of 365 mm long, 300 mm wide, and 100 mm thick. The center of the support plate was located at 150 mm from the end of the girders. The distances were chosen to replicate the experimental conditions. The vertical displacement of the support was blocked along a line in the center of the plate to allow rotations and longitudinal displacements. The Figure 5.26 shows the steel plate used to distribute the force in the girder as well as the restraints applied to the model in red.

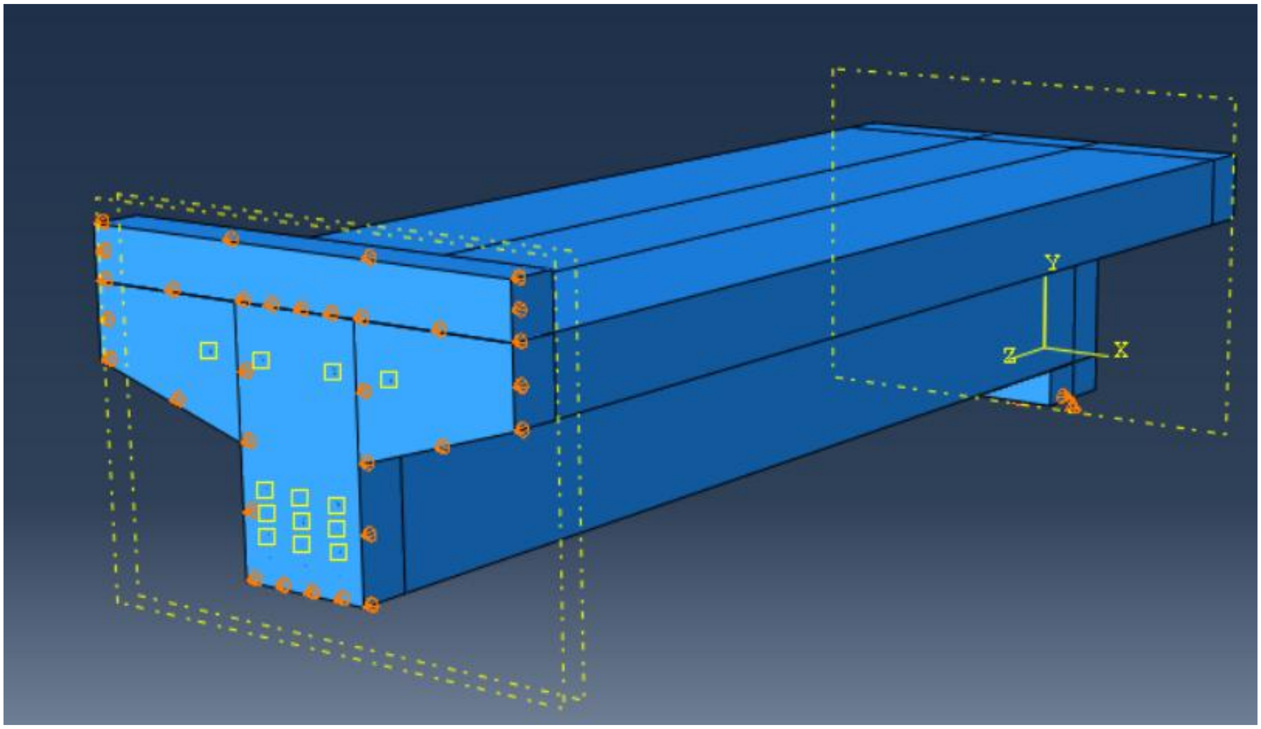

Figure 5.26 – Numerical model of girder G2 with supports and the symmetry plane

5.3.1.4 Loading steps

The loading of the beams was divided into two stages to reproduce the experimental conditions. In the first loading stage, gravitational force was applied to the entire model while the tendons were prestressed. A thermal expansion coefficient was defined for the tendons, and a temperature variation was then applied to the tendons so that the induced stress corresponded to the prestressing force. The prestress stresses applied are shown in Annex B.

In a second step, the beam was loaded to failure with displacement control via the loading plate. The loading time was chosen sufficiently long so that the analysis could be considered quasi-static. It means that every model has been verified so that the ratio E_c/E_i remains below 2% during the loading phase, where E_c is the kinetic energy of the model and E_i is the internal deformation energy.

5.3.2 FEM results

In this section, the force-displacement curves and the cracking patterns measured by the FE models are presented and compared with the experimental ones. Then, the models are used to evaluate the compression chord stress distribution in the uncrack section of girders. Finally, the integration of shear stresses is done and the compression chord total force are shown and analyzed.

5.3.2.1 Girder G2

Figure 5.27 presents the numerical and experimental mechanical behaviour of girder G2. The force-displacement curve is well reproduced by the model. The girder rigidity in the elastic phase and non-linear phase is identical; discrepancies start close to the ultimate strength. Around 1100 kN, the force stabilizes on the experimental curve with a significant ductility, whereas numerical shear capacity is slightly higher with a rapid decrease in strength. The experimental plateau is related to the maximal shear contribution provided by the HPFRC; however, it would have been expected the shear capacity decreases after the ultimate load. A plausible explanation for this behaviour is that tendon slippage occurred and increased artificially ductility at ultimate load.

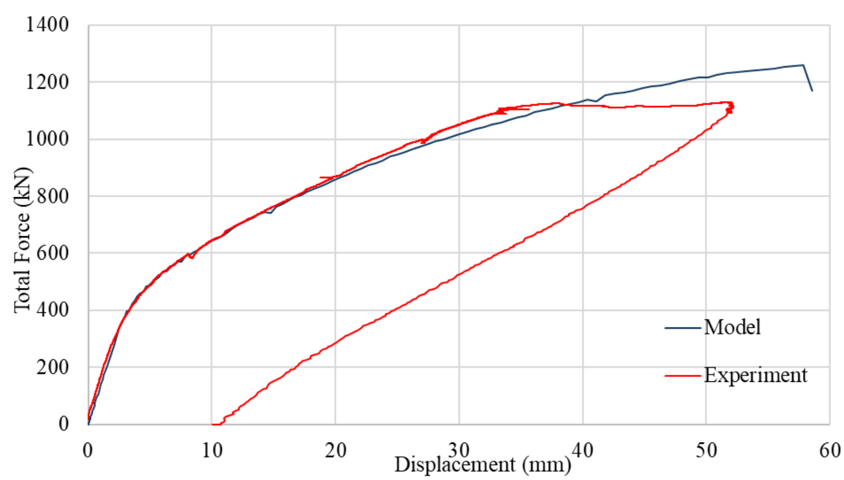

Figure 5.27 – Numerical and experimental mechanical behaviour of girder G2

Figure 5.28 shows one extremity of girder G2 after the shear test was completed, where the tendons are visible. The tendons, initially cut just after the extremity of the girder before the formwork removal, are not aligned anymore with the external face. This confirms the tendons slipped during the test. However, it is impossible de know when the slippage occurred, progressively during the test or mainly at the ultimate loading. This later option is considered the most probable, since a progressive slippage would have reduced the experimental girder stiffness during the nonlinear phase, while it stayed constant until the ultimate strength was achieved. This behaviour could not be reproduced by the model that was considering a perfect bond with reinforcement.

Figure 5.28 – Extremity face of girder G2 showing tendon slippage after the shear test

Figure 5.27 presents the numerical and experimental cracking patterns of girder G2. Figure 5.29a shows the principal tensile strains of the numerical model and Figure 5.29b illustrates DIC principal strains. Vertical bending cracks and inclined shear cracks show similar patterns in the experiment and the model. Numerical and experimental critical shear cracks start at around 1450 mm from the girder extremity and end at the same position and height of the flange around 360 mm from the mid-span. In both cases, the critical shear cracks are the result of the merging of different shear cracks.

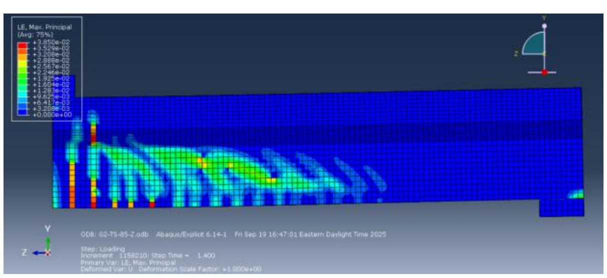

a) Model

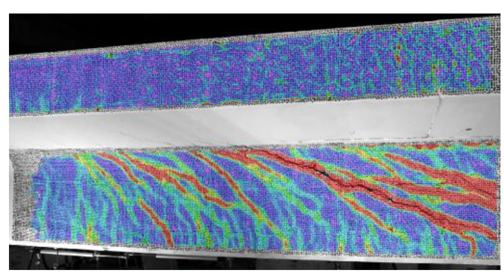

b) DIC

Figure 5.29 – Numerical and experimental crack pattern of girder G2

The model replicate with a good accuracy the global mechanical behaviour of the girder, the ultimate strength and the crack pattern. Even though the tendons slipped in the test and not in the model, the model should provide a good representation of the shear stress in the uncracked concrete over the shear crack at 1100 kN, where numerical and test results are the same (Figure 5.29).

Figure 5.30a shows the position (green vertical line) where the shear stresses were extracted in the girder. The position is above the tip of the critical shear crack and only the uncracked elements were selected. The shear stress distribution over the cross-section is presented in Figure 5.30b. One can observe that the uncracked area reaches the region with variable web width at external face, but is limited in the flange in the central region of the cross-section. The integration of the shear stresses in the compression chord considering the width of the elements yielded a force contribution of **191 kN**.

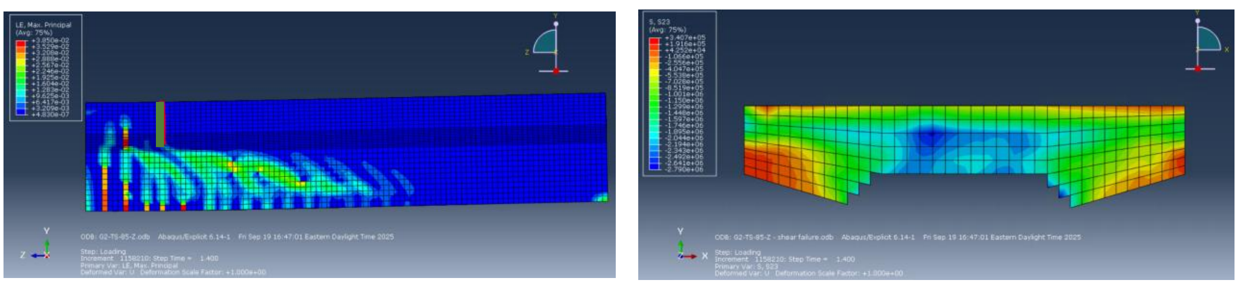

a) Uncracked elements showed by the vertical green line

b) Shear stress distribution in the cross-section

Figure 5.30 – Shear stress numerical results of girder G2

5.3.2.2 Girder G3

Figure 5.31 shows FEM and experimental force-displacement curves of girder G3. The force-displacement curve is well reproduced by the model, but some differences can be noted. The model rigidity in the elastic phase is slightly higher and at the non-linear phase the rigidity slowly decreases until the peak force of around 1600 kN is achieved. The experimental curve, after the linear phase, keeps a constant rigidity until 1400 kN of total force. At this force, the rigidity drops and stays constant until failure. Even though these differences exist, the experimental and model curves are very close one to the other. In conclusion, the model well represents the mechanical behaviour of the girder G3.

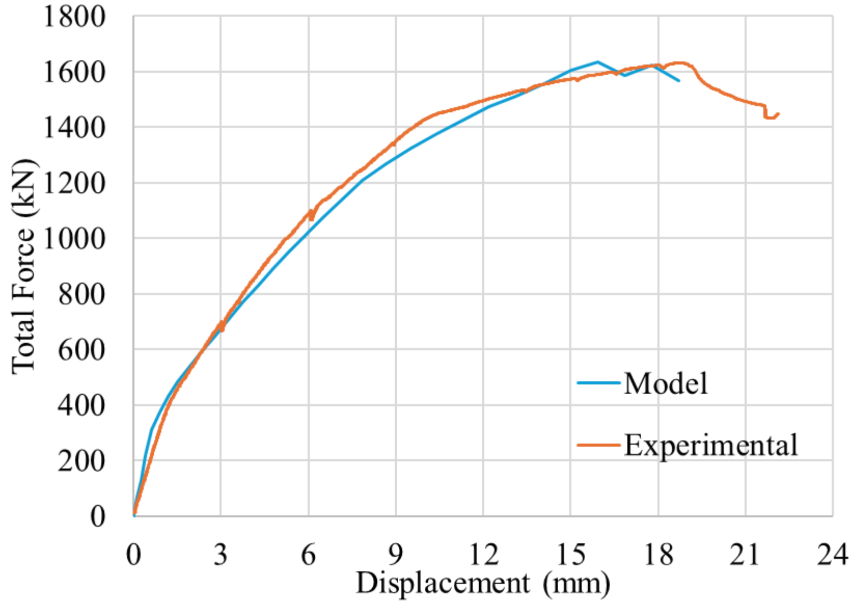

Figure 5.31 – Force vs displacement of EPM3D model and experimental value of girder G3

Two pictures are presented in Figure 5.32, the principal tensile strains of the numerical model and the one of the DIC. Some similarities can be noted between these two pictures. Vertical bending cracks and inclined shear cracks have similar patterns. Numerical and experimental critical shear cracks start at around 300 mm from the girder extremity and end at the same position and height of the flange around 150 mm from the mid-span. In both cases, the critical shear cracks are the result of the merging of different shear cracks.

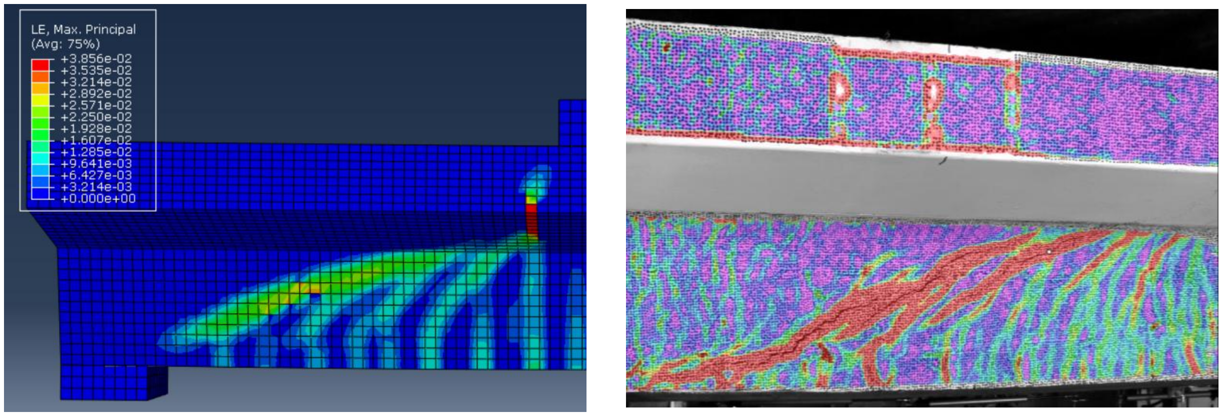

a) FEM b) DIC

Figure 5.32 - Crack pattern from girder G3

The model replicate with a good accuracy the global mechanical behaviour of the girder, the ultimate strength and the crack pattern. Even though the force-displacement curves present some differences, the model should provide a good representation of the shear stress distribution in the uncracked concrete over the shear crack at 1600 kN, where numerical and test results are the same (Figure 5.31).

The Figure 5.33a shows the position (green vertical line) where the shear stresses were extracted in the girder. The position is above the tip of the critical shear crack and only the uncracked elements were selected. The shear stress distribution is presented in Figure 5.33b. The integration of the shear stresses with consideration of the width of the elements yielded a total force value of 336 kN.

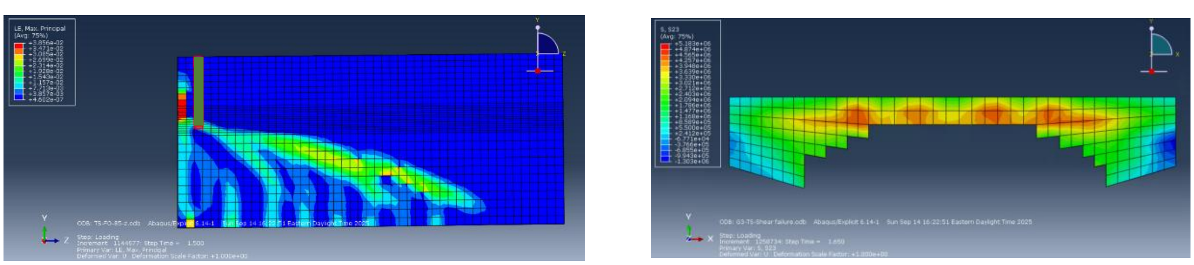

a) Uncracked elements b) Shear stresses

Figure 5.33 – FEM results of girder G3

5.3.2.3 Girder G4

Girder G4 was the specimen chosen to calibrate all the models.Figure 5.34￼ shows FEM and experimental force-displacement curve of girder G4. The model accurately replicates the mechanical behaviour observed in the experiment. Both the model and the experimental curves are identical on the linear phase. On the non-linear phase, a small difference can be noted. Even though the rigidity is similar throughout the loading, the model presented a higher rigidity at the beginning of the non-linear phase that was responsible for the small difference on the non-linear phase. After 1500 kN of force, the experimental curve stabilises due probably to the tendons' slippage until 18.5 mm of displacement was achieved. This phenomenon was not reproduced by the model that is considering a perfect bond between concrete and tendons. Since the DIC analysis on the girders ended at peak force, there was no need to also reproduce the strength plateau on the numerical model. The tensile post-peak behavior of the HPFRC was chosen in a way that the ultimate force of the model matched the experimental data, thus both curves have an ultimate load around 1500 kN.

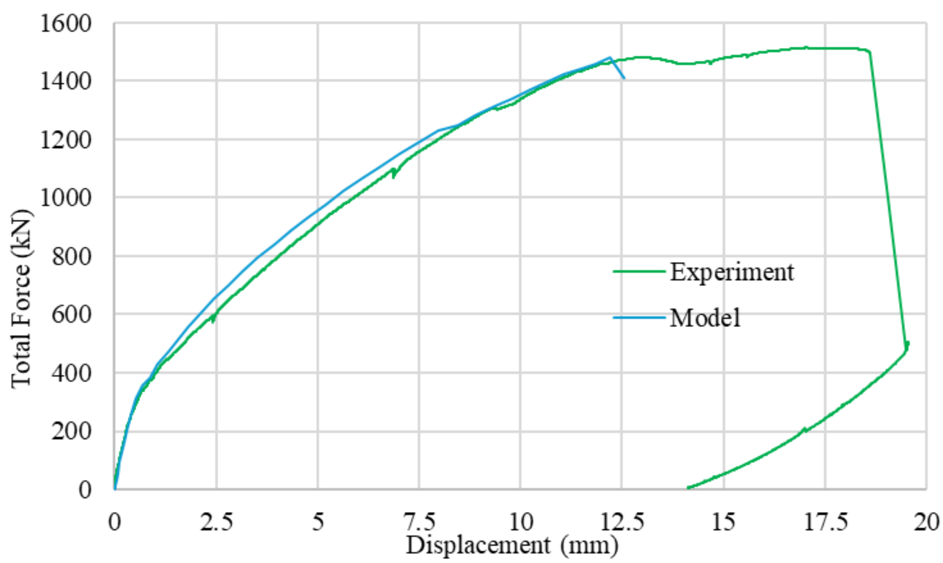

Figure 5.34 - Force vs displacement of EPM3D model and experimental value of G4

Two pictures are presented in Figure 5.35, the principal tensile strain of the numerical model and the critical crack pattern detected by the algorithm on the DIC results. Some similarities can be noted. Unlike girders G2 and G3, the critical shear crack is not made of previous formed shear cracks. It is made of a single crack that got longer and wider throughout the experiment. The crack begins at the bottom, close to the support, and goes towards the upper section of the specimen. Because of the rectangular cross-section of girder G4, the tip of the crack does not have a change of angle like girders G2 and G3.

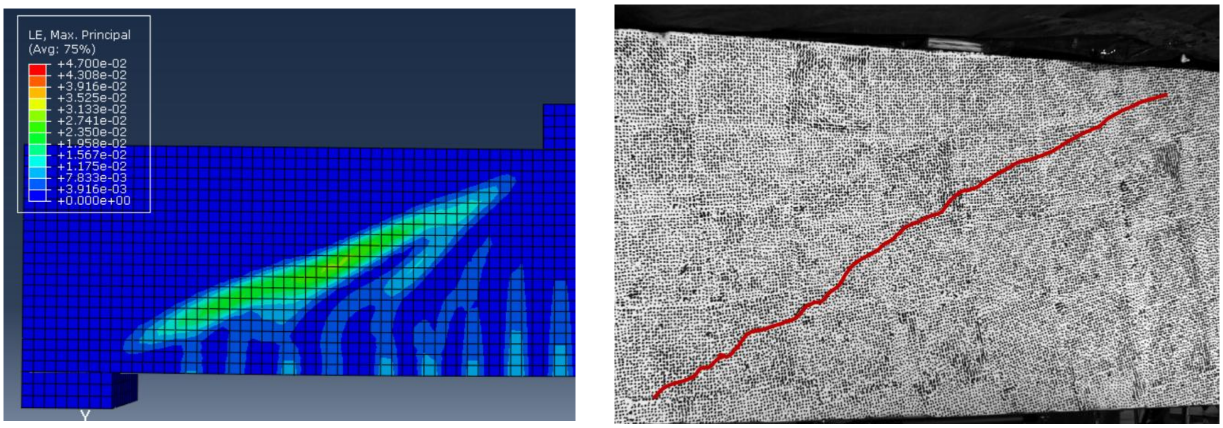

a) FEM b) DIC

Figure 5.35 - Crack pattern from of girder G4

The model replicates with a good accuracy the global mechanical behaviour of the girder, the ultimate strength and the crack pattern. Even though the model cannot replicate the post-peak behaviour of the girder, the model should provide a good representation of the shear stress in the uncracked concrete over the shear crack at 1450 kN, where numerical and test results are the same (Figure 5.34). In Figure 5.36a, the position at which the shear stresses were extracted is presented with the vertical green line. The position is above the tip of the critical shear crack and only the uncracked elements were selected. The shear stress distribution in that region is presented in Figure 5.36b. The integration of the shear stresses with consideration of the width of the elements yielded a total force value of 160 kN.

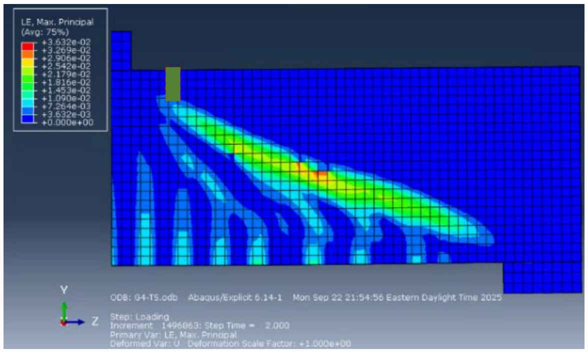

a) Uncracked elements

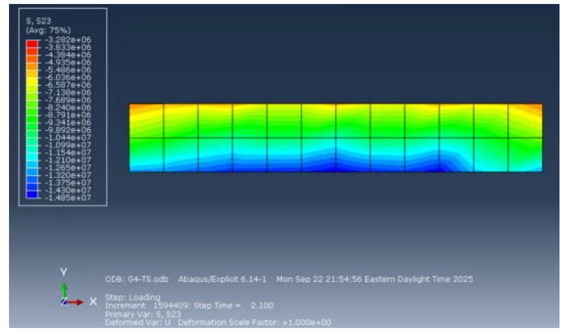

b) Shear stresses

Figure 5.36 – FEM results of girder G4

5.3.3 Compression cord (V_{cc}) results

The compression chord vertical contributions are summarized in Table 5.3. The biggest compression chord contribution comes from the girder G3, followed by G2 and finally by G4. It is difficult to explain why the difference between the compression chord contributions of girders G2 and G4 is so small, given that G2 is prestressed and has a T-shaped geometry and girder G4 is non-prestress and has a rectangular shape. It is important to compare girders to their respective experimental ultimate load and the contributions of all shear resisting mechanisms to understand these results. This discussion will be finally made in the next section.

Table 5.3 – Compression chord summary results

Variables	G2	G3	G4
Compression Chord vertical shear component (kN)	190	336	160

5.4 Contribution of shear mechanisms

5.4.1 Shear mechanisms in experiments

Table 5.4 summarized results described in previous sections for each girder tested in shear. All values presented are the total vertical contribution of each shear mechanisms, V_{fib} and V_{agg}

computed with DIC in captured zones and manual adjustments in non captured ones, and V_{cc} with FE models. The fibre efficiency coefficient γ_f evaluated experimentally (Section 4.6) is also shown. This coefficient was applied to the V_{fib} contributions to account for the difference in fibre orientation and density between the characterization specimens and the girder at failure locations. Other mechanisms do not depend on fibre contribution and are thus not factored by this factor. The total shear resistance was calculated with the Equation (5.7). The ratio between the total calculated value (V_{total}) and the experimental ultimate load value (V_{exp}) is presented Table 5.4.

Table 5.4 – Shear forces provided by each resisting mechanism and comparison with the experimental resistance

Specimen	γ_f	V_{fib} (Total) (kN)	V_{fib} (Factored) (kN)	V_{agg} (kN)	V_{cc} (kN)	V_{total} (kN)	V_{exp} (kN)	Ratio V_{total}/V_{exp}
G2	0.33	652	215	87	191	493	580	85%
G3	0.36	700	525	171	336	759	822	92%
G4	0.39	1098	428	116	160	704	740	95%

$$V_{total} = \gamma_f V_{fib} + V_{cc} + V_{agg} \tag{5.7}$$

The ratio V_{total}/V_{exp} is higher than 85 % for all girders analysed, it means the evaluation of each shear mechanisms made in Chapter 5 nearly reproduced the full capacity of HPFRC girders described in Chapter 4. Girder G4 has the highest ratio among them with 95 % of accuracy, while girders G2 and G3 have lower values of 85 % and 92 % respectively. This observation was expected, since the DIC captured all the critical shear crack in girder G4, while some assumptions were taken to complete uncaptured regions for girders G2 and G3. Besides, the accuracy of shear resistance prediction for girder G4 demonstrates that the DIC algorithm developed to evaluate the relative movement between shear crack surfaces, and the calculation methods to compute the shear stress distribution and the integration of vertical shear forces are adequate.

As girders G2 and G3 present slightly lower ratio V_{total}/V_{exp}, it may indicate that assumptions taken to manually compute V_{fib} and V_{agg} in uncaptured regions by the DIC (crack opening varies linearly and fixed crack angle) increase uncertainty. However, the V_{total} values show reasonable error below 15% to the experimental values.

The general conclusion is that the shear capacity is well predicted by the consideration of each contribution of the resistance mechanisms based on DIC analysis and FE models.

5.4.2 Proportion of each shear mechanisms

The resisting mechanism V_{cc}, V_{fib} and V_{agg} are presented as a percentage of the total calculated force in Table 5.5. It is necessary to transform the forces into percentages to remove effect of beam length in the analysis. It is thus possible to discuss how resisting mechanisms are modified by the presence of prestress, change of geometry and change of shear span.

Table 5.5 – Ratios of each resisting mechanism in relation to the maximum calculated force

Specimen	Girder configuration	V_{fib} (factored)	V_{agg}	V_{cc}	V_{total}
G2	6m prestressed T-girder	43.6%	17.6%	38.7%	100%
G3	3m non-prestressed T-girder	33.2%	22.6%	44.3%	100%
G4	3m non-prestressed rectangular girder	60.8%	16.4%	22.7%	100%

The analysis is started with girder G4 having the rectangular shape without prestress. Girder G4 presents the highest V_{fib} contribution with 61% of the total calculated force, with 16 % and 23 % of contributions coming from the aggregate interlock V_{agg} and the compression chord V_{cc} respectively. The fibres thus provided a very significant bridging effect across the shear crack. The aggregate interlock has a limited effect. The main mechanism of the shear resistance of reinforced concrete girder without fibre and stirrups is the aggregate interlock(Campana et al., 2013b, since the critical shear crack is usually steep and located close to the support. ***In this project the presence of fibres has changed the crack pattern***

of the critical shear crack. Instead of having a steep crack, girder G4 showed a flatter inclined shear crack like in a beam with stirrups. The compression chord contribution of girder G4 is low to moderate, while the one of a reinforced rectangular beam is generally negligible. (Campana et al., 2013b)

Girder G3 distinguishes from girder G4 by its T-shape. As expected, the flange has increased the area of the uncracked region and enhanced strongly the compression chord contribution (similar effect for girder G2). Therefore, the highest shear contribution mechanism for girder G3 became V_{cc} with 44%, followed by V_{fib} at 33% and V_{agg} at 23%. V_{agg} remains in the same proportion in comparison to girder G4, but V_{fib} was reduced significantly. The critical shear crack length (Table 5.6) was similar in girders G3 and G4. Thus, the reduction in V_{fib} is mainly related to the average crack width of 5.2 mm (Table 5.6), much larger than the measured one in girder G4 of 1.2 mm, which decreased the fibre bridging on the crack.

Table 5.6 – Critical shear crack characteristics in HPFRC girders

	G2	G3	G4
Crack length (mm)	835	1006	986
Crack height (mm)	284	343	511
Average crack angle	19	19	27
Average crack opening (mm)	5.0	5.2	1.2

Girder G2 differs from girder G3 by the prestressing and the beam length, thus the shear-to-span ratio was 6.45 rather than 3.1. The V_{cc} and V_{agg} contributions difference between girders G2 and G3 is about 5 %, while the difference on V_{fib} is more than 10 %. So, the prestress improved mostly the V_{fib} contribution. This could be related to the angle of the shear crack versus the prestress where the fibres and the aggregate interlock were acting. Prestress was horizontal and the aggregate interlock was acting mainly horizontally at shear crack extremities, while fibres bridging was occurring in inclined part of the shear crack. It is probable that the impact of the prestress on shear mechanisms is improved where cracks are perpendicular or inclined versus the prestress, therefore favoring V_{fib} in the girder rather than V_{agg}.

As a summary, the compression chord contribution $V_{cc}$was affected positively mainly by the presence of the flanges. The fiber tensile contribution V_{fib} was positively affected by the smaller crack angle that the prestress and the flanges have imposed. The aggregate interlock contribution V_{agg} represented the smaller contribution in all girders, mostly due to the flat crack angle of the shear crack extremities in the girder tested and to the small portion of crack extremities where it occurred.

5.4.3 Shear mechanisms with code comparison

Table 5.7 presents data of the advanced analysis made with the DIC and the FE model to compute the shear resistance and the predicted shear resistance according to the CSA-S6 standard. V_c for advanced analysis represents V_{agg}+V_{cc} (V_{dowel} neglected in the project), while its correspond to V_{cc}+V_{agg}+V_{dowel} in the code. At the bottom of the table the ratio of the shear resistance measured with advanced analysis ($A_{dvanced}$) and the shear resistance according to the CSA standard is presented (V_{CSA}).

Table 5.7 – Comparison between Advanced analysis and CSA-S6 standard

Variables	G2		G3		G4	
	In-depth analysis	CSA S6.19	In-depth analysis	CSA S6.19	In-depth analysis	CSA S6.19
Teta (degree)	19	35	19	35	27	35
W_v (mm)	5.0	2.1	5.2	2.2	1.2	2.2
V_c (kN)	278	155	507	117	276	137
V_{fib} (kN)	215	154	252	149	428	127
V_{total} (kN)	493	309	759	254	704	263
$V_{Advanced}/V_{csa}$	1.60		2.99		2.68	

One can observe large discrepancies between the results obtained by the advanced analysis and CSA for the shear crack angles and crack opening, as it was already mentioned in Section 4.7. The additional conclusion from Table 5.7 is how much the code underestimates each shear resisting mechanism in HPFRC girders. V_c computed with the code equations is about 36 % of the value obtained with advanced analysis, and V_{fib} about 17 %. Globally, the code total resistance represents 36 % to 57 % of the reality.

The code cannot capture correctly the effect of prestress, geometry and shear span on V_{fib} ***or*** V_c. Indeed, the code ultimate resistance varies marginally for the three girders tested, contrarily to the one obtained with advanced analysis. The girder shape effect could be at least improved in the CSA standards by considering the flange area contribution in shear, which is neglected presently. As the flange contribution may be limited for usual T-girder with thin flange, it is very significant for the T-girder with thicker flange like in this project.

Figure 5.37 shows the ratio of experimental and expected shear resistance (V_{exp}/V_{model}) versus the calculated longitudinal strain of the database of shear tests used by Foster (Foster et al., 2018) to verify the accuracy of his model adopted in the CSA-S6 shear resistance model for FRC structural components. Data points gathered from this study (girders G2, G3 and G4) were added in the figure. As stated in Section 2.4.2.1, the database used by Foster considered only beams tested with a shear span-to-depth ratio a/d ≥ 2.5 and a fibre content of 0.25 to 0.5 %. The girders in this study respected the first rule but did not fulfill the second requirement with a fibre content of 1%. The ratio presented on the figure for the girders of this study were presented on Table 5.7 ($V_{Advanced}/V_{CSA}$) and the calculated strains are presented in Annex B.

The database used by Foster provided V_{exp}/V_{model} ratios from 0.9 up to 2.8 for longitudinal strain from 30 x10^{-6} to 900 x10^{-6}. One can observe that the smaller the strain, the larger the V_{exp}/V_{model} ratios, in other words the greater the conservatism of the Foster et al.'s model adopted in the CSA. The points that have a calculated longitudinal strain higher than 500 x10^{-6} show a lower underestimation of the model with an average V_{exp}/V_{model} ratio of 1.5.

The girders from this study have V_{exp}/V_{model} ratios of 1.87 up to 3.24 with calculated longitudinal strain of 740 x10^{-6} to 926 x10^{-6}. These values are different to the data spectrum obtained by Foster et al. Girder G2 is the closest to Foster et al.'s dataset points, with a 1.87 ratio at 740 x10^{-6} calculated strain. Girders G3 and G4 have much higher ratios than Foster et al.'s dataset for strain larger than 900 x10^{-6}, but for calculated strain lower of 100 x10^{-6} similar ratios are shown in Foster et al.'s dataset.

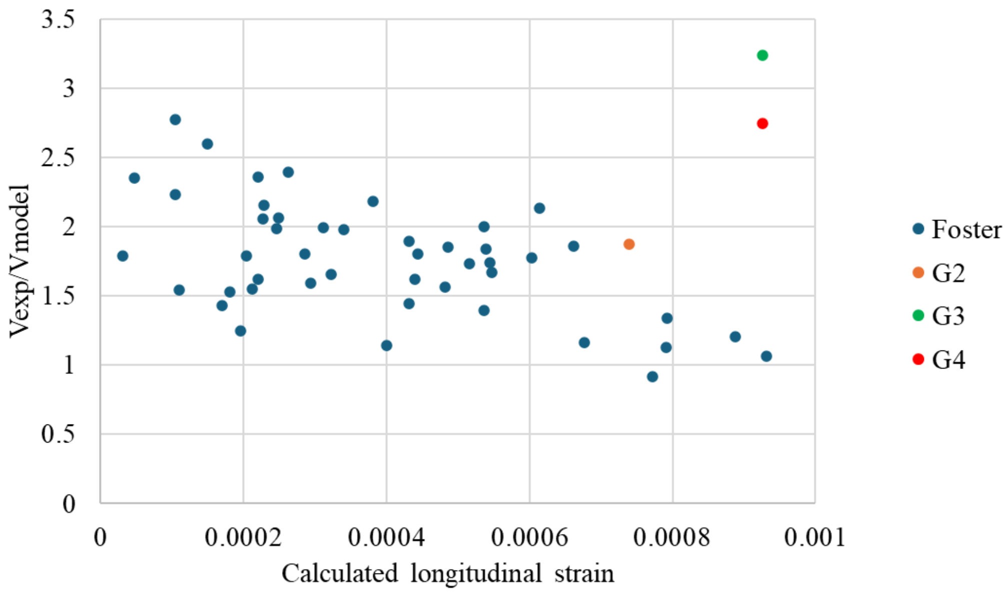

Figure 5.37 – Ratio of experimental and expected shear resistance versus calculated longitudinal strain *adapted from (Foster et al., 2018)*

Two reasons could explain the conservativism of the datapoints gathered from this study in Figure 5.37. The first explanation is that the Foster et al.'s model adopted in CSA underestimates even more the shear capacity of FRC components with fibre dosage higher than 0.5 %. The second explanation maybe related with the girder geometry. As mentioned previously, the flanges change considerably the resisting mechanism. By neglecting the flange, the Foster et al.'s model underestimates more significantly the shear resistance of T-shape girder with thick flange tested.

5.5 Conclusions

This chapter presented an in-depth analysis of the shear behaviour of high-performance fibre-reinforced concrete (HPFRC) girders through the utilisation of digital image correlation (DIC) measurements and nonlinear finite element (FE) models. The methodology combined experimental kinematic data with theoretical and numerical models to separate the total shear resistance into its individual mechanisms: fibre tensile contribution, aggregate interlock contribution, compression chord contribution, and dowel action. Missing data from non-captured crack regions were reconstructed using physically consistent assumptions, while the finite element model provided complementary insight into the stress distribution within the compression zone. The adopted hybrid experimental–numerical methodology enabled a highly detailed and accurate interpretation of the internal shear transfer processes, showing strong agreement with experimental resistance. The main findings can be summarized as follows:

The decomposition of the shear resistance into individual mechanisms shows that the proposed methodology reproduces the experimental shear capacity with high accuracy. The ratio between experimental and calculated shear resistance $V_{\text{exp}}/V_{\text{calc}}$ exceeded 85% for all girders, reaching 95% for girder G4, 92% for girder G3, and 85% for girder G2, confirming that the main shear-resisting mechanisms were correctly captured despite limited DIC coverage in some regions.

In terms of relative contributions, fibre tensile resistance was the dominant mechanism in the rectangular non-prestressed girder G4, accounting for 61 % of the total shear resistance, while aggregate interlock and compression chord contributed 16 % and 23 %, respectively. For the non-prestressed T-shaped girder G3, the presence of flanges significantly increased the compression chord contribution, which became the governing mechanism at 44 %, followed by fibre tensile resistance at 33 % and aggregate interlock at 23 %. For the prestressed T-shaped girder, the fibre tensile resistance was the dominant mechanism at 44 %, followed closely by the compression chord one at 39 % and the aggregate interlock at 18 %.

Overall, aggregate interlock remained the least significant mechanism in all tested configurations, consistently contributing less than 25% of the total shear resistance, mainly due to large crack openings and flat crack angles at failure. These quantitative results demonstrate that shear resistance in HPFRC girders without stirrups is governed primarily by fibre tensile resistance and compression chord action, with their relative importance strongly influenced by girder geometry and prestressing.

The comparison between experimental, advances analysis and code-based predictions highlighted substantial discrepancies. The CSA-S6 standard including the Foster et al.'s model for shear capacity of FRC components systematically underestimated the total shear resistance by 40-60%, whereas the advanced analytical approach yielded deviations below 15% relative to experimental values. This clearly indicates that the CSA-S6 standard equations do not fully account for the combined effects of fibre reinforcement, prestressing and complex geometries.

Considering the observed discrepancies, it is recommended that future shear resistance model adopt separate analytical expressions for each shear-resisting mechanism, instead of relying on a single empirical formulation. Distinct equations for fibre tensile resistance, aggregate interlock, compression chord, and dowel action would provide a more rational and physically representative basis for predicting shear behaviour in HPFRC elements. However, to support the implementation of such equations, further experimental campaigns involving detailed analysis of each mechanism are required. These campaigns should explore a broader range of fibre contents, prestressing levels, and geometries to ensure the generality and reliability of the proposed formulations.

In summary, the hybrid methodology developed in this chapter, combining experimental data, DIC and FE analysis, was effective to accurately identify and quantify the individual shear-resisting mechanisms in HPFRC girders. The results not only confirm the dominant role of the fibre tensile contribution and compression chord in the total shear resistance but also reveal the limitations of current design equations in the CSA-S6 standard. Incorporating mechanism-based equations into future code provisions would allow for more accurate and optimized designs of HPFRC structural members, contributing to more efficient and durable infrastructure solutions.

CHAPTER 6 CONCLUSIONS AND RECOMMENDATIONS

The research project focused on developing a prestressed girder made of HPFRC with reduced height and integrated slab for short-span bridges. The girder was designed and then validated experimentally. A set of techniques was developed to understand how the shear resisting mechanisms behaved. This chapter will first review the project objectives and then summarize the main conclusions. Finally, recommendations will be made for future research.

6.1 Recall of objectives

The general objective of this study is to finalize the design of a prestressed bridge girder made of high-performance fibre-reinforced concrete (HPFRC) with an integrated slab for integration in urban bridges of City of Montreal, as well as to evaluate the resistance mechanisms involved in the shear behaviour of HPFRC girders. The specific objectives were:

- Optimize and validate the design of a prestressed bridge girder in HPFRC.
- Evaluate in laboratory the impact of the prestress, the shear span and the girder shape on the shear resistance of HPFRC girders.
- Evaluate different shear resisting mechanisms in HPFRC girder.
- Provide recommendations to improve shear strength evaluation of design codes for HPFRC girders.

6.2 Conclusions

6.2.1 Girder design

The prestressed HPFRC bridge girder developed includes an integrated slab and has a low height to reduce the global height of bridge deck and increase clearance under bridges in urban areas. The use of partial prestressing with high strength reinforcing bars provides sufficient longitudinal flexural strength, while limiting the risk of cracking at top and lower surface and thus the risk of strand corrosion. The arrangement of the stirrups is simplified in comparison to conventional prestress girder. Finally, the durability of the beam should be excellent thanks to the good crack control provided by the HPFRC with 1%-vol. fibre dosage.

The geometry of the bridge girder illustrated in Figure 4.4 is presented below:

- The T-shape girder has a total heigh of 620 mm with an integrated slab of 1165 mm of width.
- The girder has a constant web width of 360 mm to allow 100 mm tendons spacing and facilitate flow of the HPFRC during the casting process.
- The layout of the tendons and longitudinal flexural reinforcement is made of nine tendons T15 and three 22 mm A1035 reinforcing bars distributed over four layers. The high strength rebars are located on the lower layer.
- The arrangement of the stirrups consists of one branch of a C-shaped 10M rebars spaced at 180 mm.

The proposed design for the 15-m HPFRC girders provide adequate bending and shear resistances at ultimate limit state and service limit state considering the CL-750 truck and according to the CSA-S6 code. The maximum bending resistance measured in laboratory on 6-m girders was 1940 kNm, while the factored design bending moment was 1695 kNm. The maximal crack opening at the service moment 924 kNm was measured at 0.07 mm, inferior to the 0.15 mm limit. The bending resistance of the 6-m HPFRC girder was well predicted with the AIS sectional analysis software.

Although the shear conditions differ between a 6-m girder of the experimental campaign and those expected for the 15 m bridge girder (a/d ratio, shear crack angle, etc.), the ultimate shear capacity (593 kN) of the 6-m girder without stirrups was superior to the factored design shear load of the 15-m girder (483 kN). Therefore, the prestressed T-shaped HPFRC girder without stirrup fulfilled requirement in shear, the girder with stirrups will easily surpass the requirement. The shear resistance of the 6-m HPFRC girder was significantly underestimated by the CSA-S6 code.

6.2.2 Shear resistance study

The experimental campaign carried out on HPFRC girders of different lengths, prestress level and cross-section allowed the comparison of actual shear strengths with the predicted values obtained with the CSA-S6 code. In general, the predicted shear strengths were overly underestimating experimental ones, corresponding around 34% to 51% of the actual shear strength.

This underestimation occurs mainly because the V_c component on the code for FRC beams was fitted with experimental data from ordinary concrete and not updated to take into consideration the effects that fibres have on the crack kinematics. The addition of steel fibres, along with the use of prestressing and optimized T-shaped geometries, fundamentally modifies the internal shear transfer mechanisms of concrete. As a result, existing empirical or semi-empirical models, fitted with ordinary concrete experimental data, fail to accurately predict the complex behaviour of HPFRC girders under shear loading.

The experimental campaign carried out on HPFRC girders of different lengths, prestress level and cross-section, combined with advanced Digital Image Correlation (DIC) and Finite Element (FE) analysis, allowed evaluation of three shear resistance mechanisms: fibre tensile contribution, aggregate interlock, and compression chord effect. Based on this analysis, it was possible to predict the actual shear resistance of HPFRC girders with an error lower than 10%. This accuracy has validated the reliability of the developed computational and experimental methodologies, allowing comparison of each shear resistance mechanism.

The compression chord (23% to 44% of the total resistance) and fibre contribution (33% to 61%) were the most dominant contributors of the total shear strength of HPFRC girders, while the aggregate interlock played a relatively minor role, contributing less than 20 %.

The study on shear mechanism also emphasized that the inclusion of prestress, the geometry of the girder (especially the presence of flanges), and variations in the shear span all significantly affected the internal shear transfer. Prestressing enhances the compression zone, which increases the contribution of the compression chord to the overall shear resistance, a mechanism largely absent from most current code formulations. Similarly, the presence of a T-shaped flange modifies the crack angle and width, further modifying the relative tensile contribution of fibres and aggregate interlock. These observations underline the inadequacy of considering the concrete contribution to shear as a single term, as done in most existing codes.

In conclusion, the study confirms that the shear resistance of HPFRC girders depends on several important factors such as the fibre content, prestressing level, geometry, and shear span. The combination of computational and experimental methodologies showed a strong correlation, over 90 %, between predicted and observed behaviour, establishing a reliable framework for future design optimization. The current standards, while ensuring safety, are overly conservative and fail to exploit the full structural potential of HPFRC. Consequently, this research recommends the recalibration of shear resistance formulations to explicitly include the effects of fibre orientation, crack angle and width variation, and compression chord contribution, particularly for prestressed and T-shaped HPFRC girders.

6.3 Recommendations

The thesis demonstrated large discrepancies between CSA-S6 code predictions and experimental shear resistance of prestress HPFRC girders. Two main reasons were suggested for the discrepancy observed between code predictions and experimental results. The first one was that the code does not consider the effect of geometry on the shear resistance (the compression chord contribution), and the second one was that the code underestimate significantly the contribution of fibres into the shear design provisions.

Future experimental studies should be carried out to define the flanges influence on the shear crack kinematics (crack angle, crack opening and crack slip). For such effect, complete DIC data must be acquired from the experimental campaign. Different sets of cameras should be installed to obtained DIC measurement both on vertical and inclined surfaces of girders studied.

As it was pointed out, the actual shear provisions were set on FRC girders with a low content of fibres (< 0.5% on volume) and mainly on rectangular beams and I-beams with thin flange. It is suggested to complete new experimental campaigns on FRC girders with higher fibre content having I or T-shapes with thick flanges.

It was shown by Foster (Foster et al., 2018) that shear resistance of FRC with lower longitudinal strains at failure ($\varepsilon_x \leq 500$ x10-6) are underestimated more significantly. It is thus proposed to carry out experiments on FRC girders with small tensile strains providing detailed information on crack kinematics to better calibrated code provisions.

By systematically quantifying each shear mechanism, the thesis demonstrates that the mechanical response of HPFRC girders cannot be reliably captured through present analytical equations regrouping effects of few mechanisms. Based on experimental findings, it seems preferable to develop an equation for each shear mechanism contribution to better reflect actual stress transfer behaviour within HPFRC girders.

REFERENCES

[1] A. S. Bah *et al.*, "Assessing the condition state of a concrete bridge combining visual inspection and nonlinear deterioration model," *Structure and Infrastructure Engineering*, vol. 20, no. 2, pp. 149–164, 2024, doi: 10.1080/15732479.2022.2081987.

[2] S. Verger Leboeuf, "développement de joints de connexion en bfup pour des dalles de pont préfabriquées," Master, Polytechnique, Montreal, 2016.

[3] B. Marleau, "Comportement à la fatigue de joints en béton fibré à ultra-hautes performances entre dalles préfabriquées de ponts," Master, Polytechnique Montreal, Montreal, 2017.

[4] B. Massicotte, A. Nour, L. Faggio, and N. Cordoni, "Design and construction of SFRC bridge decks – Building on past experience and recent developments.," in *FRC 2014 Joint ACI-fib International Workshop Fibre Reinforced Concrete: from Design to Structural Applications*, Montreal: fib, 2014.

[5] Cordoni Nicola, " Design of Precast and Prestressed Steel Fibre Reinforced Concrete T-Girders," Master, Polytehcnique Montreal, Montreal, 2015.

[6] Rachello Adrien, "Développement d'une poutre de pont précontrainte en béton renforcé de fibres avec dalle intégrée," Master, Polytechnique Montreal, Montreal, 2023.

[7] P. Zhang, S. Han, S. Ng, and X. H. Wang, "Fiber-Reinforced Concrete with Application in Civil Engineering," 2018, *Hindawi Limited*. doi: 10.1155/2018/1698905.

[8] A. E. Naaman, "Fiber reinforced concrete: five decades of progress," ABEC Publicacoes, Jul. 2018, pp. 35–56. doi: 10.21452/bccm4.2018.02.01.

[9] J. C. Walraven, "High performance fiber reinforced concrete: Progress in knowledge and design codes," in *Materials and Structures/Materiaux et Constructions*, Nov. 2009, pp. 1247–1260. doi: 10.1617/s11527-009-9538-3.

[10] V. Afroughsabet, L. Biolzi, and T. Ozbakkaloglu, "High-performance fiber-reinforced concrete: a review," Jul. 01, 2016, *Springer New York LLC*. doi: 10.1007/s10853-016-9917-4.

[11] J.-P. Charron and C. Desmettre, “Intérêt de l’utilisation des bétons renforcés de fibres pour la construction d’ouvrages d’art durables.,” École Polytechnique de Montréal, Montreal, 2013.

[12] S. C. Paul, G. P. A. G. van Zijl, and B. Šavija, “Effect of fibers on durability of concrete: A practical review,” Oct. 02, 2020, *MDPI AG*. doi: 10.3390/ma13204562.

[13] H. Z. Hassan and N. M. Saeed, “Fiber reinforced concrete: a state of the art,” Dec. 01, 2024, *Discover*. doi: 10.1007/s43939-024-00171-w.

[14] T. M. Pham, “Fibre-reinforced concrete: State-of-the-art-review on bridging mechanism, mechanical properties, durability, and eco-economic analysis,” *Case Studies in Construction Materials*, vol. 22, Jul. 2025, doi: 10.1016/j.cscm.2025.e04574.

[15] Ş. Yazici, G. Inan, and V. Tabak, “Effect of aspect ratio and volume fraction of steel fiber on the mechanical properties of SFRC,” *Constr. Build. Mater.*, vol. 21, no. 6, pp. 1250–1253, Jun. 2007, doi: 10.1016/j.conbuildmat.2006.05.025.

[16] S. C. Lee, J. H. Oh, and J. Y. Cho, “Compressive behavior of fiber-reinforced concrete with end-hooked steel fibers,” *Materials*, vol. 8, no. 4, pp. 1442–1458, 2015, doi: 10.3390/ma8041442.

[17] I. LÖFGREN, “Fibre-reinforced Concrete for Industrial Construction - a fracture mechanics approach to material testing and structural analysis,” DOCTOR OF PHILOSOPHY, Sweden, Göteborg, 2005.

[18] J.-P. Charron, clelia Desmettre, and C. Androuët, “Utilisation de béton renforcé de fibres (BRF) pour les glissières en béton pour chantier (GBC),” Montreal, Jan. 2016.

[19] S. Aidarov, A. Nogales, N. Tošić, and A. de la Fuente, “Influence of fiber orientation on flexural-based design of steel fiber-reinforced concrete slabs: Experimental and numerical program,” *Structural Concrete*, vol. 25, no. 2, pp. 956–972, Apr. 2024, doi: 10.1002/suco.202300754.

[20] T. Plagué, C. Desmettre, and J. P. Charron, “Influence of fiber type and fiber orientation on cracking and permeability of reinforced concrete under tensile loading,” *Cem. Concr. Res.*, vol. 94, pp. 59–70, Apr. 2017, doi: 10.1016/j.cemconres.2017.01.004.

[21] P. B. Sakthivel and S. Vijay Aravind, “Flexural strength and toughness of steel fiber reinforced concrete beams,” *Asian Journal of Civil Engineering*, vol. 21, no. 8, pp. 1309–1330, Dec. 2020, doi: 10.1007/s42107-020-00279-3.

[22] M. N. Soutsos, T. T. Le, and A. P. Lampropoulos, “Flexural performance of fibre reinforced concrete made with steel and synthetic fibres,” *Constr. Build. Mater.*, vol. 36, pp. 704–710, Nov. 2012, doi: 10.1016/j.conbuildmat.2012.06.042.

[23] D. Y. Yoo, Y. S. Yoon, and N. Banthia, “Flexural response of steel-fiber-reinforced concrete beams: Effects of strength, fiber content, and strain-rate,” *Cem. Concr. Compos.*, vol. 64, pp. 84–92, Nov. 2015, doi: 10.1016/j.cemconcomp.2015.10.001.

[24] H. C. Mertol, E. Baran, and H. J. Bello, “Flexural behavior of lightly and heavily reinforced steel fiber concrete beams,” *Constr. Build. Mater.*, vol. 98, pp. 185–193, Nov. 2015, doi: 10.1016/j.conbuildmat.2015.08.032.

[25] J. A. Torres and E. O. L. Lantsoght, “Influence of fiber content on shear capacity of steel fiber-reinforced concrete beams,” *Fibers*, vol. 7, no. 12, 2019, doi: 10.3390/fib7120102.

[26] H. S. Merdas and M. A. Shallal, “Efficiency of Steel Fibers in Improving the Performance of Concrete Beams without Shear Reinforcement,” *Salud, Ciencia y Tecnologia - Serie de Conferencias*, vol. 3, Mar. 2024, doi: 10.56294/sctconf2024830.

[27] A. N. Dancygier and Z. Savir, “Effects of Steel Fibers on Shear Behavior of High-Strength Reinforced Concrete Beams,” *Advances in Structural Engineering*, vol. 14, no. 5, pp. 745–761, Oct. 2011, doi: 10.1260/1369-4332.14.5.745.

[28] W. Xue, X. Liu, W. Jing, Z. Yao, C. Gao, and H. Li, “Experimental study and mechanism analysis of permeability sensitivity of mechanically damaged concrete to confining pressure,” *Cem. Concr. Res.*, vol. 134, Aug. 2020, doi: 10.1016/j.cemconres.2020.106073.

[29] Desmettre. clelia, “Contribution à l’étude de la perméabilité du béton armé sous sollicitations statiques et cycliques,” Doctor of Philosophy, Polytechnique Montreal, Montreal, 2011.

[30] Frank J. Vecchio and Michael P. Collins, “The Modified Compression-Field Theory for Reinforced Concrete Elements Subjected to Shear,” *ACI*, Mar. 1986.

[31] L. A. Montoya-Coronado, C. Ribas, J. G. Ruiz-Pinilla, and A. Cladera, "Time-history analysis of aggregate interlock in reinforced concrete beams without stirrups," *Eng. Struct.*, vol. 283, May 2023, doi: 10.1016/j.engstruct.2023.115912.

[32] R. C. Fenwick and T. Paulay, "MECHANISMS OF SHEAR RESISTANCE OF CONCRETE BEAMS," 1968.

[33] Gambarova, "A new approach to the analysis of the confinement role in regularly cracked concrete elements.," 1981.

[34] J. C. Walraven, "Fundamental Analysis Of Aggregate Interlock," 1981.

[35] Surendra P., Shah, and C. Babendreier, *High Strength Concrete - Proceedings of a Workshop Held at the University of Illinois at Chicago Circle*. 1979.

[36] TAYLOR H. P. J., "Investigation Of The Forces Carried Across Cracks In Reinforced Concrete Beams In Shear By Interlock Of Aggregate," *Transport and Road Research Laboratory (TRRL)*, 1970.

[37] P. S. Chana, "Investigation of the mechanism of shear failure of reinforced concrete beams," *Magazine of Concrete Research*, vol. 39, no. 141, pp. 196–204, Dec. 1987, doi: 10.1680/macr.1987.39.141.196.

[38] P. Huber, T. Huber, and J. Kollegger, "Investigation of the shear behavior of RC beams on the basis of measured crack kinematics," *Eng. Struct.*, vol. 113, pp. 41–58, Apr. 2016, doi: 10.1016/j.engstruct.2016.01.025.

[39] J. Košćak, D. Damjanović, M. Bartolac, and I. Duvnjak, "Shear behavior of RC beams without transverse reinforcement: An analysis of crack kinematics and transfer mechanisms based on stereophotogrammetric measurements," *Eng. Struct.*, vol. 255, Mar. 2022, doi: 10.1016/j.engstruct.2022.113886.

[40] F. Autrup, H. B. Jørgensen, M. F. Ruiz, and L. C. Hoang, "Mechanical modelling of dowel action and the influence of small amounts of shear reinforcement on the shear-transfer actions in RC beams," *Structural Concrete*, vol. 24, no. 5, pp. 5928–5946, Oct. 2023, doi: 10.1002/suco.202300082.

[41] E. N. Vintzēleou and T. P. Tassios, “Mathematical models for dowel action under monotonic and cyclic conditions,” *Magazine of Concrete Research*, vol. 38, no. 134, pp. 13–22, Mar. 1986, doi: 10.1680/macr.1986.38.134.13.

[42] E. O. L. Lantsoght, “How do steel fibers improve the shear capacity of reinforced concrete beams without stirrups?,” Oct. 15, 2019, *Elsevier Ltd*. doi: 10.1016/j.compositesb.2019.107079.

[43] G. N. J. Kani, “The Riddle of Shear Failure and its Solution,” *ACI Journal Proceedings*, vol. 61, no. 4, 1964, doi: 10.14359/7791.

[44] M. W. T. Mak and J. M. Lees, “Arch action in reinforced concrete subjected to shear,” *Eng. Struct.*, vol. 274, Jan. 2023, doi: 10.1016/j.engstruct.2022.115096.

[45] M. D. Kotsovos, “Mechanisms of ‘shear’ failure,” *Magazine of Concrete Research*, vol. 35, no. 123, pp. 99–106, Jun. 1983, doi: 10.1680/macr.1983.35.123.99.

[46] C. R. Ribas González and M. Fernández Ruiz, “Influence of flanges on the shear-carrying capacity of reinforced concrete beams without web reinforcement,” *Structural Concrete*, vol. 18, no. 5, pp. 720–732, Oct. 2017, doi: 10.1002/suco.201600172.

[47] A. Cladera, A. Marí, C. Ribas, J. Bairán, and E. Oller, “Predicting the shear-flexural strength of slender reinforced concrete T and I shaped beams,” *Eng. Struct.*, vol. 101, pp. 386–398, Oct. 2015, doi: 10.1016/j.engstruct.2015.07.025.

[48] A. Ayensa, E. Oller, B. Beltrán, E. Ibarz, A. Marí, and L. Gracia, “Influence of the flanges width and thickness on the shear strength of reinforced concrete beams with T-shaped cross section,” *Eng. Struct.*, vol. 188, pp. 506–518, Jun. 2019, doi: 10.1016/j.engstruct.2019.03.057.

[49] S. Campana, M. F. Ruiz, A. Anastasi, and A. Muttoni, “Analysis of shear-transfer actions on one-way RC members based on measured cracking pattern and failure kinematics,” *Magazine of Concrete Research*, vol. 65, no. 6, pp. 386–404, Mar. 2013, doi: 10.1680/macr.12.00142.

[50] M. Fernández Ruiz, A. Muttoni, and J. Sagaseta, “Shear strength of concrete members without transverse reinforcement: A mechanical approach to consistently account for size and strain effects,” *Eng. Struct.*, vol. 99, pp. 360–372, 2015, doi: 10.1016/j.engstruct.2015.05.007.

[51] F. Cavagnis, M. Fernández Ruiz, and A. Muttoni, “An analysis of the shear-transfer actions in reinforced concrete members without transverse reinforcement based on refined experimental

measurements," *Structural Concrete*, vol. 19, no. 1, pp. 49–64, Feb. 2018, doi: 10.1002/suco.201700145.

[52] R. Ruiz, M. Fernández Ruiz, L. Todisco, and H. Corres, "Shear resistance of prestressed HPFRC beams without stirrups: A mechanical analysis of shear-transfer actions based on detailed experimental measurements," *Eng. Struct.*, vol. 306, May 2024, doi: 10.1016/j.engstruct.2024.117711.

[53] Michael P. Collins, Denis Mitchell, Perry Adebar, and Frank J. Vecchio, "A General Shear Design Method," *ACI Struct. J.*, Jan. 1996.

[54] Evan C. Bentz, Frank J. Vecchio, and Michael P. Collins, "Simplified Modified Compression Field Theory for calculating Shear Strength of Reinforced Concrete Elements," 2006.

[55] CSA, "CSA A23.3. Design of concrete structures. ," 2019.

[56] V. Sigrist, E. Bentz, M. F. Ruiz, S. Foster, and A. Muttoni, "Background to the fib Model Code 2010 shear provisions - Part I: Beams and slabs," *Structural Concrete*, vol. 14, no. 3, pp. 195–203, 2013, doi: 10.1002/suco.201200066.

[57] fédération internationale du béton, Ed., *fib Model Code for concrete structures*. Lausanne: Ernst & Sohn, a Wiley brand, 2013.

[58] CEN, "Eurocode 2: Design of concrete structures-Part 1-1: general rules for buildings (EN 1992-1-1).," 2010, *European Committee for Standardization, Brussels*.

[59] P. F. Miguel, M. A. Fernández, J. Hegger, and M. Schmidt, "Shear Resistance of Members Without Shear Reinforcement in Presence of Axial Forces in the Next Eurocode 2," *Hormigón y Acero*, Jan. 2023, doi: 10.33586/hya.2023.3112.

[60] O. B. Olalusi and C. Viljoen, "Assessment of simplified and advanced models for shear resistance prediction of stirrup-reinforced concrete beams," *Eng. Struct.*, vol. 186, pp. 96–109, May 2019, doi: 10.1016/j.engstruct.2019.01.130.

[61] D. D. L. Araújo, F. G. T. Nunes, R. D. Toledo Filho, and M. A. S. de Andrade, "Shear strength of steel fiber-reinforced concrete beams," *Acta Scientiarum. Technology*, vol. 36, no. 3, p. 389, Feb. 2014, doi: 10.4025/actascitechnol.v36i3.19005.

[62] Sharma, “Shear Strength of Steel Fiber Reinforced Concrete Beams,” *ACI Journal Proceedings*, vol. 83, no. 4, 1986, doi: 10.14359/10559.

[63] R. Narayam Swamy, “Influence of Steel fibers on the Shear Resistance of Lightweight Concrete I-Beams,” *ACI Struct. J.*, vol. 90, no. 1, 1993, doi: 10.14359/4201.

[64] E. Slater, M. Moni, and M. S. Alam, “Predicting the shear strength of steel fiber reinforced concrete beams,” *Constr. Build. Mater.*, vol. 26, no. 1, pp. 423–436, Jan. 2012, doi: 10.1016/j.conbuildmat.2011.06.042.

[65] B. Singh Negi and K. Jain, “Shear resistant mechanisms in steel fiber reinforced concrete beams: An analytical investigation,” *Structures*, vol. 39, pp. 607–619, May 2022, doi: 10.1016/j.istruc.2022.03.061.

[66] A. B. Sturm, P. Visintin, and D. J. Oehlers, “Mechanics of Shear Failure in Fiber-Reinforced Concrete Beams,” *Journal of Structural Engineering*, vol. 147, no. 3, Mar. 2021, doi: 10.1061/(ASCE)ST.1943-541X.0002934.

[67] N. Gehri, J. Mata-Falcón, and W. Kaufmann, “Cracked Membrane Model for Strain-Softening Fiber-Reinforced Concrete,” *Journal of Structural Engineering*, vol. 151, no. 1, Jan. 2025, doi: 10.1061/JSENDH.STENG-13524.

[68] D. R. Sahoo and A. Sharma, “Effect of Steel Fiber Content on Behavior of Concrete Beams with and without Stirrups,” *ACI Struct. J.*, vol. 111, no. 5, Sep. 2014, doi: 10.14359/51686821.

[69] W. Kaufmann, A. Amin, A. Beck, and M. Lee, “Shear transfer across cracks in steel fibre reinforced concrete,” *Eng. Struct.*, vol. 186, pp. 508–524, May 2019, doi: 10.1016/j.engstruct.2019.02.027.

[70] A. Marì Bernat, N. Spinella, A. Recupero, and A. Cladera, “Mechanical model for the shear strength of steel fiber reinforced concrete (SFRC) beams without stirrups,” *Materials and Structures/Materiaux et Constructions*, vol. 53, no. 2, Apr. 2020, doi: 10.1617/s11527-020-01461-4.

[71] E. O. L. Lantsoght, “How do steel fibers improve the shear capacity of reinforced concrete beams without stirrups?,” Oct. 15, 2019, *Elsevier Ltd*. doi: 10.1016/j.compositesb.2019.107079.

[72] R. Narayanan and I. Y. S. Darwish, "Use of Steel Fibers as Shear Reinforcement," *ACI Struct. J.*, vol. 84, no. 3, 1987, doi: 10.14359/2654.

[73] H. H. Dinh, G. J. Parra-Montesinos, and J. K. Wight, "Shear Strength Model for Steel Fiber Reinforced Concrete Beams without Stirrup Reinforcement," *Journal of Structural Engineering*, vol. 137, no. 10, pp. 1039–1051, Oct. 2011, doi: 10.1061/(asce)st.1943-541x.0000362.

[74] K. Marar, Ö. Eren, and H. Roughani, "The influence of amount and aspect ratio of fibers on shear behaviour of steel fiber reinforced concrete," *KSCE Journal of Civil Engineering*, vol. 21, no. 4, pp. 1393–1399, May 2017, doi: 10.1007/s12205-016-0787-2.

[75] S. J. Foster, A. Agarwal, and A. Amin, "Design of steel fiber reinforced concrete beams for shear using inverse analysis for determination of residual tensile strength," *Structural Concrete*, vol. 19, no. 1, pp. 129–140, Feb. 2018, doi: 10.1002/suco.201700100.

[76] E. Cuenca, "On Shear Behavior of Structural Elements Made of Steel Fiber Reinforced Concrete," 2015. [Online]. Available: http://www.springer.com/series/8790

[77] W. Kaufmann, A. Amin, A. Beck, and M. Lee, "Shear transfer across cracks in steel fibre reinforced concrete," *Eng. Struct.*, vol. 186, pp. 508–524, May 2019, doi: 10.1016/j.engstruct.2019.02.027.

[78] R. Ruiz, L. O. Doniak, L. Todisco, and H. Corres, "Database of shear tests for prestressed fibre reinforced concrete beams without vertical stirrups and comparison with code provisions," *Structural Concrete*, vol. 24, no. 4, pp. 4565–4576, Aug. 2023, doi: 10.1002/suco.202201130.

[79] E. O. L. Lantsoght, "Database of shear experiments on steel fiber reinforced concrete beams without stirrups," *Materials*, vol. 12, no. 6, 2019, doi: 10.3390/ma12060917.

[80] E. O. L. Lantsoght, "Database of shear experiments on steel fiber reinforced concrete beams without stirrups," *Materials*, vol. 12, no. 6, Mar. 2019, doi: 10.3390/ma12060917.

[81] Canadian Standards Association, "Canadian Highway Bridge Design Code," Toronto, 2019.

[82] Ministère des Transports et de la Mobilité durable., "Manuel de conception de structure," Montréal, 2024.

[83] Correlated Solutions, "Vic-3D Testing Guide," version 7.

[84] F. Beaurivage, “Influence of structural parameters on FRC strain hardening,” Master, Polytechnique, Montreal, 2009.

[85] S. Delsol and J.-P. Charron, “Numerical modelling of UHPFRC mechanical behavior based on fiber orientation,” Jan. 2013.

[86] G. Ruocci *et al.*, “Digital Image Correlation and Noise-filtering Approach for the Cracking Assessment of Massive Reinforced Concrete Structures,” *Strain*, vol. 52, no. 6, pp. 503–521, Dec. 2016, doi: 10.1111/str.12192.

[87] N. Gehri, J. Mata-Falcón, and W. Kaufmann, “Automated crack detection and measurement based on digital image correlation,” *Constr. Build. Mater.*, vol. 256, Sep. 2020, doi: 10.1016/j.conbuildmat.2020.119383.

[88] S. Campana, M. F. Ruiz, A. Anastasi, and A. Muttoni, “Analysis of shear-transfer actions on one-way RC members based on measured cracking pattern and failure kinematics,” *Magazine of Concrete Research*, vol. 65, no. 6, pp. 386–404, Mar. 2013, doi: 10.1680/macr.12.00142.

[89] Correlated Solutions, *VIC-3D - Reference Manual*, Version 7. Columbia, 2021.

[90] B. Massicotte and M. Ben Ftima, “EPM3D-v3 – A user-supplied constitutive model for the nonlinear finite element analysis of concrete structures,” Montreal, Aug. 2017.

[91] F. Cavagnis, M. Fernández Ruiz, and A. Muttoni, “An analysis of the shear-transfer actions in reinforced concrete members without transverse reinforcement based on refined experimental measurements,” *Structural Concrete*, vol. 19, no. 1, pp. 49–64, Feb. 2018, doi: 10.1002/suco.201700145.

[92] E. Wilson, *Three-Dimensional Static and Dynamic Analysis of Structures.* California: Computers and Structures, Inc, 2005.

APPENDIX A DESIGN CALCULATIONS

A.1 SAP2000 input values

Details of the bridge with 8 girders wide are given in Figure A. 1. The other bridges analysed in this research project used the same input values as the ones shown in this section.

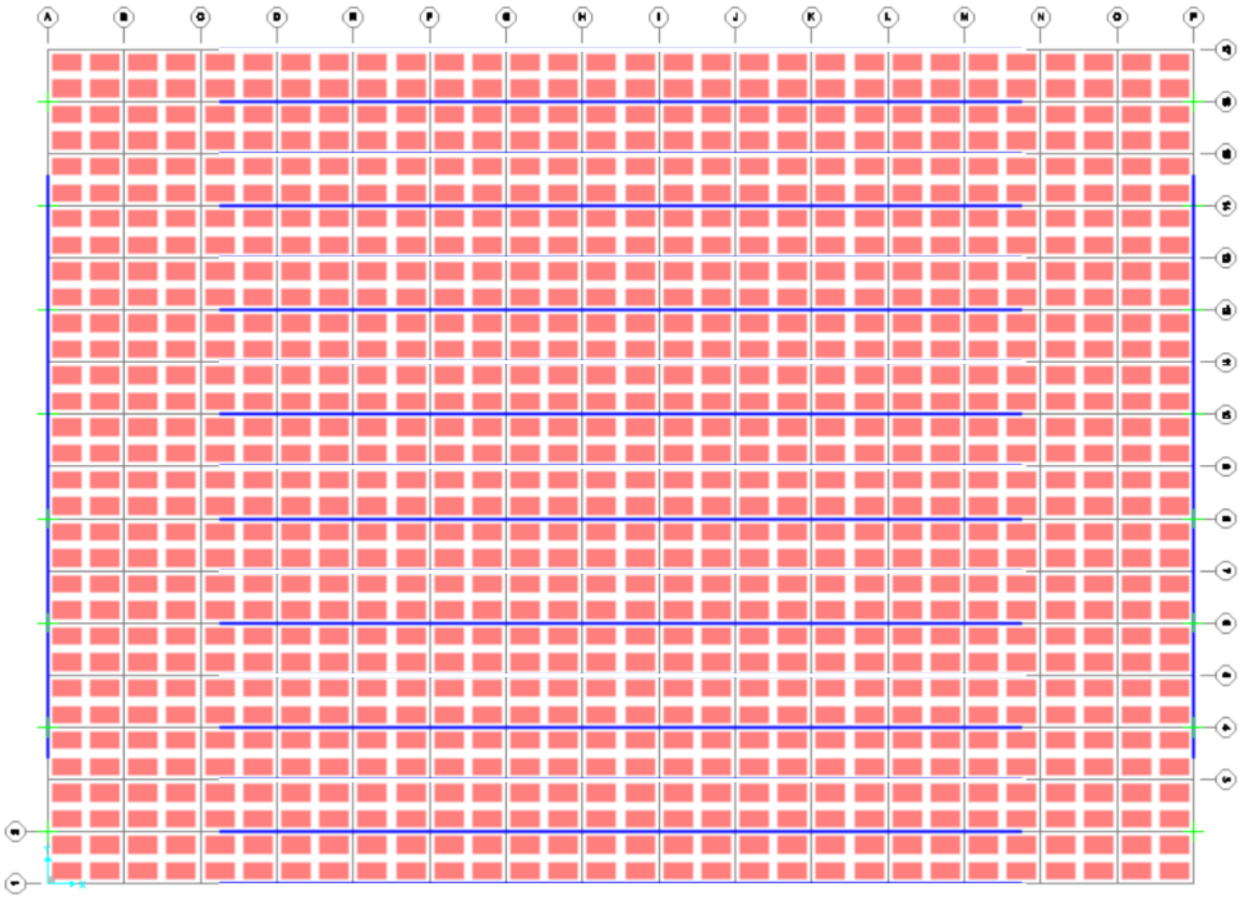

Figure A. 1 - SAP2000 numerical model. Lines in blue represent frame objects and squares in red represent shell elements.

The girder geometrical properties are presented in Figure A. 2. And are illustrated in Figure A. 1, by the longitudinal blue lines.

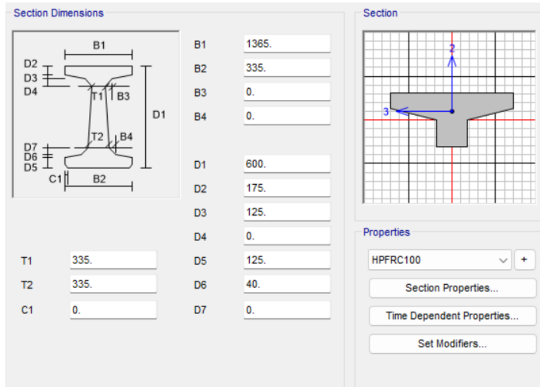

Figure A. 2 - Girder geometrical properties

As it is possible to see in Figure A. 3, besides the longitudinal beams used, transversal beams were also used to simulate the bridge diaphragms. The size of the diaphragms was determined according to MTQ recommendations and are presented bellow.

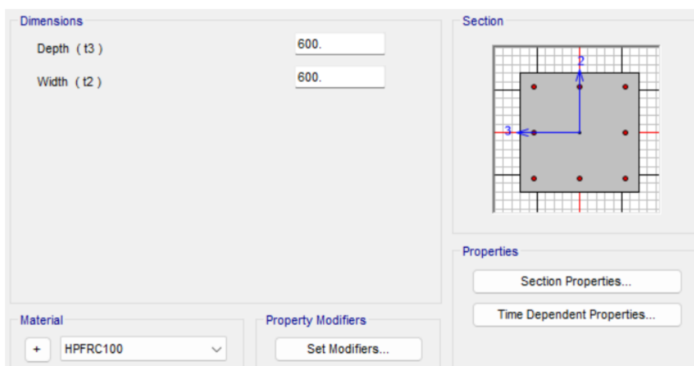

Figure A. 3 – Geometrical constraints of bridge diaphragms

The decision for analysing the bridge with shell elements and frame objects was taken so that not only the bending moments of the girders were analysed but also the transversal bending moments of the slabs. This methodology shortened the time necessary for the analysis.

The use of this methodology however required the modification of the properties of the longitudinal frame object added (Girder elements). The parameter modified was the moment of inertia number 3 which is the moment of inertia linked to the longitudinal bending resistance. The reason to modify this moment of inertia is to not increase artificially the rigidity of the structure.

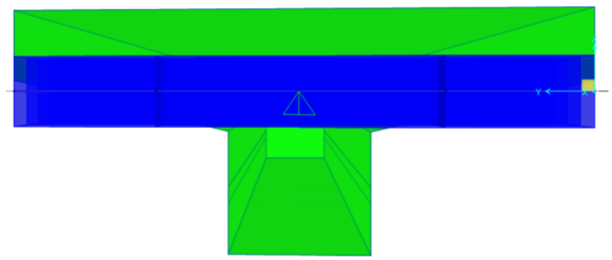

Figure A. 4 - Extruded elements extracted from SAP2000

As it is possible to see in Figure A. 4, the shell element and the frame object share the same nodes where the shell element crosses the frame object. If a modifier is not applied to the frame object, the total rigidity of the system will be equal to the rigidity of the girder plus the rigidity of the slab, which is something not wanted. So, the moment of inertia of the slab, with the coordinate system located at the center of gravity of the slab, was removed from the total moment of inertia of the beam.

Another modifier was used to account for the correct shear distribution between the elements. Not adding such modifiers would in theory increase the shear resisted by the web of the girder and decrease the shear resisted by the slabs.(Wilson, 2005) So, the area of the slab was removed from the total area of the frame object. The modifiers used are presented below in Figure A. 5.

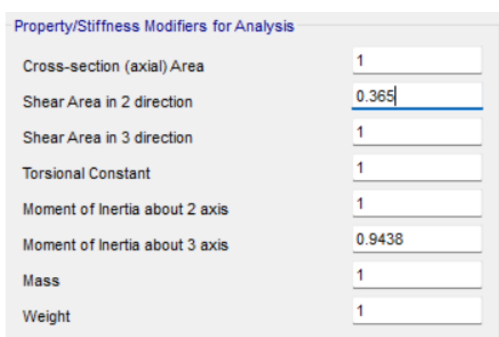

Figure A. 5– Modifiers applied to SAP2000 model

The concrete properties used at the analysis are presented below in Figure A. 5.

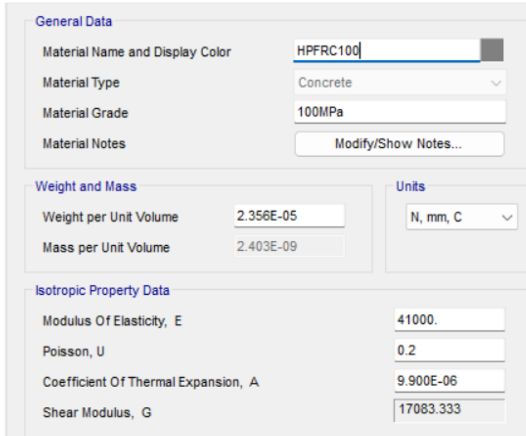

Figure A. 6 - HPFRC properties used at the SAP2000 model

A.2 AIS input information

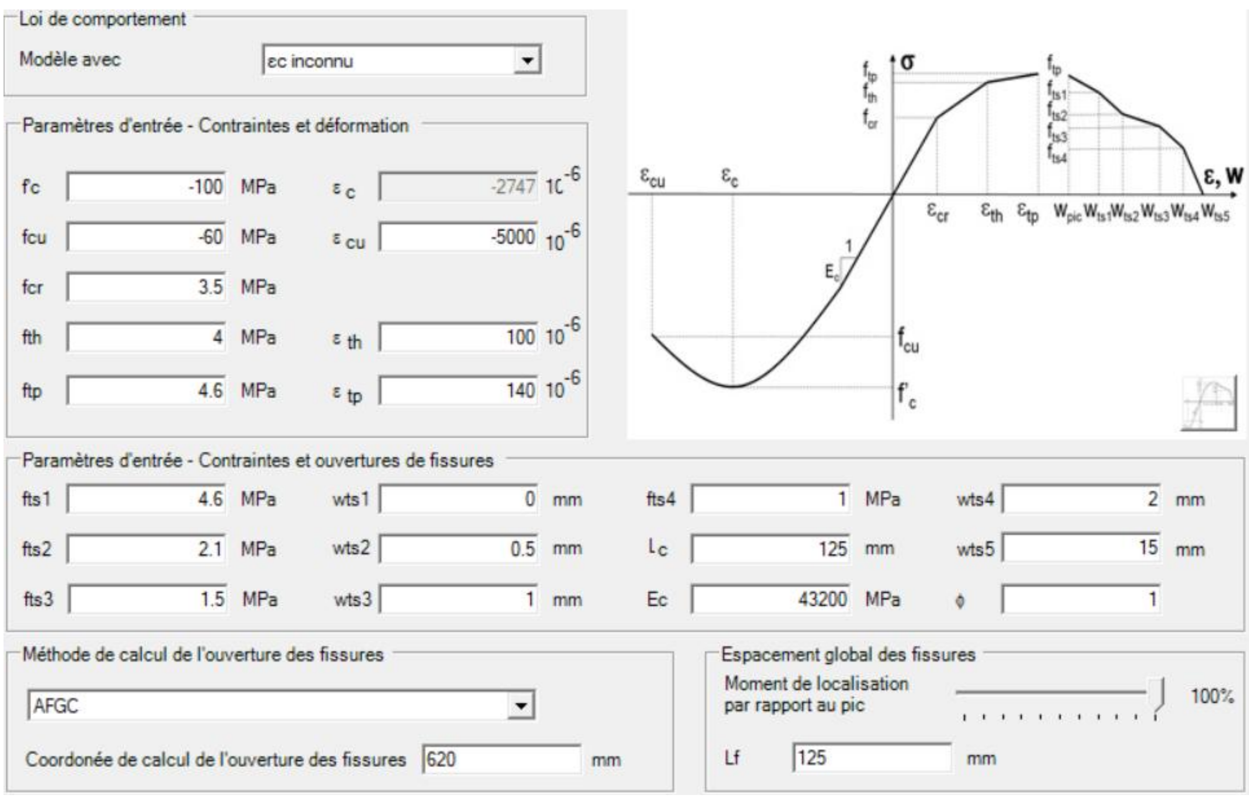

Figure A. 7 - HPFRC properties used at the AIS model

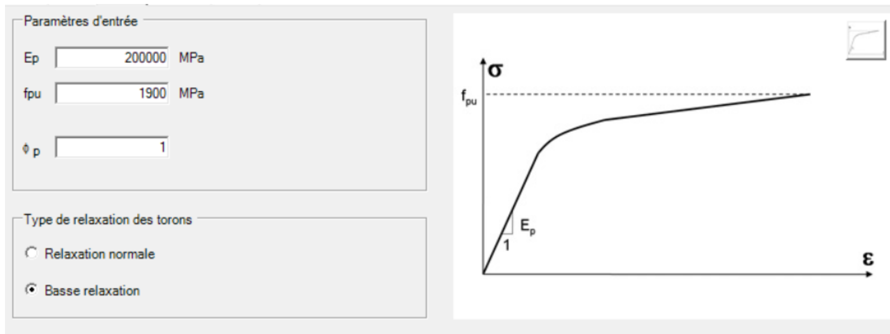

Figure A. 8 - Tendon properties used at the AIS model

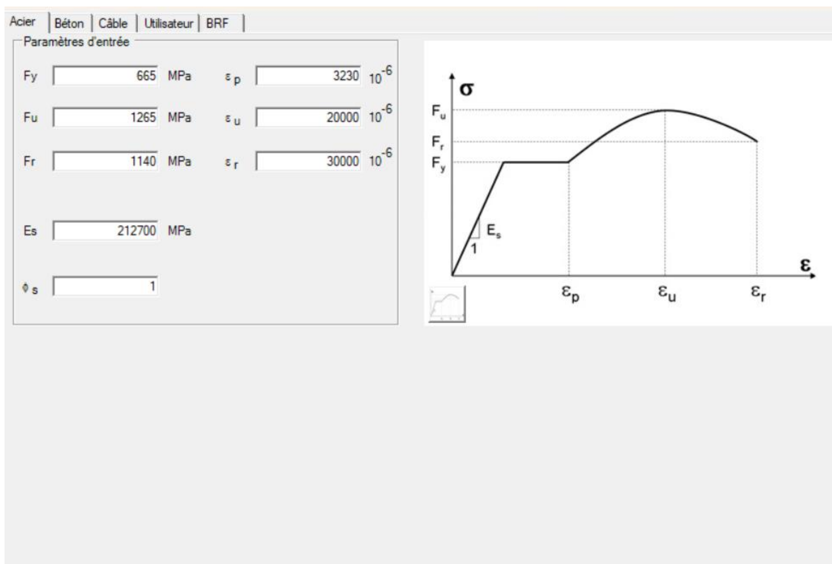

Figure A. 9– High strength reinforcement properties used at the AIS model

Table A. 1 – A400W rebar table values

A400W	
Strain (%)	Stress (Mpa)
0.00	0
0.18	418
1.65	425
5.00	535
17.00	573

Table A. 2 – A1035 rebar table values

A1035	
Strain (%)	Stress (Mpa)
0.00	0
0.42	830
0.70	946
1.70	1096
5.40	1148
7.00	1027

Table A. 3 – Tendon rebar table values

Tendon	
Strain (%)	Stress (Mpa)
0.00	0
0.79	1554
1.00	1776
1.20	1820
5.70	1924

APPENDIX B EXPERIMENTAL CALCULATIONS

B.1 Prestress design of G1

Table B. 1 – Geometric and material properties considered for the prestress design of G1

Geometric Information		
A	0.408	m2
I	0.010	m4
C.G	0.388	m
fck	100	MPa
fci	50	MPa
fcri	-2.83	MPa
h	0.60	m
Tension limit at transfer:	-1.41	MPa
Compression limit at transfer:	30	Mpa
Tension limit after prestress loss	-4.00	MPa
Compression limit after prestress loss	45	MPa

Table B. 2 - Material factors used

Material Factors:	
Tendons	0.95
Reinforcem	0.9
Concrete	0.75

Table B. 3– Tendon layout and prestress considered after long-term losses for G1.

y	Number of tendons per layer	Prestress (MPa)
57.5	0	0
107.5	3	1265
157.5	3	1265
207.5	3	1265
527.5	4	800

Table B. 4 – Stresses calculation at every section of G1 after long term losses

x		0	0.5	1	1.5	2	2.5	3
Self-weight	Bending (Top)	0.0	0.3	0.5	0.7	0.8	0.9	0.9
	Bending (Bottom)	0.0	-0.5	-0.9	-1.3	-1.5	-1.6	-1.7
Prestress	Pure compression	3.9	3.9	3.9	3.9	3.9	3.9	3.9
	Bending (Top)	-5.3	-5.3	-5.3	-5.3	-5.3	-5.3	-5.3
	Bending (Bottom)	9.8	9.8	9.8	9.8	9.8	9.8	9.8
Sum of stresses on Top		**-1.5**	-1.2	-1.0	-0.8	-0.7	-0.6	-0.6
Sum of stresses on Bottom		13.7	13.2	12.8	12.4	12.2	12.1	12.0

B.2 Prestress design of G2

Table B. 5 – Geometric and material properties considered for the prestress design of G2

Geometric Information		
A	0.408	m2
I	0.010	m4
C.G	0.388	m
fck	100	MPa
fci	50	MPa
fcri	-2.83	MPa
h	0.60	m
Tension limit at transfer:	-1.41	MPa
Compression limit at transfer:	30	Mpa
Tension limit after prestress loss	-4.00	MPa
Compression limit after prestress loss	45	MPa

Table B. 6 - Tendon layouts and prestress considered after long-term losses for G2.

y	Number of tendons per layer	Prestress (MPa)
57.5	0	0
107.5	3	909
157.5	3	909
207.5	3	909
527.5	4	405

Table B. 7 - Stresses calculation at every section of G2 after long term losses

x		0	0.5	1	1.5	2	2.5	3
Self-weight	Bending (Top)	0.0	0.3	0.5	0.7	0.8	0.9	0.9
	Bending (Bottom)	0.0	-0.5	-0.9	-1.3	-1.5	-1.6	-1.7
Prestress	Pure compression	3.5	3.5	3.5	3.5	3.5	3.5	3.5
	Bending (Top)	-4.8	-4.8	-4.8	-4.8	-4.8	-4.8	-4.8
	Bending (Bottom)	8.8	8.8	8.8	8.8	8.8	8.8	8.8
Sum of stresses on Top		-1.3	-1.0	-0.8	-0.6	-0.5	-0.4	-0.4
Sum of stresses on Bottom		12.3	11.8	11.4	11.1	10.8	10.7	10.6

B.3 Theoretical shear resistance

For the experimental program, 3 different shear designs were considered. The first one is for G1, the second one is for G2, and the last one is valid for G3 and G4.

B.3.1 - G1

G1 is the 6m, vertically reinforced girder, with full prestress. Since a bending failure was needed, stirrups were positioned inside the specimen. Below on Table B. 8 it is possible to see the variables used to calculate the shear resistance of the 6m specimen. And on Table B. 9 and Table B. 10 the expected shear resistance is calculated at each section of the specimen.

Table B. 8- Shear resistance variables for the design of a 6m specimen (G1).

dv	0.45	m
Es	200.0E+9	Pa
Ap	1.26E-03	m2
As	1.17E-03	m2
fpo	1.25E+09	Pa
sze	300.00	mm
fc	100	Mpa
bw	0.36	m
ϕfib	7.50E-01	-
ϕc	7.50E-01	-
γf	5.00E-01	-
ϕs	9.00E-01	-

Table B. 9 - Shear resistance mechanism components at each 0.5m of the girder (G1)

x	0	0.5	1	1.5	2	2.25	2.5	3
Moments (Nm)	000.00E+0	252.50E+3	505.00E+3	757.50E+3	1.01E+6	1.14E+6	1.26E+6	1.44E+6
Shear force (N)	505.0E+3	505.0E+3	505.0E+3	505.0E+3	505.0E+3	505.0E+3	505.0E+3	505.0E+3
epslon_x	-581.3E-6	-518.9E-6	63.0E-6	645.0E-6	1.2E-3	1.5E-3	1.8E-3	2.2E-3
beta	0.40	0.40	0.37	0.20	0.14	0.12	0.11	0.09
teta (degree)	29.00	29.00	29.44	33.51	37.59	39.63	41.66	44.53
wv (mm)	0.23	0.23	0.30	1.01	1.80	2.23	2.69	3.39
fw	4.00	4.00	4.00	4.00	2.24	1.80	1.80	1.54
vfib (N)	347.9E+3	347.9E+3	341.7E+3	291.2E+3	140.3E+3	104.8E+3	97.5E+3	75.4E+3
Vc (N)	482.1E+3	482.1E+3	440.5E+3	245.0E+3	169.7E+3	147.1E+3	129.8E+3	111.4E+3
Vs_necessary (N)	-325.0E+3	-325.0E+3	-277.1E+3	-31.2E+3	195.0E+3	253.1E+3	277.6E+3	318.2E+3
Av (m2)	0.0002	0.0002	0.0002	0.0002	0.0002	0.0002	0.0002	0.0002
s (m)	0.1	0.1	0.1	0.1	0.1	0.1	0.1	0.1
Vs_used (N)	579.8E+3	579.8E+3	569.4E+3	485.3E+3	417.5E+3	388.2E+3	361.2E+3	326.8E+3
Vr (N)	1.4E+6	1.4E+6	1.4E+6	1.0E+6	727.6E+3	640.1E+3	**588.6E+3**	513.6E+3

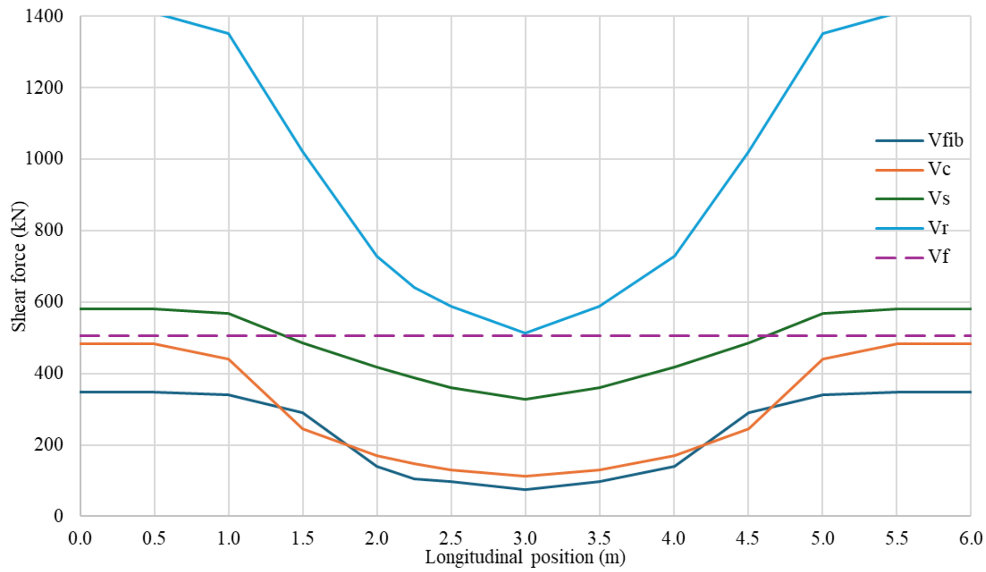

Figure B. 1– Graphic of shear resistance mechanism at every section of G1

B.3.2 - G2

G2 is the 6m girder, partially prestressed with stirrups on only one half of the specimen. To ease the fabrication process, the same stirrup layout was used on G1 and G2. Below on Table B. 10 is possible to see the variables used to calculate the expected shear resistance of the t-beam without stirrups. And on Table B. 11 and Table B. 12 the expected shear resistance is calculated at each section of the specimen.

Table B. 10 - Shear resistance variables for the design of a 6m specimen (G2).

dv	0.45	m
Es	200.0E+9	Pa
Ap	1.26E-03	m2
As	1.17E-03	m2
fpo	9.00E+08	Pa
sz	446.4	mm
sze	1041.60	mm
fc	100	Mpa
bw	0.36	m
ϕfib	1.00E+00	-
ϕc	1.00E+00	-
γf	3.30E-01	-
ϕs	1.00E+00	-

Table B. 11 - Shear resistance mechanism components at each 0.5m of the girder (G2)

x	**0**	**0.5**	**1**	**1.5**	**2**	**2.25**	**2.5**	**3**
Moments (Nm)	000.00E+0	140.35E+3	280.70E+3	421.05E+3	561.40E+3	631.58E+3	701.75E+3	800.00E+3
Shear force (N)	280.7E+3	280.7E+3	280.7E+3	280.7E+3	280.7E+3	280.7E+3	280.7E+3	280.7E+3
epslon_x	-589.1E-6	-554.4E-6	-231.0E-6	92.5E-6	416.0E-6	577.7E-6	739.4E-6	965.9E-6
beta	0.25	0.25	0.25	0.22	0.16	0.14	0.12	0.10
teta (degree)	29.00	29.00	29.00	29.65	31.91	33.04	34.18	35.76
wv (mm)	0.36	0.36	0.36	0.53	1.14	1.46	1.78	2.26
fw	4.00	4.00	4.00	4.00	3.78	3.12	2.46	1.80
vfib (N)	306.2E+3	306.2E+3	306.2E+3	298.2E+3	257.5E+3	203.5E+3	153.7E+3	106.0E+3
Vc (N)	327.5E+3	327.5E+3	327.5E+3	287.6E+3	201.6E+3	175.4E+3	155.3E+3	133.7E+3
Vs_necessary (N)	-352.9E+3	-352.9E+3	-352.9E+3	-305.0E+3	-178.5E+3	-98.2E+3	-28.3E+3	40.9E+3
Av (m2)	2E-11	2E-11	2E-11	2E-11	2E-11	2E-11	2E-11	2E-11
s (m)	0.1	0.1	0.1	0.1	0.1	0.1	0.1	0.1
Vs_used (N)	64.4E-3	64.4E-3	64.4E-3	62.7E-3	57.3E-3	54.9E-3	52.6E-3	49.6E-3
Vr (N)	633.6E+3	633.6E+3	633.6E+3	585.7E+3	459.2E+3	378.9E+3	**309.0E+3**	239.8E+3

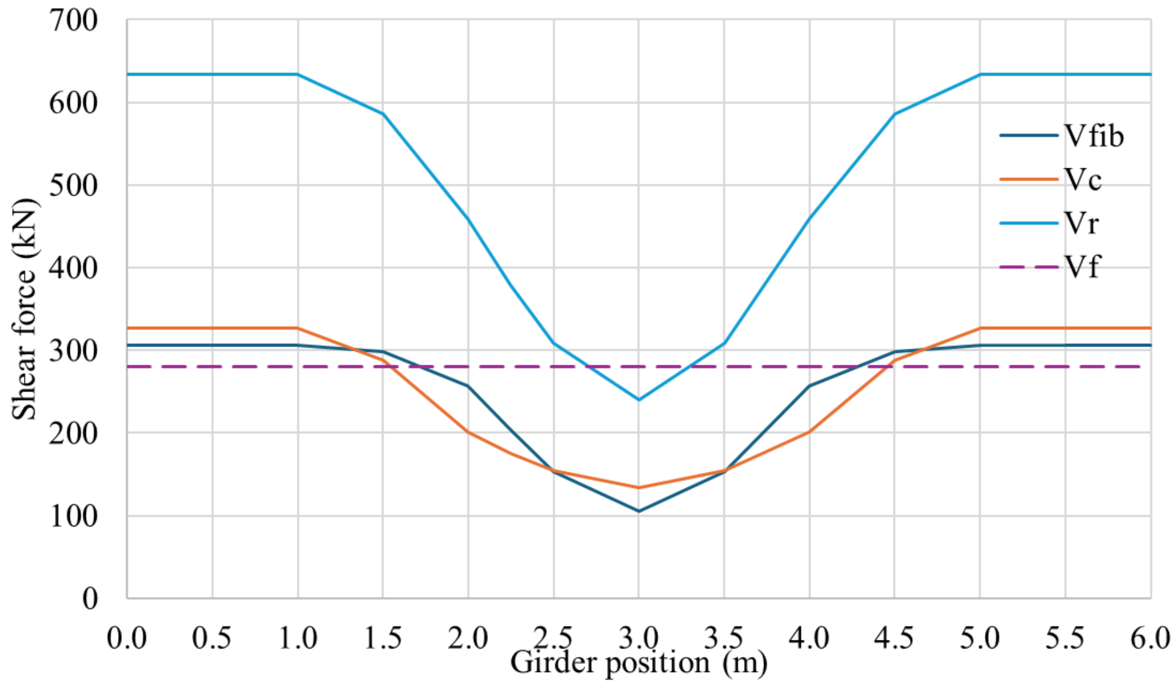

Figure B. 2- Graphic of shear resistance mechanism at every section of G2

B.3.3 - G3

G3 and G4 are the 3m specimens used to study shear. They have different geometry and no prestress. Since the S6.19 code does not differentiate the shear resistance between a rectangular beam and a T-beam, both beams should have the same expected resistance. However, the following calculations take into consideration the experimental fiber orientation of each beam, so a small difference can be noted. Below on Table B. 12 is possible to see the variables used to calculate the expected shear resistance of G3. And on Table B. 13 the expected shear resistance is calculated at each section of the specimen.

Table B. 12 - Shear resistance variables for the design of a 3m specimen (G3).

dv	0.45	m
Es	200.0E+9	Pa
Ap	1.26E-03	m2
As	1.17E-03	m2
fpo	0.00E+00	Pa
sz	446.4	mm
sze	1041.60	mm
fc	100	Mpa
bw	0.36	m
ϕfib	1.00E+00	-
ϕc	1.00E+00	-
γf	3.60E-01	-
ϕs	1.00E+00	-

Table B. 13- Shear resistance mechanism components at each 0.5m of the girder (G3)

x	**0**	**0.5**	**1**	**1.5**
Moments (Nm)	000.00E+0	138.89E+3	277.78E+3	375.00E+3
Shear force (N)	277.8E+3	277.8E+3	277.8E+3	277.8E+3
epslon_x	571.6E-6	605.9E-6	926.0E-6	1.2E-3
beta	0.14	0.13	0.11	0.09
teta (degree)	33.00	33.24	35.48	37.05
wv (mm)	1.44	1.51	2.17	2.66
fw (Mpa)	3.12	2.90	1.80	1.80
vfib (N)	222.4E+3	204.8E+3	116.9E+3	110.4E+3
Vc (N)	176.3E+3	171.5E+3	137.1E+3	120.2E+3
Vr (N)	398.7E+3	376.3E+3	**253.9E+3**	230.5E+3

B.3.4 – G4

G3 and G4 are the 3m specimens used to study shear. They have different geometry and no prestress. Since the S6.19 code does not differentiate the shear resistance between a rectangular beam and a T-beam, both beams should have the same expected resistance. However, the following calculations take into consideration the experimental fiber orientation of each beam, so a small difference can be noted. Below on Table B. 14 is possible to see the variables used to calculate the expected shear resistance of G4. And on Table B. 15 the expected shear resistance is calculated at each section of the specimen.

Table B. 14 - Shear resistance variables for the design of a 3m specimen (G4).

dv	0.45	m
Es	200.0E+9	Pa
Ap	1.26E-03	m2
As	1.17E-03	m2
fpo	0.00E+00	Pa
sz	446.4	mm
sze	1041.60	mm
fc	100	Mpa
bw	0.36	m
ϕfib	1.00E+00	-
ϕc	1.00E+00	-
γf	3.60E-01	-
ϕs	1.00E+00	-

Table B. 15- Shear resistance mechanism components at each 0.5m of the girder (G4)

x	**0**	**0.5**	**1**	**1.5**
Moments (Nm)	000.00E+0	138.89E+3	277.78E+3	375.00E+3
Shear force (N)	277.8E+3	277.8E+3	277.8E+3	277.8E+3
epslon_x	571.6E-6	605.9E-6	926.0E-6	1.2E-3
beta	0.14	0.13	0.11	0.09
teta (degree)	33.00	33.24	35.48	37.05
wv (mm)	1.44	1.51	2.17	2.66
fw (Mpa)	3.12	2.90	1.80	1.80
vfib (N)	240.9E+3	221.9E+3	126.6E+3	119.5E+3
Vc (N)	176.3E+3	171.5E+3	137.1E+3	120.2E+3
Vr (N)	417.2E+3	393.4E+3	**263.7E+3**	239.7E+3

B.5 Prestress loss for G1 and G2

Table A.2.1 - Tendon layouts and prestress considered after long term losses for G1.

y	Number of tendons per layer	Prestress (MPa)
57.5	0	0
107.5	3	1256
157.5	3	1256
207.5	3	1256

Table A.2.2 - Tendon layouts and prestress considered after long term losses for G2.

y	Number of tendons per layer	Prestress (MPa)
57.5	0	0
107.5	3	900
157.5	3	900
207.5	3	900

APPENDIX C SPECIMEN DRAWINGS (AS BUILT)

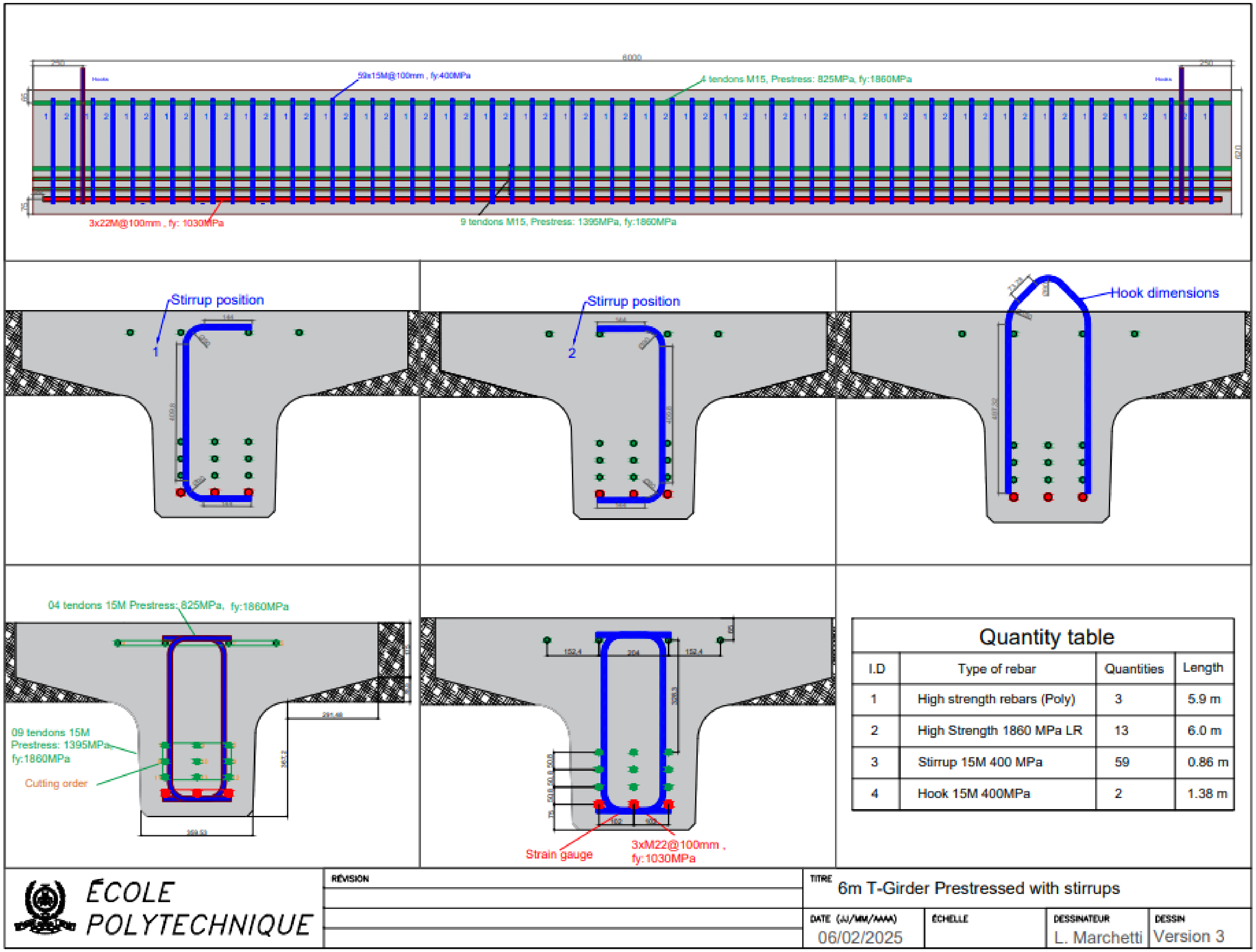

Quantity table

I.D	Type of rebar	Quantities	Length
1	High strength rebars (Poly)	3	5.9 m
2	High Strength 1860 MPa LR	13	6.0 m
3	Stirrup 15M 400 MPa	59	0.86 m
4	Hook 15M 400MPa	2	1.38 m

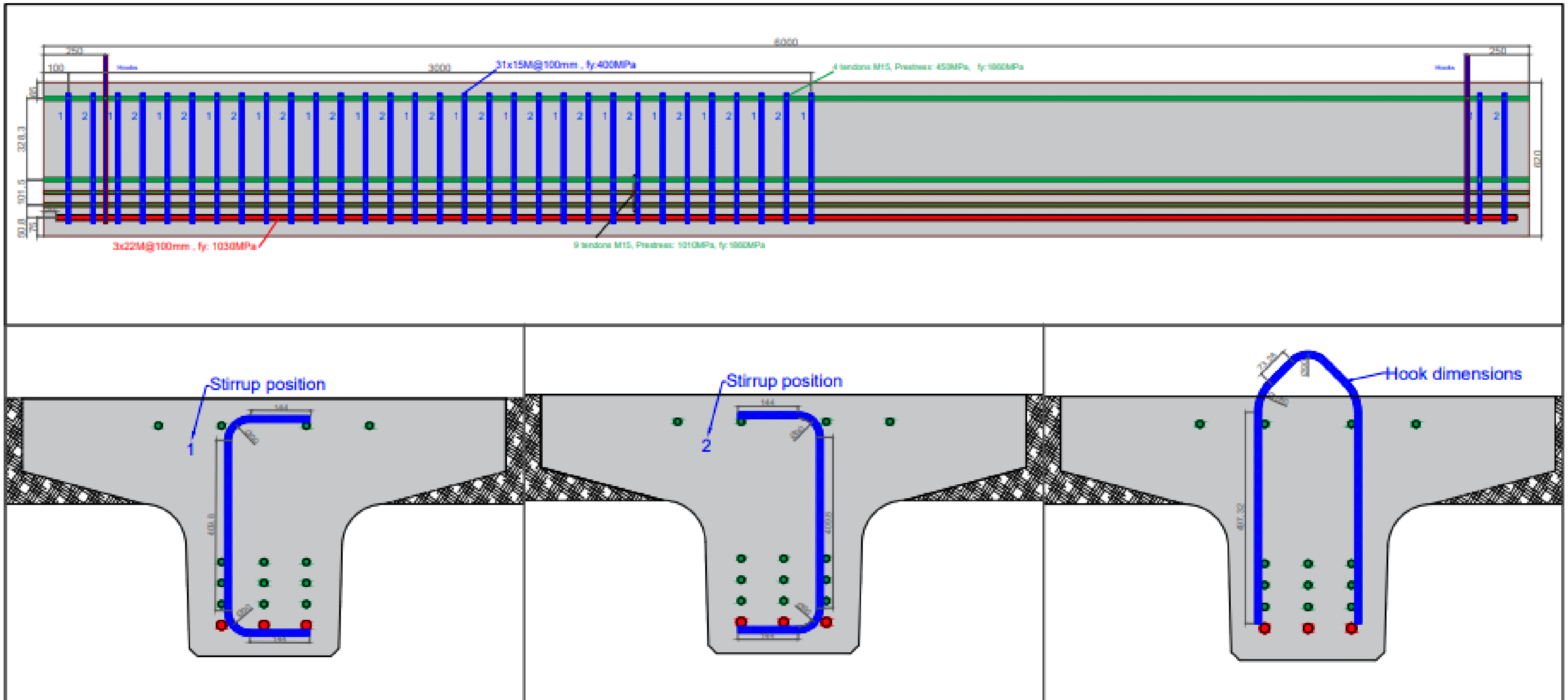

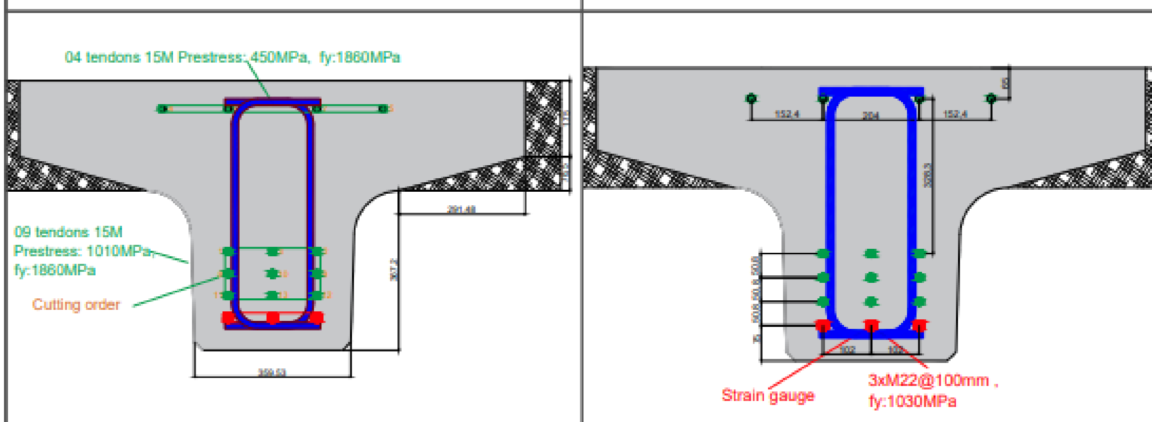

Quantity table			
I.D	Type of rebar	Quantities	Length
1	High strength rebars (Poly)	3	5.9 m
2	High Strength 1860 MPa LR	13	6.0 m
3	Stirrup 15M 400 MPa	33	0.86 m
4	Hook 15M 400MPa	2	1.38 m

ÉCOLE POLYTECHNIQUE

RÉVISION

TITRE 6m T-Girder Prestressed without stirrups

DATE (JJ/MM/AAAA)	ÉCHELLE	DESSINATEUR	DESSIN
06/02/2025		L. Marchetti	Version 3

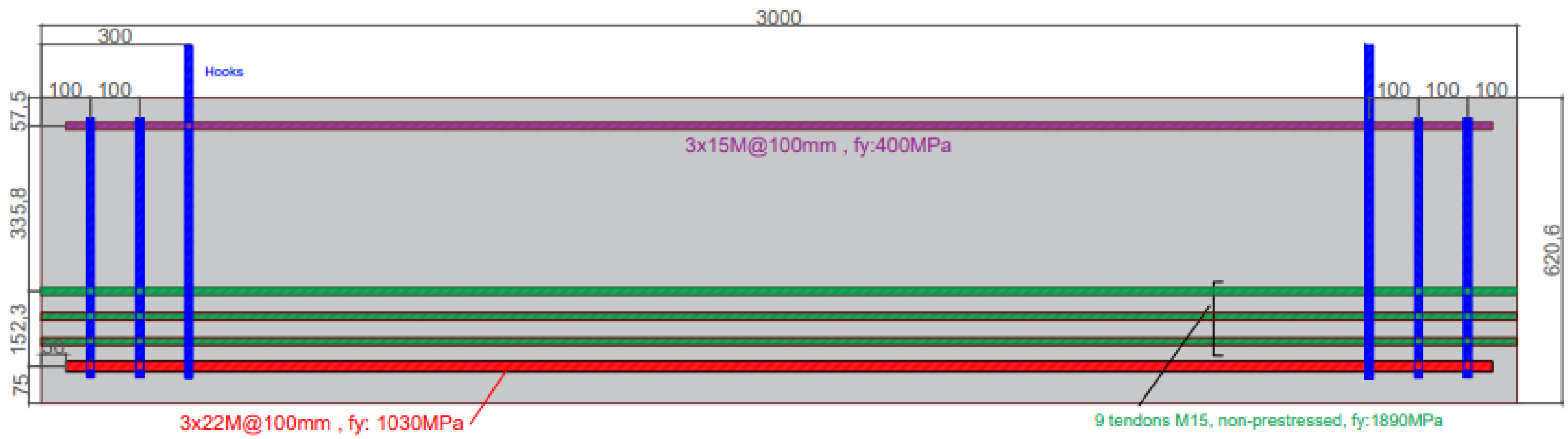

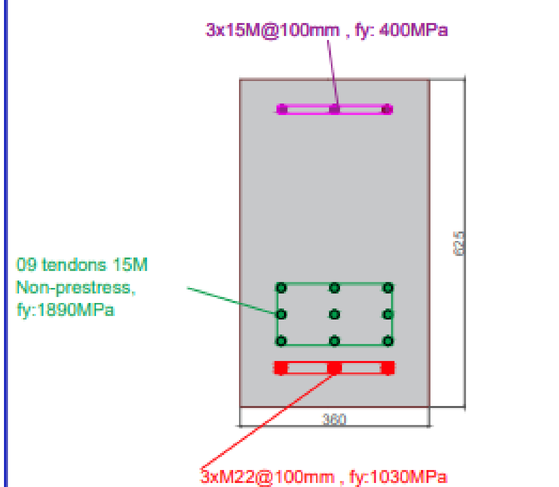

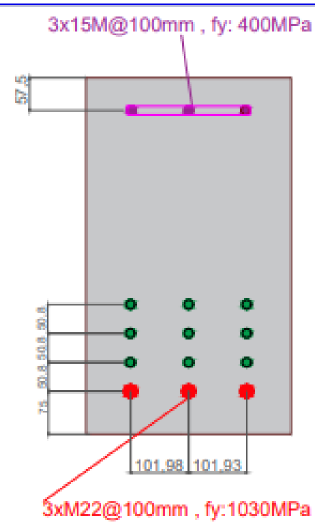

Quantity table

I.D	Type of rebar	Quantities	Length
1	High strength rebars (Poly)	3	2.9 m
2	High Strength 1860 MPa LR	9	3.0 m
3	Stirrup 15M 400 MPa	4	0.86 m
4	Hook 15M 400MPa	2	1.38 m
5	15M 400MPa rebar	3	2.9 m

ÉCOLE POLYTECHNIQUE

RÉVISION	TITRE			
	3m Rectangular Girder			
	DATE (JJ/MM/AAAA)	ÉCHELLE	DESSINATEUR	DESSIN
	06/02/2025		L. Marchetti	Version 3

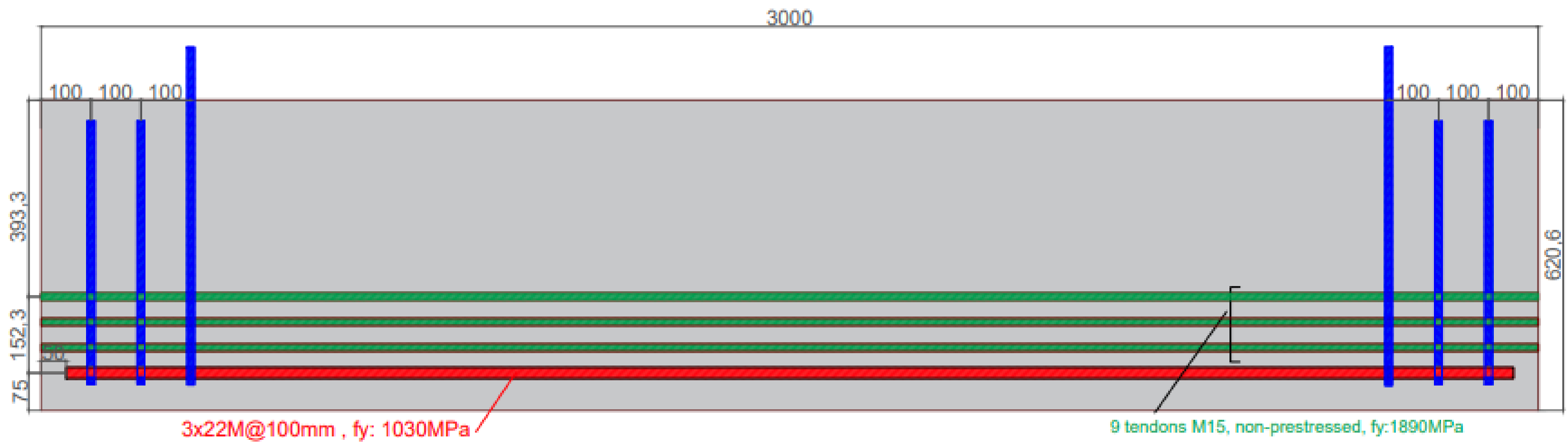

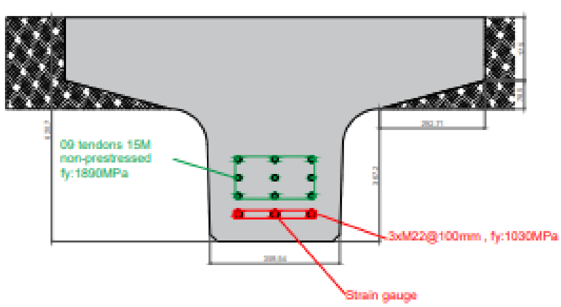

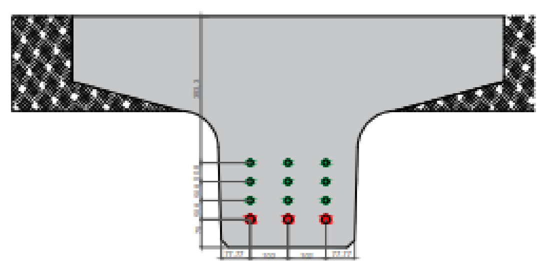

Quantity table

I.D	Type of rebar	Quantities	Length
1	High strength rebars (Poly)	3	2.9 m
2	High Strength 1860 MPa LR	9	3.0 m
3	Stirrup 15M 400 MPa	4	0.86 m
4	Hook 15M 400MPa	2	1.38 m

ÉCOLE POLYTECHNIQUE

RÉVISION	TITRE 3m T-Girder Non-Prestressed			
	DATE (JJ/MM/AAAA) 06/02/2025	ÉCHELLE	DESSINATEUR L. Marchetti	DESSIN Version 3

APPENDIX D MATLAB PROGRAM

D.1 Converting DIC data into crack points

```
myFolder = "C:\Users\Luiz Marchetti Neto\OneDrive - polymtl.ca\Desktop\Master's Project\Matlab\DIC results\P4";
filePattern = fullfile(myFolder, '*.mat');
thefiles = dir(filePattern);
load(myFolder+"\"+thefiles(1).name)
E1 = zeros(size(e1, 1), size(e1, 2), length(thefiles));
Disp_x = zeros(size(e1, 1), size(e1, 2), length(thefiles));
Disp_y = zeros(size(e1, 1), size(e1, 2), length(thefiles));
x_pos = zeros(size(e1, 1), size(e1, 2), length(thefiles));
y_pos = zeros(size(e1, 1), size(e1, 2), length(thefiles));
e1_P4 = zeros(size(e1, 1), size(e1, 2), length(thefiles));
for k = 1 : length(thefiles)
    load(myFolder+"\"+thefiles(k).name)
    Disp_x(:,:,k) = u;
    Disp_y(:,:,k) = v;
    x_pos(:,:,k) = X;
    y_pos(:,:,k) = Y;
    e1_P4(:,:,k) = e1;
    %30 to 135 is to adjust some noise in the data (varies from beam to
    %beam)
    for ln = 1:size(e1, 2)
        [pks,locs] = findpeaks(e1(1:size(e1, 1), ln), MinPeakHeight=0.45e-3);
        if isempty(locs) == 1
            E1(:,ln, k) = 0; % Assign zero to diff if no peaks are found
        else
            for cln = 1:length(locs)
                E1(locs(cln), ln, k) = pks(cln); % stablish the center of the crack
            end
        end
    end
end
save("e1_P4","e1_P4")
save("crack_path_P4","E1")
save("disp_x_P4","Disp_x")
save("disp_y_P4","Disp_y")
save("x","X")
save("y","Y")
```

D.2 Isolating critical crack, extracting coordinates and generating crack opening and crack slip

```
load("C:\Users\Luiz Marchetti Neto\OneDrive - polymtl.ca\Desktop\Master's Project\Matlab\Matlab - scripts\P4 Full Crack\crack_path_P4.mat")
myFolder = "C:\Users\Luiz Marchetti Neto\OneDrive - polymtl.ca\Desktop\Master's Project\Matlab\Matlab - scripts\P4 Full Crack";
load(myFolder+"\"+"disp_x_P4")
load(myFolder+"\"+"disp_y_P4")
load(myFolder+"\"+"x")
load(myFolder+"\"+"y")
crack = table([],[],[],[],[], 'VariableNames',["strain","x","y","disp_x","disp_y"]);
E1_test = E1;
for i = 1:size(E1_test,1)
    for j = 1:size(E1_test,2)
        if E1_test(i,j) == 0
            continue
        else
            line = {E1_test(i, j), X(i, j), Y(i, j), Disp_x(i, j), Disp_y(i, j)};
            crack = [crack; line];
        end
    end
end

a = (crack.x>-290 & crack.x<600 & crack.strain<0.016);
crack(a,:) = [];

a = (crack.x>-100 & crack.x<0 & crack.strain<0.035);
crack(a,:) = [];

a = (crack.x>500 & crack.y<150);
crack(a,:) = [];
a = (crack.x>700 & crack.y<240);
crack(a,:) = [];
a = (crack.x<-263);
crack(a,:) = [];
a = (crack.x>726);
crack(a,:) = [];
a = (crack.y>250);
crack(a,:) = [];
a = (crack.x>200 & crack.y<-200);
crack(a,:) = [];
a = (crack.x<640 & crack.strain<0.007);
crack(a,:) = [];
a = (crack.y<225 & crack.strain<0.01);
crack(a,:) = [];
a = (crack.y>-200 & crack.y<130 & crack.strain<0.03);
crack(a,:) = [];
```

```
a = (crack.y>-250 & crack.y<130 & crack.strain<0.042);
crack(a,:) = [];
a = (crack.y>100 & crack.y<200 & crack.strain<0.018);
crack(a,:) = [];
a = (crack.y>100 & crack.y<175 & crack.strain<0.025);
crack(a,:) = [];
a = (crack.y>-100 & crack.y<-50 & crack.strain<0.075);
crack(a,:) = [];
a = (crack.y<-275);
crack(a,:) = [];
a = (crack.x>50 & crack.x<150 & crack.strain<0.0965);
crack(a,:) = [];
crack = sortrows(crack, {'x', 'y'}, {'descend', 'descend'});

sub_table = table([],[],[],[],[], 'VariableNames',["strain","x","y","pos_x","pos_y"]);
for i=1:size(crack,1)
    [row_y, column_y] = find(abs(Y-table2array(crack(i,"y"))) < 0.0001);
    [row_x, column_x] = find(abs(X-table2array(crack(i,"x"))) < 0.0001);
    row = row_x(ismember(row_x,row_y));
    column = column_x(ismember(column_x,column_y));
    line = {table2array(crack(i,"strain")), abs(table2array(crack(i,"x")) - table2array(crack(1,"x"))), abs(table2array(crack(i,"y")) - table2array(crack(1,"y"))), row(1), column(1)};
    sub_table = [sub_table; line];
end
non_changed = crack;
clear crack
crack = sub_table;
clear sub_table
for i=1:size(crack,1)
    if table2array(crack(i,"strain")) == E1(table2array(crack(i,"pos_x")), table2array(crack(i,"pos_y")))
        continue
    else
        i
    end
end

data_base = table([],[],[],[],[],[],[],'VariableNames',["x","y","dx1t","dy1t","dx2t","dy2t","angle"]);
x_pos = 1:size(Disp_x,2);
y_pos = 1:size(Disp_y,1);
angle = [];
for i = 1:size(crack,1)-1
    delta_y = table2array(crack(i+1,"y")) - table2array(crack(i,"y"));
    delta_x = table2array(crack(i+1,"x")) - table2array(crack(i,"x"));
    angle = [angle;atan(delta_y/delta_x)];
end

angle(1:18,1) = sum(angle(1:18,1))/18;
```

```
angle(19:28,1) = sum(angle(19:28,1))/9;
angle(29:42,1) = sum(angle(29:42,1))/13;
angle(43:74,1) = sum(angle(43:74,1))/31;
angle(75:83,1) = sum(angle(75:83,1))/8;
angle(84:92,1) = sum(angle(84:92,1))/8;
angle(93:99,1) = sum(angle(93:99,1))/6;
angle(100:121,1) = sum(angle(100:121,1))/21;
angle(122:139,1) = sum(angle(122:139,1))/17;
angle(140:193,1) = sum(angle(140:193,1))/53;
angle(194:205,1) = sum(angle(194:205,1))/11;
angle(206:224,1) = sum(angle(206:224,1))/17;
angle(225:232,1) = sum(angle(225:232,1))/7;
angle(233:308,1) = sum(angle(233:308,1))/75;
angle(309:323,1) = sum(angle(309:323,1))/14;
angle(324:376,1) = sum(angle(324:376,1))/52;
angle(377:382,1) = sum(angle(377:382,1))/5;
angle(383:559,1) = sum(angle(383:559,1))/176;
angle(560:575,1) = sum(angle(560:575,1))/15;
angle(576:595,1) = sum(angle(576:595,1))/19;
angle(596:605,1) = sum(angle(596:605,1))/9;
angle(606:644,1) = sum(angle(606:644,1))/38;
for i = 1:size(crack,1)-1
    loc_y_pre = table2array(crack(i,"pos_x"));
    loc_x_pre = table2array(crack(i,"pos_y"));
    beta = 1.5708-angle(i,1);
    if rad2deg(beta)>80
        offset_x = 6;
        offset_y = 0;
    else
        offset_x = 6;
        offset_y = round(offset_x*tan(beta));
    end
    dx1t = Disp_x(loc_y_pre+offset_y, loc_x_pre - offset_x);
    dy1t = Disp_y(loc_y_pre+offset_y, loc_x_pre - offset_x);
    dx2t = Disp_x(loc_y_pre-offset_y, loc_x_pre + offset_x);
    dy2t = Disp_y(loc_y_pre-offset_y, loc_x_pre + offset_x);
    line = {table2array(crack(i,"x")), table2array(crack(i,"y")), dx1t, dy1t, dx2t, dy2t, angle(i,1)};
    data_base = [data_base;line];
end

final_data = table([],[],[],[],[],'VariableNames',["x","y","slip","crack_opening","angle"]);
for i =1:size(data_base, 1)
    diff_x = table2array(data_base(i,"dx1t"))-table2array(data_base(i,"dx2t"));
    diff_y = table2array(data_base(i,"dy1t"))-table2array(data_base(i,"dy2t"));
    x_lin = diff_x*cos(angle(i,1))-diff_y*sin(angle(i,1));
    y_lin = diff_x*sin(angle(i,1))+diff_y*cos(angle(i,1));
    line = {table2array(data_base(i,"x")), table2array(data_base(i,"y")), abs(x_lin), abs(y_lin), angle(i,1)};
```

```
    final_data = [final_data;line];
end

```